Nonlinear physical modelling and dynamic analysis of cantilever beams in confined axial flow

Filipe Soares

To cite this version:

Filipe Soares. Nonlinear physical modelling and dynamic analysis of cantilever beams in confined axial flow. Mechanical engineering [physics.class-ph]. Instituto superior técnico (Lisbonne), 2024. English. ⟨NNT : ⟩. ⟨tel-04456405⟩

HAL Id: tel-04456405
https://theses.hal.science/tel-04456405v1

Submitted on 14 Feb 2024

UNIVERSIDADE DE LISBOA
INSTITUTO SUPERIOR TÉCNICO

Nonlinear physical modelling and dynamic analysis of cantilever beams in confined axial flow

Filipe da Cruz Soares

Supervisor:	Doctor José Manuel Vieira Antunes
Co-Supervisors:	Doctor Vincent Georges Mickael Debut Doctor Christophe Vergez

Thesis approved in public session to obtain the PhD Degree in
Mechanical Engineering

Jury final classification: **Pass with Distinction**

2024

UNIVERSIDADE DE LISBOA
INSTITUTO SUPERIOR TÉCNICO

Nonlinear physical modelling and dynamic analysis of cantilever beams in confined axial flow

Filipe da Cruz Soares

Supervisor:	Doctor José Manuel Vieira Antunes
Co-Supervisors:	Doctor Vincent Georges Mickael Debut Doctor Christophe Vergez

Thesis approved in public session to obtain the PhD Degree in
Mechanical Engineering

Jury final classification: **Pass with Distinction**

Jury

Chairperson:	Doctor Hélder Carriço Rodrigues, Instituto Superior Técnico, Universidade de Lisboa
Members of the Committee:	Doctor Njuki Mureithi, Polytechnique Montréal, Canadá Doctor Júlio Martins Montalvão e Silva, Instituto Superior Técnico, Universidade de Lisboa Doctor Pedro Manuel Leal Ribeiro, Faculdade de Engenharia, Universidade do Porto Doctor José Manuel Vieira Antunes, Instituto Superior Técnico, Universidade de Lisboa Doctor António Manuel Relógio Ribeiro, Instituto Superior Técnico, Universidade de Lisboa Doctor Pedro da Graça Tavares Alvares Serrão, Instituto Superior Técnico, Universidade de Lisboa

Funding Institution: FCT - Fundação para a Ciência e a Tecnologia

2024

Abstract

The work presented in this thesis deals with the fluid-structure interaction of a flexible cantilevered beam subject to axial flow in a confined passage. This problem represents a benchmark example of flow-induced vibrations, whose fundamental behaviour can be found in numerous practical applications. The inherent nonlinear nature of this archetypal physical system leads to a wide variety of complex dynamics that is, to this day, not yet fully understood. Contrary to most past studies, mainly focused on the critical conditions leading to flutter instabilities, this thesis is focused on the physical modelling and analysis of post-critical dynamics. Modelling efforts are pursued on a one-dimensional framework composed of a flexible cantilever beam surrounded by incompressible flow on its upper and lower sides. The flow is modelled by bulk-flow equations and dissipative effects are included in the form of distributed and localised head-loss terms. An analytical formulation based on formal solutions of the flow fields is first proposed, leading to a compact system of nonlinear ODEs that can be used for the temporal integration of post-critical regimes. Moreover, the inclusion of a contact model allowed for the calculation of limit-cycle oscillations with intermittent impacts between the beam and the channel walls. A more comprehensive study of the nonlinear dynamics was then pursued using methods for the continuation of periodic solutions and bifurcation analysis. To this aim, a *Tau-Galerkin* method for the spatial discretization of the coupled system was developed, leading to reduced formulations that can deal with time-dependent nonlinear flow boundary conditions in a well-posed manner and are suited for the use of bifurcation analysis tools. Results illustrate many aspects of the behaviour observed experimentally including subcritical bifurcations and hysteresis, zones of multi-stability, quasi-periodic and chaotic motions. Experiments were conducted to validate modelling results and provide a detailed account of nonlinear regimes encountered, including vibro-impact dynamics. Aside from providing novel insights into the physics of fluttering beams and suggesting news avenues of research, is it hoped that the methods and results presented can stimulate similar studies in the field of flow-induced vibrations.

Keywords: fluid-structure interaction; flow-induced vibrations; beam in axial flow; nonlinear dynamics; bifurcation analysis.

Resumo

O trabalho apresentado nesta tese trata a interação fluido-estrutura de uma viga encastrada-livre sujeita a escoamento axial num canal confinado. Este problema representa um exemplo de referência de vibrações induzidas por escoamento, cujo comportamento fundamental pode ser encontrado em inúmeras aplicações práticas. A natureza não linear inerente desse sistema físico arquetípico conduz a uma ampla variedade de comportamentos dinâmicos que, até hoje, ainda não são bem compreendidos. Contrariamente à maioria dos estudos anteriores, maioritariamente focados nas condições críticas que levam a instabilidades do tipo *flutter*, nesta tese o foco é dado à modelação física e análise da dinâmica pós-crítica. Os esforços de modelação são realizados num contexto unidimensional composto por uma viga flexível cercada por um escoamento incompressível nos seus lados superior e inferior. O escoamento é modelado por equações de tipo *bulk-flow* e os efeitos dissipativos são incluídos através de termos de perda de carga distribuída e localizada. Uma formulação analítica baseada em soluções formais dos campos de velocidade e pressão é inicialmente proposta, levando a um sistema compacto de equações ordinárias não lineares que podem ser usadas para a análise de regimes pós-críticos. Além disso, a inclusão de um modelo de contato permite o cálculo de oscilações de ciclo limite com impactos intermitentes entre a viga e as paredes do canal. Um estudo mais abrangente da dinâmica não linear foi feito usando métodos para a continuação de soluções periódicas e análise de bifurcações. Para isso, um método *Tau-Galerkin* para a discretização espacial do sistema acoplado foi desenvolvido, levando a formulações reduzidas aptas a lidar com condições aos limites não-lineares e dependentes do tempo de uma maneira bem colocada. Esta formulação é também adequada para o uso de ferramentas de análise de bifurcações.Os resultados ilustram vários aspetos do comportamento observado experimentalmente, incluindo bifurcações subcríticas e histerese, zonas de multi-estabilidade, movimentos quasi-periódicos e caóticos. Experiências foram conduzidos para validar os resultados do modelo e fornecer um relato detalhado dos regimes não lineares encontrados, incluindo a dinâmica de vibro-impactos. Além de fornecer novas perspetivas sobre a física de placas vibrantes em escoamento e sugerir novos caminhos de pesquisa, espera-se que os métodos e resultados apresentados possam estimular estudos semelhantes no campo de vibrações induzidas por escoamento.

Palavras-chave: interação fluido-estrutura; vibrações induzidas por escoamento; vigas sob escoamento axial; dinâmica não linear; análise de bifurcações.

Contents

Acknowledgements

First of all, I would like to thank my supervisors José Antunes, Vincent Debut and Christophe Vergez for their advice and guidance throughout the last four years. There is no doubt your mentorship has made me grow as a scientist but, more importantly, your endless curiosity and enthusiasm for science and research has been truly inspiring. I am truly grateful to have had your company over the last few years and hope to continue working closely with you in the years to come.

I would also like to thank the whole team at the Laboratoire de Mécanique et d'Acoustique for the welcoming reception as well as the many helpful discussions and unhesitant support. A particular thanks to Bruno Cochelin for the many suggestions regarding the numerical intricacies of Manlab as well as Fabrice Silva, Etienne Gourc and Vincent Long for their support during the experiments.

I would also like to thank my parents, grandparents and brothers for all their support and enthusiasm. Finally, I would like to thank my wife Olga Pavlovska for her unwavering support throughout these years and her seemingly endless patience.

List of symbols

Unless explicitly stated, the upper dash $\bar{a}$ and tilde-hat $\tilde{a}$ correspond, respectively, to the steady and fluctuating components of a particular variable, following the convention $a(x,t) = \bar{a}(x) + \tilde{a}(x,t)$. Moreover, the dashes in $a'(x)$ represent spatial derivatives $\partial / \partial x$, while the upper dots $\dot{a}(t)$ denote time derivatives $\partial / \partial t$. Below is a list of symbols used throughout this thesis as well as an indication of where they are defined.

a	Pseudo-arc length parameter, Eq.(5.4)
$a_{\max}$	Upper bound of “working domain”, Eq.(5.8)
$a_{c,n}$	Auxiliar variable, Eq.(3.21)
A^*	Amplitude of limit cycle oscillation, Eq.(6.13) or Eq.(A.1)
A_m	Peak modal displacement amplitude, Section 5.2.2
$A_c(x,t)$	Auxiliar variable, Eq.(3.3)
$\bar{A}_{c,n}(x)$	Auxiliar variable, Eq.(3.16)
$A_{mn},[\mathbf{A}]$	Spatial operator 2D matrix, Eq.(4.17)
α	Dimensionless parameter governing gravity-induced tension, Eq.(C.3)
$b_{c,n}$	Auxiliar variable, Eq.(3.21)
$B_c(x,t)$	Auxiliar variable, Eq.(3.3)
$\bar{B}_{c,n}(x)$	Auxiliar variable, Eq.(3.16)
$B_{sn},[\mathbf{B}]$	Spatial operator 2D matrix, Eq.(4.17)
β_m	Solution coefficients for the beam equation, Eq.(2.4)
$\beta(\ )$	Beta function, Eq.(6.11)

c	Channel index, $c = 1$ for upper or $c = 2$ for lower; Clearance gap, Section 6.1
c^*	Dimensionless clearance gap, Section 6.1
$c_{c,n}$	Auxiliar variable, Eq.(3.21)
$C_c(x,t)$	Auxiliar variable, Eq.(3.3)
$\bar{C}_{c,n}(x)$	Auxiliar variable, Eq.(3.16)
$C_{sn},[\mathbf{C}]$	Spatial operator 2D matrix, Eq.(4.17)
d_c	Auxiliar variable, Eq.(3.21)
$D_c(x,t)$	Auxiliar variable, Eq.(3.3)
$\bar{D}_{c,n}(x)$	Auxiliar variable, Eq.(3.16)
$D_{msn},[\mathbf{D}]$	Spatial operator 3D matrix, Eq.(4.17)
$\delta p(x,t)$	Pressure difference between channels, Eq.(2.12)
e	Thickness of beam
E	Young modulus
E_f	“Equivalent” Young modulus, Eq.(6.6)
e_c	Auxiliar variable, Eq.(3.21)
$E_c(x,t)$	Auxiliar variable, Eq.(3.3)
$\bar{E}_c(x)$	Auxiliar variable, Eq.(3.16)

$E_{rn}, [\mathbf{E}]$	Spatial operator 2D matrix, Eq.(4.14)
ε	Small tolerance parameter, Sections 3.4.2, 5.1.2 or 5.3.1
f	Fanning friction coefficient, Eq.(2.25)
f_0	Frequency of limit cycle
$F_i(x,t)$	Impact force, Eq.(3.26)
$F_m(t)$	Modal forces, Eq.(2.12)
$\bar{F}_c(x)$	Auxiliar variable, Eq.(3.16)
$F_{nsr}, [\mathbf{F}]$	Spatial operator 3D matrix, Eq.(4.14)
$\phi_m(x)$	Mode shape of the m^{th} beam mode, Eq.(2.5)
ϕ	Modal phase difference, Section 5.2.2
g	Acceleration of gravity, Appendix C
$\mathbf{g}(t)$	Vector containing variables of a periodic solution, Eq.(5.1)
$\mathbf{G}$	Vector containing variables and control parameter of a periodic solution, Eq.(5.5)
G_{mn}	Spatial operator 2D matrix, Eq.(C.5)
h	Harmonic index, Eq.(5.1)
$h_c(x,t)$	Fluctuating channel height, Eq.(2.18)
H	Harmonic truncation, Eq.(5.1)
H^*	Confinement ratio, Eq.(2.40)
$H_1(x)$	Fixed profile of the upper channel
$H_2(x)$	Fixed profile of the lower channel
$H_{tr}, [\mathbf{H}]$	Spatial operator 2D matrix, Eq.(4.14)
H_0	Total height of both channels
H_L	Height of channel at exit, Eq.(5.14)
η	Width of hysteresis loop, Eq.(1.13)

i	Imaginary unit
I	Moment of inertia
$[\mathbf{I}]$	Identity matrix
k_i	Impact stiffness, Eq.(3.26)
k_i^*	Dimensionless impact stiffness, Section 3.4.8
K_L	Exit head-loss coefficient, Section 2.2.2
K_0	Entry head-loss coefficient, Section 2.2.2
L	Length of beam
λ	Control parameter for continuation, Section 5.1.2
m	Index for beam modes
m_0	Total mass of beam, Section 2.3
m_m	Modal mass of the m^{th} beam mode,
M	Modal truncation, Eq.(2.6)
M^*	Fluid-beam mass ratio, Eq.(2.33)
n	Index for velocity field expansions
N	Truncation of velocity expansions, Eq.(4.5)
ω_0	Beam characteristic frequency, Eq.(2.29)
ω_m	Angular frequency of the m^{th} beam mode
Ω^*	Dimensionless frequency
Ω_0	Frequency of limit cycle (dimensionless)
$[\Omega]$	Diagonal matrix containing modal frequencies
$p_c(x,t)$	Flow pressure field in channel c
$\breve{p}_r(t)$	Coefficients of the pressure field expansion in upper channel, Eq.(4.6)

$\widehat{p}_r(t)$	Coefficients of the pressure field expansion in lower channel, Eq.(4.6)
$P_L(t)$	Pressure at downstream reference chamber, Section 2.2.2
$P_0(t)$	Pressure at upstream reference chamber, Section 2.2.2
$\mathbf{P}(t)$	Vector containing pressure expansion coefficients, Section 4.1.3
$q_m(t)$	Modal displacement coefficients, Eq.(2.5)
$Q_c(t)$	Global unsteady flow rate in channel c, Eq.(3.1)
$\mathbf{Q}(t)$	Vector containing modal displacements, Section 4.1.3
r	Index for velocity expansion coefficients
$r_m(t)$	Modal velocity coefficients
R	Truncation of pressure expansions, Eq.(4.6)
$\mathbf{R}(t)$	Vector containing modal velocities
Re	Reynolds number, Eq.(1.4) or Eq.(2.26)
ρ	Density of fluid
ρ_s	Density of beam
s	Alternative index for velocity expansion coefficients
S	Cross-sectional area of the beam, $w \times e$
St	Strouhal number, Eq.(1.5)
S_{mr}	Spatial operator 2D matrix, Eq.(4.8)
$S_c(t)$	Constant of integration representing entry pressure, Eq.(3.2)
t	Time variable
T_0	Period of limit cycle
$T_n(x)$	Chebyshev polynomials of the first kind, Eq.(4.1)
$\bar{T}_n(x)$	Shifted Chebyshev polynomials, Eq.(4.3)
$u(r)$	Flow velocity profile, Eq.(6.10)
$u_c(x,t)$	Flow velocity field in channel c
$\breve{u}_r(t)$	Coefficients of the velocity field expansion in upper channel, Eq.(4.5)
$\widehat{u}_r(t)$	Coefficients of the velocity field expansion in lower channel, Eq.(4.5)
U^*	Reduced flow velocity, Eq.(1.1) or Eq.(2.39)
U	Flow velocity
U_{max}	On-axis flow velocity, Eq.(6.10)
U_{avg}	Average flow velocity, Eq.(6.12)
$\mathbf{U}(t)$	Vector containing velocity expansion coefficients
$v(x,t)$	Impact violation, Eq.(3.26)
ν	Dynamic viscosity of the fluid
w	Width of beam (spanwise)
w^*	Aspect ratio of beam, Section 6.1
$w(x)$	Kernel for Chebyshev orthogonality, Eq.(4.2)
$\bar{w}(x)$	Kernel for shifted Chebyshev orthogonality, Eq.(4.4)
x	Space variable
$y(x,t)$	Transverse displacement of the beam
$y_L(t)$	Beam-tip displacement, Eq.(5.9)
$[Z]$	Diagonal matrix containing modal damping ratios, ζ_m
ζ_m	Damping ratio of the m^{th} beam mode

Supplementary Material

As a complement to this thesis, a series of videos files are provided, pertaining to the experimental part of this work. The files contain slow-motion videos, showing the transverse beam motion recorded during the experiments. The used high-speed camera was operating at 240 frames per second (fps). In the provided video files however, frames are shown at a frequency of 30 fps.

Two sets of videos are provided. The first set pertains to the experiments conducted in a symmetric system (described in Chapter 6), and each video file illustrates the motion of the same beam (constant mass-ratio M^*) at different reduced flow velocities U^*. The files in this first set are labelled:

→ "video_M0.258.mp4";
→ "video_M0.485.mp4";
→ "video_M0.63.mp4";
→ "video_M0.98.mp4";
→ "video_M4.mp4".

The second set of files pertain to the experiments conducted in an asymmetric system (described in Appendix D), where flow resistance is gradually increased in the left channel why the right channel is unobstructed. Two files are provided:

→ "video_increasing_resistance.mp4";
→ "video_overview.mp4".

The file labeled "video_increasing_resistance.mp4" shows slow-motion videos of a single beam (constant mass-ratio M^*), for various flow resistances in the left channel. The file labeled "video_overview.mp4" shows a quick overview of the experimental procedure, for clarity.

If these files are not available to the reader, they can be provided following a request sent to the following e-mail address: filipedcsoaresmail.com

Abbreviations

ANM	Asymptotic Numerical Method
CFD	Computational Fluid Dynamics
DAE	Differential-Algebraic Equations
DMD	Dynamic Mode Decomposition
FB	Fold Bifurcation
FIV	Flow Induced Vibrations
FSI	Fluid-Structure Interaction
HB	Hopf Bifurcation
HBM	Harmonic Balance Method
LCO	Limit Cycle Oscillation
ODE	Ordinary Differential Equation
PDE	Partial Differential Equation
SVD	Singular Value Decomposition
TB	Torus Bifurcation
VIV	Vortex Induced Vibrations

Chapter 1

Introduction

The work in this thesis concerns the fluid-structure interaction of a flexible beam subject to axial flow. Perhaps the most familiar example is that of a flag flapping under steady wind. The inherent nonlinear nature of this archetypal physical system leads to a wide variety of complex dynamical behavior that has attracted the attention of scientists over many decades and, to this day, various aspects of their behavior are not yet fully understood. Aside from having become a benchmark problem in the field of flow-induced vibrations, its fundamental behavior is found in numerous engineering contexts and industrial applications. In this chapter we start by discussing some fundamental aspects of flow-induced vibrations to introduce important concepts and clarify some common misconceptions. A literature review, necessarily compact, is presented to provide the reader with the theoretical context of the problem and an idea of the work done so far. We also discuss some of the unanswered questions in the field and the motivations behind the present work. To conclude, a summary of the original contributions of this work is presented.

1.1 Context and some fundamental concepts

This work deals with the nonlinear modelling and dynamical analysis of slender flexible beams under axial flow. This is a classic example of fluid-elasticity whereby, under the action of passing flow, a flexible plate can exhibit a variety of both static and dynamic instabilities leading to buckling, limit-cycle oscillations, hysteresis, quasi-periodic and even chaotic motions. The literature on the subject is vast and a number of comprehensive reviews can be found, for example, in the textbook by Michael Païdoussis *Fluid-Structure Interactions: Slender Structures in Axial Flow* (2004), or in reviews by Shelley and Zhang (2011) or Yu et al. (2019). Even though in this work focus is given to incompressible flows in subsonic conditions, it is also worth mentioning the monograph by Earl H. Dowell *Aeroelasticity of Plates and Shells* (1975) which also deals with compressible and supersonic flows.

In this thesis we focus on one of the most studied cases, where the plate is clamped at the upstream end and free downstream, i.e. the cantilevered plate. This configuration is similar to the familiar example of a flag flapping in the wind. At this point it is worth mentioning that, throughout literature, the structural element in this type of systems is often described by various terms: strip, sheet, panel, film, plate, beam, etc. Moreover, a commonly used terminology is that of a flapping *flag*. Naively, one might think that the term *flag* is employed to describe a planar structure that has very low (or perhaps even negligible) bending stiffness. However, virtually all studies in the field employ models of what a mechanical engineer would term a *plate*. Additionally, when the spanwise direction is ignored, as is often the case, the structure can be regarded as a *beam*. Following this, perhaps more generic, mechanical engineering convention, we will henceforth refer to the structure as a plate or beam.

By far the most studied configuration is that of a finite plate in open-flow, where confinement effects from the presence of nearby rigid walls are ignored. In this thesis we study the case of beams in confined configurations i.e. in *channel flow*. In terms of linear dynamics and small amplitude oscillations, the core essence of the problem is very close to open-flow configurations, with the effect of confinement being mostly quantitative, i.e. even though the confinement affects critical velocities and stability boundaries, the qualitative character of the instabilities (characteristic beam motion, frequencies, etc.), remain approximately the same. However, in the nonlinear case, strong flow nonlinearities and dissipative effects as well as the possibility of contact between the beam and the side walls will lead to more complex behavior, that is qualitatively different from that found in open-flow cases.

By and large, modelling efforts are generally pursued under the assumption that flow and structural spanwise effects can be considered negligible. Additionally, if the *beam* thickness e is considered small compared to its characteristic length $e \ll L$, the problem can be reduced to one with two-dimensional flow and one-dimensional structural motion, as illustrated in Figure 1.1. Here, the beam is centralized along the channel, resulting in a symmetric system.

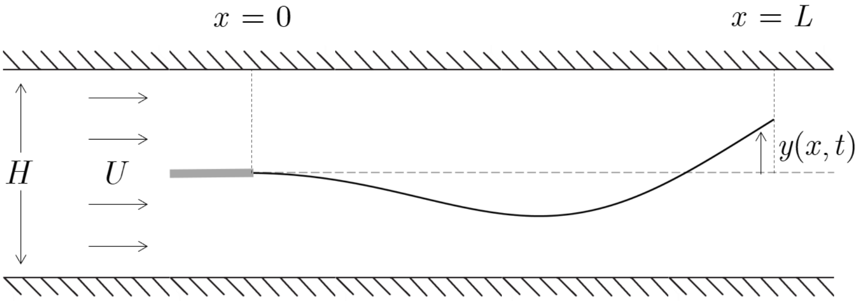

Figure 1.1 – Diagram of the considered system composed of a cantilever beam in two-dimensional confined axial flow.

1.1.1 Predominant dimensionless parameters

Under the most simplistic scenario, considering an inviscid and incompressible flow without confinement ($H = \infty$) and a uniform conservative beam, most developed models lead to systems whose dynamical behavior is controlled by solely two dimensionless parameters: a reduced flow velocity U^* and a fluid-beam mass ratio M^*. The reduced flow velocity U^* is typically given in the following form

$$U^* = \frac{U}{\omega_0 L} \tag{1.1}$$

where U is the velocity of the incoming flow, L is the length of the beam and ω_0 is some characteristic frequency of the beam that relates its elastic and inertial forces. In essence, this reduced velocity can be viewed as the inverse of a Strouhal number, relating a characteristic (wave) velocity associated with the beam and the velocity of the incoming flow. The fluid-beam mass ratio M^* is commonly given by

$$M^* = \frac{\rho_f L}{\rho_s e} \tag{1.2}$$

where ρ_f and ρ_s are the densities of the fluid and the beam, respectively, and e denotes the beam thickness. This parameter normalizes the inertial forces of the fluid by the mass (per unit length) of the beam. Low values of M^* will represent systems with either a light fluid or a heavy/short beam (typical in air/gas flow contexts) while large values of M^* will be associated with a dense fluid or a light/long beam (typical in liquid flow contexts).

By now it is well-established that the mass-ratio and reduced velocity (M^*, U^*) play a dominant role in defining the dynamics of the system. However, when more complex configurations are studied, other important dimensionless parameters come into play. In confined configurations with symmetric channels (as in Figure 1.1), the confinement ratio is introduced

$$H^* = \frac{H}{L} \tag{1.3}$$

Additionally, dissipative effects at the flow and structural levels are also known to be important in defining the system dynamics. Internal losses in the structure are generally described by some dimensionless damping coefficient (such as the modal damping ratio ζ, commonly used in modal frameworks). Viscous effects in the flow are generally represented by a Reynolds number Re (or equivalent dimensionless parameter), defined in a scenario of steady confined flow by

$$\mathrm{Re} = \frac{HU}{\nu} \tag{1.4}$$

where ν is the kinematic viscosity of the fluid.

1.1.2 Flutter instability and nonlinear dynamics

At sufficiently low velocities U^*, systems with finite values of M^* will stay in a stable equilibrium configuration: the beam remains static and aligned with the flow direction. Beyond a specific critical velocity U_c^*, this equilibrium loses its stability and the beam starts to oscillate at increasingly larger amplitudes. At a certain moment, nonlinear forces come into play and the system typically converges to a stable oscillatory state: a limit cycle oscillation (LCO). The periodic oscillations of the system are maintained due to an interaction between the fluctuating flow pressure forces (that transfer energy to the beam) and the beam's restoring elastic forces. The character of this dynamical instability is discussed in more detail in subsequent sections. At this point it suffices to say that this dynamic instability and the development of periodic limit cycles is an iconic feature of this type of systems and, depending on the particular configuration (M^*, U^*), the character of the ensuing nonlinear oscillations can vary immensely. To illustrate, Figure 1.2 shows long exposure photographs of different plate motions in the experiments conducted by Taneda (1968) in open-flow.

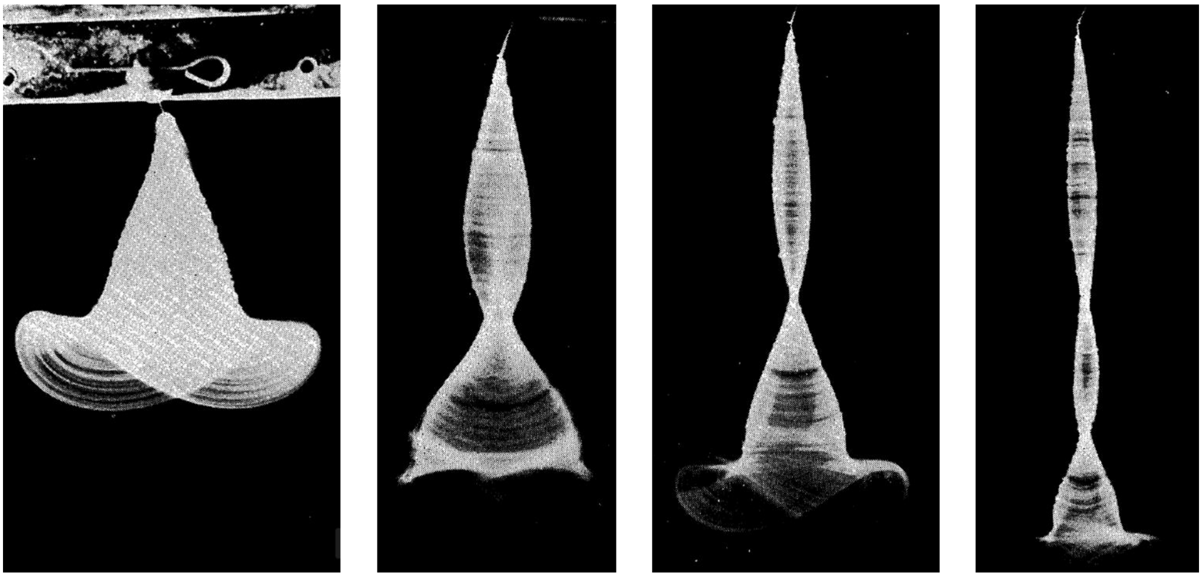

Figure 1.2 – Long exposure photographs by Taneda of plates made of blanket material with pinned-free boundary conditions oscillating in an open-flow configuration (Taneda, 1968).

Aside from the well-known periodic responses, experiments have shown that these nonlinear systems can also lead to quasi-periodic and even chaotic motions in specific ranges of (M^*, U^*) (Chen et al., 2014) (Huang, 1995) (Abderrahmane & Païdoussis, 2011). Additionally, virtually all experimental studies have reported hysteretic behavior (Jankee & Ganapathisubramani, 2022) (Eloy et al., 2012). That is, when gradually increasing flow velocities, an initially static plate will start to oscillate at a specific critical velocity U_c^*, while when decreasing flow velocity, an initially oscillating plate will come to rest at a different critical velocity $U_{hys}^* < U_c^*$. Even though widely reported in experimental studies, these nonlinear phenomena remain, for the most part, poorly understood as experimental results are typically inconclusive and models often fail to recreate these behaviors. Finally, it is worth noting that in confined configurations, experiments have shown the common occurrence of limit cycles oscillations including intermittent impacts between the plate and the side walls (Wu & Kaneko, 2005) (Gallegos & Sharmaa, 2019) (Aurégan & Depollier, 1995). However, as of yet, no studies have explored this behavior in a systematic manner. The work of this thesis is motivated partly by the demand for a better understanding of some of these complex nonlinear behaviors. The general prospect is to provide a framework for the comprehensive nonlinear analysis of these systems, that can hopefully help clarify some of the persistent unanswered questions in the field.

1.2 Vortex shedding, flow separation and excitation mechanisms

The field of flow-induced vibrations (FIV) encompasses a wide variety of dynamical systems whose distinguishing feature is the advent of mechanical vibrations resulting from interactions with adjacent flow. Before delving into the details of our specific problem, it is worth discussing some fundamental aspects and clarify some common misconceptions regarding the physical mechanisms leading to flow-induced vibrations.

In the literature of the subject, FIV are often categorized in different ways in order to specify certain characteristics of the excitation mechanism of a particular system (Kaneko et al., 2008) (Païdoussis et al., 2011) (Modarres-Sadeghi, 2022). A few examples of different categories of FIV systems, commonly found in literature, are: vortex-induced vibrations (VIV), galloping, flutter or buffeting. The fundamental differences between these types of systems are oftentimes nuanced and different researchers frequently adopt different categorizations. The aim of this section is to provide some disambiguation between the character of these different FIV systems and underline how they relate to the physical system studied in this thesis. In this context we also hope to provide the less familiar reader with an introduction to some fundamental concepts regarding flow-induced vibrations using simple examples.

1.2.1 Rigid cylinder in cross flow

Consider the typical example of flow passing through a rigid cylinder. The cylinder has a diameter D and the fluid has kinematic viscosity ν and is moving at velocity U. Here, the Reynolds number is defined by $\mathrm{Re} = UD / \nu$. By now, it is well established (Modarres-Sadeghi, 2022) that at sufficiently low Reynolds numbers ($\mathrm{Re} < 10$), no flow separation occurs and the streamlined flow simply passes around the cylinder (*Creeping flow*). Then, at around $10 < \mathrm{Re} < 50$, flow separation occurs and two symmetric and static vortices are formed in the wake (*Föppl vortices*). Beyond approximately $\mathrm{Re} > 50$, several vortices start shedding while propagating downstream. This periodic pattern is termed a *von Kármán vortex street* and is composed of vortices that shed alternatively on each side of the cylinder. The latter two cases are illustrated in Figure 1.3.

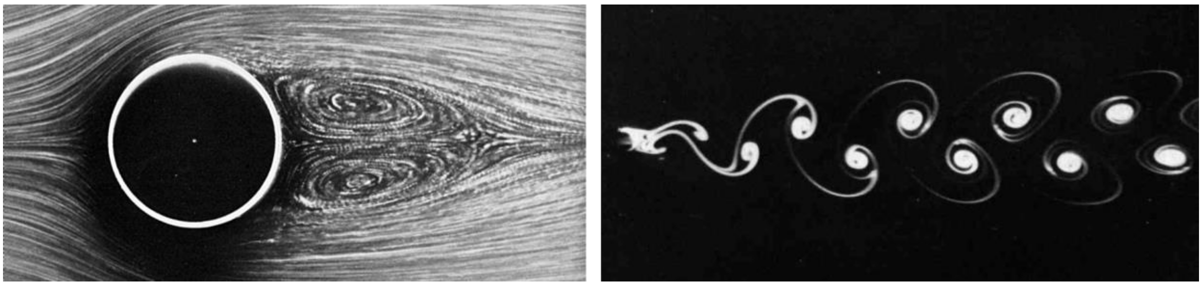

Figure 1.3 – Experimental flow visualizations of the static and symmetric Föppl vortices (left) and a von Kármán vortex street (right) formed by the presence of a rigid cylinder (Dike, 1982).

The angular frequency of the vortex shedding ω_v can be estimated by

$$\omega_v = \frac{USt}{D} 2\pi \tag{1.5}$$

where St is the dimensionless Strouhal number that, although dependent on the Reynolds number, for an isolated cylinder remains approximately constant at $St \approx 0.2$ for a large range of Re.

1.2.2 Two simple models of flow-induced vibrations

We start by discussing the well-known problem of vortex-induced vibration (VIV). Consider now a similar system, where the rigid cylinder is replaced by a mass-spring-damper, as illustrated in Figure 1.4(a). The rigid cylinder is allowed to move solely in the vertical direction (perpendicular to the flow). The equation of motion of this system can be described generically by

$$m\ddot{y}(t) + c\dot{y}(t) + ky(t) = F_y(t) \tag{1.6}$$

where m, c and k are the mass, damping and stiffness (per unit length) of the oscillator, y is its vertical displacement and $F_y(t)$ is a vertical lift force applied on the oscillator by the surrounding flow.

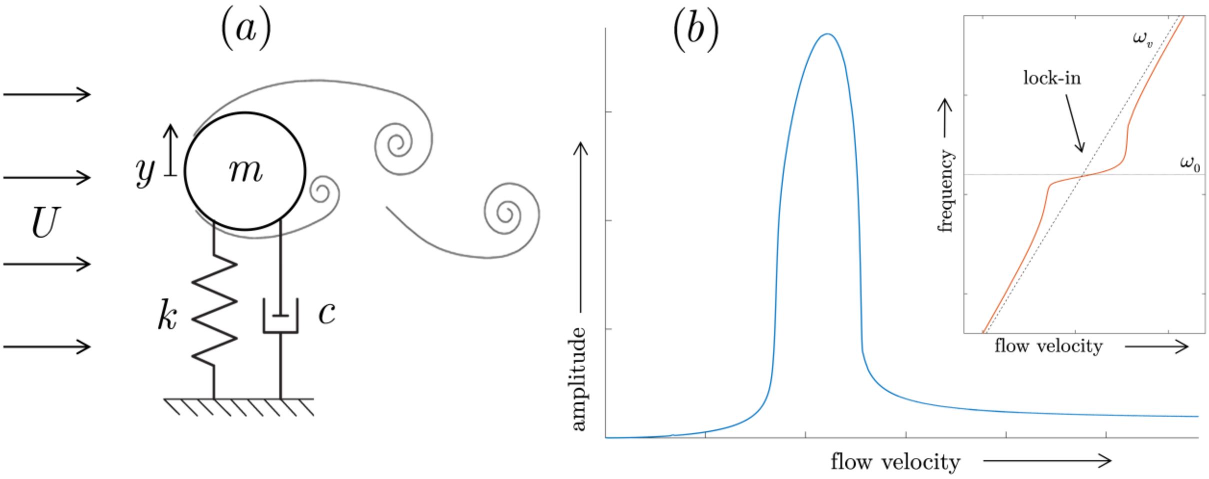

Figure 1.4 – (a) Diagram of the single-degree-of-freedom system leading to vortex-induced vibrations and (b) an illustration of the system response in terms of amplitude and frequency as a function of flow velocity. The "lock-in" phenomenon is seen when the frequency of vibration deviates from the expected vortex shedding frequency, when $\omega_v \approx \omega_0$.

Following our discussion on the formation of von Kármán vortex streets, one might conjecture that alternating fluid forces will induce the motion of the elastically mounted cylinder and, as an initial approximation, attempt to model the lift force in the following form

$$F_y(t) = \bar{F}\sin(\omega_v t) \tag{1.7}$$

where $\bar{F}$ is a constant coefficient dependent on the geometry and flow characteristics, e.g. $\bar{F} \sim D\rho U^2$. This would lead to the classical case of a *forced harmonic oscillator*, where large amplitude oscillations occur when the frequency of the vortex shedding approximates that of the oscillator $\omega_v \approx \omega_o = \sqrt{k / m}$. However, this simple model relies on the strong assumption that fluid forces are independent of the motion of the cylinder. In fact, this prevents it from recreating important aspects of the experimental observed behavior. Firstly, at very low mass-ratios $m^* = m / \rho D^2$ or damping $\zeta = c / 2\omega_0 m$, this model largely overpredicts experimentally observed oscillations amplitudes. Secondly, it does not capture the so-called "lock-in" phenomena observed in experiments whereby, near "resonance" $(0.8 < \omega_v / \omega_0 < 1.2)$, the shedding frequency ω_v deviates from the expected Strouhal line (1.5) and follows the oscillation frequency of the cylinder. This shows that strong fluid-structure coupling effects occur when $\omega_v \approx \omega_0$, and illustrates how the "forced" oscillator model is unable to capture the fundamental physics of the problem. This type of models can nevertheless be regarded as a plausible approximation when the vortex shedding frequency is far from that of the oscillator, i.e. $\omega_v / \omega_0 \ll 0.8$ or $\omega_v / \omega_0 \gg 1.2$.

Many other, more realistic, models have been proposed to study this phenomenon (Païdoussis et al., 2011). One of the most popular model-types, introduced by Hartlen & Currie (1970), is that of a *coupled wake-oscillator,* which relies on the explicit account of the flow's wake dynamics. A dimensionless version of this type of model can be described by

$$\begin{gathered}\ddot{y}(t) + \left(2\zeta\delta + \frac{c_1}{m^*}\right)\dot{y}(t) + \delta^2 y(t) = \frac{c_2}{m^*} q(t) \\ \ddot{q}(t) + c_3(q(t)^2 - 1)\dot{q}(t) + q(t) = c_4 \ddot{y}(t)\end{gathered} \tag{1.8}$$

where $q(t)$ is a dimensionless lift coefficient representing the wake dynamics; c_{1-4} are constant coefficients retrieved from experimental comparisons and $\delta = 1 / StU_r$, where U_r represents a dimensionless reduced flow velocity. An example of the system response, in terms of amplitude and frequency of oscillation, as a function of the incoming flow velocity is illustrated in Figure 1.4(b). Here we do not delve into the derivation and role of the different dimensionless parameters to avoid overloading the reader (more information can be found in reference literature (Païdoussis et al., 2011) (Modarres-Sadeghi, 2022)). The key features to extract from this model and its behavior can be summarized as follows:

→ The wake is modelled by a Van der Pol equation. For small values of q, $q^2 < 1$ resulting in a negative damping term, while $q^2 > 1$ leads to positive damping. This seems reasonable as it leads to the expected limit cycle behavior (vortex shedding) that occurs even in the presence of a rigid cylinder.

→ Coupling is bi-directional, i.e. the structure is excited by the lift forces from the wake, which in turn are influenced by the cylinder motion.

→ The evolution of the frequencies of oscillations shown in Figure 1.4(b) clearly shows how the frequencies of the two oscillators coalesce when $\omega_s \approx \omega_0$, effectively describing the "lock-in" phenomenon observed experimentally.

→ Large amplitude oscillations occur in a restricted range of velocities, when the vortex shedding frequency is near the frequency of the oscillator.

This improved model is able to recreate the essential aspects of the behavior observed experimentally and suggests that VIV arise as a product of a fluid-elastic instability, rather than from a simple forcing excitation from the flow. Nevertheless, they differ from other types of fluid-elastic instabilities, that can occur regardless of the presence of vortex shedding.

Even if we neglect the presence of vortex shedding, other fluid lift forces might incur in a structure, leading to FIV. When considering a structure with cylindrical cross-section (as before), the mean lift force always opposes its motion due to the symmetry of the profile, negating the possibility of an instability. However, other profile shapes do not necessarily behave in this way. Consider now a body with noncircular cross-section, similarly modelled as a mass-spring-damper, as shown in Figure 1.5(a). Here, D denotes a vertically projected surface area.

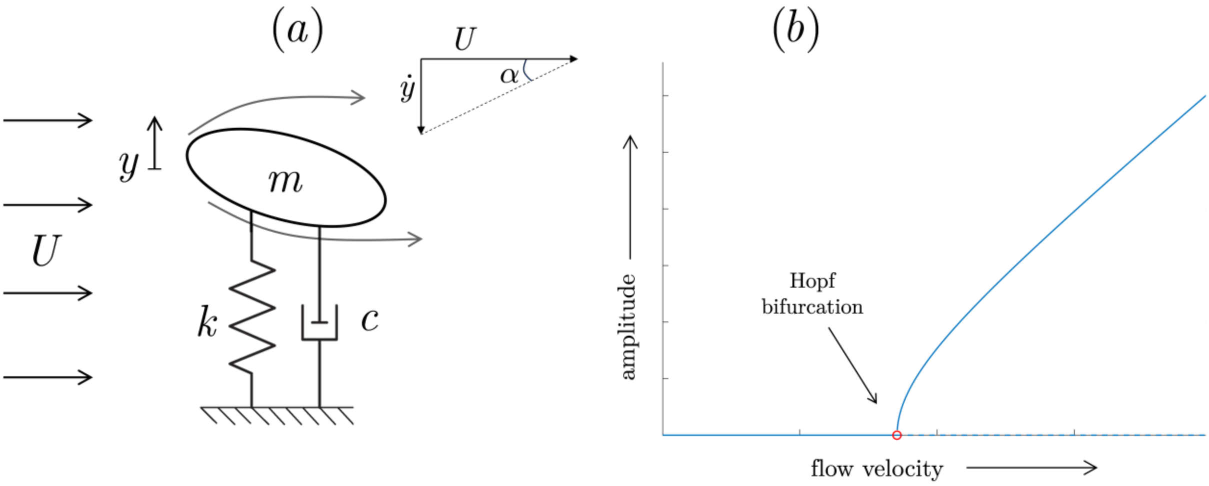

Figure 1.5 – (a) Diagram of the single-degree-of-freedom system leading to a galloping instability and (b) an illustration of the system amplitude response for increasing flow velocity.

The equation of motion is the same as in (1.6), but now the lift force is modelled by (Modarres-Sadeghi, 2022)

$$F_y(t) = \frac{1}{2}\rho D U^2 C_y(\alpha) \tag{1.9}$$

where C_y is a lift force function dependent on the incidence angle α between the incoming flow velocity U and the vertical velocity $\dot{y}$ of the oscillator, as illustrated in Figure 1.5(a). In the small angle approximation, we get $\alpha \approx \dot{y} / U$. The function C_y depends on the geometry of the cross-section and is typically constructed from polynomial fitting to experimental results. These experiments are performed in steady flow conditions in which lift flow forces are measured when a rigid structure with the same cross-sectional profile is placed at different angles of attack. Typical models used high-order polynomials for an accurate description of C_y. Here, for simplicity, we assumed a 3rd order polynomial in the form

$$C_y(\alpha) = A_1\alpha + A_3\alpha^3 \tag{1.10}$$

where A_1 and A_3 are constant coefficients. The coupled system can then be formulated as

$$m\ddot{y} + \left[c - \frac{\rho D}{2}\left(A_1 U + A_3 \frac{\dot{y}^2}{U}\right)\right]\dot{y} + ky = 0 \tag{1.11}$$

Notice that, in this case, the alternating flow force is dependent on the oscillator velocity $\dot{y}$ and can lead to a negative damping term. A dynamic instability will take place at velocities greater than a critical velocity U_c, calculated from the linearized form of (1.11)

$$U_c = \frac{2c}{\rho D A_1} \tag{1.12}$$

This critical point is referred to as a Hopf bifurcation, whereby the eigenvalues of the associated linearized system have null real part (neutrally stable). That is, when $U > U_c$, exponentially growing oscillations will take place as the flow induced negative damping exceeds the viscous damping c of the oscillator. Eventually, nonlinear forces restrict the exponentially growing trend and lead to stable limit cycle oscillations. This simple system represents a canonical example of flow-induced vibrations of the self-excited type, commonly referred to as a *galloping*. It is worth noting that the term galloping is typically referred to instabilities occurring in single degree-of-freedom (DoF) systems while its sister term *flutter* is typically employed in systems with multiple DoF, where the coupling between two (or more) mechanical modes is a prerequisite for the loss of stability (Kaneko et al., 2008). Nevertheless, the essential nature of the excitation mechanism is the same in both cases: a positive energetic feedback loop caused by the interaction between flow forces and the structural motion.

It is worth underlining that, in such systems, vortex shedding can still occur, however, it is not the root cause for the flow-induced vibrations. Here, the flow forces leading to instability are assumed in a *quasi-steady* scenario, where the frequency of the oscillation is low compared to the vortex shedding frequencies. Even though both VIV and galloping pertain to a fluid-elastic instability, one can point a few qualitative distinctions between then:

- → In VIV, large amplitude oscillations occur in a restricted range of incoming velocities (when $\omega_v \approx \omega_0$). In a galloping-type instability, this restricted range is not typically seen and limit-cycles oscillations are generally observed for large velocities ranges beyond the critical point.
- → In VIV, the oscillations are typically limited to amplitudes of about one diameter, due to the nature of the vortex dynamics. That is, the nonlinear forces limiting the amplitude of oscillations are associated with the fluid. On the other hand, galloping-type

> instabilities do not have such restrictions and oscillation amplitudes generally increase monotonically with flow velocity. Ultimately, it is structural nonlinearities and, in the worst cases, rupture that will typically limit oscillation amplitudes at very large velocities.

In the following section we illustrate how the problem of a plate subject to axial flow relates more closely to a galloping-type instability than to VIV, even though vortex shedding can still occur downstream of the trailing edge of the plate.

As a final note, it is worth pointing out that, for flows with sufficiently large Reynolds number, turbulent effects will also excite elastic structures. However, the unsteady fluctuations from turbulent flow typically lead to a broadband excitation that is essentially uncoupled from the structure, i.e. these forces can generally be regarded as independent from the structural motion and modelled as a random forced excitation.

1.2.3 Flow around a fluttering plate

When considering a thin beam in axial flow, vortex shedding does take place at the trailing edge but, generally, the frequency of vortex shedding is much larger than that of the plate oscillations (if no bluff body is place upstream of the plate). This is illustrated clearly by the remarkable images of Zhang et al. (2000), taken from an experiment where a silk filament was placed in flowing soap film, shown in Figure 1.6 (a) and (b), for the static and oscillating cases, respectively. We notice that, in the static case (a), a von Kárman vortex street is formed at the trailing edge of the plate. However, the time and length scales of the vortex shedding are notably smaller compared to the oscillations of the plate. A similar type of fine-scales vortex shedding is seen for the oscillating case (b), but unlike in the static case, the vortices are not of alternating-sign, but of the same sign, resembling a Kelvin-Helmholtz instability (Balde & Étienne, 2011). The sign of the vortices alternates at each half stroke of the plate tip.

The question of flow separation along the plate boundary in oscillating states has also been posed often. Over the last years, several experiments (Watanabe et al., 2002) (Zhang et al., 2000), as well as results from CFD models (Gibbs et al., 2014), have come to conclude that significant flow separation does not occur along the plate. These can be noted both in the images from Zhang et al. (2000) (Figure 1.6 (b)) as well as those from the experiments of Watanabe et al. (2002) using smoke injectors (Figure 1.6 (c)). Even though flow patterns can become more complex after the trailing edge, it is now well established that the flow field around the plate's surface will generally remain attached. These observations have motivated many researchers to model the fluid-structure interaction assuming potential flow around the plate, which greatly simplifies the equations of motion. This assumption is proven to be reasonable as these models are able to recreate, at least qualitatively, many aspects of the experimentally observed dynamics.

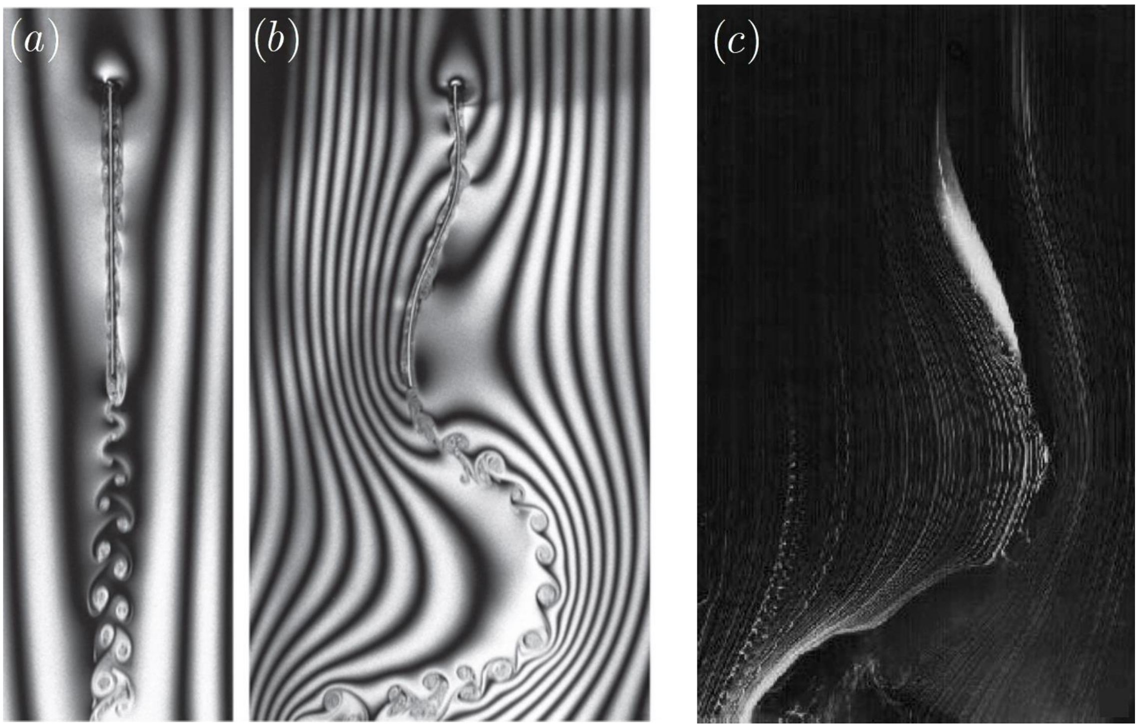

Figure 1.6 – Flow visualizations of cantilevered structures in axial flow. (a) and (b) represent the static and oscillating cases respectively, in the experiments of Zhang et al. (2000) using filaments immersed in soap film; flow visualization is achieved via interference patterns under a sodium lamp. (c) shows a frame of an oscillating paper strip from the experiments of Watanabe et al. (2002), where streamlines are visualized using smoke injectors.

1.3 A brief literature review

The dynamics of a flexible plate immersed in uniform axial flow is a widely studied subject and represents a canonical example of self-sustained flow-induced vibration (Païdoussis, 2004) (Nagakura et al., 2014). Systems of this type present a wide variety of dynamical behavior and some aspects of their physical modelling remain a challenging task to this day. Moreover, because similar systems can be found in a large number of practical applications (e.g. paper industry, flutter-based energy harvesting, wind musical instruments, palatal snoring, etc.), it has motivated a large body of literature, dealing with various plate-flow configurations and using diverse modelling approaches (Alben, 2015) (Hidalgo et al., 2015) (Aurégan & Depollier, 1995) (Avanzini & Walstijn, 2004).

Flexible plates in axial flow can lose stability via both static (divergence) and dynamical (flutter) instabilities. One of the most important features defining their dynamics are the plate's boundary conditions, for which the works of Kornecki et al. (1976) and Guo & Païdoussis (2000) present elucidative results. The authors explored the critical flow velocities for plates with various boundary conditions and the associated type of instabilities emerging. Ignoring spanwise deformations, they studied analytical solutions of 2D linearized models, based on inviscid incompressible flow (with different treatments for the flow boundary conditions), where the instability is caused by perturbation pressures stemming from the linearized unsteady Bernoulli equation at the fluid-beam boundary. Their results show that beams can lose stability by divergence (static instability), single-mode flutter or coupled-mode flutter (dynamic instabilities), depending on the support conditions at the leading and trailing edges. In summary, their results suggested that beamss fixed at both ends (pinned or clamped) first lose stability by divergence but can also, under some configurations, undergo post-divergent flutter instabilities. Plates free at the trailing end always lose stability by flutter, either of single-mode or coupled-mode type, depending on particular flow-beam configurations. These conclusions are analogous to the role of edge conditions in the sister problem of flexible cylindrical pipes conveying internal flow (Païdoussis & Issid, 1974). Finally, the case of a plate free at its leading end is perhaps the most challenging configuration which has in recent times attracted a lot of attention (Tavallaeinejad, et al., 2021). This is generally referred to as the *inverted flag* problem and both theoretical and experimental studies have shown a wide variety of behaviors: (1) in a linear stability context, multiple equilibriums can co-exist and both flutter and divergence instabilities occur; (2) nonlinear behaviors also show sub-critical bifurcations, symmetry breaking, chaos, etc. Here, however, focus is given to the canonical case of cantilever plates, clamped at the leading end and free at the trailing end, i.e. the *standard flag* (Yu, Liu, & Amandolese, 2019).

Back in 1879, Lord Rayleigh was perhaps the first scientist addressing the oscillations of a cantilever plate in axial flow theoretically in his publication *On the instability of jets* (1879). He considered the dynamics of a 2D vortex sheet evolving in inviscid flow and related this to the "flapping of sails". As was discussed in the previous section, we now know that, even though Rayleigh's model might be appropriate to describe the vortex street in the wake of the plate, it is not necessarily the cause of its dynamic instability. In the case of cantilevered plates, it is now well-established that the underlying mechanism leading to the flutter instability is an irreversible energy transfer from the flow to the plate caused by a phase difference between the fluid pressure and the plate bending motion (Balint & Lucey, 2005). In broad terms, the plate motion will induce pressure fluctuations in the flow, and vice-versa. Under particular plate-flow conditions, this creates a positive energetic feedback loop that leads to exponentially growing oscillations. Even though vortex shedding occurs at the trailing-edge, the thin plate thickness will generally lead to vortex shedding frequencies that are much higher than the plate's oscillations.

1.3.1 Linear stability analysis and the "cascading" boundary

The experimental work of Taneda in the mid-1960s (1968) anticipated many of the experimental and modelling studies of the past decades. He reported that the oscillations of cantilever plates in axial flow can present a variety of "flapping modes", with one or multiple "necks", as illustrated previously in Figure 1.2. He was also the first to report hysteretic behavior as well as multi-stability, where two oscillatory states with different frequencies can co-exist under the same flow conditions. Moreover, his work was the first to report chaotic motions at high flow speeds.

Recent studies have shed some light onto the nature of the beam motions with one or multiple "necks". Out of many examples in recent publications, in the work of Shoele & Mittal (2016), we find some elucidating results regarding the influence of relevant non-dimensional parameters like the fluid-beam mass ratio M^*, the reduced velocity U^* as well as the confinement ratio H^*. Following the previously mentioned studies, a two-dimensional potential and incompressible flow was considered. The behavior of the system is examined in linearized conditions to draw stability boundaries in the (M^*,U^*) plane. A typical result is shown in Figure 1.7.

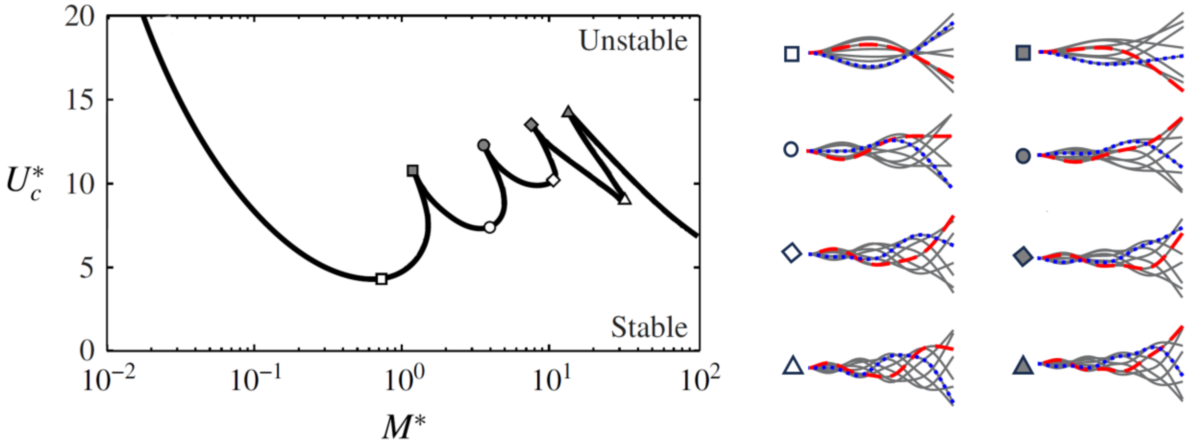

Figure 1.7 – Stability boundary in the (M^*,U^*) plane. The plots on the right describe the neutrally stable (complex) modes and snapshots of the beam motions (in grey) associated with various points along the stability boundary (left). Results were taken from Shoele & Mittal (2016).

Their results show that, at low mass ratios M^* (heavy beams), the instability motion involves the coupling of the first two *in-vacuo* beam modes, commonly referred to as "single-neck" solutions. Note that, in reference literature the term "neck" is typically used to describe the locations with smaller amplitude motion in the beam's motion. However, as mass ratios increase, near $M^* \approx 0.15$, the initial single-neck mode ceases to be the principal instability, being replace by a double-neck solution, where the presence of the third *in-vacuo* beam mode becomes prominent. The same process repeats as successive "mode-transitions" occur, whereby multiple higher-order fluttering modes prevail. Although not shown here, with each mode transition, there is also an abrupt increase in the frequency of oscillation. This type of "cascading" boundary is now a well-established result, appearing in a wide variety of numerical studies using different flow models (Huang & Zhang, 2013) (Zhao et al., 2012) (Eloy et al., 2007). Most importantly however, they are qualitatively confirmed by experimental results (Nagakura & Kaneko, 1993) (Païdoussis, 2004).

1.3.2 The effects of confinement

Several theoretical and experimental studies have addressed the role of the confinement (Doaré et al., 2011) (Nagakura & Kaneko, 1993) (Tosi & Colonious, 2019). Their effects are still not entirely clear, and might vary under different levels of confinement, since they have to be contextualized to specific flow conditions, where the influence of circulatory or 2-D flow effects, viscous/boundary-layer effects, turbulence, etc., might differ. Nevertheless, some general tendencies have been observed. Narrower confinements (smaller H^*) will lead to an increase of the inertial effects of the fluid and a slight overall lowering of the critical velocities. The former is equivalent to say that a smaller H^* will have the same effect as increasing the fluid density ρ_f (and hence the mass ratio M^*). The later means confinement will have a destabilizing effect, even though this effect is in general secondary, particularly when discussing relatively narrow confinements. Moreover, as discussed in the study by Tosi & Colonious (2019), a narrower confinement will also lead to an increase of viscous flow effects.

1.3.3 Modelling approaches

More recently, the advances in computational efficiency have enabled the possibility to simulate these fluid-structure interaction (FSI) systems numerically by solving the Navier-Stokes equations in 2-D and 3-D domains (Huang & Sung, 2010) (Tetlow & Lucey, 2009) . These FSI models allow a more accurate representation of the physics and provide a useful validation tool for simpler analytical models, indicating under which conditions they are able to describe more complex 2-D/3-D phenomena (Tosi & Colonious, 2019). However useful, Computational Fluid Dynamics (CFD) models still require considerable computational time, which becomes a handicap when analyzing problems whose behavior depends on a wide variety of parameters. Nevertheless, we emphasize the work of Cisonni et al. (2017) that, despite considerable computational effort (reported a staggering 150,000 CPU hours of computation time), managed to present a wide set of reference results describing the variation of stability boundaries in terms of the most pertinent non-dimensional parameters: the reduced velocity U^*, mass ratio M^*, confinement ratio H^* and Reynolds number Re. It is worth noting, however, that these are limited to laminar flow conditions. Furthermore, for a more thorough parameter mapping, 1-D models based on simplified equations of motion, are not only more computationally efficient but also more tractable, and may provide valuable insights into the essential physics of the problem. Notably, the discernment of relevant dimensionless parameters and interpretation of results often becomes more intuitive.

In the context of simplified approaches, we note the work of Nagakura & Kaneko (1993) that have used leakage-flow theory to model the linear stability of a cantilever beam in a confined passage. Based on the work of Inada & Hayama (1990), they formulate a 1-D problem where flow pressure and velocity inside the channels are taken as cross-sectionally averaged. These are simplifying assumptions used since the 1970s, under the designation of "bulk-flow models" (Hirs, 1973). The confinement is restricted to symmetric channels of constant cross-section, viscous effects are accounted for by a distributed friction term and the energy losses at the trailing edge are encapsulated by a localized head-loss term, imposed at the end boundary condition. Despite its simplicity, modelling results corroborate remarkably well with those from other, more intricate, models. Additionally, these can easily cope with turbulent flow effects using a simple distributed head-loss term. For example, Tosi & Colonius (2019) have positively validated the stability results from a similar simplified model against those from direct numerical simulations using the Navier-Stokes equations in a 2-D domain. They underline the potential of such modelling approaches as critical velocities converge over a wide range of mass ratios and Reynolds numbers, at least for relatively narrow passages. As the confinement ratio increases, larger discrepancies are seen, likely due to circulatory 2-D flow effects that are neglected in the simplified leakage flow model.

Despite the large body of literature published on the subject over the last decades, many important aspects of the underlying physics are still not well understood. For example, we underline the fact that most models greatly underestimate critical velocities, particularly for relatively heavy beams. In many cases, measured critical velocities can be twice as large as the predicted values. An illustrative comparison is shown in Figure 1.8 taken from Shoele & Mittal (2016).

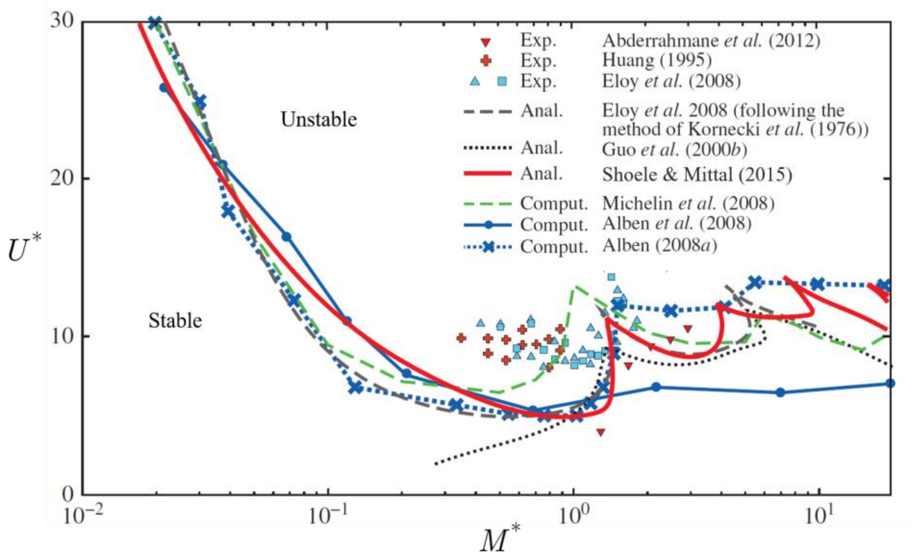

Figure 1.8 – Critical stability boundaries in the (M^*, U^*) plane for a beam in unbounded flow. Symbols represent experimental data while drawn lines stem from various numerical and analytical studies. This figure was taken integrally from (Shoele & Mittal, 2016).

This is a widely discussed topic and several researchers have hypothesized over the reasons for this disparity. The stabilizing effects of, for example, drag-induced tension on the plate, flow viscosity or three-dimensional plate deformations have all been discussed as potential factors (Morris-Thomas & Steen, 2009) (Tang & Païdoussis, 2007). But perhaps the most convincing studies in this regard are those of Doaré et al. (Doaré, Sauzade, & Eloy, 2011) (Doaré, Mano, & Ludena, 2011). Here the authors analyze the effect of spanwise confinement. That is, the distance between the edges of the plate and the spanwise walls, the so-called “clearance gap”. In most models, assuming 2-D flow, this effect is neglected. The authors present a model that accounts for these three-dimensional edge effects and compare it to experimental results. In essence, their model describes how the presence of the open “side-edges” will lead to a decrease of the average pressure jump across the plate. Their model presents results that are significantly closer to experimental ones. Moreover, when the clearance gap is gradually decreased, model results converge to those from 2-D models. More importantly however, they have indicated that this convergence is so slow that 2-D conditions are virtually unattainable experimentally. So far, this seems to be the most convincing hypothesis explaining the consistent underestimation of critical velocities by most 2-D models. Despite the promising results, this question is still not fully resolved and further studies, potentially considering boundary layer and turbulent edge effects, are necessary to reach more definitive conclusions.

1.3.4 Nonlinear dynamics

On the whole, modelling efforts pursued so far are generally focused on stability boundaries, using linearized equations of motions. Knowledge of the conditions for instability and the dependence of various parameters on stability boundaries is undeniably an important aspect of the FSI system dynamics. However, this gives us little insights about the ensuing nonlinear behavior, which might be of valuable interest in various practical applications, giving information about the working regimes in energy harvesting devices (Tosi et al., 2021), wind musical instruments (Avanzini & Walstijn,2004) or human snoring (Aurégan & Depoilleier,1995). For example, the fact that linearized models (by default) ignore hysteretic behavior, means they will predict stable equilibria when oscillating states may co-exist. Naturally, such simplifications can have disastrous effects in applications where oscillating behavior needs to be avoided. To illustrate the commonly observed hysteresis phenomenon, Figure 1.9 presents experimental results by Eloy et al. (2008).

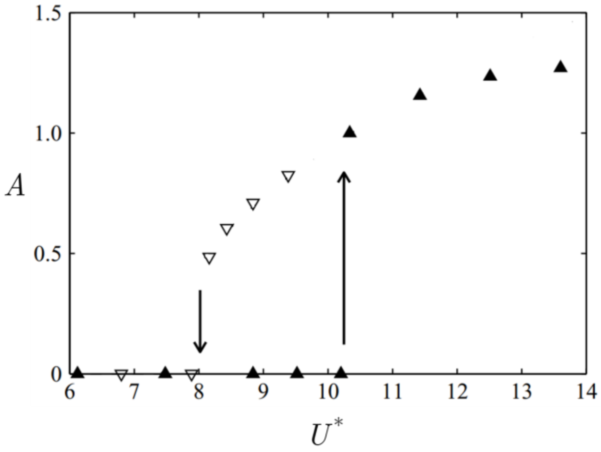

Figure 1.9 – Example of the hysteresis behavior commonly observed in experiments. Oscillating amplitude A (arbitrary units) is shown as a function of the reduced flow velocity U^* in the ascending (filled triangles) and descending (open triangles) cases. Results are taken integrally from Eloy et al. (2008).

This phenomenon is relatively common in flow induced vibrations and is defined by: (1) when gradually increasing flow velocity, the static plate will start oscillating at a given critical velocity U_1^* while (2) when gradually decreasing flow velocity, an initially oscillating plate will re-stabilize at a different critical velocity U_2^*, where $U_2^* < U_1^*$. Often, the degree of hysteresis is quantified by the hysteresis loop width η, given in percentage by

$$\eta = 100 \times \frac{U_1^* - U_2^*}{U_1^*} \tag{1.13}$$

In the context of unbounded flows, a large number of experimental studies can be found, illustrating the array of possible limit cycles arising in this type of systems (Taneda, 1968) (Tang et al., 2003) (Yadykin et al., 2001). The list of numerical studies dealing with the simulation of post-critical nonlinear regimes is less extensive. Nevertheless, over the last 10-15 years, a number of studies have provided results from temporal simulations, using different nonlinear models, that are able to recreate some features of the behavior observed in experiments. We underline the work of Tang & Païdoussis (2007) who considered a nonlinear model using lumped vortices to calculate the pressure difference across a 2-D inextensible beam. Overall, the calculated limit-cycle oscillations compare qualitatively well with experiments, even though subcritical bifurcations and hysteresis loops were not observed. Using a similar model, Michelin et al. (2008)

have also been able to model limit-cycle oscillations and have indeed observed hysteretic behavior, although the hysteresis loop width was much smaller (~4%) than values reported experimentally (20-60%). Up to today, the phenomenon of hysteresis is still poorly understood and most models predict a super-critical bifurcation (no hysteresis). The works of Eloy et al. (2008 & 2012) have given considerable attention to this topic and various hypothesis have been proposed to explain the occurrence of hysteresis: three-dimensional flow effects, influence of spanwise deformations of the plate, viscous effects, the influence of the plate's aspect ratio, amongst others. However, no definite conclusions have been reached and this is still a widely discussed open question in the field. Finally, we underline the model developed by Chen et al. (2014) that was able to recreate quasi-periodic dynamics observed in experiments, and suggested the "route to chaos" is caused by torus bifurcations.

The calculation of nonlinear dynamics in *confined* flow scenarios, however, is much scarcer. In these cases, strong flow nonlinearities need to be taken into account. More importantly however, many experimental observations report the regular occurrence of impacts between the beam and the channel walls (Wu & Kaneko, 2005) (Gallegos & Sharmaa, 2019) (Aurégan & Depollier, 1995). Hence, the nonlinear modelling becomes a non-trivial task as both the flow and the wall-structure contact phenomena need to be accounted for. A few nonlinear models have been developed for confined configurations using direct methods to solve the Navier-Stokes equation in 2-D (Balint & Lucey, 2005) as well as more compact one-dimensional leakage-flow models (Wu & Kaneko, 2005). However, both these studies neglect the possibility of contact and hence are limited to relatively narrow regions of the parameter space, where limit-cycles without contact occur. On this point it is worth mentioning that experiments reporting beam-wall impacts generally provide only descriptive accounts. The sole study presenting a systematic characterization of limit-cycles with intermittent impacts in systems with fluttering plates has only recently been published (Lee et al., 2021). Here, the authors examine an experimental configuration composed of a vertical flexible plate placed near a single parallel rigid wall.

The common factor between all the nonlinear modelling results presented, in both open and confined flow, is that they rely on time-domain integrations of the nonlinear equations of motion. Although these methods allow for an assessment of the possible nonlinear regimes, they are often computationally expensive and moreover, provide only a "discrete" point-wise description of the ensuing nonlinear dynamics for a given set of fixed parameter values. In general, for broader and more systematic parametric studies, they can be considered a less adequate tool.

The natural next step in the nonlinear analysis of fluttering beams in axial flow is the use of algorithms for the continuation of periodic solutions. Unlike the point-wise description given by time-domain integrations, bifurcation analysis may provide a wider comprehensive overview of the nonlinear dynamics, as periodic solutions as sought out in a continuous manner with respect to a particular "control" parameter. Many algorithms are available for these types of studies though, in this thesis, we will use the so-called Asymptotic Numerical Method (ANM), popular for its numerical efficiency (Woiwode et al., 2020). The continuation algorithm is used in conjunction with the harmonic balance method (Krack & Gross, 2019), a useful and commonly used tool in these contexts, whereby the time-dependent variables of a nonlinear ODE/DAE system are expanded in a Fourier series, and periodic solutions are then calculated by solving for the Fourier coefficients of the (time) discretized nonlinear algebraic system. This type of analysis, particularly in the context of simplified formulations, can contribute significantly to the understanding of the underlying physics occurring in these FSI systems and perhaps clarify some persistent and unanswered questions in the field like: the sub/super-critical nature of the encountered Hopf bifurcations, the existence of multi-stability regions, the occurrence of aperiodic/chaotic dynamics, amongst others. We believe the methods presented herein provide an initial impulse towards a more comprehensive analysis of the nonlinear dynamics occurring in these FSI system and hope they can help clarify some of these delicate questions.

1.4 Thesis aims and overview

The motivation behind this thesis starts from the premise that the fluid-structure interaction of flexible cantilever beam subject to axial flow represents a benchmark example of flow-induced vibrations whose complex dynamical behavior is still not well understood. The research done over the last several decades has given significant attention to the linear stability analysis, focusing on the prediction of critical velocities and the influence of different parameters on the frontier separating static from oscillatory states. Despite some quantitative disparities, linearized models developed so far have been able to recreate many core aspects of the dynamics observed experimentally. On the other hand, the nature of the post-critical behavior and ensuing nonlinear dynamics is more complex, and many aspects of the behavior observed in experiments are still not well understood, even at a fundamental level. With this said, the work of this thesis was motivated by a deeper understanding of the nonlinear dynamics of fluttering beams in axial flow. As opposed to more “realistic” - and computationally expensive - CFD models, this work focuses on the analyses of a “simplified” physical model that, nevertheless, contains the essential nonlinear features of these systems. This framework allows for a more refined analysis of the nonlinear dynamics, broad parametric studies and also a more intuitive interpretation of results.

The original contributions of this thesis can be summarized by the following points:

1. *Development of a nonlinear analytical formulation based on formal solutions of the flow fields.* Considering a 1-D bulk-flow in a channel of potentially variable cross-section, an exact analytical formulation for the pressure and velocity fields is presented. When coupled to the equations of motion of a flexible beam, this formulation allows for the description of the full nonlinear dynamics of the coupled system. Discretizing the beam motion in terms of M modes of vibration, the continuous system of PDEs is converted into a set of solely $2M+2$ nonlinear ODEs ($2M$ structural equations plus two flow equations, one for each channel) that can be solved in the time-domain at very modest computational times. This allows for the computation of post-critical nonlinear dynamics of the system. The linearized version of the formulation also results in a compact system for the analysis of stability boundaries in terms of different dimensionless parameters. This approach is described in Chapter 3.

2. *Introduction of an elastic contact model to simulate the vibro-impact dynamics between the fluttering beam and the channel walls.* It is well known from experimental observations that, in confined configurations, a fluttering beam will often impact against the confinement walls.

However, previous nonlinear modelling efforts have not dealt with this phenomenon, and were hence limited to the calculation of limit-cycles without impacts. Here we introduce a pragmatic contact model that is able to simulate purely elastic impacts between the beam and the wall while avoiding numerical issues associated with singularities in the flow equations in the presence of a channel closure. This allowed, for the first time, the calculation of diverse limit-cycle oscillations including intermittent impact regimes.

3. *Proposal of a Tau-Galerkin approach for the discretization of the system of nonlinear PDEs.* In broad terms, the system of PDEs of the bulk-flow coupled model is converted into a set of time-dependent equations (ODEs and algebraic) by developing all variables in terms of an efficient series of space-dependent orthogonal functions. The beam motion is developed in terms of its mode shapes while the flow pressure and velocity fields in each channel are developed in terms of Chebyshev polynomials. A Tau-variant of the Galerkin approach enables the enforcement of the nonlinear time-dependent boundary conditions in a well-posed manner. Ultimately, the resulting system is a set of nonlinear DAEs that can be truncated at any suitable numbers of terms, leading to exploitable reduced formulations. The presented framework is well suited to the use of bifurcation analysis tools for the continuation of periodic solutions. Moreover, the generic character of the proposed methodology can also be adapted to different systems in the field of fluid-structure interaction, providing compact time-dependent formulations for nonlinear analysis. This approach is described in detail in Chapter 4.

4. *Dynamical analysis of the system using continuation-based numerical methods and bifurcation analysis.* Based on the developed Galerkin formulation, we provide an initial impulse for a comprehensive nonlinear dynamic analysis of these systems using, for the first time, methods for the continuation of periodic solutions and bifurcation analysis. The set of time-dependent equations is time-discretized via the harmonic balance method (HBM) and the continuation of periodic solutions in terms of one, or multiple, system parameters is achieved using the asymptotic numerical method (ANM). This type of analysis provides a broad overview of the possible dynamics and may help clarify some ill-explained phenomena commonly observed in experiments. The widely discussed question of hysteresis and sub-critical bifurcations is studied in detail and, additionally, a numerical method for an “augmented” linear stability analysis is proposed, allowing the continuation of Hopf bifurcation branches, including their sub- or super-critical nature. The same method, based on constrained continuation, also allows for the prediction of grazing boundaries, i.e. frontier separating limit cycle regions with and without intermittent impacts. The nonlinear dynamics are explored with respect to various dimensionless parameters and results illustrate a large variety of nonlinear behaviors including: internal resonances, regions with multiple oscillatory solutions, torus bifurcations and associated quasi-periodic motions, amongst others (these concepts will be introduced later). Aside from providing novel insights into the physics of fluttering beams and suggesting news avenues of research, it is hoped that the

methods and results presented can stimulate similar studies in the field of flow-induced vibrations. This topic is the discussed in Chapter 5.

5. *Experiment studies for model validation and characterization of the nonlinear dynamics.* An experimental set-up composed of a small-scale wind tunnel working in suction was used to validate various aspects of the novel modelling results presented previously. Additionally, the collected data provides a detailed documentation of the nonlinear dynamics of beams in channel flow including limit-cycles with intermittent impacts. The role and general character of the impacts and how they change as a function of the reduced velocity is examined. Moreover, the question of hysteresis and sub-critical bifurcations is discussed and experimental results are confronted with previously proposed hypothesis regarding, for example, the influence of the plate's aspect ratio on the width of hysteresis loops. At a qualitative level, experimental results compare well with modelling predictions. However, the simplicity of the proposed model prevents a more refined quantitative comparison. Notably, we report larger hysteresis loops than predicted and an overall underestimation of the stability boundaries. All aspects of the experimental work are discussed in Chapter 6.

Finally, as a product of the work conducted during this thesis, three scientific articles were published in international journals:

- → F. Soares, J. Antunes, V. Debut, C. Vergez, B. Cochelin and F. Silva, "A nonlinear analytical formulation for the 1D modelling of a flexible beam in channel flow," *Journal of Fluids and Structures,* vol. 113, 2022.
- → F. Soares, J. Antunes, V. Debut, C. Vergez, B. Cochelin and F. Silva, "A Galerkin formulation for the nonlinear analysis of a flexible beam in channel flow," *Journal of Fluids and Structures,* vol. 118, 2023.
- → F. Soares, C. Vergez, J. Antunes, V. Debut, B. Cochelin and F. Silva, "Bifurcation analsyis of cantilever beams in channel flow," *Journal of Sound and Vibration,* vol. 567, 2023.

as well as two articles presented at international conferences:

- → F. Soares, J. Antunes, V. Debut, C. Vergez, B. Cochelin and F. Silva, "Analytical 1D model of the flow-structure interaction in snoring," *European Nonlinear Dynamics Conference,* (ENOC2020+2), Lyon, France.
- → F. Soares, J. Antunes, V. Debut, C. Vergez, B. Cochelin and F. Silva, "On the bifurcations of a fluttering plate in confined axial flow," *Forum Acousticum 2023,* FA2023, Torino, Italy.

Chapter 2

A simplified nonlinear model of the fluid-structure interaction

In this chapter we present the nonlinear physical model of the fluid-structure interaction problem studied in this thesis. The simplified model describes the dynamics of a cantilever beam surrounded by confined axial flow in its upper and lower sides. The motion of the flexible beam is described in a modal framework. Using bulk-flow equations, the flow pressure and velocity fields are taken as cross-sectionally averaged and the problem reduces to a one-dimensional system of coupled partial differential equations. Two types of flow dissipation are included: (1) a distributed frictional term representing viscous/boundary layer losses along the domain and (2) localized head-loss terms accounting for the pressure losses occurring outside the domain. The former can be related to the Reynolds number, via the frictional coefficient often depicted in the classical Moody diagrams. The later are included in the boundary conditions using a quasi-steady Bernoulli relation. The model also accounts for the possibility of channels with variable cross-section, which may be useful for recreating more complex scenarios found in various practical applications. The equations of motions are presented in dimensionless form and the key dimensionless parameters, studied extensively throughout this thesis, are introduced.

The proposed nonlinear physical model, illustrated in Figure 2.1, describes the fluid-structure interaction of a flexible beam confined by flow on each upper and lower sides. The formulation presented in the following is generic in that it can, in principle, be applied to beams with arbitrary boundary conditions as well as with flow in either direction. Moreover, it also accounts the possibility of channels with variable cross-section, which may be of practical interest for various applications (e.g. design of flutter-based energy-harvesting devices (Tosi, 2018), in modelling of human snoring (Aurégan & Depollier, 1995), etc.) Here we present the formulation in its generic form even though, in this thesis, focus will be given to the particular case of a cantilever beam subject to flow in the positive x-direction.

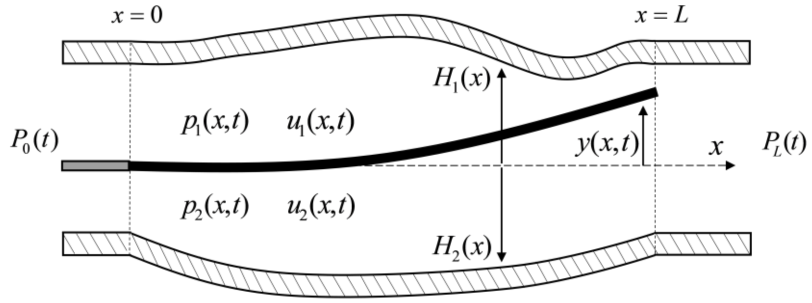

Figure 2.1 – Schematic description of the 1D model.

2.1 Structural dynamics

The linear dynamics of the flexible structure considered here are described in a modal framework. This framework presents a discrete representation of the vibrations of a 1-D continuous structure in terms of its modes of vibration, using the associated modal parameters: modal frequencies, damping ratios, masses and mode shapes. It is generic in the sense that modal parameters can be estimated either through a variety of theoretical models (Euler-Bernoulli, Timoshenko, etc.) or through experimental modal identification methods. Additionally, it provides a practical mathematical description of continuous models, as partial differential equations (PDEs) are approximated by a finite set of linearly independent ordinary differential equations (ODEs). In the following we illustrate the modal decomposition for the simple case of a damped cantilever beam with uniform cross-section. Note however that more complex scenarios can eventually be treated: using different beam models, considering beams with variable cross-section, added punctual masses or springs, etc.

From the several beam models available in literature (Slaughter, 2001), here we have used the 1-D linear Euler-Bernoulli beam equation. Starting from a conservative beam, with isotropic material properties and uniform cross-section, the equation of motion is given by

$$\rho_s S \frac{\partial^2 y(x,t)}{\partial t^2} + EI \frac{\partial^4 y(x,t)}{\partial x^4} = 0 \tag{2.1}$$

where $y(x,t)$ is the transverse displacement, ρ_s is the density, S is the cross-sectional area, E is the Young's modulus and I is the second moment of area. Moreover, the boundary conditions associated with cantilever beam, clamped at one end $x=0$, and free at the other $x=L$ are given by

$$\begin{aligned} & y(0,t)=0 \quad ; \quad \frac{\partial y}{\partial x}(0,t)=0 \\ & \frac{\partial^2 y}{\partial x^2}(L,t)=0 \quad ; \quad \frac{\partial^3 y}{\partial x^3}(L,t)=0 \end{aligned} \tag{2.2}$$

In the absence of external forcing, we look for solutions of the system (2.1)-(2.2) in free-vibration in the form $y(x,t)=\phi(x)e^{-i\omega t}$, where i is the imaginary unit. Using the boundary conditions (2.2), we eventually reach the characteristic equation

$$\cosh(\beta L)\cos(\beta L)+1=0 \tag{2.3}$$

whose solutions β_m allow us to retrieve the modal frequencies of the beam

$$\omega_m=(\beta_m L)^2\sqrt{\frac{EI}{\rho_s S}} \tag{2.4}$$

as well as its mode shapes

$$\phi_m(x)=\cos(\beta_m x)+\cosh(\beta_m x)-\left[\frac{\cos(\beta_m L)+\cosh(\beta_m L)}{\sin(\beta_m L)-\sinh(\beta_m L)}\right]\sin(\beta_m x)+\sinh(\beta_m x) \tag{2.5}$$

Subsequently, we develop the beam displacement in terms of a truncated series of M beam modes

$$y(x,t)=\sum_{m=1}^{M}\phi_m(x)q_m(t) \tag{2.6}$$

where $q_m(t)$ are modal displacements. Replacing the development (2.6) in the original PDE (2.1) leads to

$$\rho_s S\sum_{m=1}^{M}\phi_m(x)\ddot{q}_m(t)+EI\sum_{m=1}^{M}\frac{\partial^2\phi_m(x)}{\partial x^4}q_m(t)=0\ , \quad \text{for} \quad m=1,2\ldots M \tag{2.7}$$

where the upper-dots denote time-derivatives. After the typical Galerkin projection (multiplication by $\phi_n^T(x)$ and integrating over the length L), we obtain

$$\rho_s S\sum_{m=1}^{M}\ddot{q}_n(t)\int_0^L\phi_m^T(x)\phi_n(x)dx+EI\sum_{m=1}^{M}q_m(t)\int_0^L\phi_m^T(x)\phi_n{}^{iv}(x)dx=0 \tag{2.8}$$

Noting that the fourth-spatial derivative of the mode shapes can be written as $\phi_n{}^{iv}(x)=\beta_n^4\phi_n(x)$, and combining with expression (2.4) as well as the orthogonality condition

$$\int_0^L\phi_m^T(x)\phi_n(x)dx=\begin{cases} L/4 & \text{if } n=m \\ 0 & \text{if } n\neq m \end{cases} \tag{2.9}$$

we eventually reach a set of M linearly independent ODEs

$$m_m\ddot{q}_m(t)+m_m\omega_m^2 q_m(t)=0\ \ , \quad m=1,\,2\,\ldots\,M \tag{2.10}$$

where the modal masses m_m are, for a uniform cantilever beam, a quarter of its total mass, $m_m = \rho_s SL / 4$. Subsequently, assuming a proportional damping model, the internal losses in the beam can be included in the modal equations of motion without affecting the orthogonality properties, hence maintaining a set of linearly independent equations. The damped version of the modal equations is given by

$$m_m\ddot{q}_m(t) + 2m_m\omega_m\zeta_m + m_m\omega_m^2 q_m(t) = 0 \quad , \quad m = 1,\, 2\, \ldots\, M \tag{2.11}$$

where ζ_m is the modal damping ratio.

The beam is then subject to fluid forces given by the pressure difference between the upper and lower channels $\delta p(x,t) = p_2(x,t) - p_1(x,t)$. Projection of this force field unto the beam modes leads to the modal forcing terms

$$F_m(t, q_m, \dot{q}_m, \ddot{q}_m) = w\int_0^L \delta p(x,t)\phi_m(x)dx \quad , \quad m = 1,\, 2\, \ldots M \tag{2.12}$$

where w is the beam's width (spanwise length). Placing the forcing terms on the right-hand-side of (2.11) results in the final set of fluid-forced beam modal equations

$$\ddot{q}_m(t) + 2\omega_m\zeta_m\dot{q}_m(t) + \omega_m^2 q_m(t) = F_m(t, q_m, \dot{q}_m, \ddot{q}_m)\big/ m_m \quad , \quad m = 1,\, 2\, \ldots\, M \tag{2.13}$$

As usual, the second-order system (2.13) can also be described by a set of $2M$ first-order ODEs in terms of the modal displacements $q_n(t)$ and velocities $r_n(t) = \dot{q}_n(t)$

$$\begin{cases} \dot{q}_m(t) = r_m(t) \\ \dot{r}_m(t) + 2\omega_m\zeta_m r_m(t) + \omega_m^2 q_m(t) = F_m(t)\big/ m_m \end{cases} , \quad \text{for } m = 1,\, 2\, \ldots M \tag{2.14}$$

It should be noted that, for simplicity, we have neglected the effect of geometric nonlinearities of the beam. Including these nonlinear terms, although inconsequential for a linear stability analysis, could be important for the estimation of large amplitude beam oscillations. This was a conscious choice made based two arguments. Firstly, since we seek to better understand fundamental aspects of this complex fluid structure interaction problem, the simplest cases should be treated first for a clearer interpretation of results. That is, if many nonlinear aspects of the problem are included in the model (geometric and material nonlinearities, conservative and dissipative flow nonlinearities, etc.), association of certain dynamical patterns with specific nonlinear terms becomes a more difficult task. Secondly, as will be discussed in the following section, the bulk-flow model used here assumes relatively narrow flow confinements. Contrary to systems dealing with open-flow, beam motion in these configurations is restricted by contact with the walls of a narrow channel, and it is therefore less likely that nonlinear geometric effects will be of paramount importance, as is the case of unconfined configurations.

Even though we have neglected these effects, including terms describing geometric nonlinearities could be incorporated in the model in a straightforward manner. For example, assuming an inextensible isotropic Euler-Bernoulli beam, the equation of motion including up to third-order nonlinearities is given by (Nayfeh & Pai, 2004)

$$\rho_s S \frac{\partial^2 y}{\partial t^2} + EIy^{iv} + EI[y'(y'y'')']' + \frac{\rho_s S}{2}\left[y' \int_L^x \left(\frac{\partial^2}{\partial t^2}\int_0^x y'^2 \, dx\right) dx\right]' = 0 \tag{2.15}$$

where upper dashes denote spatial derivatives, and the last two terms describe the geometric and inertia nonlinearities, respectively. These nonlinear terms can be projected in the modal basis leading to two extra terms to be added on the right-hand-side of the modal equations (2.11)

$$F_m^{geo}(t) = \sum_{i,j,k}^{M} \Psi_m^{ijk} q_i q_j q_k \quad ; \quad F_m^{ine}(t) = \sum_{i,j,k}^{M} \Lambda_m^{ijk} (q_k \dot{q}_i \dot{q}_j + q_k q_i \ddot{q}_j) \tag{2.16}$$

where the spatial operator matrices, Ψ and Λ, are given by

$$\Psi_n^{ijk} = -EI \int_0^L \left[\phi_i'(\phi_j'\phi_k'')'\right]' \phi_n dx \quad ; \quad \Lambda_n^{ijk} = -\rho S \int_0^L \left[\phi_k' \int_L^x \int_0^x \phi_i'\phi_j' dx dx\right]' \phi_n dx \tag{2.17}$$

To clarify, these nonlinear terms are not used in this thesis. They are mentioned here just as an example of how the structural model could easily be refined.

2.2 Fluid dynamics

In the context of bulk-flow theory (Hirs, 1973) (Antunes & Piteau, 2010) (Piteau & Antunes, 2012), we assume that channel heights are relatively small compared to the characteristic length of the system L. In such scenarios, the variations in the flow pressure $p(x,y,z,t)$ and velocity $u(x,y,z,t)$ fields along its cross-section can generally be considered negligible, and hence, the flow variables are taken as the cross-sectionally averaged, $p_c(x,t)$ and $u_c(x,t)$, where the index c denotes the upper $(c=1)$ or lower $(c=2)$ channels. One thus reduces drastically the modelling and computational complexity of the problem to a 1D formulation. Fluctuating channel heights $h_c(x,t)$ are defined in terms of the beam motion $y(x,t)$ and the fixed channel profiles $H_c(x)$ as

$$\begin{cases} h_1(x,t) = H_1(x) - y(x,t) = H_1(x) - \sum_{m=1}^{M} \varphi_m(x) q_m(t) \\ h_2(x,t) = H_2(x) + y(x,t) = H_2(x) + \sum_{m=1}^{M} \varphi_m(x) q_m(t) \end{cases} \tag{2.18}$$

where $H_1(x)$ and $H_2(x)$ are the distances from the upper and lower walls to the beam equilibrium position, respectively. It is worth noting that we assume changes along the channel cross-section $\partial H_c / \partial x$ are sufficiently smooth to avoid flow separation. In cases where discontinuities in the cross-section are present, different formulations must be derived. Namely, the inclusion of head-loss terms localized along the domain should be discussed.

Derivation of the 1-D bulk-flow equations under these assumptions can be found for example in (Antunes & Piteau, 2010) for incompressible flows. The continuity and momentum equations of the flow in each channel $c = 1,2$ are given by

$$\frac{\partial h_c}{\partial t} + \frac{\partial}{\partial x}(h_c u_c) = 0 \tag{2.19}$$

$$\rho\left[\frac{\partial}{\partial t}(h_c u_c) + \frac{\partial}{\partial x}(h_c u_c^2)\right] + h_c \frac{\partial p_c}{\partial x} + \tau_c^w + \tau_c^b = 0 \tag{2.20}$$

where ρ is the fluid density while τ_c^w and τ_c^b are the shear stresses at the two interfaces (fluid-wall and fluid-beam) in each channel. Following the bulk-flow approach, the tangential stresses will be formulated as a head-loss model, given by

$$\tau_c^{w,b} = \frac{1}{2}\rho\, u_c \mid u_c \mid f_c^{w,b} \tag{2.21}$$

where f_c^w and f_c^b are the Fanning friction coefficients for each interface. These terms describe distributed head-losses which encapsulate, in a simplified manner, viscous, turbulent or boundary layer effects. To maintain a generic formulation, we keep the modular term $u_c \mid u_c \mid$, instead of its quadratic simplification u_c^2. This allows for the treatment of flow in both directions, as well as locally reverse flow, which may occur at large amplitude beam motions. Additionally, we assume both interfaces have equivalent frictional properties, hence $f_c^w = f_c^b = f$. Then, the momentum equation can also be re-written more compactly as

$$\frac{\partial u_c}{\partial t} + u_c \frac{\partial u_c}{\partial x} + \frac{1}{\rho}\frac{\partial p_c}{\partial x} + \frac{u_c \left|u_c\right|}{h_c} f = 0 \tag{2.22}$$

noting that, when neglecting the frictional term, it reduces to its commonly used inviscid form

$$\frac{\partial u_c}{\partial t} + u_c \frac{\partial u_c}{\partial x} + \frac{\partial p_c}{\partial x} = 0 \tag{2.23}$$

where dependence on the fluctuating channel heights $h_c(x,t)$ vanishes.

2.2.1 Distributed losses

It is well known that the Fanning friction coefficient f depends on the Reynolds number Re, and the solid/flow interface rugosity. The literature on this topic is vast and several models have been developed to approximate experimental observations (Hirs, 1973) (Blevins, 1984) (Idel'Cik, 1994). The simplest, and most commonly used models, start from the assumption that f has a dependency relation to the Reynolds number, different in laminar and turbulent flows. Typical values of f for smooth surfaces are: $0.001 < f < 0.01$ for turbulent flows, and $0.01 < f < 1$ for laminar flows (Blevins, 1984). Some models combine the two relations (laminar and turbulent) to describe the friction factor in the full range of flows, including mixed laminar-turbulent flows. For example, in (Piteau & Antunes, 2012), the authors have proposed an analytical approximation based on the commonly used model, established from empirical data of steady flow (Blevins, 1984) (Idel'Cik, 1994), given by

$$\begin{cases} f = 12\,\mathrm{Re}^{-1} & \text{for} \quad \mathrm{Re} < \mathrm{Re}_0 \quad \text{(laminar)} \\ f = 0.055\,\mathrm{Re}^{-0.25} & \text{for} \quad \mathrm{Re} > \mathrm{Re}_0 \quad \text{(turbulent)} \end{cases} \tag{2.24}$$

where Re_0 is the Reynolds number separating laminar from turbulent flow ranges. Based on these relations, Piteau & Antunes proposed a mixed formulation, applicable in the whole range of Reynolds number, given by

$$f = 12\,\mathrm{Re}^{-1} + 0.055\,\mathrm{Re}^{-1/4} \tag{2.25}$$

To illustrate, Figure 2.2 compares the relations (2.24) with the mixed-flow analytical approximation (2.25).

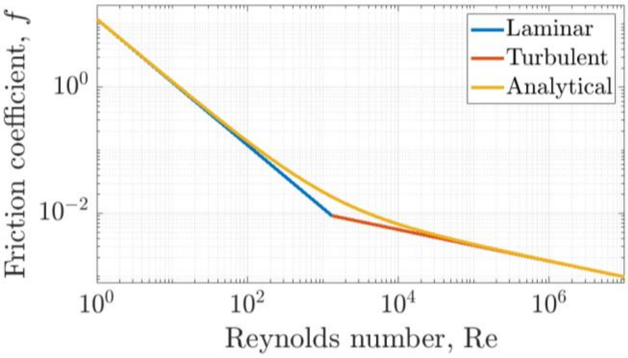

Figure 2.2 – Comparison between Hirs friction model (2.24) with the continuous analytical approximation (2.25).

The Reynolds number Re in (2.25) can be expressed in terms of the system variables by

$$\mathrm{Re} = \frac{2h(x,t)\left|u(x,t)\right|}{\nu} \tag{2.26}$$

where ν is the kinematic viscosity of the fluid. Replacing (2.26) in the approximation (2.25), would lead to analytical formulations describing distributed losses, including variations of Reynolds number along the domain, as well as in time, in a simple quasi-steady manner. These, and other more elaborate unsteady formulations for the flow frictional effects, might be of interest to include in the future as they eliminate incertitude and guesswork concerning this parameter, however, at the cost of increasing model complexity. With that said, in this work we will take f to be constant for the sake of simplicity, which might be a more reliable assumption in turbulent ranges, where experiments show lower or even negligible Reynolds-dependency (Blevins, 1984). Nevertheless, at least under linearized conditions, maintaining a constant f will accurately correspond to steady flow conditions with a specific Reynolds number and, relying on expression (2.25), we are able to directly compare stability boundaries predicted by our model to results from more complete 2-D viscous models presented in literature.

2.2.2 Boundary conditions

Aside from the distributed losses, we must include as well the localized dissipative effects at the boundaries. These are enforced at the boundary conditions and aim to encapsulate, in a simplified manner, the energy losses occurring at the boundary and outside the computational domain. The complex phenomena associated with these energy losses is diverse and can vary significantly with beam boundary conditions, local geometry (e.g. area constriction/expansion), and flow conditions. However, a simple and common approach is to use a quasi-steady Bernoulli relation which includes head-loss terms, whose coefficients are taken from empirical data. This method is commonly used to treat leakage-flow instabilities (Inada & Hayama, 1990) and has also been used to model the flutter of cantilever beams in channel flow (Nagakura & Kaneko, 1993). Here, the boundary conditions are set as if two reference pressure chambers (where flow velocity is zero) exist far enough from the boundaries of the domain, as illustrated in Figure 2.3. Then, the localized head-loss terms will represent energy losses occurring in the path between the reference chambers and the computational domain entrance/exit.

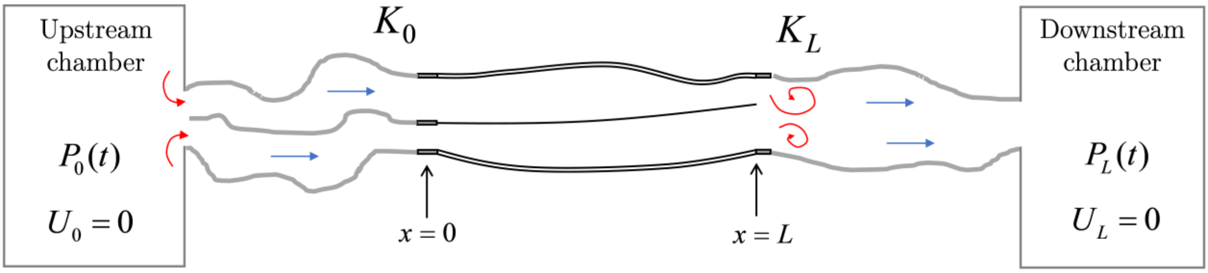

Figure 2.3 – Illustration of the system implicitly assumed by the boundary conditions with localized head-losses.

The second order system (2.19)-(2.20) is then submitted to the following flow boundary conditions at $x = 0$ and $x = L$:

$$p_c(0,t) + \rho\frac{1}{2}u_c^2(0,t) = P_0(t) - \rho\frac{1}{2}u_c(0,t)\left|u_c(0,t)\right|K_0 \tag{2.27}$$

$$p_c(L,t) + \rho\frac{1}{2}u_c^2(L,t) = P_L(t) + \rho\frac{1}{2}u_c(L,t)\left|u_c(L,t)\right|K_L \tag{2.28}$$

where K_0 and K_L are the singular head-loss coefficients at the boundaries; $P_0(t)$ and $P_L(t)$ are the imposed pressures at each reference chambers.

Notice that a head-loss coefficient is a very convenient way of condensing very complex 3D physical flow phenomena into a single and easily measured experimental parameter, which can naturally fit a simplified 1D flow model. Also notice that, as explicitly stated by equations (2.27) and (2.28), the loss-coefficients K_0 and K_L impose definite relations between the flow pressure and velocity fields at $x = 0$ and $x = L$. Therefore, even if K_0 and K_L stand for physical phenomena arising at the system boundaries and beyond, these coefficients definitely control the flow pressure and velocity fields within the computational domain $0 \le x \le L$.

For the particular case of a cantilevered beam, the head-loss coefficient K_0 is bound to have a minimal effect on the dynamics, as it acts on the clamped end of the beam. For steady inflow (in the positive $x-$direction), it actually acts as a control-valve, limiting the flow energy entering the domain. In symmetric configurations, this parameter does not affect dynamics qualitatively. However, notice that the coefficient K_0 (and K_L) can be set to different values in the upper and lower channels, inducing an asymmetry in flow resistance. In these asymmetric scenarios it can indeed play an important role. As a side note, such asymmetric configurations were studied experimentally during this thesis, and the reader will find an interesting set of results and discussion in Appendix D.

On the other hand, the complex effects expected at the trailing-edge suggest that K_L will have a significant effect on the coupling dynamics. Actually, vorticity, circulatory effects or flow separation are not considered explicitly in this model, as done in some previous work (Tang & Paidoussis, 2007) (Chen et al., 2014) (Kornecki et al., 1976). Nevertheless, their associated energy losses are accounted for implicitly through K_L.

As a note, Kaneko et al. (1992) have developed a model using similar head-loss coefficients. In their model, the authors assume values equivalent to $K_L = 1$ and $K_0 = 0$. Even though they only explored symmetric configurations, it is worth noting that experimental results correlated well with the predicted stability boundaries and associated frequencies. Moreover, Tosi and Colonius (2019), compared the linear stability results stemming from a similar 1D model to simulations of a nonlinear 2D model. They showed that, using $K_0 = 0$ and $K_L = 1$, flutter boundaries are remarkably well predicted for a wide range of dimensionless parameters, provided the channel heights remain reasonably small compared to the beam length, as assumed by the bulk-flow equations used.

Following reference literature, in this work we have considered constant values for K_0 and K_L. However, it is worthwhile noting that one could eventually consider variable coefficients $K_0(t)$ and $K_L(t)$ dependent on particular geometric configurations, or local Reynolds number, in a quasi-steady manner, see Perotin (1994). Notably, models considering the delicate flow conditions at the trailing edge and their dependence to the dynamic channel motion, $h(L,t)$ or $\dot{h}(L,t)$ for example, could eventually be explored. Even more involved unsteady formulations for $K_0(t)$ and $K_L(t)$ might be attempted, for instance in the spirit of the unsteady formulations proposed for the skin-friction coefficient $f(t)$ in pipe flow, see the review by Shamloo et al. (2015). By postulating here that $f(x,t) \approx \bar{f}$, $K_0(t) \approx \bar{K}_0$ and $K_L(t) \approx \bar{K}_L$, there are obviously the implicit assumption that $\left|f(x,t) - \bar{f}\right| / \bar{f} \ll 1$, $\left|K_0(t) - \bar{K}_0\right| < \varepsilon$ and $\left|K_L(t) - \bar{K}_L\right| / \bar{K}_L \ll 1$.

2.3 Dimensionless equations of motion and key dimensionless parameters

The equations of motion of the coupled system are converted to dimensionless form following literature standards. The spatial scaling is normalized by the system length L. It is worthwhile noting that, spatial scaling could also be made with reference to a channel height H_1. However, this choice is less generic considering the possibility of asymmetric channels $H_1 \neq H_2$, or channels with variable cross-section $H_c(x)$. Moreover, normalizing to the system's length also allows for comparisons with models considering unconfined open-flow $H_c = \infty$. The inertial scaling is defined by the beam's total mass $m_0 = \rho_s S L$. Finally, time-scales are normalized to the characteristic angular frequency ω_0 (or period T_0) of the beam, given by

$$\omega_0 = \frac{2\pi}{T_0} = \frac{1}{L^2}\sqrt{\frac{EI}{\rho_s S}} \tag{2.29}$$

This reference frequency ω_0 is the standard in literature as opposed to, for example, the fundamental frequency of the beam ω_1. This is the case likely because it does not depend on the beam boundary conditions and hence allows for comparisons between different systems with pinned, clamped or free boundaries.

With that said, the dimensionless space and time variables are given by

$$x = \hat{x}\big/L \quad ; \quad t = \hat{t}\omega_0 \tag{2.30}$$

where here the upper-hat denote their physical counterparts. The structural equations are normalized by a factor of $1\big/m_0\omega_0^2 L$, leading to

$$\begin{gathered}\ddot{q}_m(t) + 2\omega_m\zeta_m\dot{q}_m(t) + \omega_m^2 q_m(t) = \frac{M^*}{m_n}\int_0^1 \delta p(x,t)\phi_m(x)dx \ , \\ \text{for} \ \ m = 1,\ 2\ \ldots\ M\end{gathered} \tag{2.31}$$

where the variables associated with the beam motion are given by

$$\begin{aligned} m_m &= \hat{m}_m\big/m_0 &&; \quad \omega_m = \hat{\omega}_m\big/\omega_0 \\ y(x,t) &= \hat{y}(\hat{x},\hat{t})\big/L &&; \quad q_m(t) = \hat{q}_m(\hat{t})\big/L \\ \dot{q}_m(t) &= \hat{\dot{q}}_m(\hat{t})\big/\omega_0 L &&; \quad \ddot{q}_m(t) = \hat{\ddot{q}}_m(\hat{t})\big/\omega_0^2 L \end{aligned} \tag{2.32}$$

and M^* is a fluid-beam mass ratio, defined explicitly by

$$M^* = \frac{\rho L}{\rho_s e} \tag{2.33}$$

where e is the beam thickness. Similarly, the continuity and momentum equations for the flow, as well as the associated boundary conditions, are normalized by a factor of $1\big/\rho\omega_0^2 L$ leading to

$$\frac{\partial h_c}{\partial t} + \frac{\partial}{\partial x}(h_c u_c) = 0 \tag{2.34}$$

$$\frac{\partial u_c}{\partial t} + u_c\frac{\partial u_c}{\partial x} + \frac{\partial p_c}{\partial x} + \frac{u_c\left|u_c\right|}{h_c}f = 0 \tag{2.35}$$

$$p_c(0,t) = P_0(t) - \frac{1}{2}u_c^2(0,t) - \frac{1}{2}u_c(0,t)\left|u_c(0,t)\right|K_0 \tag{2.36}$$

$$p_c(L,t) = P_L(t) - \frac{1}{2}u_c^2(L,t) + \frac{1}{2}u_c(L,t)\left|u_c(L,t)\right|K_L \tag{2.37}$$

where the dimensionless flow velocities, pressures and fluctuating channels are related to their physical counterparts by

$$u_c(x,t) = \frac{\hat{u}_c(\hat{x},\hat{t})}{\omega_0 L} \quad ; \quad p_c(x,t) = \frac{\hat{p}_c(\hat{x},\hat{t})}{\rho\omega_0^2 L^2} \quad ; \quad h_c(x,t) = \frac{\hat{h}_c(\hat{x},\hat{t})}{L} \tag{2.38}$$

Additionally, it is important to highlight other dimensionless parameters that play a dominant role in defining the system's dynamical behavior, and will hence be studied throughout this thesis. One of them is a reduced velocity U^*, defined by the sum of the static component of the flow velocity entering each channel in relation to the beam characteristic frequency ω_0 and length L, that is

$$U^* = \frac{\bar{\hat{u}}_1(0) + \bar{\hat{u}}_2(0)}{2\omega_0 L} = \frac{\bar{\hat{u}}_1(0) + \bar{\hat{u}}_2(0)}{2}\sqrt{\frac{\rho_s S L^2}{EI}} \tag{2.39}$$

where the upper-dash denote a steady (non-fluctuating) component, such that $u_c(x,t) = \bar{u}(x) + \tilde{u}(x,t)$. Together with the fluid-beam mass-ratio M^*, the pair (M^*, U^*) represent the two key dimensionless parameters affecting the system dynamics. Throughout literature, and also in this work, results for stability boundaries and bifurcation branches will often be presented in the (M^*, U^*) plane. Another important dimensionless parameter, in the context of confined flow, is the so-called confinement ratio H^*, which we define here for the case of channels of constant height $H_1, H_2 = \text{const}$,

$$H^* = \frac{H_1 + H_2}{L} \tag{2.40}$$

In relation to the confinement, we can also define a channel asymmetry ratio $A^* = H_1 / H_2$ for cases where the beam is placed closer to either the upper or lower walls. In later chapters, some results are presented for asymmetric configurations, but in general, focus is given to symmetric configurations. Hence, $A^* = 1$ is assumed unless stated otherwise.

In relation to energy losses, two important parameters, whose influence will be analyzed in this thesis, are (1) the structural internal losses, described by the modal damping ratios ζ_n; and (2) viscous losses in the flow, described the Reynolds number Re. For convenience, modal damping will typically be assumed uniform in all modes, i.e. $\zeta_n = \zeta \; \forall n$. As discussed earlier, viscous losses will be modelled through a distributed head-loss term controlled by a frictional coefficient f, whose associated Reynolds number is calculated from expression (2.25).

2.4 Summary

The content presented in this chapter can be summarized by the following points:

→ A physical model describing the nonlinear interaction of a flexible beam surrounded by confined axial flow is derived. Using bulk-flow theory, the flow fields are taken as cross-sectionally averaged and the mathematical model reduces to a system of one-dimensional coupled partial differential equations.

→ The motion of the flexible beam is modelled in terms of its modes of vibration, reducing the structural PDE into a finite set of linearly independent ODEs.

→ Distributed flow dissipation is included using a frictional term, which aims to encapsulate viscous and boundary layer effects in a simplified manner. Values for the frictional coefficient are approximated from empirical data in steady flow, for both laminar and turbulent regimes. These values are directly related to Reynolds number via the typical Moody's diagram.

→ Localized head-losses are also included at the boundary conditions. These aim to describe, in a compact manner, the pressure losses occurring at the boundaries and outside the domain, caused by complex dissipative phenomena (turbulence, vorticity, flow separation, etc.), notably those occurring at the trailing edge of the beam.

→ The system of equations is presented in dimensionless form, and the primary dimensionless parameters, extensively studied throughout this thesis, are defined.

Chapter 3

An analytical formulation based on formal solutions

In this chapter we present a nonlinear analytical resolution to a simplified one-dimensional model of a cantilever beam in confined axial flow. The present analytical approach is based on the formal solutions for the flow velocity and pressure fields and leads to a compact system for linear stability analysis, but also to a nonlinear formulation of the fluid-structure interaction. Additionally, the formulation also provides compact analytical expressions for the steady and linearized cases, which may be useful tool in underlying key dimensionless parameters and their association with specific dynamical behavior. As reported by many previous experimental studies, fluttering beams in confined passages often lead to impacts between the beam and the side-walls. Here, the inclusion of a regularized contact model allows for the computation of the full nonlinear dynamics, including intermittent impacts. Linear stability results are compared to previously published results using 2-D CFD models, and the relative merits of the model are discussed. Subsequently, temporal integrations are used to study the post-stable dynamics of the nonlinear coupled system. A variety of limit cycles, (1) with and without impacts, (2) in symmetric and asymmetric configurations and (3) with impacts both at the beam tip and along its length, are shown to illustrate the diversity of dynamics encountered. Moreover, we show that, at large flow velocities, particular model configurations can lead to aperiodic dynamics, a phenomenon reported in several experimental observations.

3.1 Analytical solutions of the nonlinear flow equations

The analytical resolution presented here is inspired by the work of Antunes & Piteau (2010, 2012). In their work, analytical expressions for the fluid forces between two parallel plates are derived, leading to a single mode nonlinear lumped-parameter formulation, describing the interaction dynamics of a discrete oscillator subject to axial flow, including both distributed and singular head-losses terms. Here, we developed on the same idea, and apply it to the coupling of axial flow to a continuous flexible structure.

Integrating the continuity equation (2.19) with respect to x leads us to a formal solution for the velocity fields in each channel c:

$$u_c(x,t) = \frac{Q_c(t) - \int \dot{h}_c(x,t)dx}{h_c(x,t)} \tag{3.1}$$

where the "constants" of integration (actually, time domain functions) $Q_c(t)$ represent the global unsteady flow rates in each channel. After replacement of (3.1) in the momentum equation (2.22) and again integrating with respect to x, we obtain the formal solution for the pressure field in each channel,

$$p_c(x,t) = \int \left\{ \begin{array}{c} \dfrac{\int \ddot{h}_c dx}{h_c} - 2\dfrac{\dot{h}_c \int \dot{h}_c dx}{h_c^2} + \dfrac{h_c^{'} \left(\int \dot{h}_c dx\right)^2}{h_c^3} \\ -\dfrac{1}{h_c}\dot{Q}_c(t) + 2\left(\dfrac{\dot{h}_c}{h_c^2} - \dfrac{h_c^{'} \int \dot{h}_c dx}{h_c^3}\right) Q_c(t) \\ +\dfrac{h_c^{'}}{h_c^3} Q_c(t)^2 + f\left(\dfrac{\left(\int \dot{h}_c dx - Q_c(t)\right)\left|\int \dot{h}_c dx - Q_c(t)\right|}{h_c^3}\right) \end{array} \right\} dx + S_c(t) \tag{3.2}$$

where spatial and temporal derivatives are denoted by an upper dash and dot, respectively. The new "constants" of integration $S_c(t)$ describe the pressure at the entrance of the channels $S_c(t) = p_c(0,t)$, i.e. the pressure after the effect of the localized head-losses at $x = 0$. Note that the integral terms in (3.1) and (3.2) correspond to primitives (indefinite integrals) as their constants of integration are combinedly encapsulated in $Q_c(t)$ and $S_c(t)$.

From here on, to simplify notation, we define the following auxiliary variables describing the terms in the formal solutions

$$
\begin{aligned}
&A_c(x,t) = -\frac{\int \dot{h}_c dx}{h_c} \quad ; \qquad B_c(x,t) = \frac{1}{h_c} \quad ; \\
&C_c(x,t) = \frac{\int \ddot{h}_c dx}{h_c} - 2\frac{\dot{h}_c \int \dot{h}_c dx}{h_c^2} + \frac{\left(\int \dot{h}_c dx\right)^2}{h_c^3}\left[h_c^{'} + f\,\mathrm{sign}\left(\int \dot{h}_c dx - Q_c(t)\right)\right] \;; \\
&D_c(x,t) = 2\left\{\frac{\dot{h}_c}{h_c^2} - \frac{\int \dot{h}_c dx}{h_c^3}\left[h_c^{'} + f\,\mathrm{sign}\left(\int \dot{h}_c dx - Q_c(t)\right)\right]\right\} \;; \\
&E_c(x,t) = \frac{1}{h_c^3}\left[h_c^{'} + f\,\mathrm{sign}\left(\int \dot{h}_c dx - Q_c(t)\right)\right] \;;
\end{aligned}
\tag{3.3}
$$

To enforce the boundary conditions, we replace the formal solutions (3.1) and (3.2) into the boundary conditions (2.27) and (2.28). After some algebra, we obtain two expressions for the constant of integration $S_c(t)$, in terms of $Q_c(t),\ \dot{Q}_c(t)$ and the beam motion $A_c(x,t) - E_c(x,t)$. At the leading edge ($x = 0$) we have simply

$$
S_c(t) = P_0 - \frac{1}{2}[1 + \mathrm{sign}(Q_c(t))K_0][B_c(0,t)Q_c(t)]^2 \tag{3.4}
$$

while at the trailing edge ($x = 1$) we get

$$
\begin{aligned}
&S_c(t) = P_L(t) + \left(\int B_c(1,t)dx\right)\dot{Q}_c(t) \\
&-\left\{\int D_c(1,t)dx + A_c(1,t)B_c(1,t)\left[1 - \mathrm{sign}\begin{pmatrix} A_c(1,t) \\ +B_c(1,t)Q_c(t)\end{pmatrix} K_L\right]\right\}Q_c(t) \\
&-\left\{\int E_c(1,t)dx + \frac{B_c^2(1,t)}{2}\left[1 - \mathrm{sign}\begin{pmatrix} A_c(1,t) \\ +B_c(1,t)Q_c(t)\end{pmatrix} K_L\right]\right\}Q_c^2(t) \\
&-\frac{A_c^2(1,t)}{2}\left[1 - \mathrm{sign}\begin{pmatrix} A_c(1,t) \\ +B_c(1,t)Q_c(t)\end{pmatrix} K_L\right] - \int C_c(1,t)dx
\end{aligned}
\tag{3.5}
$$

Then, combining (3.5) and (3.4), we are able to remove the constant of integration $S_c(t)$ and obtain two (one for each channel) first-order nonlinear ODEs in terms of the unsteady flow rates $Q_c(t)$,

$$
\begin{aligned}
&-\left(\int B_c(1,t)dx\right)\dot{Q}_c(t) \\
&+\left\{\int D_c(1,t)dx + A_c(1,t)B_c(1,t)\left[1-\operatorname{sign}\begin{pmatrix} A_c(1,t) \\ +B_c(1,t)Q_c(t)\end{pmatrix}K_L\right]\right\}Q_c(t) \\
&+\left\{\begin{aligned}&\int E_c(1,t)dx - \frac{B_c^2(0,t)}{2}[1+\operatorname{sign}(Q_c(t))K_0] \\ &+\frac{B_c^2(1,t)}{2}\left[1-\operatorname{sign}\begin{pmatrix} A_c(1,t) \\ +B_c(1,t)Q_c(t)\end{pmatrix}K_L\right]\end{aligned}\right\}Q_c^2(t) \\
&+\frac{A_c^2(1,t)}{2}\left[1-\operatorname{sign}\begin{pmatrix} A_c(1,t) \\ +B_c(1,t)Q_c(t)\end{pmatrix}K_L\right]+\int C_c(1,t)dx + P_0(t) - P_L(t) = 0
\end{aligned}
\tag{3.6}
$$

Replacement of the formal solution for the pressure fields (3.2) into the beam modal equations (2.14), leads to a set of $2N$ nonlinear ODEs, in terms of the modal components $q_n(t)$, $r_n(t)$ and the two unsteady flow rates $Q_1(t)$ and $Q_2(t)$. Together with the two flow rate ODEs (3.6), they form a closed set of first-order nonlinear differential equations describing the 1D fluid-structure model, in the form

$$
[\mathbf{A}]\{\dot{\mathbf{x}}\} + [\mathbf{B}]\{\mathbf{x}\} = \{\mathbf{C}\} \tag{3.7}
$$

where $\mathbf{x} = \{r_1(t),\ \dots\ r_N(t),\ q_1(t),\ \dots\ q_N(t),\ Q_1(t),\ Q_2(t)\}$, $[\mathbf{A}]$ and $[\mathbf{B}]$ are (generally dense) matrices of size $2N+2$, and $\{\mathbf{C}\}$ is a vector containing constant flow terms.

Effectively, we are able to discretize the continuous 1D problem into a set of ODEs. However, there are nonlinear terms associated with beam motion (e.g. $\int A_c dx$) which contain primitives with modal summations in the denominator. As these terms cannot be simplified analytically, we do not reach "true" time-space separation, in the sense that the formulation does not contain *constant* spatial operators. For time domain integrations, these terms need to be calculated at each time-step. Despite this fact, the formulation allows for temporal-integrations of the nonlinear system at very modest computational times.

3.2 Linearized equations

The flow expressions obtained in the previous section can be linearized in order to provide a compact tool for linear stability analysis, which is often the primary concern. To linearize the system, we firstly separate the governing variables into their steady (zero-order) and fluctuating (first-order) components. Here, we adopt the convention $g(x,t) = \bar{g}(x) + \tilde{g}(x,t)$. Then, by means of a Taylor-series expansion, we linearize the equations by keeping only the zero-order and first-order components. Because under linearized conditions the flow must assume a concrete direction, we will make use of plus-minus $\pm$ and minus-plus $\mp$ signs to distinguish the two scenarios, and avoid duplication of expressions. The uppers signs are used for flow in the positive direction ($P_0 > P_L$) and the lower signs for flow in the negative direction ($P_0 < P_L$).

The steady components of the velocity (3.1) and pressure (3.2) fields are given by

$$\bar{u}_c(x) = \frac{\bar{Q}_c}{\bar{h}_c(x)} \qquad ; \qquad \bar{p}_c(x) = -\frac{\bar{Q}_c^2}{2\bar{h}_c(x)^2} \mp \bar{Q}_c^2 f \int \left(\frac{1}{\bar{h}_c(x)^3} \right) dx + \bar{S}_c \tag{3.8}$$

Assuming a constant driving pressure, i.e. $P_0(t) = P_0$ and $P_L(t) = P_L$, we get, according to (2.27) and (2.28), the following steady boundary conditions at $x = 0$ and $x = 1$:

$$\bar{p}_c(0) = P_0 - \frac{1}{2}(1 \pm K_0)\bar{u}_c^2(0) \qquad ; \qquad \bar{p}_c(1) = P_L - \frac{1}{2}(1 \mp K_L)\bar{u}_c^2(1) \tag{3.9}$$

Proceeding in a similar manner as above, we replace the formal solutions (3.8) into the boundary conditions (3.9), leading to

$$\begin{aligned} \bar{S}_c &= P_0 \mp \frac{\bar{Q}_c^2}{2\bar{h}_c(0)^2} K_0 \qquad ; \\ \bar{S}_c &= P_L \pm \left(\frac{\bar{Q}_c^2}{2\bar{h}_c(1)^2} \right) K_L \pm \bar{Q}_c^2 f \int \left(\frac{1}{\bar{h}_c(1)^3} \right) dx \end{aligned} \tag{3.10}$$

which then gives the expression for the (squared) steady flow rate $\bar{Q}_c$ in each channel

$$\bar{Q}_c^2 = \frac{2(P_0 - P_L)\bar{h}_c^2(0)^2 \bar{h}_c^2(1)}{\pm \left[\bar{h}_c^2(0)K_L + \bar{h}_c^2(1)K_0 + 2\bar{h}_c^2(0)\bar{h}_c^2(1) f \left. \int \left(\frac{1}{\bar{h}_c^3(x)} \right) dx \right|_{x=1} \right]} \tag{3.11}$$

Replacing the expressions for $\bar{Q}_c$ and $\bar{S}_c$ into (3.8) will give us expressions for the steady pressure and velocity fields in term of the beam displacement only. Then, the steady pressure difference between the two channels $\delta\bar{p}(x) = \bar{p}_2(x) - \bar{p}_1(x)$ can be written explicitly

$$\delta\bar{p}(x) = (P_0 - P_L) \times \left\{ \begin{array}{l} \dfrac{\bar{h}_1^2(0)^2 \bar{h}_1^2(1) \left[\dfrac{1}{\bar{h}_1^2(x)} \pm \dfrac{K_0}{\bar{h}_1^2(0)} \pm 2f \displaystyle\int \left(\frac{1}{\bar{h}_1^3(x)} \right) dx \right]}{\pm \left[\bar{h}_1^2(0)K_L + \bar{h}_1^2(1)K_0 + 2\bar{h}_1^2(0)\bar{h}_1^2(1) f \left. \displaystyle\int \left(\frac{1}{\bar{h}_1^3(x)} \right) dx \right|_{x=1} \right]} \\ - \dfrac{\bar{h}_2^2(0)^2 \bar{h}_2^2(1) \left[\dfrac{1}{\bar{h}_2^2(x)} \pm \dfrac{K_0}{\bar{h}_2^2(0)} \pm 2f \displaystyle\int \left(\frac{1}{\bar{h}_2^3(x)} \right) dx \right]}{\pm \left[\bar{h}_2^2(0)K_L + \bar{h}_2^2(1)K_0 + 2\bar{h}_2^2(0)\bar{h}_2^2(1) f \left. \displaystyle\int \left(\frac{1}{\bar{h}_2^3(x)} \right) dx \right|_{x=1} \right]} \end{array} \right\} \tag{3.12}$$

Finally, replacing the expression for the steady pressure difference $\delta\bar{p}(x)$ into the beam's (static) equations leads to

$$\bar{q}_n = \frac{M^*}{m_n \omega_n^2} \int_0^1 \delta\bar{p}(x)\phi_n(x)dx \quad , \quad \text{for } n = 1, 2 \ldots N \tag{3.13}$$

The final steady problem then becomes a system of N nonlinear algebraic equations whose only variables are the modal displacements $\bar{q}_n$. All other parameters are set: the driving pressure $P_0 - P_L$, the head-loss coefficients K_0, K_L and f, the channel profiles $H_1(x)$ and $H_2(x)$, as well as the beam modal parameters m_n, ζ_n, ω_n and $\phi_n(x)$. This system can be solved numerically, to find the equilibrium beam configurations $\bar{q}_n$. Subsequently, all other steady variables, $\bar{Q}_c$, $\bar{S}_c$, $\bar{u}_c(x)$, $\bar{p}_c(x)$, can be calculated with the expressions given above.

We now derived the first-order terms stemming from the equations of motion. In the following, to avoid duplication of expressions, we present derivations for the upper channel only $(c = 1)$, noting that equivalent expressions can be derived for the lower channel $(c = 2)$. The fluctuating component of the velocity $\tilde{u}_1(x,t)$ is defined as

$$\tilde{u}_1(x,t) = \tilde{Q}_1(t)\bar{F}_{1,n}(x) \pm \sum_{n=1}^{N} \dot{\tilde{q}}_n(t)\bar{A}_{1,n}(x) \pm \bar{Q}_c \sum_{n=1}^{N} \tilde{q}_n(t)\bar{B}_{1,n}(x) \tag{3.14}$$

and the fluctuating pressure $\tilde{p}_c(x,t)$ is given by

$$\begin{aligned} \tilde{p}_1(x,t) = {} & \sum_{n=1}^{N} \tilde{q}_n(t) 3\bar{Q}_1^2 \int \bar{C}_{1,n}(x)\, dx \\ & -\sum_{n=1}^{N} \dot{\tilde{q}}_n(t) 2\bar{Q}_1 \int \bar{D}_{1,n}(x)\, dx - \sum_{n=1}^{N} \ddot{\tilde{q}}_n(t) \int \bar{A}_{1,n}(x) dx \\ & +\tilde{Q}_1(t) 2\bar{Q}_1 \int \bar{E}_1(x)\, dx - \dot{\tilde{Q}}_1(t) \int \bar{F}_1(x) dx + \tilde{S}_1(t) \end{aligned} \tag{3.15}$$

where, to simplify notation, the steady auxiliary variables $\bar{A}_{c,n}(x)$ - $\bar{D}_{c,n}(x)$ and $\bar{E}_c(x)$ - $\bar{F}_c(x)$ are defined as

$$\begin{aligned} & \bar{A}_{c,n}(x) = \frac{\int \phi_n(x) dx}{\bar{h}_c(x)} \quad ; \qquad \bar{B}_{c,n}(x) = \frac{\phi_n(x)}{\bar{h}_c^{\,2}(x)} \quad ; \\ & \bar{C}_{c,n}(x) = \frac{\phi_n(x)}{\bar{h}_c(x)^4}(\bar{h}_c'(x) \mp f) - \frac{\phi_n'(x)}{3\bar{h}_c^{\,3}(x)} \quad ; \\ & \bar{D}_{c,n}(x) = \frac{\int \phi_n(x) dx}{\bar{h}_c^{\,3}(x)}(\bar{h}_c'(x) \mp f) - \frac{\phi_n(x)}{\bar{h}_c^{\,2}(x)} \quad ; \\ & \bar{E}_c(x) = \frac{(\bar{h}_c'(x) \mp f)}{\bar{h}_c^{\,3}(x)} \quad ; \qquad \bar{F}_c(x) = \frac{1}{\bar{h}_c(x)} \quad ; \end{aligned} \tag{3.16}$$

To the first order, the boundary conditions at $x = 0$ and $x = 1$ become

$$\tilde{p}_c(0,t) = (-1 \mp K_0)\bar{u}_c(0)\tilde{u}_c(0,t) \quad ; \quad \tilde{p}_c(1,t) = (-1 \pm K_L)\bar{u}_c(1)\tilde{u}_c(1,t) \tag{3.17}$$

Replacing the expressions for the fluctuating velocity (3.14) and pressure (3.15) fields into the boundary conditions at $x = 0$, we get

$$\tilde{S}_1(t) = \left(-1 \mp K_0\right)\bar{u}_1(0)\bar{F}_1(0)\tilde{Q}_1(t) \tag{3.18}$$

and at $x = L$, we get

$$\begin{aligned}\tilde{S}_1(t) = &\sum_{n=1}^{N} \tilde{q}_n(t)\left[-3\bar{Q}_1^2 \int \bar{C}_{1,n}(1)\,dx - \left(1 \mp K_L\right)\bar{u}_1(1)\bar{Q}_1\bar{B}_{1,n}(1)\right] \\ &+\sum_{n=1}^{N} \dot{\tilde{q}}_n(t)\left[-2\bar{Q}_1 \int \bar{D}_{1,n}(1)\,dx - \left(1 \mp K_L\right)\bar{u}_1(1)\bar{A}_{1,n}(1)\right] \\ &+\sum_{n=1}^{N} \ddot{\tilde{q}}_n(t)\left[\int \bar{A}_{1,n}(1)dx\right] \\ &+\tilde{Q}_1(t)\left[-2\bar{Q}_1 \int \bar{E}_1(1)\,dx - \left(1 \mp K_L\right)\bar{u}_1(1)\bar{F}_{1,n}(1)\right] \\ &+\dot{\tilde{Q}}_1(t)\left[\int \bar{F}_1(1)dx\right]\end{aligned} \tag{3.19}$$

Then, combining (3.18) from (3.19), we get two linear ODEs (one for each channel) in terms of the fluctuating flow rates $\tilde{Q}_c(t)$

$$\begin{cases}\dot{\tilde{Q}}_1(t)d_1 + \tilde{Q}_1(t)e_1 + \sum_{n=1}^{N}\tilde{q}_n(t)a_{1,n} + \sum_{n=1}^{N}\dot{\tilde{q}}_n(t)b_{1,n} + \sum_{n=1}^{N}\ddot{\tilde{q}}_n(t)c_{1,n} = 0 \\ \dot{\tilde{Q}}_2(t)d_2 + \tilde{Q}_2(t)e_2 - \sum_{n=1}^{N}\tilde{q}_n(t)a_{2,n} - \sum_{n=1}^{N}\dot{\tilde{q}}_n(t)b_{2,n} - \sum_{n=1}^{N}\ddot{\tilde{q}}_n(t)c_{2,n} = 0\end{cases} \tag{3.20}$$

where the auxiliary vectors $a_{c,n}$, $b_{c,n}$, $c_{c,n}$ and scalars d_c, e_c, are given by

$$\begin{aligned} a_{c,n} &= -3\bar{Q}_c^2 \int \bar{C}_{c,n}(1)\,dx - (1 \mp K_L)\bar{u}_c(1)\bar{Q}_c\bar{B}_{c,n}(1) \\ b_{c,n} &= -2\bar{Q}_c \int \bar{D}_{c,n}(1)\,dx - (1 \mp K_L)\bar{u}_c(1)\bar{A}_{c,n}(1) \\ c_{c,n} &= \int \bar{A}_{c,n}(1)dx \\ d_c &= \int \bar{F}_c(1)dx \\ e_c &= -2\bar{Q}_c \int \bar{E}_c(1)\,dx - (1 \mp K_L)\bar{u}_c(1)\bar{F}_c(1) + (1 \pm K_0)\bar{u}_c(0)\bar{F}_c(0)\end{aligned} \tag{3.21}$$

In order to formulate the fluctuating pressure difference $\delta\tilde{p}(x,t)$, we need to replace the expression for $\tilde{S}_c(t)$ in the fluctuating pressure expression (3.15) of each channel, such that the expression for $\delta\tilde{p}(x,t)$ becomes dependent solely on the unknown time dependent variables: $\tilde{q}_n(t)$, $\dot{\tilde{q}}_n(t)$, $\ddot{\tilde{q}}_n(t)$, as well as $\tilde{Q}_1(t), \tilde{Q}_2(t)$, $\dot{\tilde{Q}}_1(t)$ and $\dot{\tilde{Q}}_2(t)$, as well as the steady solutions

$$\begin{aligned}\delta\tilde{p}(x,t) = &\,3\sum_{n=1}^{N}\tilde{q}_n(t)\left[\bar{Q}_2^2\int \bar{C}_{2,n}(x)\,dx - \bar{Q}_1^2\int \bar{C}_{1,n}(x)\,dx\right] \\ &-2\sum_{n=1}^{N}\dot{\tilde{q}}_n(t)\left[\bar{Q}_2\int \bar{D}_{2,n}(x)\,dx - \bar{Q}_1\int \bar{D}_{1,n}(x)\,dx\right] \\ &-\sum_{n=1}^{N}\ddot{\tilde{q}}_n(t)\left[\int \bar{A}_{2,n}(x)dx - \int \bar{A}_{1,n}(x)dx\right] \\ &+\tilde{Q}_2(t)\left[2\bar{Q}_2\int \bar{E}_2(x)\,dx + (-1 \mp K_0)\bar{u}_2(0)\bar{F}_2(0)\right] - \dot{\tilde{Q}}_2(t)\int \bar{F}_2(x)dx \\ &-\tilde{Q}_1(t)\left[2\bar{Q}_1\int \bar{E}_1(x)\,dx + (-1 \mp K_0)\bar{u}_1(0)\bar{F}_1(0)\right] + \dot{\tilde{Q}}_1(t)\int \bar{F}_1(x)dx\end{aligned} \tag{3.22}$$

Subsequently, we can project the pressure difference into the beam modal equations. In matrix form, the linearized modal forces $\tilde{F}_m(t)$ are then written as

$$\tilde{F}_m(t) = \begin{pmatrix} \left[\mathbf{M}_{n,m}\right]\{\ddot{\tilde{q}}_n(t)\} + \left[\mathbf{C}_{n,m}\right]\{\dot{\tilde{q}}_n(t)\} + \left[\mathbf{K}_{n,m}\right]\{\tilde{q}_n(t)\} \\ -\{\mathbf{R}_{1,m}\}\tilde{Q}_1(t) + \{\mathbf{R}_{2,m}\}\tilde{Q}_2(t) \\ +\{\mathbf{T}_{1,m}\}\dot{\tilde{Q}}_1(t) - \{\mathbf{T}_{2,m}\}\dot{\tilde{Q}}_2(t) \end{pmatrix} , \tag{3.23}$$

$$\text{for} \quad m = 1,2...N$$

where the three matrices, of size $N \times N$, and the four vectors, of size N, are given by

$$\begin{aligned}
\mathbf{K}_{n,m} &= -3\int_0^1 \left[\bar{Q}_2^2 \int \bar{C}_{2,n}(x)\,dx + \bar{Q}_1^2 \int \bar{C}_{1,n}(x)\,dx\right]\phi_m(x)dx \quad ; \\
\mathbf{C}_{n,m} &= -2\int_0^1 \left[\bar{Q}_2 \int \bar{D}_{2,n}(x)\,dx + \bar{Q}_1 \int \bar{D}_{1,n}(x)\,dx\right]\phi_m(x)dx \quad ; \\
\mathbf{M}_{n,m} &= \int_0^1 \left[\int \bar{A}_{2,n}(x)dx + \int \bar{A}_{1,n}(x)dx\right]\phi_m(x)dx \quad ; \\
\mathbf{R}_{c,m} &= \int_0^1 \left[2\bar{Q}_c \int \bar{E}_c(x)\,dx - (1 \pm K_0)\bar{u}_c(0)\bar{F}_c(0)\right]\phi_m(x)dx \quad ; \\
\mathbf{T}_{c,m} &= \int_0^1 \left[\int \bar{F}_c(x)dx\right]\phi_m(x)dx
\end{aligned} \tag{3.24}$$

Finally, letting the diagonal mass, damping and stiffness matrices of the (uncoupled) beam be M, C and K, we can build the coupled system by assembling the modal equations together with the two linearized flow ODEs (3.20). In a first-order formulation, we get

$$\begin{bmatrix} ([\mathbf{M}_{n,m}]-[M]) & \left[\mathbf{0}\right] & \{\mathbf{T}_{1,m}\}^T & -\{\mathbf{T}_{2,m}\}^T \\ \left[\mathbf{0}\right] & -\left[\mathbf{I}\right] & \{\mathbf{0}\}^T & \{\mathbf{0}\}^T \\ \{c_{1,m}\} & \{\mathbf{0}\} & d_1 & 0 \\ -\{c_{2,m}\} & \{\mathbf{0}\} & 0 & d_2 \end{bmatrix} \begin{Bmatrix} \dot{\tilde{r}}_n \\ \dot{\tilde{q}}_n \\ \dot{\tilde{Q}}_1 \\ \dot{\tilde{Q}}_2 \end{Bmatrix}$$

$$+ \begin{bmatrix} ([\mathbf{C}_{n,m}]-[C]) & ([\mathbf{K}_{n,m}]-\left[K\right]) & -\{\mathbf{R}_{1,m}\}^T & \{\mathbf{R}_{2,m}\}^T \\ \left[\mathbf{I}\right] & \left[\mathbf{0}\right] & \{\mathbf{0}\}^T & \{\mathbf{0}\}^T \\ \{b_{1,m}\} & \{a_{1,m}\} & e_1 & 0 \\ -\{b_{2,m}\} & -\{a_{2,m}\} & 0 & e_2 \end{bmatrix} \begin{Bmatrix} \tilde{r}_n \\ \tilde{q}_n \\ \tilde{Q}_1 \\ \tilde{Q}_2 \end{Bmatrix} = 0 \tag{3.25}$$

This linear system of ODEs, of size $2N+2$, can then be formulated as an eigenvalue problem to infer the stability of the system.

3.3 Results: linear stability and numerical validation

In this section, with the aim of assessing the viability of the 1D simplified modelling approach and validating our results, we compare the linear stability results from our model to reference results from literature. Even though the present modelling approach allows for channels of arbitrary shapes $H_c(x)$, we will consider only symmetric channels of constant section, i.e.

$H_1(x) = H_2(x) = H_0$, on which most literature is based on. For the same reason, we will analyze configurations with flow in the positive direction only.

3.3.1 Comparison to results from original 1D leakage-flow model

As a starting point to validate the present formulation, we compare stability results to those published by Nagakura and Kaneko (1993), who presented a similar model, with constant and symmetric channel cross-sections. We take the same model parameters used in (Nagakura & Kaneko, 1993): the beam has length $L = 200\ \text{mm}$, width $w = 100\ \text{mm}$, thickness $e = 0.2\ \text{mm}$, density $\rho_s = 8780\ \text{kg}\cdot\text{m}^{-3}$, Young's modulus $E = 1.1 \times 10^{11}\ \text{N}\cdot\text{m}^2$ and modal damping $\zeta = 0.01$; while the fluid has density $\rho = 1.2\ \text{kg}\cdot\text{m}^{-3}$, the localized head-loss coefficients are taken as $K_0 = 0$ and $K_L = 1$, and the friction coefficient $f = 0.005$. The channels are symmetric and have a constant section of height $H_0 = 2.5\ \text{mm}$. This configuration leads to the nondimensional parameters $M^* = 0.136$, $H^* = 1/40$. Figure 3.1 shows results from the two models, describing the evolution of the eigenvalues s in the complex-plane for varying driving pressure (or equivalent fluid inlet velocity U_0). We notice that the stability behavior of the various coupled modes is described identically by the two models, asserting the viability of the proposed resolution.

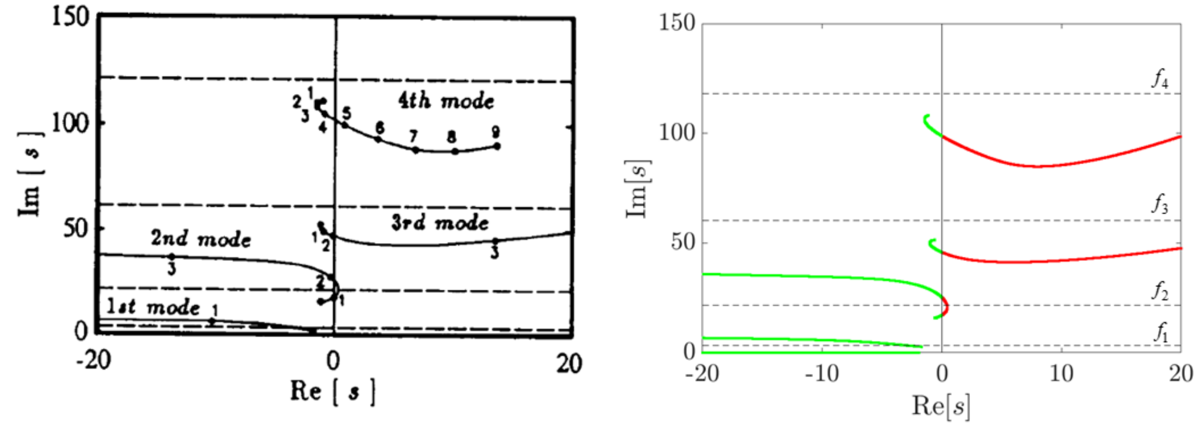

Figure 3.1 – Evolution of the eigenvalues of the coupled structure-fluid system as a function of driving pressure, shown in the complex-plane. Results from the present model are shown on the right while the analogous presented in (Nagakura & Kaneko, 1993) are on the left. The dotted lines correspond to the frequencies $f_n = \omega_n / 2\pi$ of the *in-vacuo* beam modes. Note that, following (Nagakura & Kaneko, 1993), the eigenvalues are normalized by the constant $(EI / mL^4)^{1/2}$, where m is the total mass of the beam. In the right plot, green and red lines represent stable and unstable eigenvalues.

3.3.2 Comparison to results from a 2-D viscous model

To evaluate the potential of the proposed simplified modelling approach, we now compare linear stability results to those obtained from models with more involved physics, which are presumed to provide a more realistic representation of the system dynamics. Namely, we will refer to the results presented by Cisonni et al. (2017), which have used a viscous 2D model to calculate various stability maps as a function of the non-dimensional parameters U^*, M^*, H^* and Re. In their paper (Cisonni et al., 2017), a 2D model is used to solve the nonlinear Navier-Stokes equations in the time-domain, including viscous effects. Several parametric sweeps were carried out to obtain stability curves in the nondimensional $(U^* M^*)$ plane, for several (H^*, Re) pairings. For each parametric configuration, simulations were run for at least 10 periods of oscillations, from which stability conditions and corresponding frequencies were extracted.

As a first example, Figure 3.2 shows a typical stability map in the $(U^*,\ M^*)$ plane, calculated with the present model and with the 2-D viscous model. Here, an undamped beam was considered, $\zeta_n = 0$, the confinement ratio was set at $H^* = 1/10$ and the Reynolds number at $\mathrm{Re} = 100$. Note that, in our formulation, the Reynolds number is set implicitly following relation (2.25), which leads to a friction coefficient $f \approx 0.14$. On the left are the stability boundaries in the $(U^* M^*)$ plane and on the right the frequencies of the corresponding neutrally stable modes.

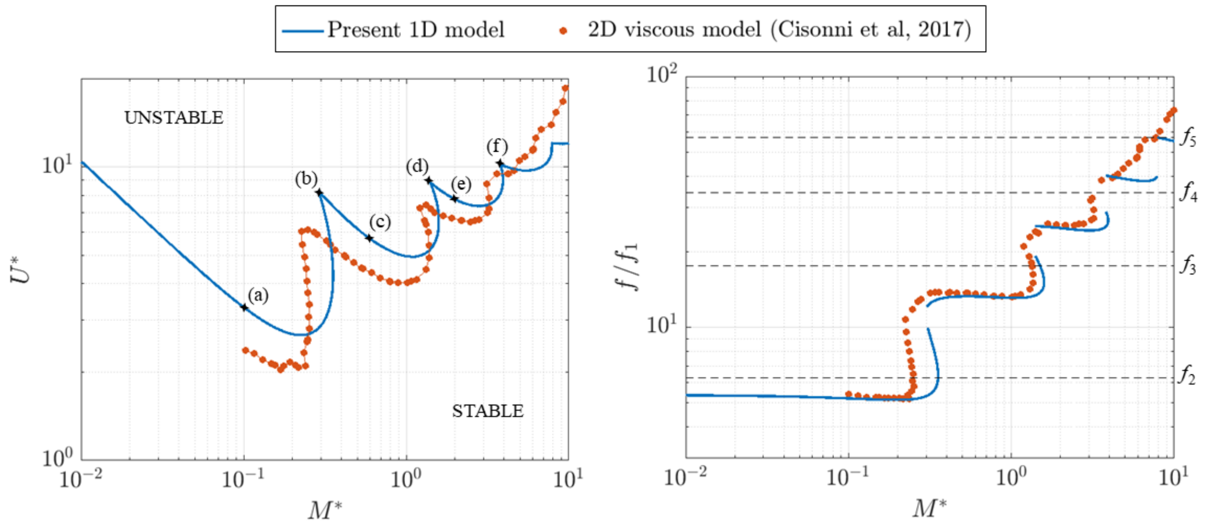

Figure 3.2 – Stability boundary in the $(U^*,\ M^*)$ plane (left) and the corresponding frequencies (right) for a system with confinement $H^* = 1/10$ and Reynolds number $\mathrm{Re} = 100$. The 2-D model results were retrieved from those presented in (Cisonni et al., 2017).

The cascading stability boundary shown in Figure 3.2 is a typical result of cantilevered structures subject to axial flow, reported in many previous studies, including models which assume inviscid flow (see review in (Shoele & Mittal, 2016)). We note that results from the present model agree qualitatively well with those from the 2D model. Despite some minor quantitative differences, the overall stability behavior of the system is well encapsulated. Namely, the sharp transitions in the stability curves, associated with the well-known mode-switching behavior as illustrated clearly by the abrupt changes in the instability frequency, are well represented. This behavior occurs at increasing mass-ratios, whereby the first unstable mode in the system transitions from lower to higher order, i.e. the main unstable (coupled) mode is dominated by *in-vacuo* beam modes of progressively higher order. To clarify, Figure 3.3 illustrates the complex mode shapes associated with the various points (a)-(f) indicated in Figure 3.2. The minor quantitative differences (slight vertical and horizontal shifts in the $M^* - U^*$ plane), are likely explained by the inherent differences in the 1D and 2D modelling approaches, namely, the explicit vs. implicit account of viscous effects or the parabolic vs. constant velocity profiles stemming from explicit/implicit account of boundary layer effects.

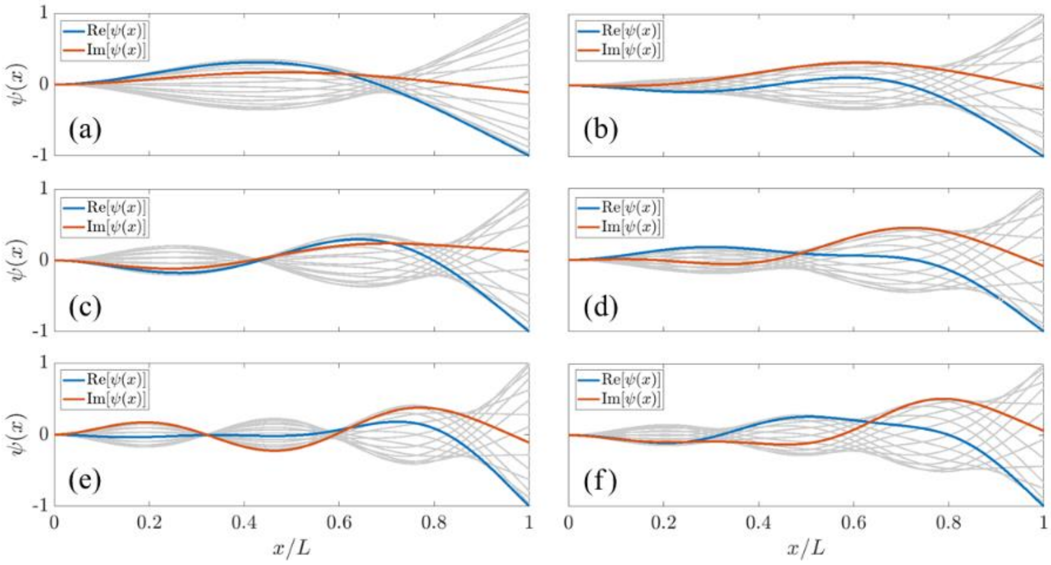

Figure 3.3 – Complex mode-shapes of the neutrally-stable modes associated with the boundary points (a)-(f) indicated in Figure 3.2. The real and imaginary parts of the mode shapes are indicated in blue and red, respectively. The grey lines illustrate the actual beam motion associated with the corresponding complex mode shapes.

3.3.3 The effect of confinement

Again, following the results from Cisonni et al, we investigate the effects of the confinement. In Figure 3.4 we show stability boundaries in the (U^*, M^*) plane for systems with different confinement ratios $H^* = [0.25,\ 0.125,\ 0.1]$. Results from our 1D model are shown on the left and results from the 2D viscous model of Cisonni et al. on the right.

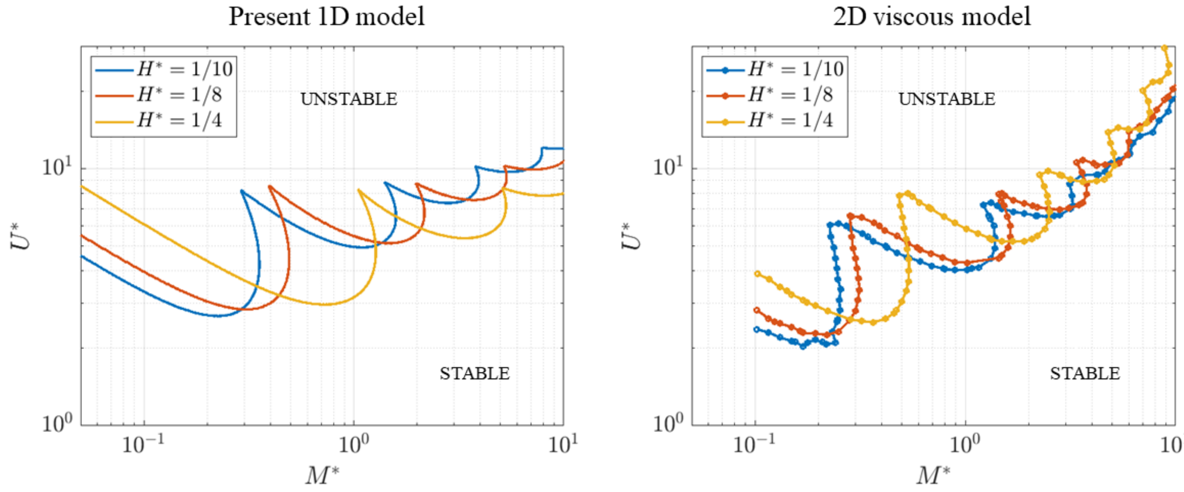

Figure 3.4 – Stability boundary in the (U^*, M^*) plane, for an undamped beam with different confinement ratios. The results from our model are shown on the left plot, while the results from

Cisonni et al. at the right. The Reynolds number was fixed at $\mathrm{Re} = 100$ (in the present model, this implies $f = 0.14$).

The two sets of stability boundaries shown in Figure 3.4 shows us that the 1D model is able to correctly predict the effects of the confinement, as the behavioral trends are well characterized, namely that larger confinements H^*: (1) tend to stabilize the system, particularly for light beams (small M^*); and (2) push the mode-switching behavior towards larger mass-ratios. The latter observation is a clear indication that the dominant feature of confinement is to provide an added-mass to the fluid. Effectively, decreasing H^* seems to have the same effect as increasing the fluid density ρ, and consequently the mass ratio M^*. However, we underline that, quantitatively, results start to deviate from those of the 2D model for larger confinement ratios. Notice that, at $H^* = 1/4$, the first modal-transition occurs at approximately $M^* = 0.5$ for the 2D model and at approximately $M^* = 1$ for the 1D model. These deviations are not unexpected since the 1-D bulk-flow equations are derived on the assumption that channel heights are small compared with the characteristic length of the system. Therefore, we expect deviations to increase for larger confinement ratios H^*. These deviations are likely explained by the fact that no explicit account of circulatory flow effects appears in the simplified 1-D bulk-flow formulation. While circulatory flow will likely have a minor influence on the flutter instability in narrower confinements, this will not be the case for wider confinements. In the limiting case of a beam in unbounded flow, the derived bulk-flow modelling approach is clearly not suitable. We also note that, on all three cases, the stability for heavier beams $\left(M^* > 5\right)$ is underestimated, with the 2D model predicting the first instabilities at larger velocities. Regarding lower confinement ratios, the lack of results from the 2D model for confinement ratios $H^* < 1/10$ prevents us from a concrete comparison. However, based on the trends of the results shown above, it is expected that the 1D model will provide accurate representations at smaller confinements.

3.4 Results: time-domain integrations and nonlinear dynamics

In this section we aim to explore the nature of the nonlinear regimes associated with a linearly unstable system through numerical time-domain integration. The set of nonlinear ODEs (3.7) was solved using MATLAB's solver `ode15i` (Matlab, 2021), an implicit scheme with variable time-stepping, which allowed fast computations by alternating between long and short time-steps (this is useful when impact dynamics are treated). This numerical scheme also prevented common numerical damping effects. Temporal integrations were started with the solutions of the steady configuration $\bar{q}_n$, $\bar{Q}_c$ as initial conditions, and a small perturbation force was applied to all beam modes to induce eventually unstable dynamics.

3.4.1 Stability and impact boundaries

As a first step to characterize the nonlinear behavior of the system, we examine the role of impacts and when they are more likely to occur. For this, a series of numerical time-domain integrations were performed in the non-dimensional parametric space (U^*, M^*). We considered a symmetric configuration with confinement ratio $H^* = 1/10$, and friction coefficient $f = 0.14$.

The simulations were run for several seconds until one of the following scenarios was encountered: (1) oscillations gradually decreased converging to the steady solution (linearly stable dynamics), (2) the oscillations grew until a stable limit cycle was reached, without the occurrence of impacts, or (3) oscillations grew until the beam eventually comes into contact with one of the walls, at which point the simulations were stopped. The difference between the latter two scenarios enabled us to estimate an "impact boundary", that is, a frontier in the (U^*, M^*) plane separating limit cycles with and without impacts. Because contact was not accounted in this first study, the beam was described by only $N = 10$ modes. All modal damping coefficients were set to $\zeta_n = 0.01$. The resulting map is shown in Figure 3.5.

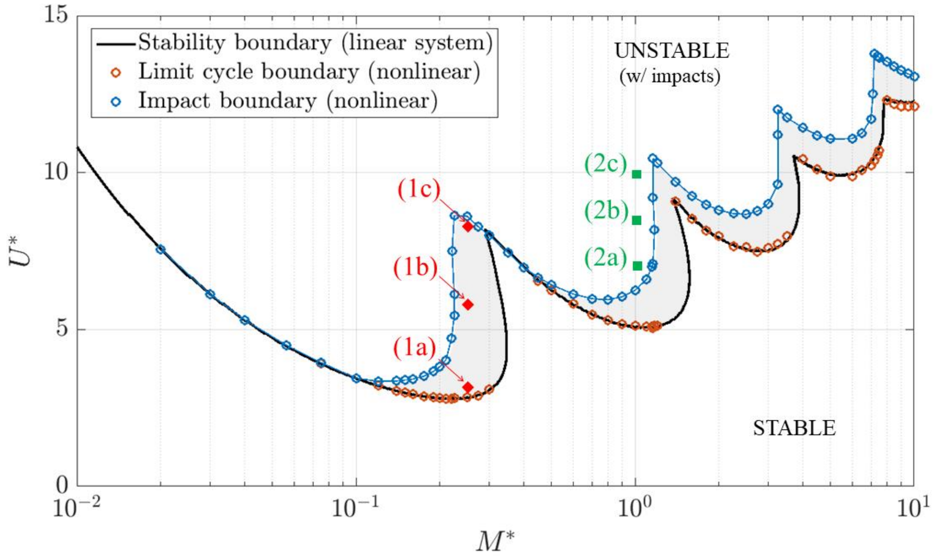

Figure 3.5 – Stability map of a system with confinement ratio $H^* = 0.1$ and friction coefficient $f = 0.14$, in the (U^*, M^*) plane. The linear stability boundary (black line) is compared to the limit cycle boundary found by the nonlinear simulations (orange dots). The impact boundary (blue line) illustrates the frontier in which linearly unstable dynamics lead to contact between the beam and the confinement walls. The nonlinear limit cycles associated with the points marked (1a-c) and (2a-c) will be shown in the following sections.

Firstly, we see that the stability boundary predicted by the linearized system is coherent with the linearly unstable dynamics observed in the nonlinear simulations. As for the impact boundary, we note that the regions in which limit cycles without impacts occur (grey area) are not extensive. Notably, we underline the fact that for small mass ratios (heavy beams or light fluids) these regions simply do not exist and the flutter instability, however weak, inevitably leads to large amplitude beam motions and eventual contact with the side walls. This seems physically plausible as the inertia of heavier beams will tend to outweigh the restoring forces from a light fluid.

At this point is it important to mention that experimental studies on similar systems (with bounded or unbounded flow) often report hysteretic behavior, suggesting the existence of a subcritical bifurcation (Aurégan & Depollier, 1995) (Eloy et al., 2008) (Tang & Paidoussis, 2007). That is: (1) when the mean flow velocity is gradually increased, an initially static beam will start fluttering at a specific critical velocity U_c, and on the other hand, (2) when the mean flow velocity is gradually decreased, an initially unstable (fluttering) beam will stabilize at a different critical velocity U_d. This phenomenon remains to this day an open question and modelling efforts generally fail to reproduce this behavior. Some authors (Eloy et al., 2008) (Tang & Païdoussis, 2007) have suggested that the fluttering instability of cantilever plates/beams could actually be supercritical (no hysteresis) and that the hysteresis found in experiments could be a product of unaccounted three-dimensional effects, i.e. edge-vortices, torsional motion of the plate, etc. As will be seen in a later chapter, these results are in fact the product of sub-critical bifurcations predicted by the model.

3.4.2 An elastic impact model

The few researchers who explored nonlinear simulations of cantilevered beams in confined axial flow, eventually encounter limitations in their solutions, at regimes where the motion of the plate is large enough that collisions with the walls become inevitable. Nevertheless, numerous experimental observations (Huang, 1995) (Aurégan & Depollier, 1995) (Fujita et al., 2007) (Alben, 2015) (Wu & Kaneko, 2005) demonstrate that nonlinear motions regularly present intermittent impacts, particularly for cases where the confinement and/or the mass ratio are low.

At this point it is worth discussing the nonlinear behavior of the flow in the eminence of a channel constriction. Firstly, it must be said that, for systems composed of fluttering cantilever beams, channel constriction (or collapse) will generally occur firstly at the beam tip. As one might expect, a local constriction of the channel initially leads to an increase of the local velocity and a decrease in local pressure, further pushing the beam towards the wall. However, this behavior is eventually limited by the effect of the nonlinear flow dissipation terms (frictional effects as well as head-losses at the trailing edge). Moreover, as the beam motion becomes very large, its inertia in the direction of a channel wall will cause a “squeeze” like effect on the fluid. In the eminence of contact, because the fluid is assumed incompressible, this “squeezing” effect will lead to an abrupt, but continuous, decrease in local velocity (and even locally reverse flow), at which point, if fluid forces are not strong enough to oppose the beam inertia, contact becomes inevitable. Naturally, this phenomenon will be more pronounced in configurations with low mass ratios (heavy beams/light fluid). Additionally, we note that compressibility effects such as propagating pressure waves, are not accounted in our model, and we do not discard the possibility that, in particular scenarios, such effects could have a meaningful impact on the dynamics of a real physical system.

As mentioned in the introduction, the addition of dynamic impacts to the fluid-structure model is a non-trivial task. Not only do we need to formulate the contact conditions between the beam and the side walls, which often implies dynamic constraints (at the displacement, velocity and acceleration levels), but also the associated contact conditions for the flow. The latter difficulty relates to the fact that the solutions for flow velocity and pressure fields present singularities at the moment of contact, i.e. when the channel height $h_c = 0$. Moreover, classical penalty methods, reliant on contact interpenetration, are naturally incompatible with the flow model used here.

In this work, we do not aim to find solutions to these delicate issues. However, we present a pragmatic approach based on a regularized impact formulation, in the spirit of classical penalty methods, that allows us to include impacts in a simple manner that is compatible with the flow formulation.

Since the fluid equations do not allow for beam penetration on the wall, the impact force is applied on the beam just before contact. That is, an impact force $F_i(x,t)$ is applied in regions of the beam which have trespassed a small regularization parameter ε, as illustrated in Figure 3.6. In essence, we allow some flow leakage at the moments of "contact", such that an impact force can applied to the beam without fully restricting the flow dynamics.

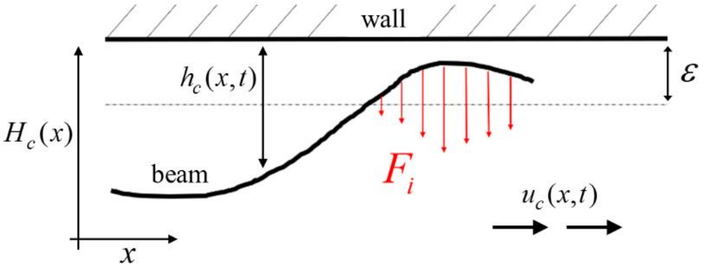

Figure 3.6 – Illustration of the beam violation right before contact and corresponding impact force.

The simplest and most commonly used approaches to describe dynamic impacts between two solids are based on the Hertz model, a purely elastic contact model (without dissipation), typically in the form

$$F_i(x,t) = \begin{cases} k_i\, v^p(x,t) & \text{if} \quad v(x,t) > 0 \\ 0 & \text{otherwise} \end{cases} \tag{3.26}$$

where k_i is an impact stiffness, $p > 1$, and the violation amplitude is given, in our case, by $v(x,t) = \varepsilon - h_c(x,t)$. The sign of $F_i(x,t)$ is defined for each channel: $F_i > 0$ for $c = 2$; $F_i < 0$ for $c = 1$. These models describe a nonlinear stiffening force proportional to a power p of the violation amplitude. For purely mechanical problems, these types of models are well behaved. However, in our problem, the inertial forces of the beam and the fluid forces might, in some cases, dominate over the contrary impact force, and penetration occurs nonetheless, i.e. $h(x,t) < 0$. For this reason, here we have pragmatically used an infinitely stiffening impact force in the form

$$F_i(x,t) = \begin{cases} k_i \tan\left[\dfrac{v(x,t)}{\varepsilon}\left(\dfrac{\pi}{2}\right)\right] & \text{if} \quad h_c(x,t) < \varepsilon \\ 0 & \text{otherwise} \end{cases} \tag{3.27}$$

where, in this case, penetration is avoided completely as the impact force tends to infinity when $h_c(x,t) \to 0$. Figure 3.7 compares the amplitude of the impact force for various values of impact stiffness k_i with the linear case (Eq. (3.26) with $p = 1$), as a function of the normalized amplitude of violation ν / ε.

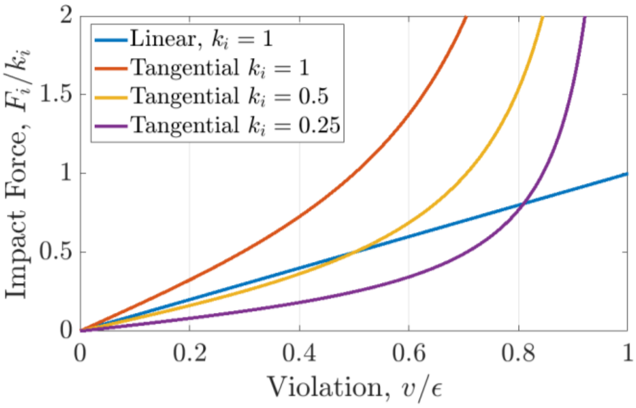

Figure 3.7 – Impact force as a function of the amplitude of violation (when $h < \varepsilon$). A linear stiffness impact model is compared to the tangential impact model for various values of stiffness k_i.

Depending on the particular physical problem to be addressed, this modelling approach can surely be refined by including dissipative terms or the flow conditions at the moments of contact. However, this simple pragmatic model is effective enough for the purposes of the current work.

3.4.3 Limit cycles without impacts

To illustrate the character of the limit cycles we start by showing the solutions to a set of configurations that lead to stable limit cycles without impacts. The configurations (1a), (1b) and (1c) - red points in Figure 3.5 – have a constant mass ratio $M^* = 0.25$ and various reduced velocities $U^* = [3.5,\ \ 6,\ \ 8]$, respectively. For each configuration (1a), (1b) and (1c), Figure 3.8 shows snapshots of the beam motion and Figure 3.9 shows the temporal evolution of the modal velocities $r_n(t)$ and the unsteady flow rates $Q_c(t)$. Additionally, in Figure 3.10 we show the phase-portrait of the beam tip, the evolution of the tip displacement $y(L,t)$, the spectra of the tip velocity and the average contribution of each *in-vacuo* beam mode to the nonlinear oscillations, expressed by the root-mean-square (RMS) value of modal displacements $q_n(t)$.

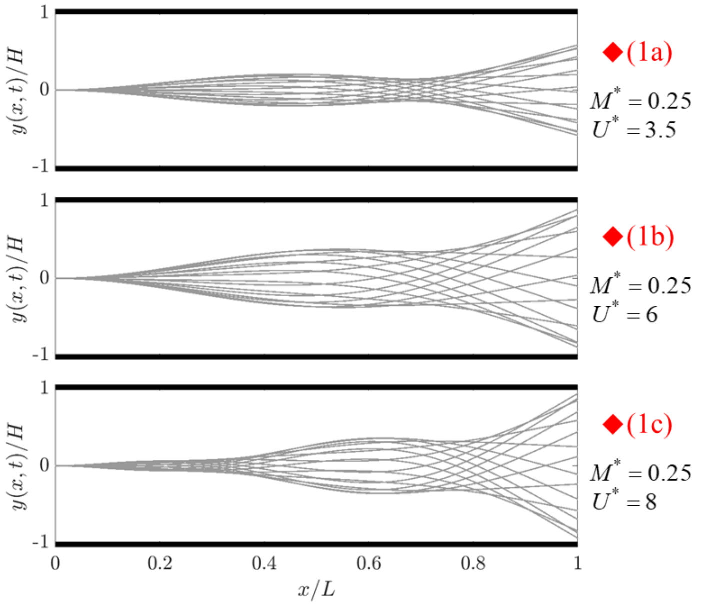

Figure 3.8 – Snapshots of the beam motion during one cycle for configurations (1a), (1b) and (1c).

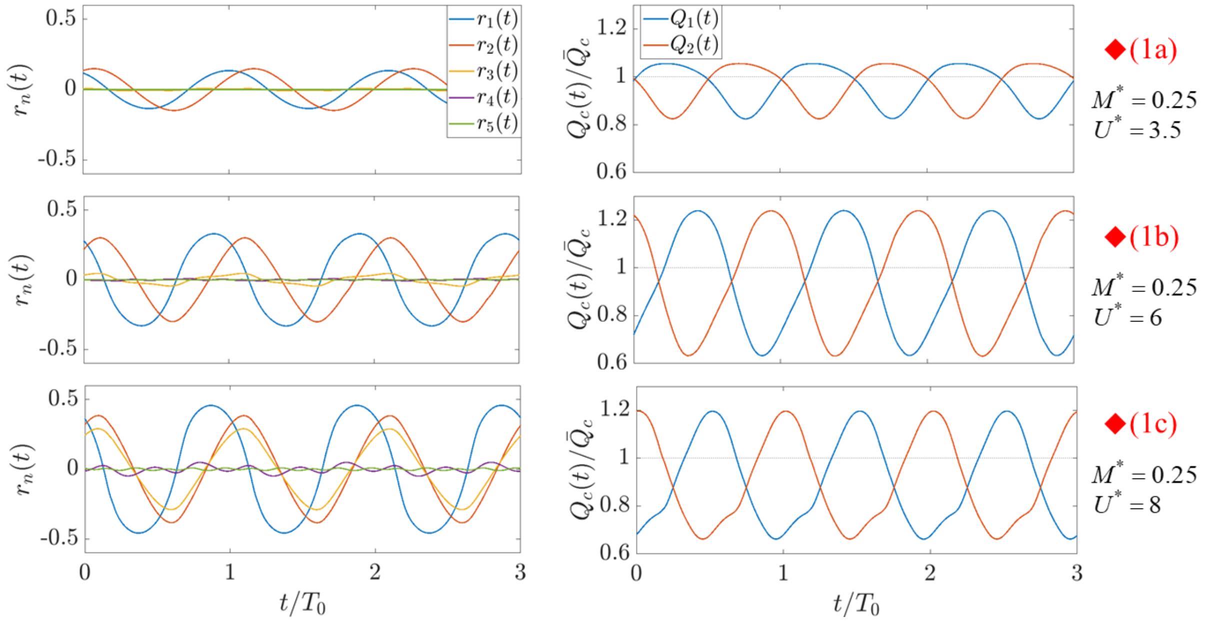

Figure 3.9 – Temporal evolution of the modal velocities $r_n(t)$ (left) and unsteady flow rates $Q_c(t)$ (right) in the limit cycles associated with configurations (1a), (1b) and (1c). For clarity, time scales are normalized by the fundamental period of the corresponding limit-cycle T_0.

Figure 3.8 shows that the amplitude of the beam motion tends to increase with increasing velocity U^*, as expected. Moreover, we notice that the beam motion also changes qualitatively. At lower velocities (1a) the motion is dominated by the first two *in-vacuo* beam modes, while at larger velocities (1b-c) the contribution of the third beam mode becomes increasingly significant, illustrating a "mode-transition", similar to what was observed in the linear stability results. Moreover, the beam motions in the various limit cycles are remarkably similar to the complex mode shapes presented in Figure 3.3, suggesting that, in these cases, the overall motion of the fluttering beam is not altered significantly by the nonlinear fluid forces.

In Figure 3.9, the modal velocities again show the appearance of the third beam mode at larger velocities (1c). We also note a growing nonlinearity with increasing velocities U^* (1b-c), as the oscillations of the modal components start to drift from the nearly sinusoidal motions seen in (1a). As expected from a symmetric system, the flow rates $Q_c(t)$ oscillate in phase opposition. Moreover, they oscillate around a value slightly lower than their steady component $\bar{Q}_c$. This means that the overall mass transport is reduced by the fluttering beam, compared to a static scenario. This seems physically plausible as, during flutter, some of the energy carried by the flow is transferred to the beam and lost through either structural dissipation or increased flow-dissipation effects (either friction along the domain or turbulent effects in the trailing edge, modelled by the distributed and localized head-loss terms, respectively).

The plots in Figure 3.10 suggest that, without intermittent impacts, the nonlinearity in the system motion is relatively weak. Naturally, the shown spectra contain only odd harmonics, as would be expected from a symmetric system. At lower velocities (1a), the motion is nearly sinusoidal, with negligible contributions from higher harmonic components while at larger velocities U^*, higher-order harmonic components become more significant, however, still relatively weak compared to the fundamental frequency (amplitudes of higher harmonics are typically 20/30 dB below the fundamental).

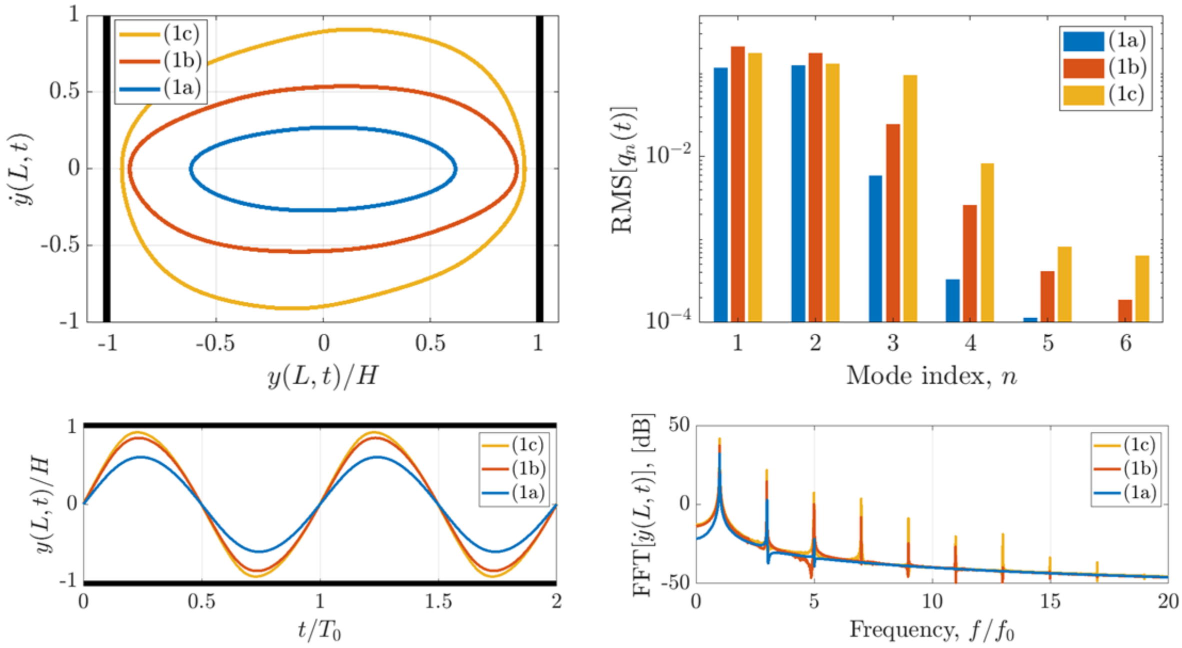

Figure 3.10 – Phase-portrait of beam tip (top-left); Root-mean-square (RMS) value of the modal displacements (top-right); beam tip displacement (bottom-left) and spectra of the tip velocity (bottom-right), for the three configurations (1a), (1b) and (1c). For clarity, time/frequency scales are normalized by the fundamental period/frequency of the corresponding limit cycle T_0 and f_0.

3.4.4 Limit cycles with impacts

Here we illustrate a few limit cycles that include intermittent impacts, namely, the solutions for the configurations indicated in Figure 3.5 by points (2a), (2b) and (2c). These configurations have a constant mass ratio of $M^* = 1$ and various reduced velocities $U^* =$ [7, 8.5, 10], respectively. For these simulations, a large number of beam modes was considered, $N = 40$, to ensure the impact dynamics are well represented. In general, the number of considered modes N should be such that the modal stiffness of the highest considered mode is somewhat larger than the impact stiffness at the point of contact x_i, that is $k_i < m_N \omega_N^2$. The effect of the impact stiffness, k_i, deserves a meaningful discussion, as it might affect the resulting limit cycles. However, we will firstly show some illustrative results and, in a following section, we will discuss the role of the impact stiffness and how it affects the resulting nonlinear behavior. In the following simulations, the non-dimensional impact stiffness was taken as $k_i^* = k_i / m_1 \omega_1^2 = 10^7$ (normalized by the stiffness of the first beam mode) and the non-dimensional regularization parameter $\varepsilon / H = 10^{-3}$.

Figure 3.11 shows snapshots of the beam motion and Figure 3.12 the evolution of the modal velocities $r_n(t)$ and the unsteady flow rates $Q_c(t)$, for the three configurations (2a), (2b) and (2c). In Figure 3.13 we show the phase-portrait of the beam tip, the evolution of the tip displacement $y(L,t)$, the spectra of the tip velocity and RMS-value of the modal displacements $q_n(t)$, for all three configurations. Moreover, we show in Figure 3.**14** the impact force applied on the beam throughout the limit cycles. The impact force is expressed as the spatial integral of $F_i(x,t)$, normalized by a reference force $F_0 = m f_1^2 H$, where m is the total mass of the beam and f_1 is the frequency of the first in-vacuo beam mode.

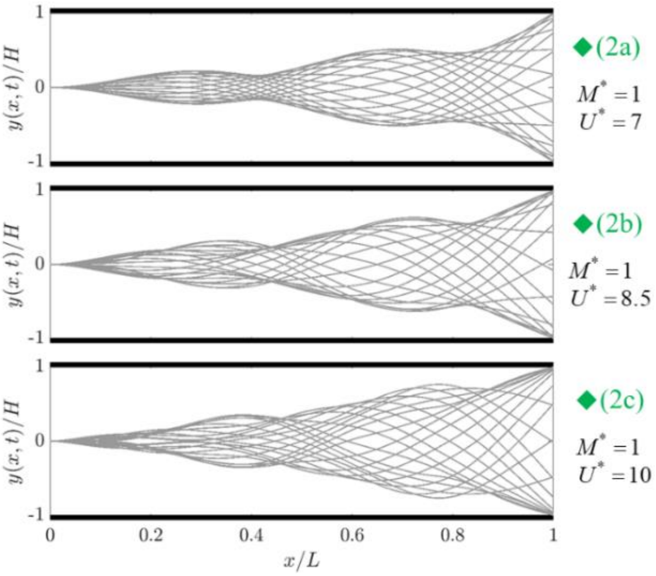

Figure 3.11 - Snapshots of the beam motion during one cycle for configurations (2a), (2b) and (2c).

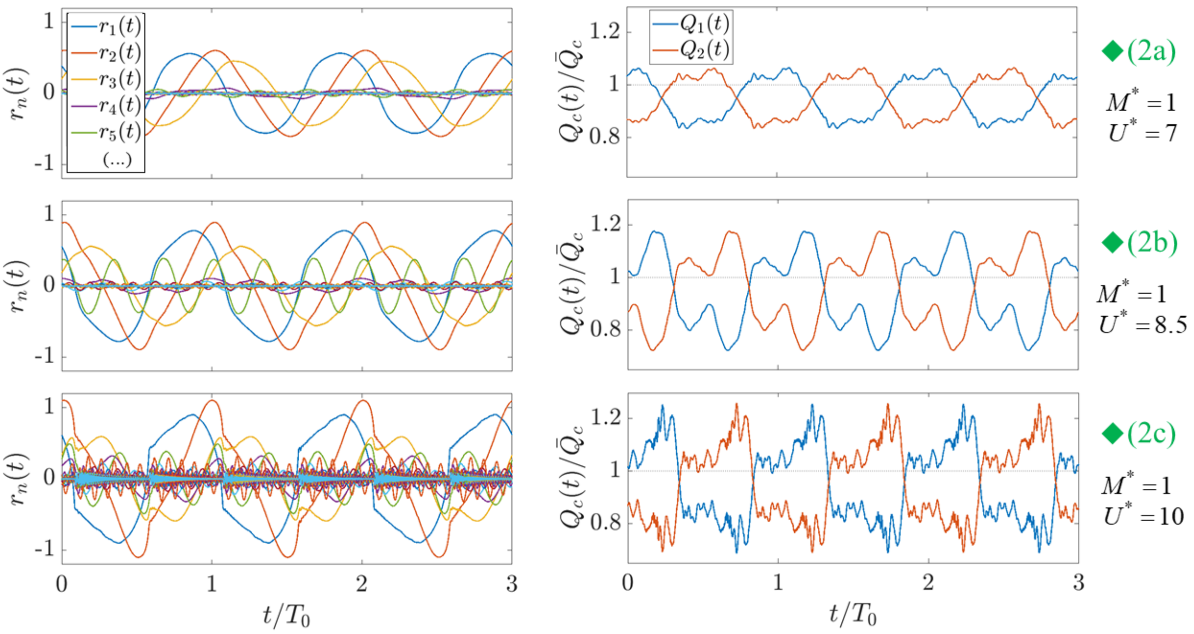

Figure 3.12 - Temporal evolution of the modal velocities $r_n(t)$ (left) and unsteady flow rates $Q_c(t)$ (right) in the limit cycles associated with configurations (2a), (2b) and (2c). For clarity, time scales are normalized by the fundamental period of the corresponding limit-cycle T_0.

In Figure 3.11 we notice that, in all cases, intermittent contact occurs solely at the tip of the beam. As the velocity U^* increases (2b-c), impacts become more violent and the beam motion becomes increasingly perturbed, as higher order beam modes are intermittently excited and start playing a more prominent role in the overall beam motion. These effects are also seen by the evolution of the modal velocities shown in Figure 3.12 and the RMS-values in Figure 3.13 . When impacts are relatively weak (2a), the tip simply "grazes" the wall and the overall beam motion is not significantly altered compared to the mode shapes estimated by the linear stability analysis.

Similarly, the oscillations of the flow rates become increasingly abrupt in the presence of violent impacts. However, it is interesting to note that sharp changes in the unsteady flow-rate (e.g. bottom-right plot in Figure 3.12) do not occur at the moments of contact but rather at the moments when the beam motion rapidly shifts from one side of the channel to the other. This effect can be illustrated, for example, by the beam-tip motion shown in Figure 3.13. Here we notice that as impacts become stronger, the overall contact time also becomes larger, meaning as well that the beam-tip will shift sides more abruptly, hence generating sharp fluctuations in the flow-rates.

In Figure 3.13 we note that the motions become increasingly nonlinear in the presence of stronger impacts. The phase-portrait shows more perturbed motions with larger gradients. Naturally, the spectra of the beam tip show a large number of high order harmonic components, increasing in amplitude as impacts become more violent. It is worth noting that, in the nonlinear regimes with stronger impacts (2c), the oscillations are not strictly periodic. Although the low frequency motions are stable, we notice small high frequency perturbations, related to the unsynchronized motion of the intermittently excited higher order beam modes. This behavior is clearly illustrated by the spectra of (2c), where we notice not only an increase in the amplitude of the harmonics, but also a visible presence of noise-like spectral behavior. Nevertheless, these motions might be tentatively classified as perturbed periodic oscillations, rather than aperiodic dynamics.

For illustrative purposes, the time and frequency scales were normalized by the fundamental period/frequency of each limit cycle. However, it is worth noting that larger reduced velocities U^* led to limit cycles with higher fundamental frequency f_0. For reference, the fundamental frequencies f_0 of the limit cycles (2b) and (2c) were 11% and 23% larger than the fundamental frequency of the (2a) limit cycle, respectively. This is not unexpected since larger velocities U^*, as well as impacts, will provide additional stiffness to the unstable FSI mode.

The impact forces represented in Figure **3.14** illustrate the fact that, during each beam-wall interaction, the beam tip impacts the wall multiple times. This chattering effect is a typical behavior of systems with impacts in multi-modal structures. In weaker impacts (2a) we notice only a few impacts of decreasing strength while in more violent regimes (2b-c) contact is composed of multiple impacts with stronger associated forces and an overall longer chattering time.

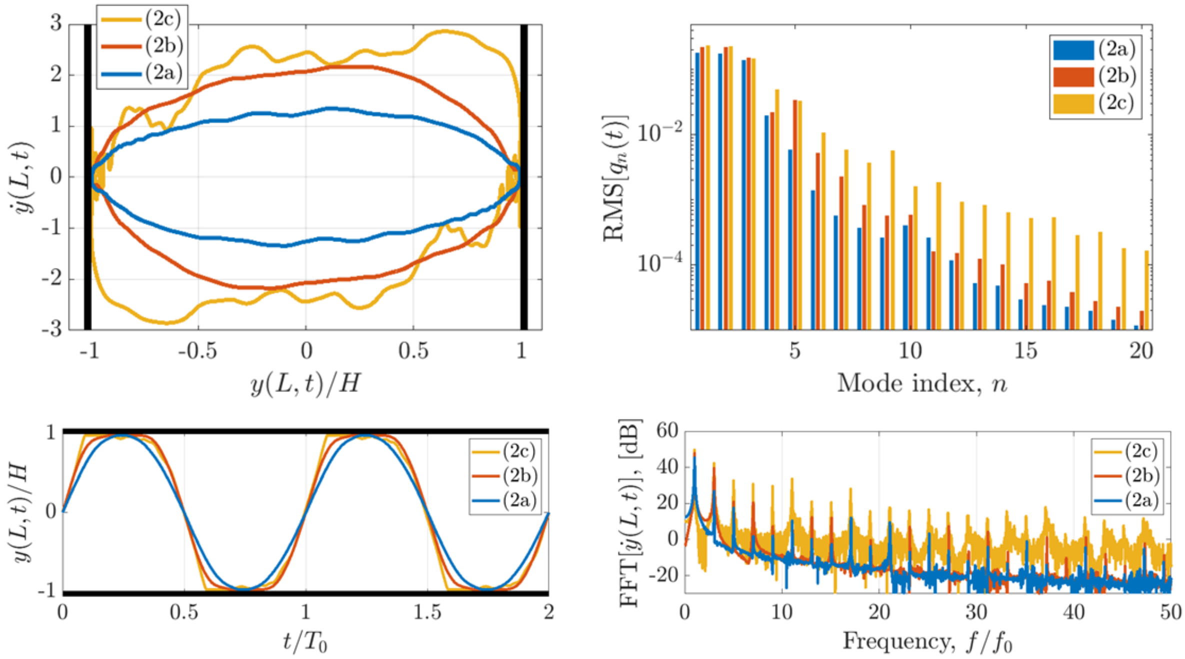

Figure 3.13 - Phase-portrait of beam tip (top-left); root-mean-square (RMS) value of the modal displacements (top-right); beam tip displacement (bottom-left) and spectra of the tip velocity (bottom-right, for the three configurations (2a), (2b) and (2c). For clarity, time/frequency scales are normalized by the fundamental period/frequency of the corresponding limit-cycle T_0 and f_0.

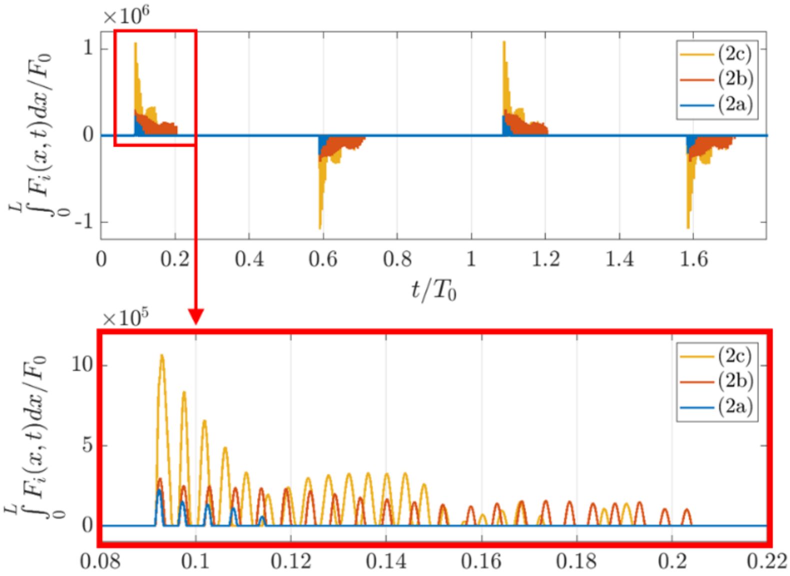

Figure 3.14 – The evolution of the non-dimensional impact force through the limit-cycles associated with configurations (2a), (2b) and (2c). For clarity, time scales are normalized by the fundamental period of the corresponding limit cycle T_0.

3.4.5 Limit cycles in asymmetric configurations

To contrast with the symmetric limit cycles shown above, we now considered a similar system where the lower channel height is taken as $H_2 = 2H_1$. The mass ratio is fixed at $M^* = 1$, as in (2a-c), and two reduced velocities are considered $U^* = \left[7, \quad 9\right]$. The following examples illustrate the typical behaviour found in asymmetric systems, leading to limit cycles with either one and two impacts per cycle. Figure 3.15 shows snapshot of the beam motion during the two asymmetric limit cycles. In Figure 3.16, we see the temporal evolution of modal velocities and flow rates. Figure 3.17 shows the phase portrait of the beam tip, the evolution of the tip displacement and the spectra of the tip velocity in the two asymmetric configurations.

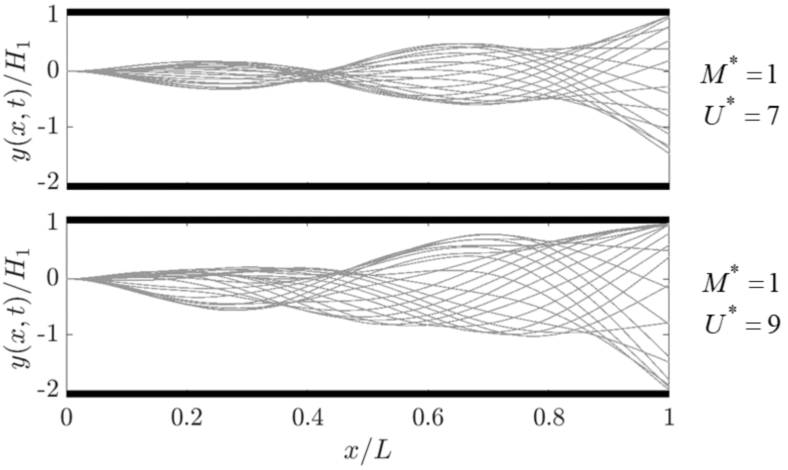

Figure 3.15 – Snapshot of the beam motion in limit cycles with impacts in asymmetric configurations.

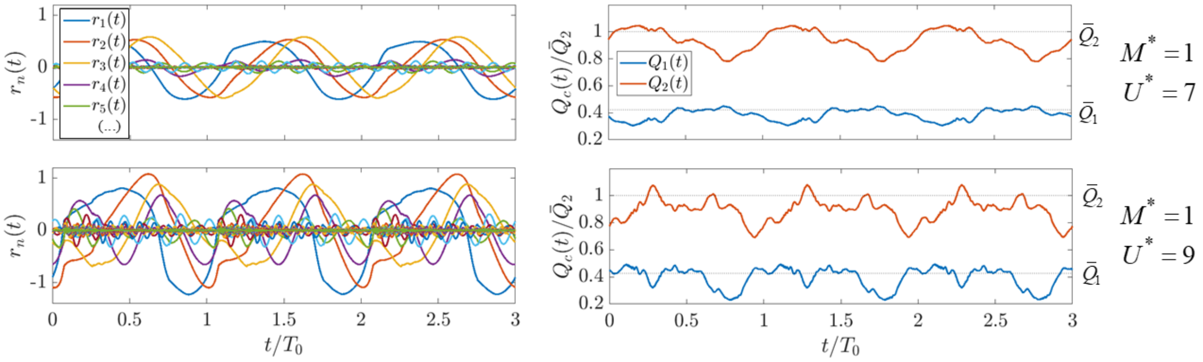

Figure 3.16 – Temporal evolution of the modal velocities (left) and unsteady flow rates (right) in the two asymmetric configurations. For clarity, time scales are normalized by the fundamental period of the corresponding limit-cycle T_0.

Once again, in the examples shown in Figure 3.15-Figure 3.17, impacts occur solely at the tip of the beam. In the $(M^* = 1 \;;\; U^* = 7)$ configuration, impacts occur only at the upper wall (one per cycle) while in the $(M^* = 1 \;;\; U^* = 9)$ configuration there are two impacts per cycle, on both the upper and lower walls. The latter case presents more violent impacts and a more distorted beam motion, which includes significant contributions from higher order beam modes. The spectra in Figure 3.**17** now shows both even and odd harmonic, as expected from an asymmetric system.

As expected in asymmetric cases, the overall flow rates are larger in the wider channel, as fluid velocities tend to equalize under the same driving pressures. Nonetheless, static flow velocities on the narrower channel $\bar{u}_1$ will actually be lower than in the wider channel $\bar{u}_2$ due to increased flow-dissipation. Consequently, the beam will feel larger perturbation pressures from the upper channel, which will push the overall beam motion towards the lower channel, as seen clearly in Figure 3.**15**.

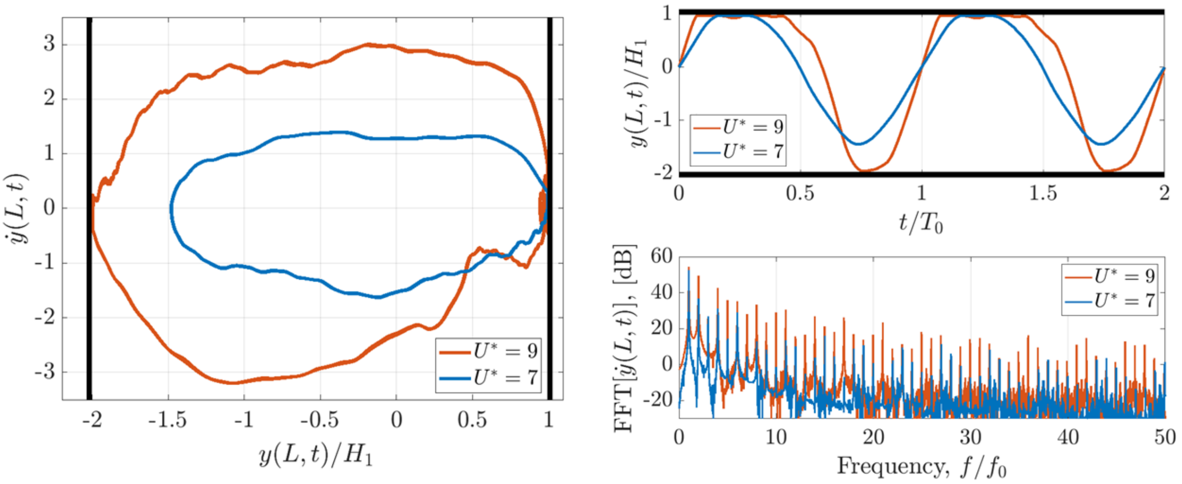

Figure 3.17 – Phase-portrait of the beam tip (left); beam tip displacement (top-right) and spectra of the beam tip velocity (bottom-right) for the two asymmetric configurations. For clarity, time/frequency scales are normalized by the fundamental period/frequency of the corresponding limit-cycle T_0 and f_0.

3.4.6 Limit cycles with impacts at multiple locations

Now we illustrate a limit cycle where, contrary to the previous, impacts occur not only at the tip of the beam. We consider an asymmetric configuration with $H_2 = 4H_1$, $M^* = 1$ and $U^* = 12$, with all other parameters as before. Figure 3.18 illustrates the character of the resulting limit cycle.

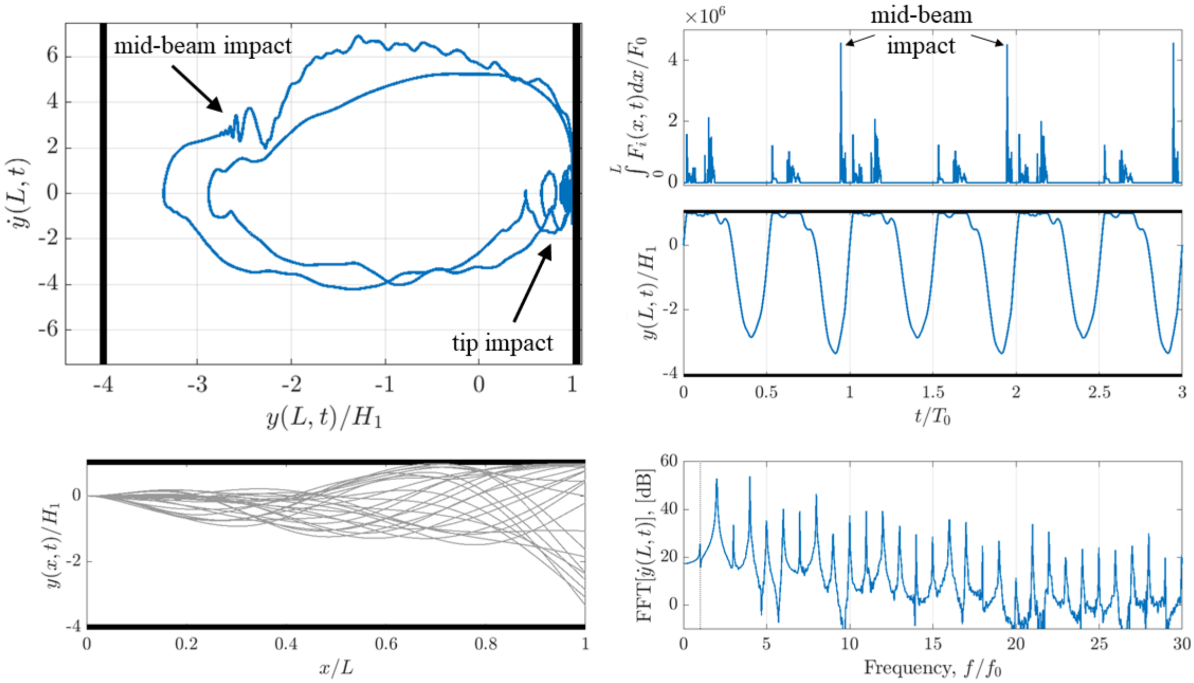

Figure 3.18 – Illustration of a limit cycle with impacts both at the tip and along the beam. Phase-portrait of the beam tip (top-left); temporal evolution of the impact force (top-right) and the tip displacement (centre-right); snapshots of the beam motion (bottom-left) and the spectra of the beam tip velocity (bottom-right). For clarity, time/frequency scales are normalized by the fundamental period/frequency of the limit cycle T_0 and f_0.

The results in Figure 3.18 are qualitatively different from those previously presented. The snapshots of the beam motion illustrate how the beam impacts the walls both at the tip and along the beam $(x / L \approx 0.7)$. In the phase-portrait of the tip motion, we notice that, throughout one cycle, the beam impacts the upper wall three times, once in a mid-beam location and twice at the beam tip.

Curiously, the spectra shows that the first harmonic component is much weaker than the second one. Furthermore, the oscillations of the tip displacement and the phase-portrait show the same effect in the temporal domain, as the “principal” motion nearly repeats itself within one cycle. These results suggest that, in this case, the mid-beam impact might induce some form of period-doubling bifurcation.

3.4.7 Aperiodic dynamics

So far, we have only examined periodic limit cycles at relatively low/moderate reduced velocities U^*. However, at larger reduced velocities, strong fluid forces and violent impacts may lead to aperiodic/chaotic dynamics. To illustrate, we now consider a symmetric system, similar to those described in previous sections, with a mass ratio $M^* = 0.05$ and reduced velocity $U^* = 25$. Figure 3.19 illustrates the irregular nature of the fluid-structure dynamics.

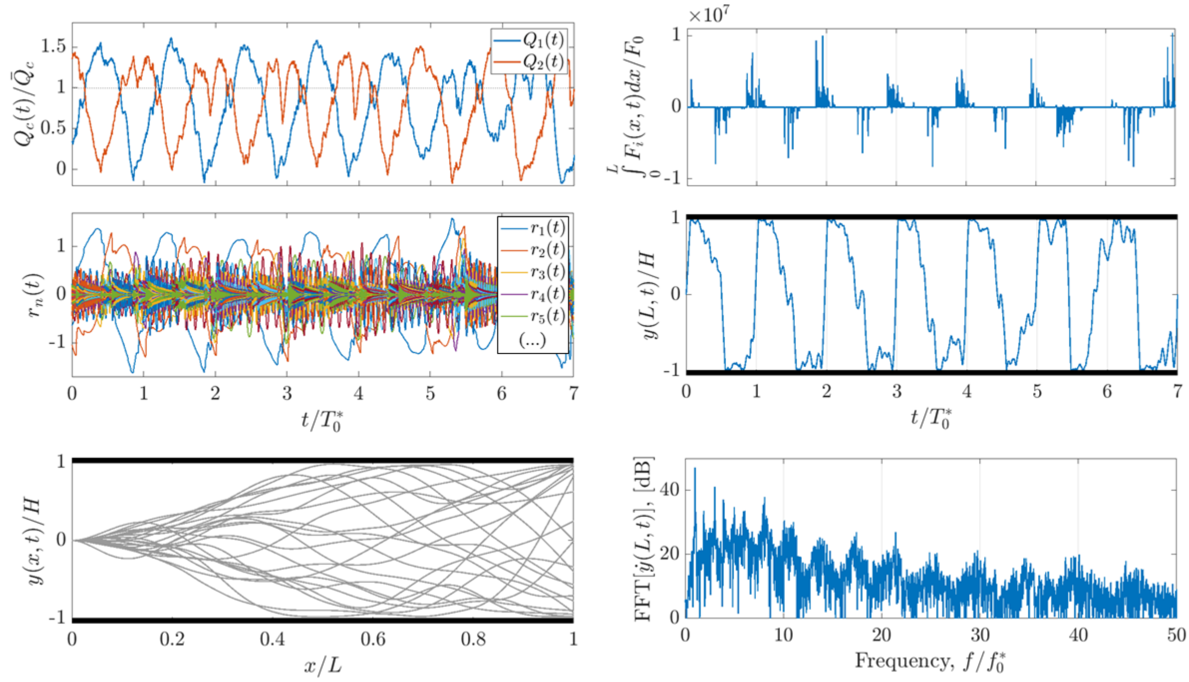

Figure 3.19 - Illustration of aperiodic dynamics in a symmetric system with $M^* = 0.05$ and $U^* = 25$. Temporal evolution of the flow rates (top-left), the nondimensional impact forces (top-right), the modal velocities (centre-left) and the tip displacement (centre-right); snapshots of the beam motion (bottom-left) and the spectra of the beam tip velocity (bottom-right). Time and frequency scales are normalized by a pseudo-fundamental period/frequency, T_0^* and f_0^*.

Notice that, despite the clear aperiodicity of the motion, there is some form of regularity in the low frequency behavior (see prominence of a low frequency component in the spectra shown in Figure 3.19). For this reason, time and frequency scales are normalized by a pseudo-fundamental period/frequency, T_0^* and f_0^*, given by the low frequency component with largest magnitude.

Contrary to the previously shown periodic behavior, here impacts occur in diverse locations along the beam, in the region $0.3 < x / L < 1$. The violent impacts at different locations strongly excite higher order beam modes, in an irregular manner. Despite this, the oscillations of the first two beam mode contributions seem have some form of regularity (see evolution of modal velocities). This relatively stable motion is more clearly illustrated by the spectra of the tip velocity, which, despite its wide-band nature, also shows the prominence of some frequencies in the low frequency range. In the previous shown example (2c), we discussed the presence of small (high frequency) perturbations to the limit cycles. The present dynamics might be seen from the perspective that these perturbations cease to have a negligible effect, and now, clearly break periodicity.

3.4.8 The effect of impact stiffness

Finally, to assess the role of the impact stiffness on the resulting nonlinear behavior, we now take one example configuration and show the resulting limit cycles calculated with different impact stiffnesses k_i. The configuration was symmetric, as above, with $H^* = 1/10$, $M^* = 0.1$ and $U^* = 8$. A total of 40 beam modes were considered, with uniform modal damping $\zeta_n = 0.01$. The impact regularization parameter was fixed at $\varepsilon / H = 10^{-3}$, and the non-dimensional impact stiffness $k_i^* = k_i / m_1\omega_1^2$, was varied from 10^5 to 10^8. Figure 3.20 shows the phase-portrait of the beam tip, the tip displacement and the spectra of the tip velocity for the limit cycles with various values of impact stiffness k_i. Additionally, Figure 3.**21** shows the impact forces applied on the beam (integrated in space) for the various limit cycles.

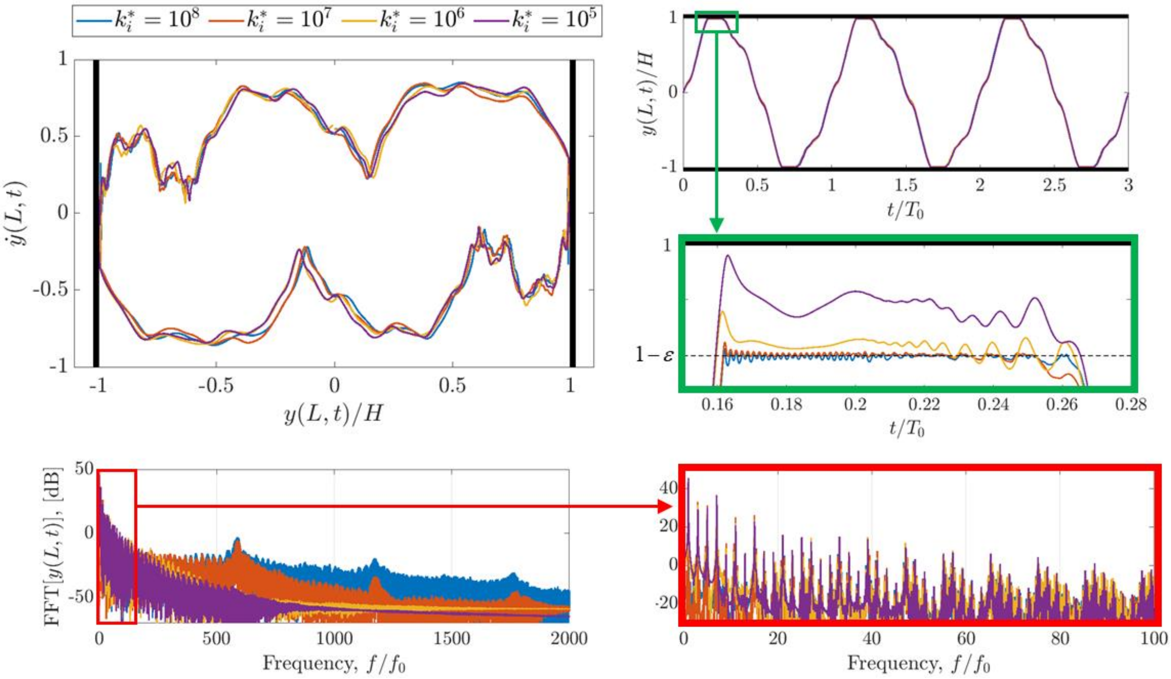

Figure 3.20 – Comparison of limit cycles with intermittent impacts, calculated with various impact stiffnesses. The phase-portrait of the beam tip (top-left); the beam tip displacement (top-right); and the spectra of the beam tip velocity (bottom). For clarity, time/frequency scales are normalized by the fundamental period/frequency of the corresponding limit-cycle T_0 and f_0.

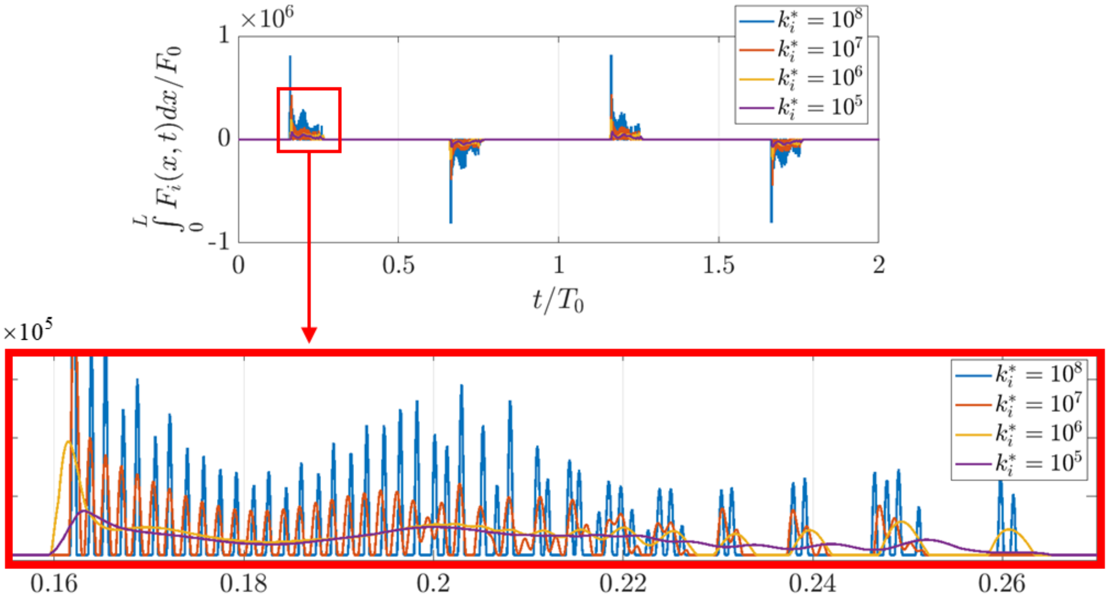

Figure 3.21 – The evolution of the non-dimensional impact force (integrated in space) through the limit-cycles for using various values of impact stiffness. For clarity, time scales are normalized by the fundamental period of the corresponding limit-cycle T_0.

The results above show us that the impact stiffness does not seem to affect the overall motion of the limit cycle. The phase-portrait of the beam tip shows only minor quantitative differences. From the evolution of the beam tip displacement during the impact, we notice that a larger impact stiffness results in very small "penetration" and a chattering of higher frequency. As the impact stiffness if softened, penetration becomes more pronounced and the chattering effects are smoothened. Despite this, the overall contact time remains fairly regular in all 4 cases. These effects are clearly illustrated by the frequency content of the tip motion. We notice that low frequency components remain nearly unchanged and noticeable differences are seen only at the high-frequencies. This example suggests that, using the current impact model, the choice of impact stiffness brings only minor quantitative changes but does not alter the overall dynamics of the system, at least in the tested range of impact stiffnesses. Many other configurations were tested (not shown here), leading to similar conclusions. However, the possibility of qualitative changes due to varying impact stiffness is not discarded and further studies are necessary.

3.5 Summary

The contents in this chapter are summarized in the following points:

→ Using formal solutions for the flow velocity and pressure fields, an analytical formulation for the flow is reached, which does not rely on any spatial discretization. Effectively, the continuous beam-flow coupled system is transformed into a set of $2M+2$ nonlinear first-order ordinary differential equations. The resulting spatial operators are time dependent but the system can nevertheless be solved numerically, through time-domain integrations or others methods, at very modest computational times.

→ The linearized version of the proposed formulation leads to a compact system of equations that can be solved numerically to obtain linear stability boundaries in terms of various dimensionless parameters of the system.

→ Results from the linear stability analysis of the proposed 1-D model were compared to reference results using more realistic 2D CFD models. Overall, results were positively validated over a wide range of mass ratios and reduced velocities, at least for relatively narrow passages. At larger confinement ratios $H^{*} > 0.2$, we notice larger errors, as flow circulatory effects become more prominent. This is expected from the simplifying assumptions made in the bulk-flow equations.

→ The common occurrence of beam-wall contact in systems with fluttering beams in confined passages has been a limiting factor in previous studies. Here, the inclusion of a regularized impact model, allows for the computation of the fully nonlinear problem, including the calculation of limit cycles with intermittent impacts. To the author's knowledge, the inclusion of impacts in this type of systems is presented here for the first time.

→ Several illustrative simulations are shown including limit cycles (1) with and without intermittent impacts, (2) in symmetric and asymmetric configurations, and (3) with impacts at the beam tip or along its length. Additionally, we illustrate that large flow velocities can lead to aperiodic/chaotic dynamics. The lack of experimental data on the ensuing nonlinear dynamics prevents us from a meaningful validation of our results, nevertheless, they seem physically plausible and consistent with reported experimental observations, at least qualitatively.

Chapter 4

A Galerkin approach

In this chapter we propose a Galerkin formulation for a one-dimensional model describing the nonlinear flow-structure interaction of a flexible beam in confined axial flow. In broad terms, the system of PDEs is converted into a set of time-dependent equations (ODEs and algebraic) by developing all variables in terms of series of space-dependent orthogonal functions. The beam motion is developed in terms of its mode shapes while the flow pressure and velocity fields in each channel are developed in terms of Chebyshev polynomials. Additionally, a tau-variant of the Galerkin approach enables the enforcement of the nonlinear time-dependent boundary conditions in a well-posed manner. Ultimately, the resulting system is a set of nonlinear differential-algebraic equations that can be truncated at any suitable numbers of terms, leading to exploitable reduced formulations. Compared to CFD and other computationally intensive methods, this type of formulations is not only more efficient, but also provide an easy discernment of relevant parameters and often a more intuitive interpretation of results. Convergence studies, in terms of both the truncation of Chebyshev polynomials and beam modes, are performed to access to what extent reduced formulations are viable in different scenarios, including linear stability analysis as well as the calculation of limit-cycle oscillations with and without intermittent impacts between the beam and the side-walls. The presented framework can serve as a basis for a comprehensive analysis of the nonlinear dynamics of flexible beams in confined flow. Namely, it is well adapted to the use of bifurcation analysis tools for the continuation of periodic solutions, which will contribute to a richer understanding of the underlying physics occurring in this type of FSI systems. Moreover, the generic methodology presented here can also be adapted to different systems in the field of fluid-structure interaction, providing compact time-dependent formulations for nonlinear analysis.

4.1 A Galerkin discretization procedure

Similarly to the expansion procedure done for the beam displacement $y(x,t)$, here we develop both the flow velocity $u_c(x,t)$ and the pressure fields $p_c(x,t)$ in terms of a series of Chebyshev polynomials of the first kind (Figure 4.1). These are well suited to, in a compact manner, describe fields with simple linear changes (something that the Fourier series cannot achieve using only a few terms, for example), but also fields of any complexity.

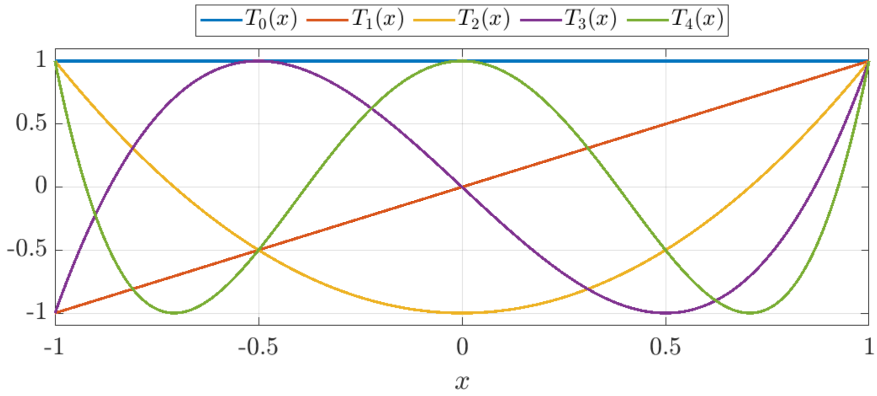

Figure 4.1 – Chebyshev polynomials of the first kind.

The Chebyshev polynomials of the first kind in the interval $x = [-1,\ 1]$ are easily computed by the following recurrent relations:

$$T_0(x) = 1 \quad ; \quad T_1(x) = x \quad ; \quad T_n(x) = 2xT_{n-1}(x) - T_{n-2}(x) \tag{4.1}$$

Similar to the Fourier series, Chebyshev polynomials constitute a complete basis of orthogonal functions. However, note that their orthogonality is not "direct", but with respect to the kernel $w(x) = (1-x^2)^{-1/2}$, that is

$$\int_{-1}^{1} \frac{T_n(x)T_s(x)}{\sqrt{1-x^2}}\,dx = \begin{cases} \pi & \text{for} \quad n = s = 0 \\ \dfrac{\pi}{2} & \text{for} \quad n = s \neq 0 \\ 0 & \text{for} \quad n \neq s \end{cases} \tag{4.2}$$

Because we need to project the Chebyshev basis in our domain interval $x = [0,\ 1]$, we introduce the shifted Chebyshev basis

$$\bar{T}_0(x) = 1 \quad ; \quad \bar{T}_1(x) = 2x - 1 \quad ; \quad \bar{T}_n(x) = 2(2x-1)\bar{T}_{n-1}(x) - \bar{T}_{n-2}(x) \tag{4.3}$$

and the associated shifted orthogonality kernel

$$\bar{w}(x) = \frac{1}{\sqrt{1-(2x-1)^2}} \tag{4.4}$$

4.1.1 Discretization of flow variables

The dimensionless velocity fields in each channel $u_c(x,t)$, truncated to $N+1$ polynomials, are given by

$$u_1(x,t) = \sum_{n=0}^{N} \bar{T}_n(x)\breve{u}_n(t) \quad ; \quad u_2(x,t) = \sum_{n=0}^{N} \bar{T}_n(x)\hat{u}_n(t) \tag{4.5}$$

and the dimensionless pressure fields, truncated to $R+1$ polynomials, give

$$p_1(x,t) = \sum_{r=0}^{R} \bar{T}_r(x)\breve{p}_r(t) \quad ; \quad p_2(x,t) = \sum_{r=0}^{R} \bar{T}_r(x)\hat{p}_r(t) \tag{4.6}$$

Note that, following standard notation, the first term in the Chebyshev series is taken at $n = 0$, i.e. $T_0(x)$. Hence, a sum of polynomials truncated to N (as above) corresponds effectively to a series of $N+1$ polynomials.

Substituting the development for the pressure fields (4.6) unto the beam equations (2.13) leads to

$$\ddot{q}_m(t) + 2\omega_m\zeta_m\dot{q}_m(t) + \omega_m^2 q_m(t) = \frac{M^*}{m_m}\sum_{r=0}^{R} S_{rm}\left(\hat{p}_r(t) - \breve{p}_r(t)\right) \tag{4.7}$$

for $m = 1,2,\cdots,M$, where the spatial operator matrix is given by

$$S_{mr} = \int_0^1 \bar{T}_r(x)\phi_m(x)dx \quad , \quad \begin{cases} r = 0,1,\cdots,R \\ m = 1,2,\cdots,M \end{cases} \tag{4.8}$$

When convenient, to avoid duplication of expressions, we will show the discretization procedure of the fluid equations only for the upper channel ($c = 1$), even though similar equations will arise for the lower channel ($c = 2$). Replacing the developments (4.5)-(4.6) into the inviscid momentum equation (2.23), leads to

$$\left(\sum_{n=0}^{N} \bar{T}_n(x)\dot{\breve{u}}_n(t)\right) + \left(\sum_{n=0}^{N} \bar{T}_n(x)\breve{u}_n(t)\right)\left(\sum_{n=0}^{N} \bar{T}_n{}'(x)\breve{u}_n(t)\right) + \left(\sum_{r=0}^{R} \bar{T}_r{}'(x)\breve{p}_r(t)\right) = 0 \tag{4.9}$$

where the upper dash X' denotes a spatial derivative $\partial/\partial x$. Similarly, replacing the developments (4.5)-(4.6) on the continuity equation (2.19) in the upper channel leads to

$$\begin{gathered} -\sum_{m=1}^{M} \phi_m(x)\dot{q}_m(t) + H_1'(x)\left(\sum_{n=0}^{N} \bar{T}_n(x)\breve{u}_n(t)\right) + H_1(x)\left(\sum_{n=0}^{N} \bar{T}_n{}'(x)\breve{u}_n(t)\right)\cdots \\ -\left(\sum_{m=1}^{M} \phi_m'(x)q_m(t)\right)\left(\sum_{n=0}^{N} \bar{T}_n(x)\breve{u}_n(t)\right) - \left(\sum_{m=1}^{M} \phi_m(x)q_m(t)\right)\left(\sum_{n=0}^{N} \bar{T}_n{}'(x)\breve{u}_n(t)\right) = 0 \end{gathered} \tag{4.10}$$

Finally, substituting (4.5)-(4.6) into the boundary conditions (2.27) and (2.28), leads to

$$\sum_{r=0}^{R} \bar{T}_r(0)\breve{p}_r(t) = P_0(t) - \frac{1}{2}\left[\sum_{n=0}^{N} \bar{T}_n(0)\breve{u}_n(t)\right]^2 - \frac{1}{2}\left[\sum_{n=0}^{N} \bar{T}_n(0)\breve{u}_n(t)\right]\left|\sum_{n=0}^{N} \bar{T}_n(0)\breve{u}_n(t)\right| K_0 \tag{4.11}$$

$$\sum_{r=0}^{R}\bar{T}_r(1)\breve{p}_r(t) = P_L(t) - \frac{1}{2}\left[\sum_{n=0}^{N}\bar{T}_n(1)\breve{u}_n(t)\right]^2 + \frac{1}{2}\left[\sum_{n=0}^{N}\bar{T}_n(1)\breve{u}_n(t)\right]\left|\sum_{n=0}^{N}\bar{T}_n(1)\breve{u}_n(t)\right| K_L \qquad (4.12)$$

4.1.2 Tau-Galerkin projection

Following the typical Galerkin procedure, the momentum and continuity equations (4.9) and (4.10) would be projected onto the polynomial series developed for the pressure and for the velocity, respectively. However, if we were to project the continuity equations into the $N+1$ Chebyshev polynomials used to expand the velocity fields and the momentum equations onto the $R+1$ polynomials used for the pressure, we would end up with an overdetermined system, i.e. $2(N+R+2)$ variables and $2(N+R+2)+4$ equations, when the four boundary conditions are taken into account. This issue arises from the fact that, unlike in the case of the beam for example, the expansion polynomials do not obey the flow boundary conditions.

Hence, we use the so-called "Tau-variant" of the Galerkin method where the projection is made onto a reduced version of the truncated polynomial series (Lanczos, 1956) (Boyd, 2000). That is, the continuity equations will be projected unto a reduced basis of only N Chebyshev polynomials and the momentum equations unto R, instead of the usual $N+1$ and $R+1$, respectively. Reducing the projection of each equation by one term, allows the construction of a determined system, including the four boundary conditions. As a note, it is unclear where to truncate the series, i.e. instead of the above mentioned truncation, both continuity equations could be truncated to $N-1$ terms instead, or the momentum equations to $R-1$ terms. All three approaches were attempted and the former was seen to be the most stable numerically.

It will become evident that the orthogonal properties of the Chebyshev polynomials are useful for the projection of the momentum equations as it greatly simplifies the resulting spatial operators. Hence, before the Galerkin projection, we pre-multiply the momentum equations by the (shifted) kernel $\bar{w}(x)$, resulting in the following set of R ordinary differential equations for the upper channel

$$\sum_{n=0}^{N}E_{nr}\dot{\breve{u}}_n(t) + \sum_{n=0}^{N}\sum_{s=0}^{N}F_{nsr}\breve{u}_n(t)\breve{u}_s(t) + \sum_{t=0}^{R}H_{tr}\breve{p}_t(t) = 0 \quad , \qquad r = 0,1,\cdots,R-1 \qquad (4.13)$$

where the associated matrices are given by

$$\begin{aligned}
E_{nr} &= \int_0^1 \bar{T}_n(x)\bar{T}_r(x)\bar{w}(x)dx = \frac{1}{2}\int_{-1}^{1}\frac{T_n(x)T_r(x)}{\sqrt{1-x^2}}dx \quad &, \quad &\begin{cases} n = 0,1,\cdots,N \\ r = 0,1,\cdots,R-1 \end{cases} \\
H_{tr} &= \int_0^1 \bar{T}_t'(x)\bar{T}_r(x)\bar{w}(x)dx = \int_{-1}^{1}\frac{T_t'(x)T_r(x)}{\sqrt{1-x^2}}dx \quad &, \quad &\begin{cases} t = 0,1,\cdots,R \\ r = 0,1,\cdots,R-1 \end{cases} \qquad (4.14) \\
F_{nsr} &= \int_0^1 \bar{T}_n'(x)\bar{T}_s(x)\bar{T}_r(x)\bar{w}(x)dx = \int_{-1}^{1}\frac{T_n'(x)T_s(x)T_r(x)}{\sqrt{1-x^2}}dx \quad &, \quad &\begin{cases} n = 0,1,\cdots,N \\ s = 0,1,\cdots,N \\ r = 0,1,\cdots,R-1 \end{cases}
\end{aligned}$$

Due to the orthogonal properties of the Chebyshev polynomials, the matrices in (4.14) have relatively simple structures: matrix E_{nr} is diagonal, H_{tr} is sparse upper triangular and the tri-dimensional matrix F_{nsr} also has similar sparsity properties. To clarify, we define these matrices explicitly in the Appendix A. For the lower channel, an equivalent set of R equations is derived, simply replacing $\breve{u}$ and $\breve{p}$ by $\hat{u}$ and $\hat{p}$, in (4.13).

Contrary to the momentum equations, in the projection of the continuity equations, the usefulness of the orthogonality properties is not clear in a general sense. From (4.10) one obtains the following sets of N nonlinear algebraic equations, which stand for the continuity equation in the upper and lower channels, respectively,

$$-\sum_{m=1}^{M} A_{mn} r_m(t) + \sum_{s=0}^{N} B_{sn} \breve{u}_s(t) - \sum_{m=1}^{M}\sum_{s=0}^{N} D_{msn} q_m(t) \breve{u}_s(t) = 0 \quad , \quad n = 0,1,\cdots,N-1 \tag{4.15}$$

$$\sum_{m=1}^{M} A_{mn} r_m(t) + \sum_{s=0}^{N} C_{sn} \hat{u}_s(t) + \sum_{m=1}^{M}\sum_{s=0}^{N} D_{msn} q_m(t) \hat{u}_s(t) = 0 \quad , \quad n = 0,1,\cdots,N-1 \tag{4.16}$$

whose dense spatial operators are given explicitly by

$$\begin{aligned}
A_{mn} &= \int_0^1 \phi_m(x) \bar{T}_n(x) dx && , \quad \begin{cases} m = 1,2,\cdots,M \\ n = 0,1,\cdots,N-1 \end{cases} \\
B_{sn} &= \int_0^1 \left[H_1'(x)\bar{T}_s(x) + H_1(x)\bar{T}_s'(x) \right] \bar{T}_n(x) dx && , \quad \begin{cases} s = 0,1,\cdots,N \\ n = 0,1,\cdots,N-1 \end{cases} \\
C_{sn} &= \int_0^1 \left[H_2'(x)\bar{T}_s(x) + H_2(x)\bar{T}_s'(x) \right] \bar{T}_n(x) dx && , \quad \begin{cases} s = 0,1,\cdots,N \\ n = 0,1,\cdots,N-1 \end{cases} \\
D_{msn} &= \int_0^1 \left[\phi_m'(x)\bar{T}_s(x) + \phi_m(x)\bar{T}_s'(x) \right] \bar{T}_n(x) dx && , \quad \begin{cases} m = 1,2,\cdots,M \\ s = 0,1,\cdots,N \\ n = 0,1,\cdots,N-1 \end{cases}
\end{aligned} \tag{4.17}$$

4.1.3 Formulation of the nonlinear coupled system

The structural modal equations, coupled with the pressure at each channel, can be described as a first-order system by defining the modal velocities $r_m(t) = \dot{q}_m(t)$. In a matrix form, it reads

$$\begin{bmatrix} [\mathbf{I}] & 0 \\ 0 & [\mathbf{I}] \end{bmatrix} \begin{Bmatrix} \{\dot{\mathbf{R}}(\mathrm{t})\} \\ \{\dot{\mathbf{Q}}(\mathrm{t})\} \end{Bmatrix} + \begin{bmatrix} 2[\boldsymbol{\Omega}][\mathrm{Z}] & [\boldsymbol{\Omega}]^2 \\ \text{-}[\mathbf{I}] & 0 \end{bmatrix} \begin{Bmatrix} \{\mathbf{R}(t)\} \\ \{\mathbf{Q}(t)\} \end{Bmatrix} = \begin{Bmatrix} [\mathbf{M}]\left[\mathbf{S}\right]\{\hat{\mathbf{P}}(t) - \breve{\mathbf{P}}(t)\} \\ 0 \end{Bmatrix} \tag{4.18}$$

where $[\boldsymbol{\Omega}]$ and $[\mathbf{Z}]$ are $M \times M$ diagonal matrices whose diagonals contain the modal frequencies and damping coefficients of the beam, respectively; the $M \times M$ diagonal matrix $[\mathbf{M}]$ is defined by $\text{diag}(\mathbf{M}) = M^* \big/ m_m$; and $\mathbf{R}(t), \mathbf{Q}(t)$, $\breve{\mathbf{P}}(t)$ and $\hat{\mathbf{P}}(t)$ are column vectors containing the M modal responses of the beam and the $R+1$ pressures at the upper and lower channels, respectively. The matrix $[\mathbf{S}]$ is a $M \times (R+1)$ matrix, whose elements are defined in (4.8).

Finally, assembling the structural equations (4.18), the flow continuity equations (4.15)-(4.16), the flow momentum equations (4.13) and the four boundary conditions (4.11)-(4.12) leads to the fully coupled nonlinear system,

$$\begin{bmatrix} [\mathbf{I}] & 0 & 0 & 0 & 0 & 0 \\ 0 & [\mathbf{I}] & 0 & 0 & 0 & 0 \\ 0 & 0 & [\mathbf{E}] & 0 & 0 & 0 \\ 0 & 0 & 0 & [\mathbf{E}] & 0 & 0 \\ 0 & 0 & 0 & 0 & 0 & 0 \\ \vdots & & & & & \vdots \\ 0 & & & & & 0 \end{bmatrix} \begin{Bmatrix} \dot{\mathbf{R}} \\ \dot{\mathbf{Q}} \\ \dot{\breve{\mathbf{U}}} \\ \dot{\widehat{\mathbf{U}}} \\ \dot{\breve{\mathbf{P}}} \\ \dot{\widehat{\mathbf{P}}} \end{Bmatrix} + \begin{bmatrix} 2[\Omega][\mathrm{Z}] & [\Omega]^2 & 0 & 0 & [\mathbf{M}][\mathbf{S}] & \text{-}[\mathbf{M}][\mathbf{S}] \\ \text{-}[\mathbf{I}] & 0 & 0 & 0 & 0 & 0 \\ 0 & 0 & 0 & 0 & [\mathbf{H}] & 0 \\ 0 & 0 & 0 & 0 & 0 & [\mathbf{H}] \\ -[\mathbf{A}] & 0 & [\mathbf{B}] & 0 & 0 & 0 \\ [\mathbf{A}] & 0 & 0 & [\mathbf{C}] & 0 & 0 \\ 0 & 0 & 0 & 0 & \{\mathbf{T}_0\}^T & 0 \\ 0 & 0 & 0 & 0 & 0 & \{\mathbf{T}_0\}^T \\ 0 & 0 & 0 & 0 & \{\mathbf{T}_L\}^T & 0 \\ 0 & 0 & 0 & 0 & 0 & \{\mathbf{T}_L\}^T \end{bmatrix} \begin{Bmatrix} \mathbf{R} \\ \mathbf{Q} \\ \breve{\mathbf{U}} \\ \widehat{\mathbf{U}} \\ \breve{\mathbf{P}} \\ \widehat{\mathbf{P}} \end{Bmatrix} = \begin{Bmatrix} \mathbf{0} \\ \mathbf{0} \\ -\breve{\mathbf{F}}_r \\ -\widehat{\mathbf{F}}_r \\ \breve{\mathbf{D}}_n \\ -\widehat{\mathbf{D}}_n \\ \breve{\mathbf{V}}_0 \\ \widehat{\mathbf{V}}_0 \\ \breve{\mathbf{V}}_{\mathrm{L}} \\ \widehat{\mathbf{V}}_{\mathrm{L}} \end{Bmatrix} \tag{4.19}$$

where the matrices $[\mathbf{A}]$, $[\mathbf{B}]$, $[\mathbf{C}]$, $[\mathbf{E}]$, $[\mathbf{H}]$ and $[\mathbf{S}]$ contain the projection coefficients for the linear terms, defined in (4.8), (4.14) and (4.17). That is:

$$\begin{array}{llll} [\mathbf{A}] = A_{nm} & \rightarrow \text{ size: } N \times M & [\mathbf{E}] = E_{rn} & \rightarrow \text{ size: } R \times (N+1) \\ [\mathbf{B}] = B_{ns} & \rightarrow \text{ size: } N \times (N+1) & [\mathbf{H}] = H_{rt} & \rightarrow \text{ size: } R \times (R+1) \\ [\mathbf{C}] = C_{ns} & \rightarrow \text{ size: } N \times N+1) & [\mathbf{S}] = S_{mr} & \rightarrow \text{ size: } M \times (R+1) \end{array} \tag{4.20}$$

The $R+1$ sized vectors describing the pressure terms on the four flow boundary conditions are given by

$$\begin{array}{ll} \{\mathbf{T}_0\} = \overline{T}_r(0) & r = 0,1,2\ldots R \\ \{\mathbf{T}_L\} \ = \overline{T}_r(1) & r = 0,1,2\ldots R \end{array} \tag{4.21}$$

All the nonlinear terms are encapsulated in the right-hand-side of (4.19). The vectors containing the nonlinear terms in the continuity equations, $\{\breve{\mathbf{D}}_n\}$ and $\{\widehat{\mathbf{D}}_n\}$, and in the momentum equations, $\{\breve{\mathbf{F}}_r\}$ and $\{\widehat{\mathbf{F}}_r\}$, are given by

$$\{\mathbf{D}_n\} = \sum_{m=1}^{M}\sum_{s=0}^{N} D_{msn} q_m(t) u_s(t) \quad ; \quad \{\mathbf{F}_r\} = \sum_{n=0}^{N}\sum_{s=0}^{N} F_{nsr} u_n(t) u_s(t) \tag{4.22}$$

where the generic $u_s(t)$ is replaced by the velocities in a particular channel, upper $\breve{u}_s(t)$ or lower $\widehat{u}_s(t)$, to obtain the corresponding vectors $\{\breve{\mathbf{D}}_n\}$ and $\{\breve{\mathbf{F}}_r\}$ or $\{\widehat{\mathbf{D}}_n\}$ and $\{\widehat{\mathbf{F}}_r\}$. Finally, the nonlinear terms in the boundary condition equations are given by

$$\begin{aligned} \mathrm{V}_0 &= P_0(t) - \frac{1}{2}\left(1 + \operatorname{sign}\left(\sum_{n=0}^{N} \overline{T}_n(0) u_n(t)\right) K_0\right)\left[\sum_{n=0}^{N} \overline{T}_n(0) u_n(t)\right]^2 \\ \mathrm{V}_{\mathrm{L}} &= P_L(t) - \frac{1}{2}\left(1 - \operatorname{sign}\left(\sum_{n=0}^{N} \overline{T}_n(1) u_n(t)\right) K_L\right)\left[\sum_{n=0}^{N} \overline{T}_n(1) u_n(t)\right]^2 \end{aligned} \tag{4.23}$$

where, again, replacing the generic $u_s(t)$ by $\breve{u}_s(t)$ or $\widehat{u}_s(t)$ will yield the corresponding vectors $\{\breve{\mathbf{V}}_0\}$ and $\{\breve{\mathbf{V}}_L\}$ or $\{\widehat{\mathbf{V}}_0\}$ and $\{\widehat{\mathbf{V}}_L\}$.

The coupled system (4.19) is a system of first-order nonlinear differential-algebraic equations (DAE) of size $2(M+N+R+2)$, where the matrix connected with the derivative vector is singular. The state differential variables are $\mathbf{R}$, $\mathbf{Q}$, $\breve{\mathbf{U}}$, $\hat{\mathbf{U}}$, and the state algebraic variables are $\breve{\mathbf{P}}$, $\hat{\mathbf{P}}$. Moreover, we note that the DAE system is of differential index-2 (Hairer & Wanner, 1996), as the algebraic equations (flow continuity) do not contain the algebraic variables $\breve{\mathbf{P}}$, $\hat{\mathbf{P}}$ explicitly. In any case, due to the orthogonality properties of the beam modes $\phi(x)$ and Chebyshev polynomials $T(x)$, the mass matrix will also be diagonal (although singular), which may bring some benefits when calculating solutions numerically.

4.1.4 Linearized system

To linearize the system containing flow nonlinear equations, we again separate the governing variables into their steady and fluctuating components $g(x,t) = \overline{g}(x) + \tilde{g}(x,t)$. For the steady system, we can simply take the original system (4.19) and remove the time-derivative terms as well as the modal velocities $\mathbf{R}$. Then, the steady system is governed by the following set of $M + 2(N + R + 2)$ nonlinear algebraic equations

$$\begin{bmatrix} [\Omega]^2 & 0 & 0 & [\mathbf{M}][\mathbf{S}] & -[\mathbf{M}][\mathbf{S}] \\ 0 & 0 & 0 & [\mathbf{H}] & 0 \\ 0 & 0 & 0 & 0 & [\mathbf{H}] \\ 0 & [\mathbf{B}] & 0 & 0 & 0 \\ 0 & 0 & [\mathbf{C}] & 0 & 0 \\ 0 & 0 & 0 & \{\mathbf{T}_0\}^T & 0 \\ 0 & 0 & 0 & 0 & \{\mathbf{T}_0\}^T \\ 0 & 0 & 0 & \{\mathbf{T}_L\}^T & 0 \\ 0 & 0 & 0 & 0 & \{\mathbf{T}_L)\}^T \end{bmatrix} \begin{Bmatrix} \overline{\mathbf{Q}} \\ \bar{\breve{\mathbf{U}}} \\ \bar{\hat{\mathbf{U}}} \\ \bar{\breve{\mathbf{P}}} \\ \bar{\hat{\mathbf{P}}} \end{Bmatrix} = \begin{Bmatrix} \mathbf{0} \\ \text{-}\{\bar{\breve{\mathbf{F}}}_\mathbf{r}\} \\ \text{-}\{\bar{\hat{\mathbf{F}}}_\mathbf{r}\} \\ \{\bar{\breve{\mathbf{D}}}_\mathbf{n}\} \\ \text{-}\{\bar{\hat{\mathbf{D}}}_\mathbf{n}\} \\ \bar{\breve{\mathbf{V}}}_0 \\ \bar{\hat{\mathbf{V}}}_0 \\ \bar{\breve{\mathbf{V}}}_\mathrm{L} \\ \bar{\hat{\mathbf{V}}}_\mathrm{L} \end{Bmatrix} \tag{4.24}$$

The steady components of the nonlinear terms, on the right-hand-side, are given by

$$\{\overline{\mathbf{D}}_n\} = \sum_{m=1}^{M}\sum_{s=0}^{N} D_{msn}\overline{q}_m\overline{u}_s \quad ; \quad \{\overline{\mathbf{F}}_r\} = \sum_{n=0}^{N}\sum_{s=0}^{N} F_{nsr}\overline{u}_n\overline{u}_s \tag{4.25}$$

$$\begin{aligned} \{\overline{\mathbf{V}}_0\} &= P_0 - \frac{1}{2}(1 \pm K_0)\left[\sum_{n=0}^{N}\overline{T}_n(L)\overline{u}_n\right]^2 \\ \{\overline{\mathbf{V}}_L\} &= P_L - \frac{1}{2}(1 \mp K_L)\left[\sum_{n=0}^{N}\overline{T}_n(L)\overline{u}_n\right]^2 \end{aligned} \tag{4.26}$$

where the generic $\overline{u}_s$ is replaced by the velocities in a particular channel, upper $\bar{\breve{u}}_s$ or lower $\bar{\hat{u}}_s$, to obtain the corresponding vectors $\{\bar{\breve{\mathbf{D}}}_n\}$, $\{\bar{\breve{\mathbf{F}}}_r\}$, $\{\bar{\breve{\mathbf{V}}}_0\}$, $\{\bar{\breve{\mathbf{V}}}_L\}$ or $\{\bar{\hat{\mathbf{D}}}_n\}$, $\{\bar{\hat{\mathbf{F}}}_r\}$, $\{\bar{\hat{\mathbf{V}}}_0\}$, $\{\bar{\hat{\mathbf{V}}}_L\}$.

For the first-order system, we simply linearize the nonlinear terms on the right-hand-side of the original system (4.19), resulting in

$$
\begin{bmatrix}
[\mathbf{I}] & 0 & 0 & 0 & 0 & 0 \\
0 & [\mathbf{I}] & 0 & 0 & 0 & 0 \\
0 & 0 & [\mathbf{E}] & 0 & 0 & 0 \\
0 & 0 & 0 & [\mathbf{E}] & 0 & 0 \\
0 & 0 & 0 & 0 & 0 & 0 \\
0 & 0 & 0 & 0 & 0 & 0 \\
0 & 0 & 0 & 0 & 0 & 0 \\
0 & 0 & 0 & 0 & 0 & 0 \\
0 & 0 & 0 & 0 & 0 & 0 \\
0 & 0 & 0 & 0 & 0 & 0
\end{bmatrix}
\begin{Bmatrix}
\dot{\mathbf{R}} \\ \dot{\mathbf{Q}} \\ \dot{\breve{\mathbf{U}}} \\ \dot{\hat{\mathbf{U}}} \\ \dot{\breve{\mathbf{P}}} \\ \dot{\hat{\mathbf{P}}}
\end{Bmatrix}
\cdots
$$

$$
+\begin{bmatrix}
2[\Omega][Z] & [\Omega]^2 & 0 & 0 & [\mathbf{M}][\mathbf{S}] & -[\mathbf{M}][\mathbf{S}] \\
-[\mathbf{I}] & 0 & 0 & 0 & 0 & 0 \\
0 & 0 & [\tilde{\mathbf{F}}] & 0 & [\mathbf{H}] & 0 \\
0 & 0 & 0 & [\tilde{\mathbf{F}}] & 0 & [\mathbf{H}] \\
-[\mathbf{A}] & -[\mathbf{D}_2] & [\mathbf{B}]-[\mathbf{D}_1] & 0 & 0 & 0 \\
[\mathbf{A}] & [\mathbf{D}_2] & 0 & [\mathbf{C}]+[\mathbf{D}_1] & 0 & 0 \\
0 & 0 & \{\tilde{\breve{\mathbf{V}}}_0\} & 0 & \{\mathbf{T}_0\}^T & 0 \\
0 & 0 & 0 & \{\tilde{\breve{\mathbf{V}}}_0\} & 0 & \{\mathbf{T}_0\}^T \\
0 & 0 & \{\tilde{\breve{\mathbf{V}}}_L\} & 0 & \{\mathbf{T}_L\}^T & 0 \\
0 & 0 & 0 & \{\tilde{\breve{\mathbf{V}}}_L\} & 0 & \{\mathbf{T}_L\}^T
\end{bmatrix}
\begin{Bmatrix}
\mathbf{R} \\ \mathbf{Q} \\ \breve{\mathbf{U}} \\ \hat{\mathbf{U}} \\ \breve{\mathbf{P}} \\ \hat{\mathbf{P}}
\end{Bmatrix}
=\{0\}
\tag{4.27}
$$

where the linearized components of the nonlinear terms are given by

$$
[\tilde{\mathbf{F}}]=\sum_{n=0}^{N}F_{nsr}\bar{u}_n+\sum_{s=0}^{N}F_{nsr}\bar{u}_s \qquad (\text{size } \ (N+1)\times R)
\tag{4.28}
$$

$$
\begin{cases}
[\mathbf{D}_1]=\sum\limits_{m=1}^{M}D_{msn}\bar{q}_m & (\text{size } \ (N+1)\times N) \\
[\mathbf{D}_2]=\sum\limits_{s=0}^{N}D_{msn}\bar{u}_s & (\text{size } \ M\times N)
\end{cases}
\tag{4.29}
$$

$$
\begin{aligned}
\{\tilde{\mathbf{V}}_0\}&=(1\pm K_0)\sum_{s=0}^{N}\bar{T}_s(0)\bar{T}_n(0)\bar{u}_s \qquad (\text{size } \ 1\times(N+1)) \\
\{\tilde{\mathbf{V}}_L\}&=(1\mp K_L)\sum_{s=0}^{N}\bar{T}_s(1)\bar{T}_n(1)\bar{u}_s \qquad (\text{size } \ 1\times(N+1))
\end{aligned}
\tag{4.30}
$$

where the generic $\bar{u}_s$ is replaced by the velocities in a particular channel, upper $\bar{\breve{u}}_s$ or lower $\bar{\hat{u}}_s$, to obtain the corresponding matrices $[\breve{\mathbf{D}}_2]$, $[\hat{\mathbf{D}}_2]$ and vectors $\{\tilde{\breve{\mathbf{V}}}_0\}$, $\{\tilde{\hat{\mathbf{V}}}_0\}$, $\{\tilde{\breve{\mathbf{V}}}_L\}$, $\{\tilde{\hat{\mathbf{V}}}_L\}$.

4.2 Convergence studies

In this section we will not present an extensive report of numerical results and will restrict ourselves to showing that the results obtained using this present Galerkin approach are positively validated by those obtained with the analytical solution (Soares et al., 2022). Here, we will focus mainly on the convergence properties of the new formulation. Several periodic solutions will be shown using various orders of truncation for our series, both in terms of the Chebyshev polynomials used for the flow variables as well as the mode shapes used for the flexible beam to access the viability for compact formulations in different scenarios.

4.2.1 Linear stability analysis

In our previous analytical formulation, which did not rely on any error-inducing (discretization) procedures regarding the flow variables, the resulting first-order linearized system was of size $2M+2$ where the variables were the modal displacements q_m and velocities r_m plus two global unsteady flow rates $\tilde{Q}_c(t)$, one for each channel. The resulting generalized eigenproblem was regular and composed of two dense non-singular matrices. The ensuing $2M+2$ eigenvalues contained $2M$ (coupled) modes associated with the various fluid-loaded beam modes plus two eigenvalues associated with the flow in each channel (trivial steady flow modes, equivalent to flow "rigid body" mode).

However, in the current formulation, the resulting linear DAE system has a singular mass matrix. Such systems are known to produce both finite and infinite eigenvalues. With a few exceptions, infinite eigenvalues are generally attributed to "nondynamic" modes, essentially trivial (for further details, see (Hairer & Wanner, 1996)). Nevertheless, the singular eigenvalue problem can be solved numerically to obtain both finite and infinite eigenvalues (Eigenvalue Solver eig(), 2022). In our linearized DAE system (4.27), of size $2(M+N+R+2)$, we obtain $2M+2$ finite eigenvalues and $2(N+R)+2$ infinite ones (this is coherent with the results from our analytical formulation). All infinite eigenvalues are associated with purely pressure-based eigenvectors (where all other components of the eigenvectors are null). This is expected since the pressure coefficients $p_r(t)$ are the algebraic variables of the DAE system.

For simplicity, we consider here configurations with flow in the positive direction, i.e. $P_L < P_0$, and symmetric channels with constant height, $H_1 = H_2$. Additionally, we will consider truncations of the Chebyshev terms equal for both the expansions of the velocity and pressure fields, i.e. $N = R$.

As an initial assessment of the current formulation and its model reduction capacities, in Figure 4.2, we compare the stability boundaries resulting from the analytical formulation against those from the current approach, using various orders of truncation N for the expansion of the flow variables. The confinement ratio was set at $H^* = 0.1$. In all cases, a relatively large number of beam modes were considered $(M = 20)$, to ensure errors associated to the beam discretization were negligible. Modal damping ratios of the beam were fixed for all modes at $\zeta_m = 0.01$.

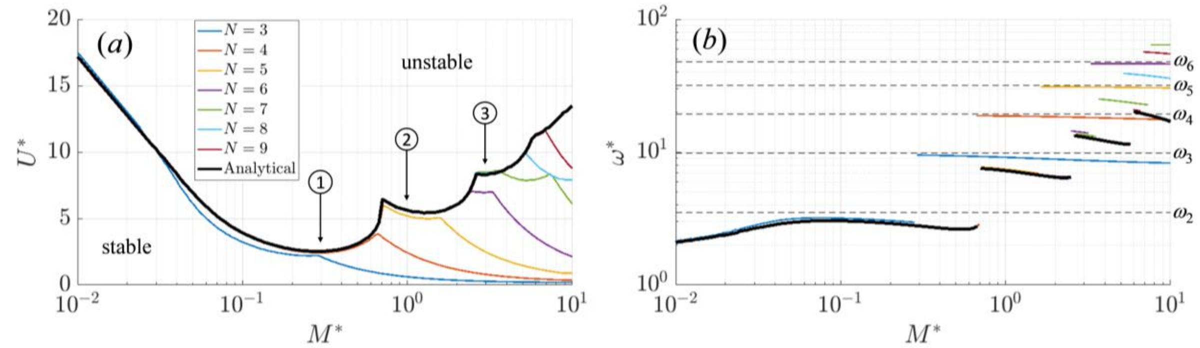

Figure 4.2 – (a) Stability boundaries in the $(M^* - U^*)$ plane for a system with confinement ratio $H^* = 1/10$, using the analytical formulation (black line) and the Galerkin formulation (colored lines) with various orders of truncation N; (b) Corresponding critical frequencies, where $\omega^* = \omega_{\text{crit}}/\omega_0$.

In Figure 4.2(a) we see the typical "cascading" stability boundary discussed in the previous chapter. To re-iterate, the "modal transitions" (occurring here at, for example, $M^* \simeq 0.7$ and $M^* \simeq 2.5$) are associated with a change in the shape of the primary unstable (coupled) mode. While at low mass ratios the primary unstable mode shape is composed primarily by components of the 1st and 2nd *in-vacuo* beam modes, as the mass ratios increase, higher order *in-vacuo* beam modes become dominant in the unstable motion. As seen clearly in Figure 4.2(b), these transitions in the stability boundary are also accompanied by a discontinuous increase in the instability frequency.

With that said, interpretation of the results regarding the convergence of the Galerkin approach becomes more intuitive. In Figure 4.2 we note that, for low-to-moderate mass ratios ($M^* \lesssim 1$), a relatively small number of polynomials in the expansion of flow variables $(N > 4)$ is sufficient for an accurate description of the stability boundary. However, as mass ratios increase the order of truncation N necessary for converge also increases. Naturally, this is explained by the fact that the spatial distribution of the fluctuations in flow velocity and pressure will accompany the prevailing beam motion. Hence, when higher-order *in-vacuo* beam modes are predominant in the unstable motion, the flow velocities and pressures will also require an expansion of Chebyshev polynomials of the same order.

Although not shown here, an investigation regarding the truncation of beam modes M was carried out. As is self-evident, conclusions are similar to those discussed above, i.e. accurate results entail that the considered number of beam modes M include the dominant components of the linearly unstable (fluid-structure coupled) mode. For relatively low mass-ratios $(M^* < 0.5)$, as is typically the case for configurations in air, two *in-vacuo* modes $(M = 2)$ are generally sufficient. For larger mass-ratios $(M^* > 0.5)$, a larger number of beam modes is necessary.

4.2.2 Nonlinear analysis

We now investigate the viability of the current formulation for solving the fully nonlinear system (including beam-wall impacts) using time-domain integrations. Here, several time-domain solutions will be presented, and compared to results from the analytical formulation, in order to assess the convergence properties of the new formulation in terms of both the truncation of the flow variables expansions $N\ (=R)$, as well as the number of considered beam modes M.

The time-domain integrations of the (numerically challenging) DAE system of differential index-2 (4.19) were performed using an implicit Runge-Kutta scheme based on a 7-stage Radau IIA method. The algorithm can be found on the Matlab's Central File Exchange (Mahooti, 2020) and was programmed by Meysam Mahooti based on the routine RADAU5 described in (Hairer & Wanner, 1996).

To illustrate the model reduction capacities of the current approach, we examine an example limit-cycle in a symmetric configuration $H_1 = H_2$, where intermittent impacts occur between the beam-tip and side walls. The main non-dimensional parameters were taken as $H^* = 1/10$, $M^* = 0.1$, $U^* = 8.5$ and $\zeta_m = 0.05$. The value of the dimensionless impact stiffness was set to $k_i = 10^5$, based on the wish to simulate relatively stiff impacts without the having to include an overwhelming amount of beam modes (it will be shown later that $M = 20$ was sufficient to describe impacts accurately). The impact regularization parameter was set to 1% of the channel height, $\varepsilon/H_0 = 0.01$, to allow a reasonable margin of contact "penetration".

Firstly, to give an overview of the resulting LCO, Figure 4.3 shows: (a) snapshots of the beam motion as well as (b) the temporal evolution of the modal velocities $r_m(t)$, (c) the flow velocity coefficients (d) and pressure coefficients in the upper channel, $\breve{p}_r(t)$ and $\breve{u}_n(t)$ (due to symmetry, the lower channel flow variables are equivalent, but in phase opposition). Here, the truncation of the beam modes and Chebyshev polynomials were set to large values, $M = N = R = 30$, deemed sufficient to describe the LCO accurately, as will be shown in the following sub-sections.

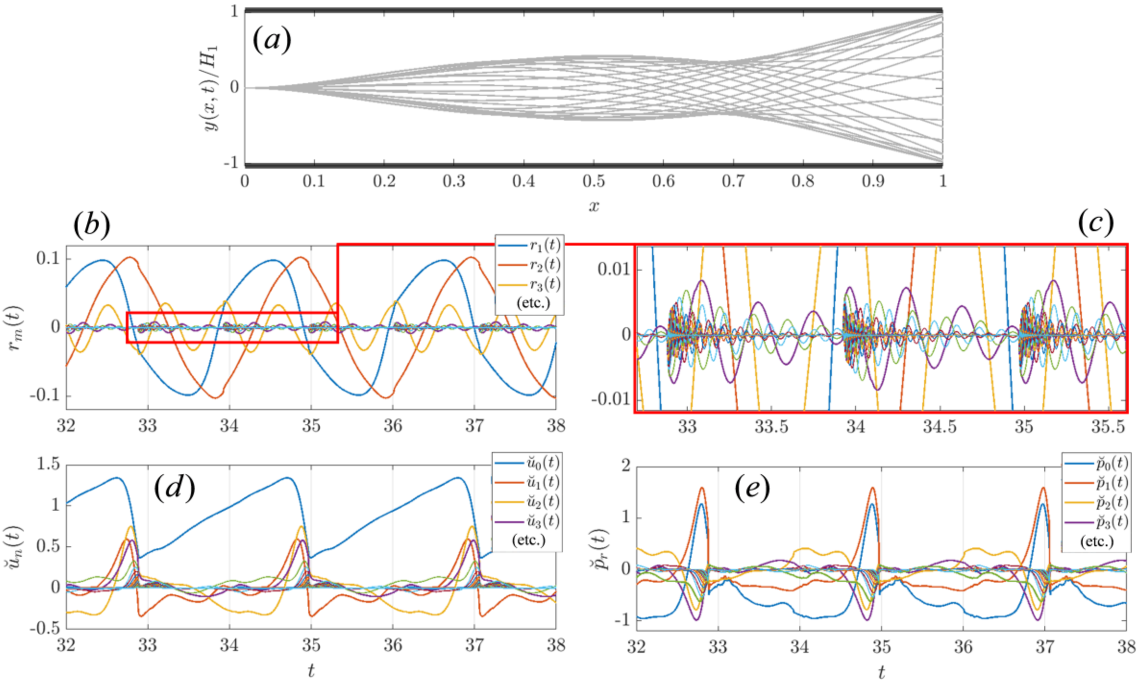

Figure 4.3 – Overview of the resulting limit-cycle oscillations: (a) snapshots of the beam motion; temporal evolution of the (b) modal velocities; (c) zoom of modal velocities; (d) velocity coefficients and (e) pressure coefficients of the flow in the upper channel.

Figure 4.3-(b) shows us that the beam motion during the LCO is dominated by the first three *in-vacuo* beam modes. Moreover, we note that higher-order beam modes are excited intermittently after each impact (Figure 4.3-(c)). Nevertheless, their influence remains small in the overall LCO pattern. In Figure 4.3-(d) and (e), we see that, in general, the most significant oscillations in the flow variables are given by the lowest order coefficients of the Chebyshev expansions $\breve{u}_{0-3}(t)$ and $\breve{p}_{0-3}(t)$. This is coherent with what was shown in linear stability analysis, in that the spatial profile of the flow oscillations will typically accompany the motion of the beam. However, right before an impact, many higher-order components $\breve{u}_{n>3}(t)$ and $\breve{p}_{r>3}(t)$ become prominent, meaning that velocity and pressure profiles will present larger (spatial) gradients at these instances.

We now assess the model reduction capacities of the present model. Periodic solutions for the configuration presented above (Figure 4.3) have been calculated, using various orders of truncations for the velocity and pressure expansions N $(= R)$. Since, in this case, intermittent impacts occur solely at the tip of the beam, and since all *in-vacuo* beam mode shapes $\phi(x)$ contain maxima at the beam-tip, a reasonable global indicator of the LCO is given by the beam-tip velocity $\dot{y}(L,t)$. Figure 4.4 shows the phase-portrait of the beam-tip (left) and the temporal evolution of the (normalized) beam-tip velocity $\dot{y}(L,t)$, in solutions calculated with various orders of truncation N. The solution obtained with the analytical formulation was also plotted for comparison, even though it is indistinguishable from the solution with $N = 8$ (plots are overlapped). Here, the number of considered beam modes was maintained fixed at a large value $M = 30$.

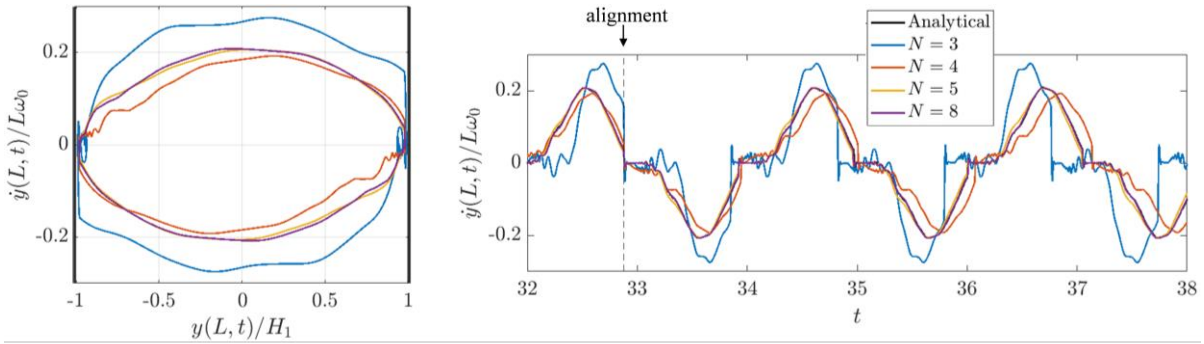

Figure 4.4 – Phase portrait of the beam-tip during an LCO with intermittent impacts (left) and temporal evolution of the beam-tip velocity $\dot{y}(L,t)$ (right), using various truncations of the Chebyshev expansions $N\,(=R)$.

From Figure 4.4 we note that, in fact, the LCO seems to be reasonably well represented by relatively low truncations orders ($N \geq 4$). At truncations above $N \geq 8$, the evolution of the beam-tip velocity (as well as the phase-portrait) is indistinguishable from the analytical results (plots are overlapped). Even at $N = 5$, we notice only very minor quantitative differences. At $N = 4$, deviations start to become more evident, with a small underestimation of the fundamental frequency of oscillation ($\sim 2\%$). Nevertheless, the overall motion remains relatively well represented. Finally, at $N = 3$ results collapse dramatically, with a gross misrepresentation of the oscillation pattern and a significant overestimation of the fundamental frequency ($\sim 8\%$).

These observations suggest that, even in the presence of impacts (strong nonlinearities) and the consequent appearance of sharp spatial gradients in the profiles of the flow pressure and velocity, the overall LCO can nevertheless be well represented by relatively low truncation orders N. That is, the occurrence of impacts does not seem to have a significant effect on the previously described logic that: the truncation order N must be sufficient to accompany the *dominant* beam motion profile. In this case, the first three *in-vacuo* beam modes dominate, and hence truncations of $N \geq 4$ will in general suffice.

To clarify, Figure 4.5 shows the velocity and pressure spatial distribution on the upper channel at a moment t_i before contact between the beam-tip and the upper wall. Here, we notice the very sharp gradients near the beam-tip ($x \approx 1$). As expected, we see that a large order of truncation N is necessary to properly describe the sharp flow gradients, which are severely misrepresented by the solutions using low truncations, showing a very prominent Gibbs effect. However, despite these severe misrepresentations, we have seen that low orders of truncation ($N \geq 4$) are effectively able to reproduce the overall LCO accurately. This could possibly be explained by two reasons: (1) the misrepresentations of the sharp flow profiles are very brief and (2) the observed Gibbs phenomena will be “dissipated” once the pressure profiles are projected unto the dominant beam modes (of relatively low-order).

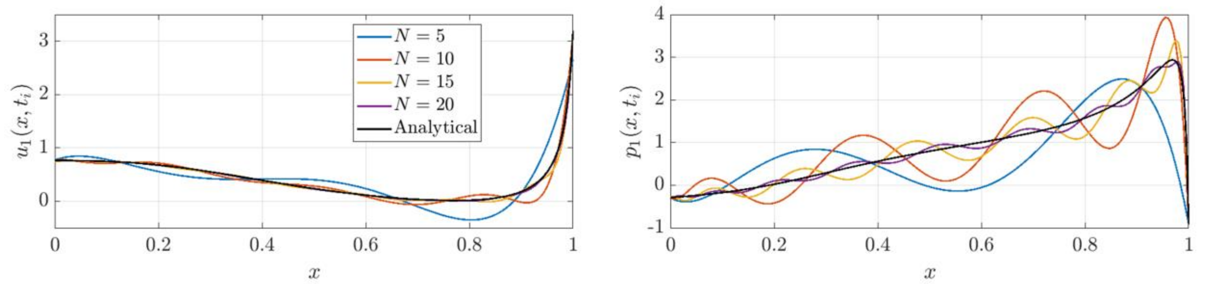

Figure 4.5 – Description of the velocity (left) and pressure (right) profiles in the upper channel at time t_i, right before contact between the beam-tip and the upper wall, using various truncations for the Chebyshev expansion $N = R$. The corresponding profiles calculated with the analytical model are shown in black.

Here it is worth underlining that we have considered the convergence of the flow fields assuming the same truncation for the pressure and velocity, i.e. $N = R$. In a linear context, where oscillations are arbitrarily small, this is a reasonable assumption as both velocity and pressure fields will tend to have the same gradients (following the beam motion) (Soares et al., 2022). However, in a nonlinear context, flow velocity and pressure profiles can differ significantly, and it is not evident which variable will present larger gradients and hence necessitate larger truncations. Moreover, this also likely a problem-dependent issue. Nevertheless, based on the numerous simulations conducted for this work, our experience suggests that often, the pressure fields will present larger gradients, as illustrated in Figure 4.5. This suggests, tentatively, that using smaller truncations for the velocity field, i.e. $N < R$, could eventually be a viable option. Nevertheless, the studies presented here, with $N = R$ for simplicity, effectively provide a conservative upper bound on the necessary truncation.

Now we examine that effect of the number of considered modes M on the resulting LCOs. Figure 4.6 shows the temporal evolution of the beam-tip velocity in various solutions using a different number of considered beam modes M. Here, the truncation of the Chebyshev expansions used for the flow variables was fixed at a large number $N = R = 30$.

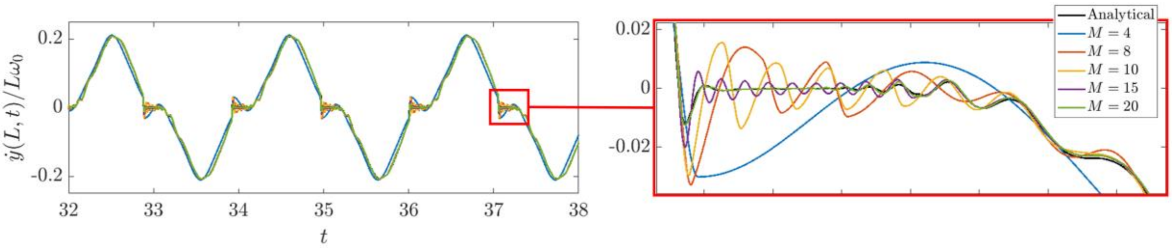

Figure 4.6 – Temporal evolution of the beam-tip velocity $\dot{y}(L,t)$ during a LCO with intermittent impacts, calculated with different number of considered beam modes M.

The results in Figure 4.6 shows us that the overall motion of the LCO does not seem to be significantly affected by the number of considered modes M, so long as $M \geq 4$. The main difference between the various solutions is concentrated at the moments of impact (right plot). Impacts generate rapid changes in the velocity of the beam-tip. Consequently, many *in-vacuo* beam modes are excited. We notice that when the number of considered modes is relatively low ($M < 20$), impacts lead to an artificial residual oscillation of the beam-tip. Moreover, is it worth noting that the frequency of these residual oscillations is approximately equal to the frequency of the highest considered mode. This suggests that, at low truncations M, the impact energy transferred to the beam, that would otherwise be distributed evenly between all modes, is going to be concentrated on the highest considered mode (stiffest mode).

To clarify this effect, the spectra (and spectral envelopes) of the beam-tip velocity are shown in Figure 4.7. In Figure 4.7-(a) we can observe that the motion of the tip is composed of many harmonic components (>100). Moreover, because the beam motion is symmetric, its spectra contain only odd harmonic components. If we perform a (spline) interpolation of the spectral peaks, we can calculate a “spectral envelope”, as illustrated in Figure 4.7-(a). In this envelope we notice several “formants”, whose frequency effectively corresponds to the frequency of the *in-vacuo* beam modes, excited during impacts. In Figure 4.7-(b), we notice these formants are modified when a different number of beam modes is considered. More concretely, the energy near the frequency of the highest considered mode M is increased.

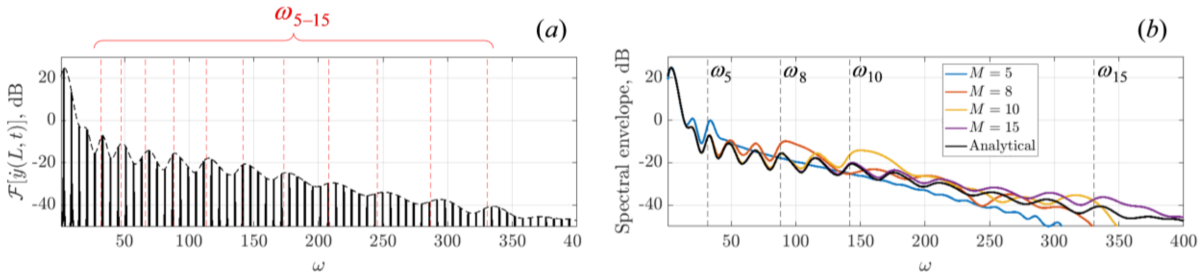

Figure 4.7 – (a) Spectra of the beam-tip velocity $\dot{y}(L,t)$ in the analytical solution; (b) Spectral envelopes of solutions with various beam mode truncations M.

Finally, it is worth noting that solutions with $M = 20$ are sufficient to rigorously describe the stiff impacts considered. This is coherent with the general presupposition that the modal stiffness of the highest considered beam mode $m_M \omega_M^2$ must be somewhat larger than the impact stiffness k_i. In this particular case, the dimensionless beam stiffness $m_{20}\omega_{20}^2 = 1.23 \times 10^5$, while the dimensionless impact stiffness $k_i = 10^5$.

4.3 Summary

The contents in this chapter are summarized by the following points:

→ A Galerkin formulation allowing the spatial discretization of a continuous nonlinear model of a flexible beam in confined flow was presented. The motion of a flexible beam was described in terms of its modes of vibration while the flow velocity and pressure fields in each channel were expanded in terms of a series of Chebyshev polynomials. The tau-variant of the Galerkin approach enabled the enforcement of the nonlinear boundary conditions in a well-posed manner.

→ The proposed approach led to a purely time-dependent system of nonlinear DAEs of index-2 and presented an elegant framework that can be used for a comprehensive study of the nonlinear dynamics of these FSI systems using tools for bifurcation analysis (harmonic balance method, continuation).

→ Comparisons with results from the previous analytical formulation validated the current approach and allowed us to assess the convergence properties and model reduction capacities of the present formulation, in the context of both linear stability analysis and the calculation of LCOs.

→ The presented convergence studies suggest that, even in the presence of strong nonlinearities stemming from beam-wall impacts, LCOs can be accurately represented using relatively low orders of truncation for the flow variables. In sum, results indicate that the orders of truncation for the expansion of flow variables should be sufficient to accompany the *dominant* beam motion. In many realistic scenarios (with mass-ratios $M^* < 2$), a truncation of $N \leq 5$ for the flow variables with only two or three beam modes will generally suffice for an accurate description of the LCOs.

→ Results suggest that even in the presence of stiff impacts, lower orders truncation of beam modes may, at least in some cases, not alter the overall oscillation pattern of the LCO, and still provide fair approximations. That is, despite the presence of intermittent impacts, the fluid-structure interaction continues to play a dominant role in the fluttering dynamics.

→ The generic methodology presented here can also be adapted to different systems in the field of fluid-structure interaction, providing compact time-dependent formulations for nonlinear analysis.

Chapter 5

Bifurcation analysis

In this chapter we provide an initial impulse for a comprehensive nonlinear study of fluid-structure interaction problems dealing with cantilever beams subject to axial flow, using methods for the continuation of periodic solutions and bifurcation analysis. We consider a one-dimensional problem, where a cantilevered beam is treated in a modal framework and the surrounding flow is modelled by bulk-flow equations. The coupled system is discretized in space and time via Galerkin procedures (modal, Tau and harmonic balance) and the continuation of periodic solutions is achieved using the asymptotic numerical method. The question of hysteresis and sub-critical bifurcations is discussed in depth and, additionally, a numerical method for an “augmented” linear stability analysis is proposed, allowing the continuation of Hopf bifurcation branches, including their sub- or super-critical nature. The same method, based on constrained continuation, also allows for the prediction of grazing boundaries, i.e. frontier separating regions with and without intermittent impacts. The nonlinear dynamics are explored with respect to various dimensionless parameters and results illustrate a large variety of nonlinear behavior including: internal resonances, regions with multiple oscillatory solutions, torus bifurcations and associated quasi-periodic motions, amongst others. Aside from providing novel insights into the physics of fluttering beams and suggesting news avenues of research, is it hoped that the methods and results presented here can stimulate similar studies in the field of flow-induced vibrations.

5.1 Method for the numerical continuation of periodic solutions

Contrary to previously derived analytical formulation (Tosi & Colonious, 2019) (Soares et al., 2022), the Galerkin approach presented in the last chapter allows us to discretize the continuous 1-D problem into a set of nonlinear time-dependent equations with constant spatial operators. This makes it compatible for use in algorithms for the continuation of periodic solutions. As opposed to time-domain simulations, bifurcation analysis can provide a much broader view of the emerging limit-cycle oscillations (LCO), and how they vary as a function of specific control parameters.

In this thesis work we have used the open-source software Manlab 4.0 (Manlab: An interactive path-following and bifurcation analysis software, s.d.) which combines the Harmonic Balance Method (HBM) for the time-discretization of the dynamical system with the Asymptotic Numerical Method (ANM) for the numerical continuation of the solution path. This software presents an efficient computational tool for the continuation of periodic solutions with respect to a control parameter, as well as their stability. Here we present only a brief explanation of the general continuation procedure used, but the interested reader can find more detailed descriptions in (Guillot, 2020) (Guillot et al., 2019) (Guillot et al., 2020).

5.1.1 Harmonic Balance Method

The HBM is an efficient method for computing the periodic solutions of a smooth dynamical system (Krack & Gross, 2019), and it consist in expanding a T -periodic solution $\mathbf{g}(t)$ of a generic ODE/DAE system in the form of a Fourier series, truncated to H harmonics,

$$\mathbf{g}(t) = \sum_{h=-H}^{H} \mathbf{g}^{(h)} e^{\mathrm{j}h\omega t} = \mathbf{g}^{(0)} + \sum_{h=1}^{H} (\mathbf{g}_c^{(h)} \cos(h\omega t) + \mathbf{g}_s^{(h)} \sin(h\omega t)) \tag{5.1}$$

where the angular frequency of oscillation is $\omega = 2\pi/T$. After the appropriate Galerkin projection, the original ODE/DAE system of size N is then converted into an algebraic system of size $N(2H+1)$.

Additionally, for autonomous systems as is the case of the model studied here, the angular frequency ω of the periodic solution is not known *a-priori*. That is, if $t \mapsto \mathbf{g}(t)$ is a periodic solution, then for all $\varphi \in \mathbb{R}$, $t \mapsto \mathbf{g}(t+\varphi)$ is also a periodic solution. To remove this phase invariance and account for the unknown ω, a so-called *phase equation* must be added to the algebraic system. For example, a commonly used condition is to assume a specific variable, say the first component $\mathbf{g}_1(t)$ of $\mathbf{g}(t)$, has a null derivative at $t = 0$, leading to

$$\sum_{h=-H}^{H} (ih\omega)\mathbf{g}_1^{(h)} = 0 \tag{5.2}$$

5.1.2 Asymptotic Numerical Method

The ANM is a continuation technique based on a high-order Taylor series expansions of the unknowns $\mathbf{g}(t)$ with respect to a control parameter λ (Cochelin, 1994). The solution branches are computed in a step-by-step manner, as in classical predictor-corrector schemes (Seydel, 1994), but because the accuracy of the high-order Taylor expansion is high, generally no correction is needed. Additionally, it provides a continuous description of the solution branch and also allows for the detection of bifurcations points automatically (Cochelin & Medale, 2013). Consider the algebraic system

$$\mathbf{R}(\mathbf{g},\lambda)=0 \tag{5.3}$$

where $\mathbf{g}\in\mathbb{R}^N$ is a vector of unknowns and $\lambda\in\mathbb{R}$ is a control parameter, and $\mathbf{R}:\mathbb{R}^N$ is a real smooth function. Let $\mathbf{G}_0=(\mathbf{g}_0,\lambda_0)$ be a regular solution of Eq. (5.3), and $\mathbf{G}_1=(\mathbf{g}_1,\lambda_1)$ be a unitary tangent vector at point $\mathbf{G}_0$. Then, a pseudo-arc length parameter a can be introduced as

$$a=(\mathbf{g}-\mathbf{g}_0)\cdot\mathbf{g}+(\lambda-\lambda_0)\cdot\lambda=(\mathbf{G}-\mathbf{G}_0)\cdot\mathbf{G}_1 \tag{5.4}$$

Note that, the definition of a (5.4) serves as a closing equation for system (5.3). That is, together with the phase equation (5.2), we obtain a determined system with $N+2$ equations for the $N+2$ variables $(\mathbf{g},\omega,\lambda)$. Then the search for a solution branch around $\mathbf{G}_0$ as an analytic function of a is given by the Taylor series expansion

$$\mathbf{G}(a)=\mathbf{G}_0+a\mathbf{G}_1+a^2\mathbf{G}_2+a^3\mathbf{G}_3+\ldots \tag{5.5}$$

The expansion (5.5) is replaced in Eq. (5.3) leading to

$$\mathbf{R}(\mathbf{G}(a))=\mathbf{R}(\mathbf{G}_0)+a\mathbf{R}_1+a^2\mathbf{R}_2+a^3\mathbf{R}_3+\ldots \tag{5.6}$$

where, truncated to an order p, we get

$$\begin{aligned}
\mathbf{R}_1 &= \left.\frac{\partial\mathbf{R}}{\partial a}\right|_{a=0} = \frac{\partial\mathbf{R}}{\partial\mathbf{G}}\mathbf{G}_1\\
\mathbf{R}_2 &= \left.\frac{1}{2}\frac{\partial^2\mathbf{R}}{\partial a^2}\right|_{a=0} = \frac{\partial\mathbf{R}}{\partial\mathbf{G}}\mathbf{G}_2-\mathbf{F}_2(\mathbf{G}_1)\\
\mathbf{R}_3 &= \left.\frac{1}{3!}\frac{\partial^3\mathbf{R}}{\partial a^3}\right|_{a=0} = \frac{\partial\mathbf{R}}{\partial\mathbf{G}}\mathbf{G}_3-\mathbf{F}_3(\mathbf{G}_1,\mathbf{G}_2)\\
&\vdots\\
\mathbf{R}_p &= \left.\frac{1}{p!}\frac{\partial^p\mathbf{R}}{\partial a^p}\right|_{a=0} = \frac{\partial\mathbf{R}}{\partial\mathbf{G}}\mathbf{G}_p-\mathbf{F}_p(\mathbf{G}_1,\ldots\mathbf{G}_{p-1})
\end{aligned} \tag{5.7}$$

with $\mathbf{F}_k$ being functions that depend only on previously computed terms in the series. Note that all equations in (5.7) share the same matrix to be inverted (i.e. the Jacobian at point $\mathbf{G}_0$). When the series (5.5) is computed up to a high-order p (here taken as 20), a working domain $[0,a_{\max}]$ can be defined as a function of a chosen residual tolerance ε. Assuming the approximation $\mathbf{R}(\mathbf{G}(a))-\mathbf{R}(\mathbf{G}(0)=a^{p+1}\mathbf{R}_{p+1}$, this leads to

$$a_{\max}=\left(\frac{\varepsilon}{\left\|\mathbf{R}_{p+1}\right\|}\right)^{\frac{1}{p+1}} \tag{5.8}$$

Finally, an end point of each continuation step is computed $\mathbf{G}(a_{\max})$, which generally needs no correction, and serves as a starting point for the next continuation step.

Additionally, in the latest version of Manlab (4.0) a quadratic formalism is used that allows for the direct computation of the Jacobian matrix and the coefficients of the Taylor series (Guillot et al., 2019). This formalism is based on the definition of auxiliar variables (and equations) such that the augmented system contains only quadratic nonlinearities. Nevertheless, it can also deal with transcendental functions ($\sin$, $\tan$, $\exp$, etc.), as described in (Karkar et al., 2013). This leads to an extremely efficient numerical tool for the continuation of periodic solutions, as well as their stability, using Hill's method (Guillot et al., 2020).

5.2 On the question of hysteresis and sub-critical bifurcations

One of the most relevant open questions in the field of flow induced vibrations is related to the nature of the Hopf bifurcations (HB) they encounter. More specifically, numerous experiments (Aurégan & Depollier, 1995) (Tang & Païdoussis, 2007) (Jankee & Ganapathisubramani, 2022) (Eloy et al., 2012) of fluttering cantilevered plates (or flags) under axial flow have shown the existence of bi-stable configurations, whereby under the same flow conditions a flexible membrane can be either oscillating (unstable equilibrium – periodic motion) or static (stable equilibrium). This leads to a hysteresis phenomenon whereby plates initially at rest will start oscillating at a specific critical velocity U_{c1}, while the same plate initially fluttering, will stop oscillating at a different critical velocity U_{c2}, where $U_{c2} < U_{c1}$. These observations suggest the existence of a sub-critical Hopf bifurcation and highlight the importance of initial conditions and/or the presence of external perturbations in the system. Understanding the physical nature of this phenomena has important practical implications as commonly used linear models will often predict non-oscillating stable regimes in configurations where oscillating ones co-exist, and can eventually arise.

The fact that the plethora of previously developed models are, for the most part, unable to predict bistable behaviour (see for example the interesting discussion in sections 3.2 and 3.4 of (Tang & Paidoussis, 2007)), has led to an extensive discussion in the literature for the last decades. By and large, the most common models found in literature use linearized equations of motion and are, by default, unable to capture eventual bistable behaviour. However, several attempts have been made to characterise the parametric-regions in which bistable behaviour occurs using experiments (Jankee & Ganapathisubramani, 2022) (Gallegos & Sharmaa, 2019) and, in fewer cases, temporal simulations using nonlinear models (Eloy et al., 2012) (Tang & Païdoussis, 2007). However, the general trend is that models often largely under-estimate the width of the hysteresis loop $(U_{c1} - U_{c2})/U_{c1}$. This discrepancy has been attributed to flow nonlinear effects and viscosity, structural damping, unaccounted three-dimensional effects (either flow effects or 3-D plate deflections) as well as undesired flatness defects. Eloy et al. (2008) have reported that plates with larger aspect ratios (width to length) lead to larger hysteresis loops and argued that, in ideal two-dimensional plates (i.e. beams, as assumed in most models), the Hopf bifurcation would be super-critical. More recently, the experimental results of Jankee and Barathram (2022) suggested that the existence of hysteresis loops are impervious to the confinement ratio $H^* = (H_1 + H_2)/L$. Nevertheless, these systems generally depend on many dimensionless parameters and hence, the parametric-regions explored by experimental studies are often limited, and definite conclusions are not easily attained. In the following sections we present some modelling results and analysis that will hopefully clarify some of the aspects discussed above.

5.2.1 Constrained continuation and an "augmented" linear stability analysis

When studying the dynamics of flexible structures under axial flow, the linear stability analysis of the system is often the primary information to extract, as it allows us to distinguish between linearly stable equilibria where no motion occurs, and unstable ones where flutter oscillations or divergence arise. For this, the equations of motion are linearized (as done in (Soares et al., 2023) for the present model), and the eigenvalues of the linearized system are used to distinguish linearly stable/unstable equilibrium. Essentially, this allows us to identify Hopf bifurcations (when the eigenvalues of the coupled system have a null real part) and draw linear stability maps in multi-parameter spaces. A typical result is shown in Figure 5.1-(a), where the stability boundaries of the equilibrium solution in the $M^* - U^*$ plane are shown for a symmetric configuration with constant channel heights $H_1(x) = H_2(x) = H_1$ and fixed dimensionless parameters $H^* = 0.1$, $\zeta_n = 0.5\%$ and $f = 0$ (inviscid flow). Note that continuation methods, as the one described in section 5.1.2, can also be used to calculate branches of Hopf bifurcations by adding constraint equations that define the HB (see for example the method described in (Guillot, 2020)).

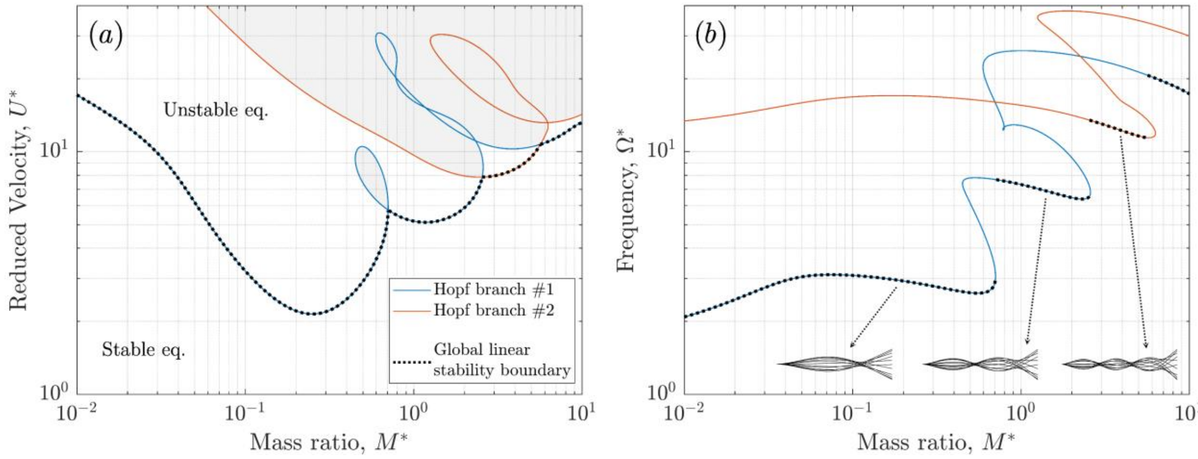

Figure 5.1 – Linear stability map for a system with constant symmetric channels and fixed parameters parameters $H^* = 0.1$, $\zeta_n = 0.5\%$ and $f = 0$: (a) Hopf bifurcation branches and global linear stability boundary in the $M^* - U^*$ plane; (b) corresponding dimensionless critical frequencies $\Omega^* = \omega^* / \omega_0$ of the neutrally stable modes. The light grey areas in (a) indicate that multiple eigenvalues of the linearized system have positive real parts. The neutrally stable mode shapes are illustrated at the bottom of (b) for the first three steps of the "cascade".

We notice there are two Hopf bifurcation branches whose combination forms a global linear stability boundary, i.e. the typical "cascading" frontier commonly found in literature. In this boundary, each step in the "cascade" corresponds to a change of shape of the primary unstable mode, as illustrated in the bottom of Figure 5.1-(b). Note as well that there are regions in the $M^* - U^*$ plane in which more than one eigenvalue of the system have positive real parts suggesting that, in these regions (in light grey), multiple periodic solutions can co-exist. The nature of the nonlinear behavior occurring in these regions will be discussed in a later section.

We start by focusing on the post-critical behavior found for relatively low mass-ratios. Figure 5.2 shows the bifurcation diagrams at constant mass-ratios: (a) $M^* = 0.075$ and (b) $M^* = 0.2$. For $M^* = 0.2$, we see a super-critical bifurcation, where a stable branch of periodic solutions stems from the HB. On the other hand, for $M^* = 0.075$ the HB is sub-critical as the emerging branch of periodic solutions is unstable. As usual in this type of sub-critical bifurcations, the solution branch later stabilizes through a fold bifurcation (FB) at a lower velocity. This type of sub-critical HB is likely the best explanation for the hysteresis effect commonly observed in experiments.

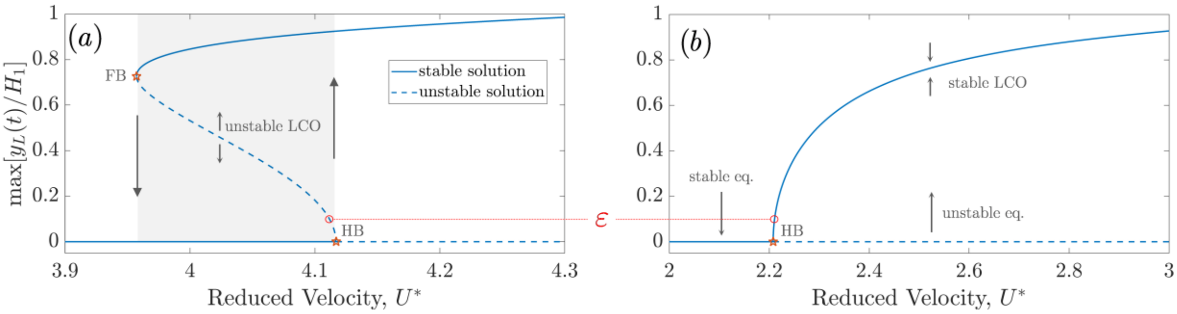

Figure 5.2 – Bifurcation diagrams of (a) a sub-critical HB at $M^* = 0.075$ and (b) a super-critical HB at $M^* = 0.2$. The light grey area in (a) corresponds to the bi-stable region where hysteresis loops will take place.

Even though linear stability analysis is, by default, unable to distinguish these two types of bifurcations, here we propose a method to calculate an "augmented" linear stability analysis. The general idea is similar to performing continuation of a Hopf bifurcation branch, but instead of adding a constraint that defines the Hopf bifurcation, we add a constraint that fixes the amplitude of oscillation of a limit-cycle. Then, if we fix the amplitude of the oscillation to a small value ε (as qualitatively illustrated in Figure 5.2 , we will effectively follow a branch of periodic solutions that is arbitrarily close to the HB branch. More importantly however, we are then able to access their stability and hence distinguish between super-critical and sub-critical bifurcations. Furthermore, since small amplitude periodic solutions are very weakly nonlinear (motion is nearly sinusoidal), the harmonic truncation H can be set to very low values (typically $2 \le H \le 3$ will suffice), leading to very fast computations.

In systems with cantilevered beams, maximal displacement during a limit-cycle oscillation will generally occur at the beam-tip $(x = 1)$. Hence, we add to our system an equation defining the physical displacement of the beam-tip

$$y_L(t) = \sum_{m=1}^{M} \phi_m(1) q_m(t) \tag{5.9}$$

Subsequently, we define our phase equation (5.2) such that the beam-tip velocity is zero at the beginning of the limit-cycle $\dot{y}_L(t=0) = 0$, i.e. beam-tip displacement is locally maximal (or minimal) at $t = 0$. Note that, at low amplitudes, oscillations will be nearly sinusoidal, and the question of complex waveforms with multiple local maxima is not posed. Then, using the harmonic balance method, the beam-tip displacement is decomposed into

$$y_L(t) = \sum_{h=1}^{H} \left(a_h \cos(h\omega t) + b_h \sin(h\omega t)\right) \tag{5.10}$$

Since at $t = 0$ the trigonometric terms reduce to $\cos(h\omega t) = 1$ and $\sin(h\omega t) = 0$, we can then formulate a constraint equation that fixes the maximal amplitude of the beam-tip during a LCO to a small value ε by simply defining

$$y_L(0) = \sum_{h=1}^{H} a_h = \varepsilon \tag{5.11}$$

Naturally, this extra equation allows us to relax another parameter of the system and hence proceed with the continuation in a two-dimensional parameter space, like the $M^* - U^*$ plane as shown in the previous example. It is worth noting that equation (5.11) does not distinguish between a maximum and minimum. In a symmetric system both (symmetric) branches stemming from the Hopf bifurcation (maximum and minimum) will yield similar results. Nevertheless, for asymmetric configurations, using a solution with a maximum at $t = 0$ will suffice to initiate the continuation procedure.

5.2.2 "Augmented" linear stability analysis of a two-mode system

To examine the nature of the sub/super-critical HB and how they vary as a function of different parameters of the system, here we present some results for a simplified configuration, considering a beam with only two *in-vacuo* modes, $M = 2$. This allows us to bypass more complex behavior that arises when several modes are taken into account, as will be seen later in this chapter. Nevertheless, this assumption is deemed valid for relatively low mass-ratios M^*, where the main fluttering instability is dominated by the dynamics of the first two *in-vacuo* beam modes. In most applications in air, this will generally suffice.

In the following sub-sections, the method for the "augmented" linear stability described earlier was used to calculate the linear stability boundaries and their sub/super-critical character as a function of various dimensionless parameters. Throughout this section, the constraint amplitude was fixed at $\varepsilon/H_1 = 0.01$, the flow expansions truncated at $N = 8$ and the Fourier expansions from the HBM were truncated at $H = 5$.

The effect of confinement on the stability boundaries of a cantilevered beam in confined flow was studied by Guo & Païdoussis (2000) and Shoele & Mittal (2016) using inviscid linearized flow equations, as well as in the work of Cisonni et al. (2017) using a nonlinear 2-D viscous CFD model. All studies conclude that narrower confinements will have a destabilizing effect, at least for heavier beams (lower M^*). Additionally, results from the 2-D viscous model (Cisonni et al., 2017) underline how confinement will also affect viscous related forces.

Here, we start by examining the simplest case, assuming inviscid flow $(f = 0)$ in a symmetric configuration. The modal damping is assumed equal for both beam modes at $\zeta_1 = \zeta_2 = 0.5\%$ and the exit pressure-loss coefficient is set to $K_L = 1$. Figure 5.3 shows the resulting linear stability boundaries in the $M^* - U^*$ plane for various confinement ratios H^*, as well as their corresponding critical dimensionless frequencies $\Omega^* = \Omega_0/\omega_0$, where Ω_0 is the frequency of the limit-cycle oscillation. The solid and dotted lines correspond to super-critical and sub-critical Hopf bifurcations, respectively, while the circles correspond to Bautin bifurcations (codimension-2 bifurcation points separating sub- from super-critical behavior along the Hopf bifurcation branch).

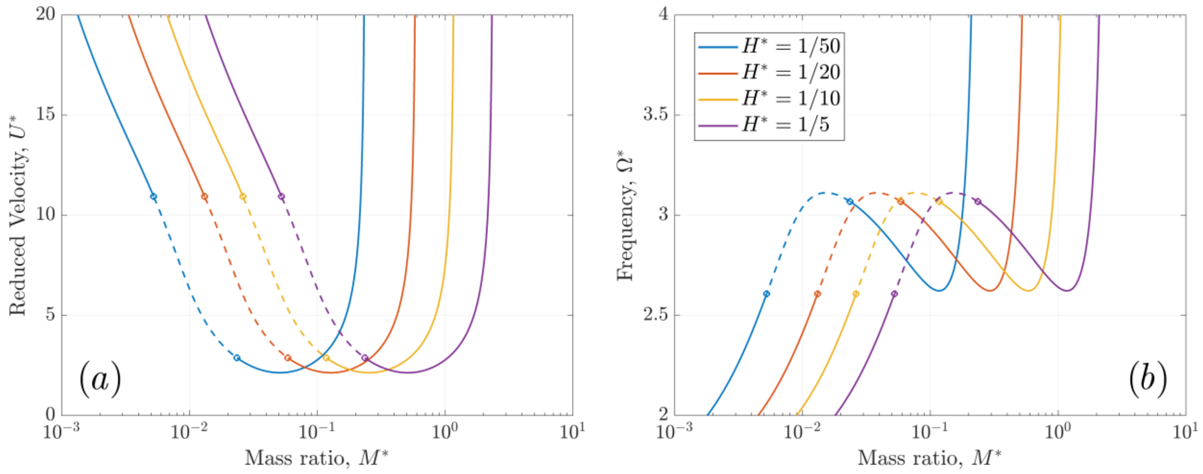

Figure 5.3 – Effect of confinement ratio H^* on (a) the linear stability boundaries in the $M^* - U^*$ plane and (b) corresponding frequencies of oscillation. Solid and dotted lines correspond to super-critical and sub-critical HB, respectively while the circles denote Bautin bifurcations.

Firstly, note that since we have considered a system with only two beam modes ($M = 2$), the stability boundaries in Figure 5.3-(a) show only one "dip", corresponding to the first step in the "cascade" of Figure 5.1. Overall, the results in Figure 5.3, show that the stability boundaries do not change qualitatively, and simply shift towards lower mass-ratios M^* as the confinement H^* narrows. Effectively, according to our simplified model, a narrower confinement serves simply to increase the inertial effects of the fluid, i.e. decreasing the confinement ratio H^* will have the same effect as increasing the density of the fluid ρ. In fact, for the inviscid case ($f = 0$) results collapse if we consider the compound dimensionless parameter M^*/H^*. This conclusion is in general agreement with results from previous models (Shoele & Mittal, 2016). However, the more complete 2-D viscous model found in (Cisonni et al., 2017) also predicts a slight overall lowering of the stability boundary when confinement is decreased, which is not captured by the current 1-D model. Nevertheless, this effect is secondary and the added flow inertia remains the dominant effect caused by confinement. Additionally, it must be noted that the bulk-flow equations used here assume small-to-moderate channel heights and results for larger H^* do not converge to the unconfined (open flow) case. Comparisons to a 2-D viscous CFD model shown in (Soares et al., 2022), have suggested a range of validity for the current model at approximately $H^* < 1/6$. Presumably, when $H^* > 1/6$, two-dimensional flow effects became non-negligible and the stability boundaries from the 1-D model gradually diverge from those of the reference 2-D model.

Finally, we notice that sub-critical bifurcations occur only in a particular region of the stability boundary, at relatively low compound mass-ratios, i.e. $0.25 < M^*/H^* < 1.1$. These results are in agreement with the conclusions from a recent experimental study (Jankee & Ganapathisubramani, 2022) which measured the effect of the mass and confinement ratios on the observed hysteretic behavior, and suggest the *existence* of hysteresis is impervious to the effect of confinement.

Furthermore, the region of M^* where the model predicts sub-critical bifurcations, agrees quantitatively with experimental observations (e.g. see Fig.7 on reference (Jankee & Ganapathisubramani, 2022)).

We now examine the effect of the structural damping ζ_n. Once again, we start by assuming inviscid flow $(f = 0)$ and uniform structural damping $\zeta_1 = \zeta_2$. Here we fix the confinement ratio to $H^* = 1/10$ and the exit-loss coefficient to $K_L = 1$. Figure 5.4 shows the linear stability boundaries in the $M^* - U^*$ plane for different values of ζ_n, as well as their corresponding frequencies.

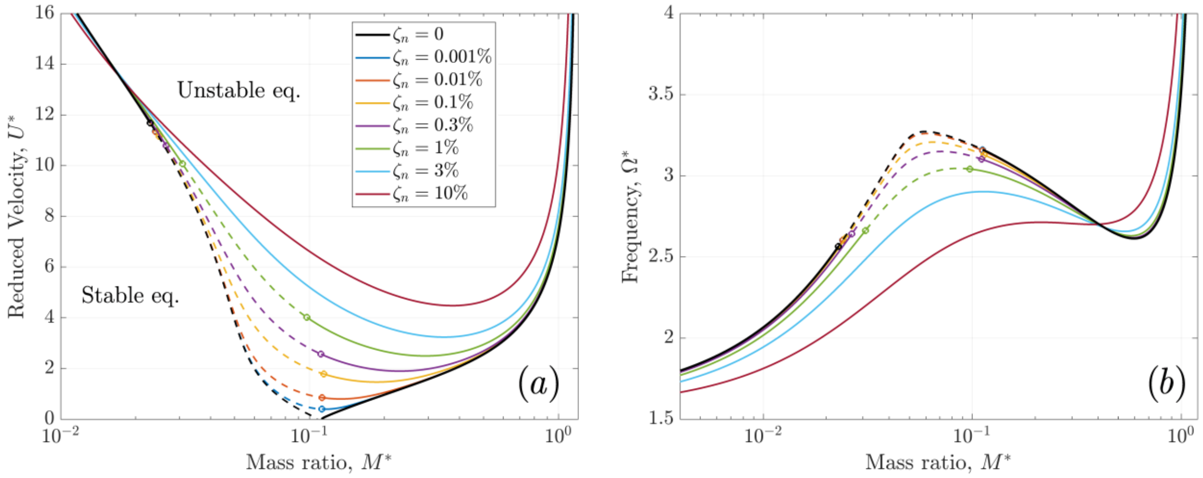

Figure 5.4 - Effect of structural damping ζ_n on (a) the linear stability boundaries in the $M^* - U^*$ plane and (b) corresponding frequencies of oscillation, in a symmetric system without frictional losses $(f = 0)$, and confinement $H^* = 1/10$. Solid and dotted lines correspond to super-critical and sub-critical HB, respectively while the circles are Bautin bifurcations.

Overall, results in Figure 5.4 show that larger structural damping will stabilize the system, as stability boundaries are pushed towards larger velocities when modal damping ζ_n is increased. Furthermore, we notice that the region where sub-critical bifurcations occur does not change significantly for relatively low damping $(\zeta_n < 0.3\%)$, remaining approximately between $0.25 < M^*/H^* < 1.1$. However, for larger damping $(\zeta_n = 1\%)$ we notice the sub-critical region narrows and finally, for highly damped beams $(\zeta_n > 3\%)$, it disappears completely, and bifurcations are super-critical for all M^*/H^*. This indicates that structural damping not only stabilises the system but also suppresses the occurrence of hysteresis.

Notably, we observe that, in the absence of structural damping $\zeta_n = 0$, the model predicts a vanishingly small critical velocity (!) at a specific singular point $M^*/H^* \approx 1.1$. This result is clearly unrealistic and stems from the fact that no structural nor flow dissipation is taken into account. However surprising, similar results were obtained by Guo & Païdoussis in (2000) when considering a conservative beam in inviscid flow. This indicates that, in the absence of dissipative terms inside the domain, a specific combination of mass and confinement ratios (M^*, H^*) will generate a naturally unstable (fluid-beam) coupled mode, where the irreversible energy transfer (from flow to structure) is unopposed. However, if either structural ζ_n or flow dissipation f are non-zero, finite critical velocities are obtained. Moreover, notice that this region of mass ratios also corresponds to the transitions between sub- and super-critical HB (Bautin bifurcations), both for conservative and nonconservative beams.

To provide a clearer perspective on the nature of the unstable fluttering beam, Figure 5.5 illustrates the contribution of each *in-vacuo* beam mode in terms of its phase difference ϕ and its peak-amplitude ratio A_2/A_1, where $A_m = \max[q_m(t)]$. Additionally, the motion of the beam is illustrated for several example configurations M^* along the stability boundary.

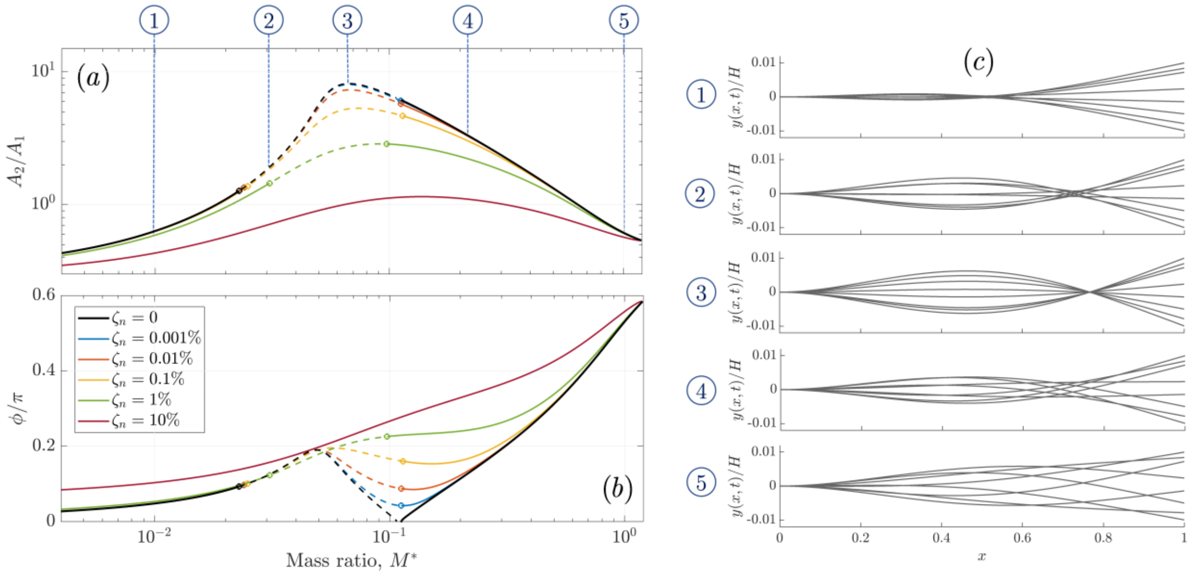

Figure 5.5 – Relative contribution of each in-vacuo beam mode in the unstable motion in terms of (a) the peak-amplitude ratio A_2/A_1 and (b) their phase difference; (c) illustrates the beam motion for various points (1-5) along the stability boundary for the conservative case $\zeta_n = 0$.

As already stated by many previous studies, the flutter instability of a cantilevered beam occurs only if at least two *in-vacuo* beam modes are considered. Figure 5.5-(a) illustrates this point as the amplitude ratio never converges to either zero or infinity, underlining that the coupling between the two *in-vacuo* beam modes is essential to the fluttering mechanism. We also note that, depending on the mass-ratio M^*, the (fluid-coupled) unstable mode is composed of different contributions from the two *in-vacuo* beam modes. For very small or very large mass ratios, the contribution of the 1st beam mode dominates, moving nearly in-phase ($\phi \sim 0$) for low mass ratios, and with $\phi \sim \pi/2$ for large mass ratios, with respect to the 2nd beam mode. At these extreme mass ratios, critical velocities are very large (see Figure 5.4). On the other hand, the M^* region where reduced velocities U^* are lower (the "wells" in the $M^* - U^*$ boundaries) correspond to motions where the 2nd beam mode dominates. Note, in point 3 of Figure 5.5-(c), that the unstable coupled mode resembles almost exactly the 2nd *in-vacuo* beam mode. In these regions (minimum U^*), the two modes move nearly in phase for lightly damped beams. Additionally, for a conservative beam, the singular point with near-zero critical-velocity corresponds to an in-phase motion between the two *in-vacuo* beam modes.

We now examine the more generic case considering flow dissipation in the form of distributed frictional losses. Note that the distributed frictional term in the momentum equation (2.23) is given by $f\left(u_c^2/h_c\right)$, where f is related to the Reynolds number as illustrated in the classical Moody diagrams (Blevins, 1984). However, for vanishingly small amplitude beam motion $\left\|q_n(t)\right\| \to 0$ (as is the case of the present quasi-linear analysis), this term can be approximated by considering only its static component, that is

$$u_c^2\left(\frac{f}{h_c}\right) = u_c^2\left(\frac{f}{\dfrac{H^*}{2} \pm \displaystyle\sum_{m=1}^{M} \varphi_m(x) q_m(t)}\right) \approx u_c^2\left(\frac{2f}{H^*}\right) \tag{5.12}$$

After the Galerkin projection, this approximation leads to extra nonlinear terms in the momentum equations in each channel, given by

$$\mathbf{G}_r = \left(\frac{2f}{H^*}\right)\sum_{n=0}^{N}\sum_{s=0}^{N}\left[\int_0^1 T_n(x)T_s(x)T_r(x)w(x)dx\right]u_n(t)u_s(t) \tag{5.13}$$

At this point it becomes clear that, when including frictional terms in the flow $(f > 0)$, narrower passages (lower confinement ratios H^*) will increase the distributed pressure losses.

Figure 5.6 shows the stability boundaries in the $M^* - U^*$ plane for various friction coefficients f, in a conservative beam $(\zeta_n = 0)$.

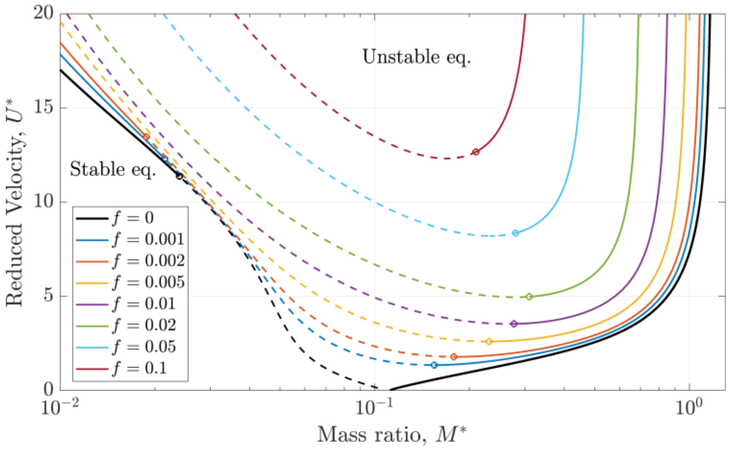

Figure 5.6 - Effect of the frictional coefficient f on the linear stability boundaries of a symmetric system with a conservative beam $(\zeta_n = 0)$ and confinement ratio $H^* = 1/10$. Solid and dotted lines correspond to super-critical and sub-critical HB, respectively while the circles are Bautin bifurcations.

Similar to the effect of the structural dissipation, larger values of the friction coefficient f will stabilize the system. On the other hand, we notice they have a significant effect on the nature of the Hopf bifurcation. As f departs from zero, the Bautin bifurcations spread apart, enlarging the regions where sub-critical bifurcations occur. For $f \geq 0.005$, all HBs at lower mass-ratios are sub-critical, and become super-critical at relatively larger mass-ratios, $0.2 < M^* < 0.3$.

5.2.3 Nonlinear analysis of hysteresis

The “augmented” linear stability analysis presented above enables the distinction between sub- and super-critical Hopf bifurcations. However, it is worth noting that hysteretic behavior is not unique to sub-critical HB, and it can also appear in super-critical ones. As an example, Figure 5.7 shows several branches of periodic solutions for a symmetric system with $H^* = 0.1$, $\zeta_n = 0.5\%$, $f = 0$, and $K_L = 1$, in terms of the normalized reduced velocity U^* / U_{crit}, where U_{crit} is the critical velocity predicted by linear stability analysis. Here two-beam modes were considered $M = 2$, the flow field expansions were truncated at $N = 10$ and the harmonic series expansion was truncated at $H = 20$.

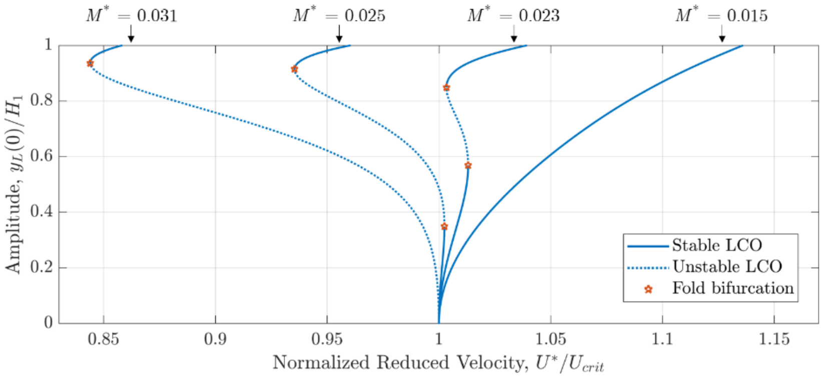

Figure 5.7 – Illustration of various cases of hysteresis: branches of periodic solutions in a symmetric system with $H^* = 0.1$, $\zeta_n = 0.5\%$, $f = 0$, $K_L = 1$, at various mass-ratios.

In Figure 5.7 we notice that super-critical bifurcations can also lead to hysteretic behaviour, as a product of two fold bifurcations. Furthermore, the minimum velocity in the branch of periodic solutions can be larger or smaller than U_{crit}. It also illustrates that the transition from sub- to super-critical HB (Bautin bifurcation) does not necessarily mean the disappearance of hysteresis. To clarify the nature of this behaviour, several branches of periodic solutions were calculated for the same parameter configuration as above. Figure 5.8 illustrates a three-dimensional bifurcation diagram where multiple solution branches (at constant M^*) are shown around the region where hysteresis is predicted.

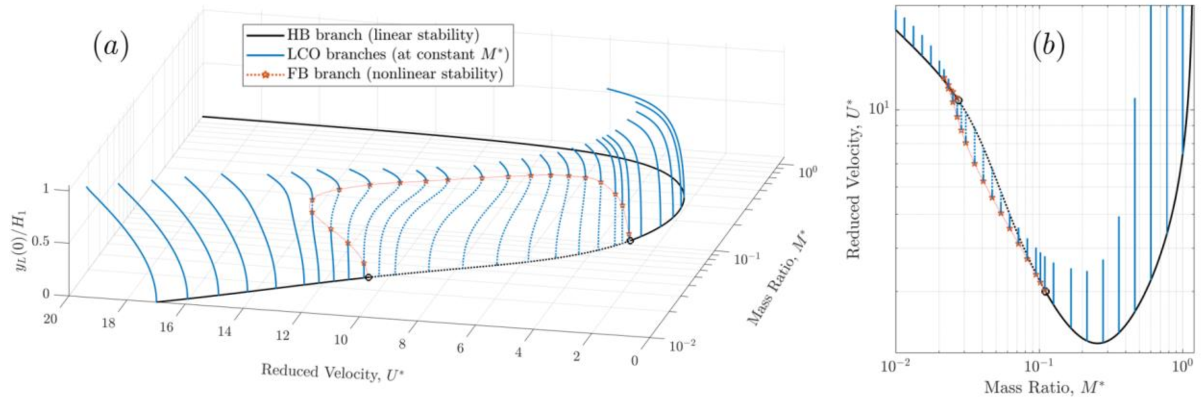

Figure 5.8 - (a) Three-dimensional view of the branches of periodic solutions (at constant M^*) stemming from the HB boundary, as well as (b) the corresponding top view ($M^* - U^*$ plane), for a symmetric system with $H^* = 0.1$, $\zeta_n = 0.5\%$, $f = 0$ and $K_L = 1$.

From Figure 5.8 is becomes clear that the Bautin bifurcations predicted in the “augmented” linear stability analysis are actually the birthing points of a fold-bifurcation branch. This FB branch travels the surface defined by the periodic solution branches and outlines a frontier separating stable from unstable periodic solutions. Depending on the particular parameter configuration, this will generate the different types of bifurcations and hysteresis loops illustrated in Figure 5.7.

It is clear that the analysis of this type of FB branch, and how it varies depending on different parameters of the system, is of paramount importance to understand and quantify the hysteresis phenomena. Even though in this work we do not conduct a detailed parametric analysis, the presented results serve as an example of potential avenues of research in the analysis of fluttering beams but also, more generally, in the field of flow-induced vibrations, where hysteresis occurs frequently in various contexts (Prasanth et al., 2011) (Colinot, 2020). Note that here, the branch of FB was not calculated directly, but interpolated from the several fold bifurcations points. However, it is worth mentioning that methods for the continuation of fold bifurcations have been developed, and can promptly be used for such type of analysis (see for example (Guillot, 2020)).

5.2.4 Hysteresis loop width

As mentioned before, one of the open questions with regard to hysteresis has to do with the discrepancy between the hysteresis loop width, $\eta = (U_{c1} - U_{c2})/U_{c1}$, measured in experiments compared to modelling predictions. Concretely, models consistently underestimate the values observed in experiments, as illustrated in Table 1.

Table 1 – Range of hysteresis loops found by several experimental and numerical studies.

Type	Study	η (%)
Experimental	(Watanabe et al., 2002)	$5-45$
	(Eloy et al., 2008)	$0-35$
	(Eloy et al. 2012)	$0-40$
	(Gallegos & Sharmaa, 2019)	$15-48$
	(Jankee & Ganapathisubramani, 2022)	$20-70$
Theoretical / Model	(Alben & Shelley, 2008)	$0-3.4$
	(Michelin et al., 2008)	4.5
	(Eloy et al., 2012)	$0-12.8$
	Current model (2023)	$0-22$

Solely from the example results shown above (Figure 5.8), assuming inviscid flow, we already notice that the current model predicts hysteresis loop widths up to $\eta = 22\%$, which fall in the same order of magnitude as the values measured experimentally. In any case, further numerical investigations are necessary to explore the behavior of the model in different parametric configurations.

As a final remark, the set of results presented here may help clarify some unanswered questions. Firstly, the present model is 1-D in nature, and hence its capacity to emulate sub-critical bifurcations and hysteresis is in contradiction with the hypothesis presented by Eloy et al. (2008), where the authors suggest the nature of the bifurcation is super-critical, but two-dimensional plate deflections (unaccounted by the models) are the cause of hysteresis. Secondly, since geometric nonlinearities in the beam are not considered, results also suggest these might not be the root cause of hysteresis. Similarly, structural dissipation has also been mentioned as a potential cause for hysteresis (Tang & Paidoussis, 2007). However, our results show that sub-critical bifurcations occur in both conservative and non-conservative beams. Moreover, our results suggest that structural dissipation will actually supress sub-critical behaviour. In sum, the simplified configurations analysed here suggest that sub-critical bifurcations and hysteresis are result of flow nonlinearities. Furthermore, even though hysteretic behaviour is observed for inviscid flow, our numerical results indicate that the inclusion of nonlinear flow dissipation will promote the occurrence of sub-critical bifurcations, once again underlying the dominant role of flow nonlinearities in the phenomena of hysteresis.

5.3 Nonlinear dynamics of a system with many beam modes

5.3.1 Calculation of grazing boundaries

It is well known from experimental studies (Aurégan & Depollier, 1995) (Gallegos & Sharmaa, 2019) (Lee, Kim, & Kim, 2021) that fluttering beams in confined flow will often lead to oscillations where the beam comes into contact with the channel walls. These systems can produce solutions both with and without intermittent impacts. Then, to provide an overview of the nonlinear behaviour of the system, it is useful to calculate a “grazing” boundary, i.e. the frontier separating periodic solutions with and without intermittent impacts. To this aim, the method presented in section 5.2.1 for the “augmented” linear stability analysis, can also be adapted for the estimation of the grazing boundary. While for the augmented linear stability analysis we add a constraint equation (5.11) that fixes the amplitude of oscillation to a arbitrarily small value ε, here we will fix the maximum beam-tip displacement to the height of the channel $H_L = H_1(1)$. That is, we replace the constraint equation (5.11) by

$$y_L(0) = \sum_{h=-H}^{H} a_h = H_L - \varepsilon \tag{5.14}$$

where an arbitrarily small value ε is subtracted from H_L, effectively representing a *near*-grazing condition. In stating this condition (5.14), we assume that contact between the beam and the channel walls will occur firstly at the beam-tip $x = 1$. Although difficult to prove in a formal sense, experimental and modelling results all suggest that the largest displacement during an LCO will happen at the beam-tip and not along the beam. Hence, when considering channels of constant height, is seems reasonable to assume that impacts will occur initially at the tip. Then, similar to what was done in section 5.2.1, we can proceed with the continuation of the near-grazing solution branches in a two-dimensional parameter space, like the usual $M^* - U^*$ plane.

For consistency, we present results for the same configuration as above, with fixed dimensionless parameters: $H^* = 0.1$, $\zeta_n = 0.5\%$, $f = 0$ and $K_L = 1$. For the spatial discretization, beam modes and the flow variable expansions were truncated at $M = 10$ and $N = 15$, respectively. Because at large amplitudes, strong nonlinearities appear, the number of harmonics were fixed at a larger number $H = 30$. This amounts to an algebraic system with approximately 5,000 variables. Figure 5.9 shows the calculated *near*-grazing boundary in the $M^* - U^*$ plane and corresponding frequencies, with $\varepsilon / H_L = 0.005$.

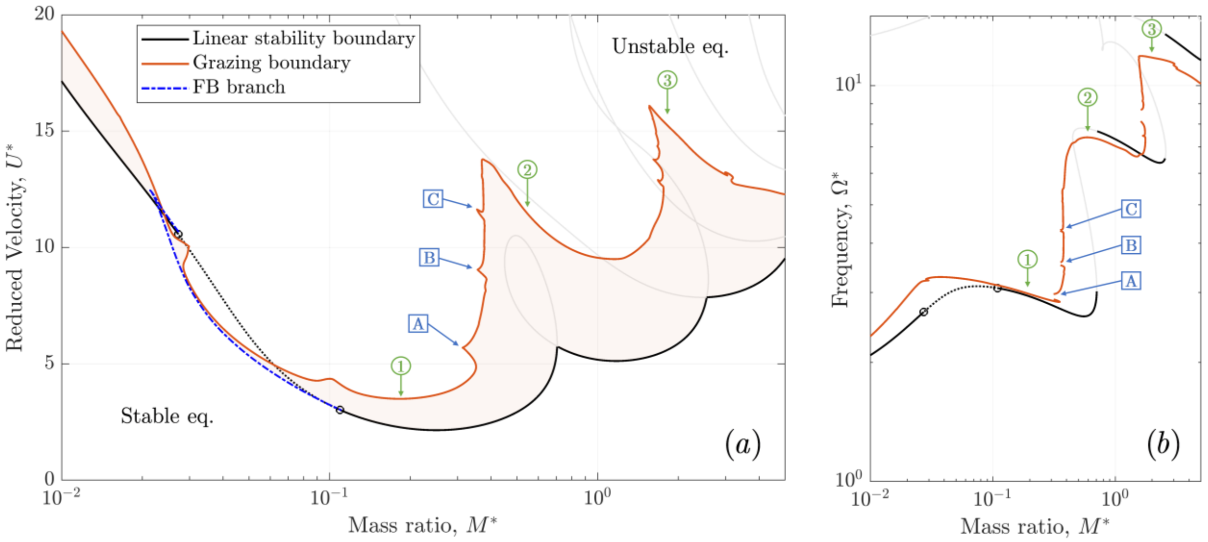

Figure 5.9 – (a) $M^* - U^*$ map illustrating the linear stability (black) and the near-grazing boundary (orange) for a symmetric system with $H^* = 0.1$, $\zeta_n = 0.5\%$, $f = 0$ and $K_L = 1$, as well as (b) its corresponding frequencies Ω^*. The blue dotted line shows the fold-bifurcation branch associated with the hysteresis region. The light orange filling describes the regions where limit

cycles without impacts will occur. The light grey curves are the Hopf bifurcation branches, as shown in Figure 5.1. Details of the solutions of the points indicated in green (1)-(3) and blue (A)-(C) are shown in Figure 5.10 and Figure 5.11, respectively.

Overall, the results in Figure 5.9-(a) indicate that at low mass-ratios (heavy beams) the regions where LCOs without impacts occur are rather narrow, and contact with the channel walls will occur shortly after the equilibrium becomes unstable. Moreover, in the sub-critical region, impacts will occur immediately after the equilibrium becomes unstable (velocities at the grazing boundary are lower than critical velocities). On the other hand, at larger mass-ratios (light beams) there are larger regions with LCOs without impacts. This is likely explained by the fact that the inertia of a heavy fluttering beam will tend to outweigh the restoring forces from the (relatively) light fluid, while lighter beams will be more easily “pushed away” from the walls by the forces of a heavy fluid. These results are coherent with those calculated earlier via temporal integrations of the analytical formulation Note however that, in this example, inviscid flow is considered, $f = 0$.

At low-mass ratios $(M^* < 0.3)$, the behaviour is similar to what was found for the simplified system (considering only 2 beam modes) presented in section 5.2.3, confirming that, for heavier beams, higher-order modes do not influence dynamics significantly (at least when impacts are not present).

The overall shape of the grazing boundary follows the same logic as the linear stability boundary, presenting a cascade-like structure, where different steps in the cascade represent changes in the primary unstable mode. To clarify, Figure 5.10 shows details of the grazing solutions at different steps of the cascade (points (1)-(3) in Figure 5.9). Similar to the results for the linear stability, the three steps of the cascade present beam motions with single-, double- or triple-neck solutions, where the first two, three and four *in-vacuo* beam modes dominate, respectively.

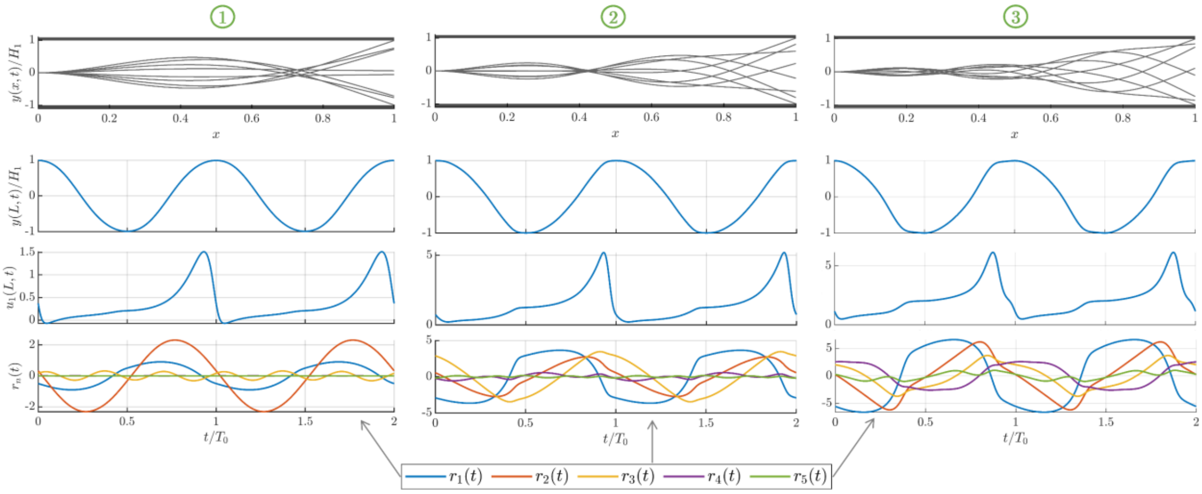

Figure 5.10 – Grazing solutions associated with different steps in the cascade (points (1)-(3) indicated in Figure 5.9). Snapshots of the beam motion (top); temporal evolution of the beam-tip displacement $y_L(t)/H_1$ (top-centre), the exit flow velocity $u_1(1,t)$ at the upper channel (bottom-centre) and the modal velocities of the first 5 beam modes (bottom). Note that the time is normalized by the period of the limit-cycle T_0, and the frequencies of the three solutions differ significantly, as seen in Figure 5.9.

However, the grazing boundary also presents some more complex behaviour, including some discontinuities at the step-transitions (e.g. points (A)-(C) indicated in Figure 5.9). To clarify, the solutions associated with points (A)-(C) are detailed in Figure 5.11.

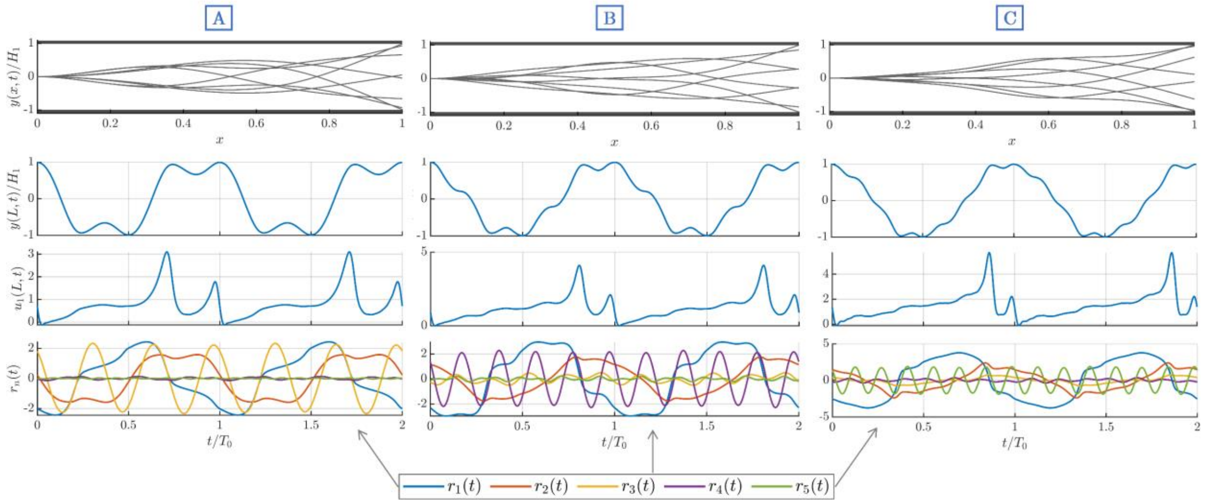

Figure 5.11 – Grazing solutions associated with different internal resonances (points (A)-(C) indicated in Figure 5.9). Snapshots of the beam motion (top); temporal evolution of the beam-tip displacement $y_L(t)/H_1$ (upper-central), the exit flow velocity $u_1(1,t)$ at the upper channel (lower-central) and the modal velocities of the first 5 beam modes (bottom).

It can be seen that these small peaks (discontinuities) effectively represent internal resonances in the system. Notice that, for point (A) the 3rd beam mode is very prominent (Figure 5.11 – bottom plot) and oscillates regularly, in a near sinusoidal fashion, at a frequency 3 times larger than the base frequency of the periodic motion Ω_0. Similarly, at points (B) and (C), the 4th and 5th beam modes oscillate at frequencies approximately 5 and 7 times the base frequency, respectively. This suggests that at these junctures, the frequency of higher-order (fluid-loaded) beam modes $\tilde{\omega}_{3,4,5}$ are close to a multiple integer of the base frequency. That is, at point (A) $\tilde{\omega}_3 \approx 3\Omega_0$, at point (B) $\tilde{\omega}_4 \approx 5\Omega_0$ and at point (C) $\tilde{\omega}_5 \approx 7\Omega_0$, leading to larger responses of higher-order modes and naturally, more complex beam motions. It is unsurprising that these internal resonances occur at the step-transitions of the cascade, since these regions are associated with an abrupt change in the frequency of the periodic solution (see Figure 5.9-(b)). Notably, at the grazing boundary, these internal resonances present solutions where the beam-tip grazes the channel walls twice during each period, as shown in Figure 5.11. Furthermore, because the system is symmetric, the spectrum of the beam motion contains only odd harmonics, and hence internal resonances occur only at odd multiples of the base frequency. Nevertheless, it is likely that an asymmetric system, where even harmonics are also present, will generate additional internal resonances.

It is also worthwhile analysing the fluid dynamics associated with the grazing solutions, represented in Figure 5.**10** and Figure 5.**11** by the exit velocity $u_1(1,t)$ in the upper channel (note that, due to symmetry, the velocities in the lower channel will be similar, with a half-period lag). As the beam-tip approaches the upper wall, the exit flow velocity increases and subsequently decreases abruptly right before the beam-tip reaches its maximum displacement. This sudden decrease in flow velocity is a product of a squeeze-like effect caused by the beam inertia on the (incompressible) fluid as well as the nonlinear flow dissipation governed by head-loss term $u|u|K_L$, and leads to local velocities close to zero, and even locally reversed flow in some cases. Once the constriction starts to widen, flow velocities are gradually restored. In the solutions presented in Figure 5.11 this process is repeated twice during each cycle.

5.3.2 Dynamics near the modal-transition region

Once the frontier separating periodic solutions with and without intermittent impacts is defined, we can now analyse in more detail the nature of the LCOs in the contactless regions. Namely, we now examine the solutions at moderate mass-ratios $(0.1 < M^* < 1)$, where the first cascade transition occurs and notably, where linear stability analysis predicts regions with multiple unstable equilibria. The 3-D plots shown in Figure 5.12 give an overview of the periodic solutions occurring in this region. Dimensionless and discretization parameters were taken as in the previous sub-section.

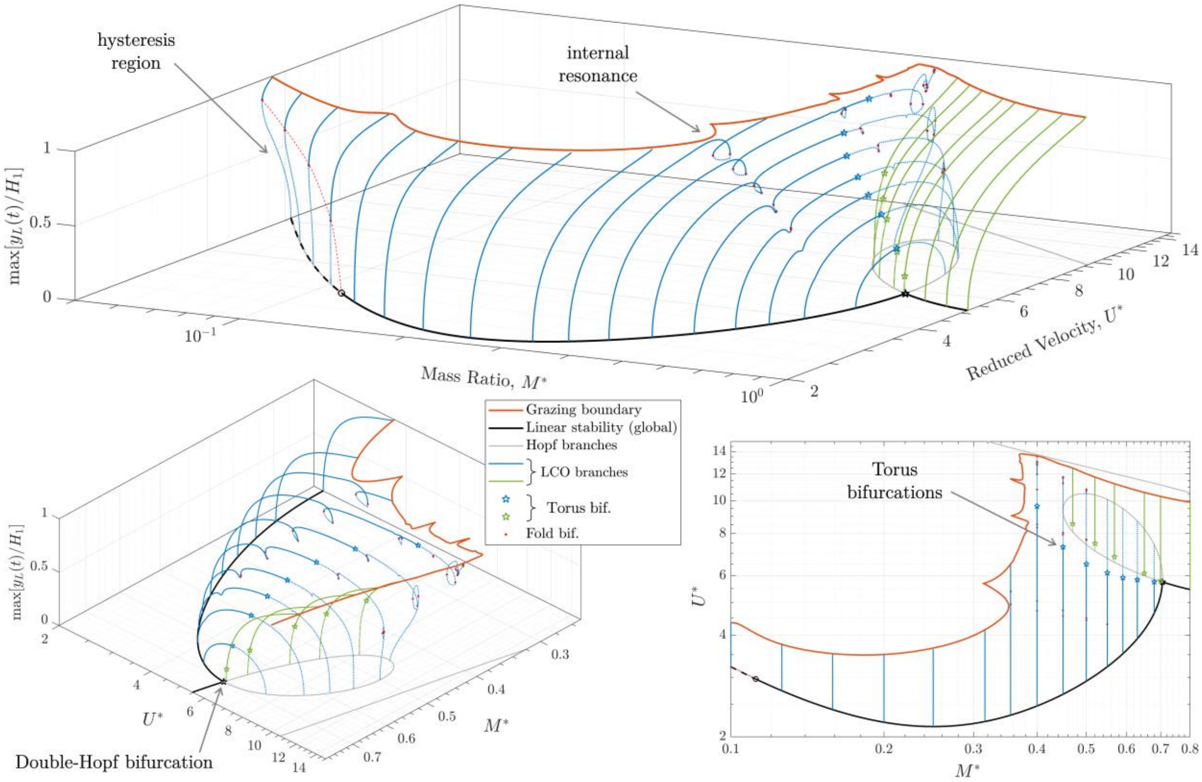

Figure 5.12 – Various perspectives of a three-dimensional bifurcation diagram showing branches of periodic solutions at constant M^* (blue and green lines) stemming from the calculated Hopf bifurcations, at low-moderate mass-ratios $(0.05 < M^* < 1)$. The black and orange lines denote the (global) linear stability and grazing boundaries, respectively.

The overview presented in Figure 5.12 shows that away from the step-transition $(0.3 < M^* < 0.7)$, periodic solutions tend to have a fairly regular pattern, simply increasing in amplitude with increasing velocity U^*, with no relevant qualitative changes. However, near the step-transitions more complex dynamical behaviour arises. These include, for example (1) loops in the solutions branches caused by internal resonances, (2) regions where multiple oscillatory solutions co-exist and (3) torus bifurcations and associated quasi-periodic solutions. In the following we examine these phenomena in more detail.

In Figure 5.12 we note several sequences of loops in the solution branches (blue), with fold bifurcations located at the turning points. As was discussed previously, these loops are associated with internal resonances of the system. As solutions come closer to the grazing boundary (where beam motion is of larger amplitude), the internal resonance loops become more pronounced. To better illustrate the phenomena, Figure 5.13 shows the distribution of mean modal energy E_m in the beam along the solution branch at constant mass-ratio $M^* = 0.4$. Note that E_m is dimensionless, normalized by the reference energy $E_0 = m_0 \omega_0^2 L^2$., and given explicitly by

$$E_m = \left(\frac{m_m}{2}\right)\left(\frac{1}{T_0}\right)\int_0^{T_0} \left(\dot{q}_m^2(t) + \omega_m^2 q_m^2(t)\right) dt \tag{5.15}$$

where $q_m(t)$ and $\dot{q}_m(t)$ can be calculated directly using the coefficients from the harmonic balance expansion.

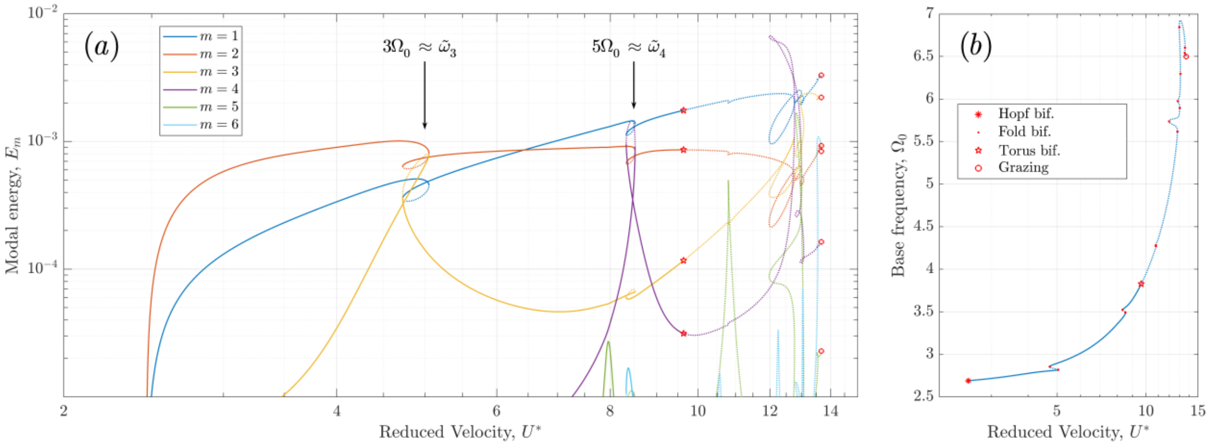

Figure 5.13 – Illustration of internal resonances. (a) Evolution of the modal energy distribution in the beam as a function of the reduced velocity U^* along the solution branch at $M^* = 0.4$; and (b) the corresponding frequency. Solid and dotted lines denote stable and unstable solutions, respectively.

We note that the underlying periodic solution is dominated by the first two beam modes (blue and red lines in Figure 5.13). As U^* increases, the frequency Ω_0 also increases and, at specific velocities, higher-order modes are locally excited. The internal resonances $\tilde{\omega}_3 / \Omega_0 = 3$ and $\tilde{\omega}_4 / \Omega_0 = 5$ are highlighted in Figure 5.13, however, many other internal resonances occur at larger velocities. Nevertheless, the periodic solution branch loses its stability through a torus bifurcation at around $U^* = 9.7$. Hence, solutions at $U^* > 9.7$ will likely lead to quasi-periodic motions (this will be discussed in detail subsequently).

Notably, Figure 5.12 illustrates the nature of the change in periodic solutions as mass-ratios pass through the cascade's step-transition. The periodic solutions where the first two beam modes are dominant (blue lines) start to decrease in amplitude as mass-ratios increases, and eventually disappear at the turning point of the Hopf branch $(M^* \approx 0.7)$. Meanwhile, a new surface of periodic solutions emerges at $M^* \approx 0.45$ (green lines), corresponding to periodic solutions where the third beam mode is dominant. Beyond the step-transition $(M^* > 0.7)$, this second surface of solutions (green) is unique. However, there are overlapping regions where both solution branches co-exist. To clarify, Figure 5.14 shows the evolution of the two solution branches as a function of the reduced velocity U^*, for a constant mass-ratio $M^* = 0.5$.

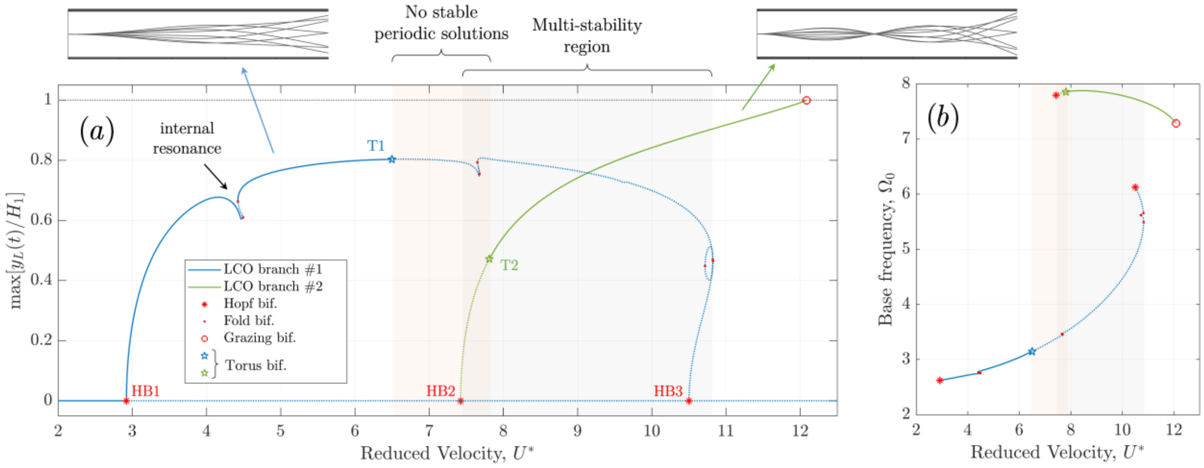

Figure 5.14 – Illustration of the mode-transition and multi-stability regions: (a) bifurcation diagram at constant mass-ratio $M^* = 0.5$, illustrating the two branches of periodic solutions with respect to the reduced velocity U^*; (b) Evolution of the base frequency associated with each solution branch. The light-orange area indicates that no stable periodic solution exists, while the light-grey area denotes that more than one solution branch exists, either stable or unstable.

Then, once the equilibrium becomes unstable, we can then identify three qualitatively different scenarios:

1. *Single stable periodic solution*: where typical (periodic) limit-cycle oscillations will arise;
2. *No stable periodic solutions*: will generally lead to quasi-periodic oscillations, i.e. motion whose spectra is composed by a linear combinations two (or more) harmonic series whose base frequencies are incommensurable;
3. *Multiple periodic solutions, stable or unstable, co-exist:* the system dynamics will be governed by initial conditions and can converge to either periodic or quasi-periodic motion.

To clarify the nature of the ensuing periodic and quasi-periodic regimes, Figure 5.15 shows details of three solutions obtained via temporal integration with $U^* = [6,\ 9,\ 7]$. Initial conditions were set at the equilibrium position (beam at rest and steady flow) and a small perturbation force was applied to induce flutter. Figure 5.15 shows the resulting periodic/quasi-periodic solutions sometime after motion stabilises.

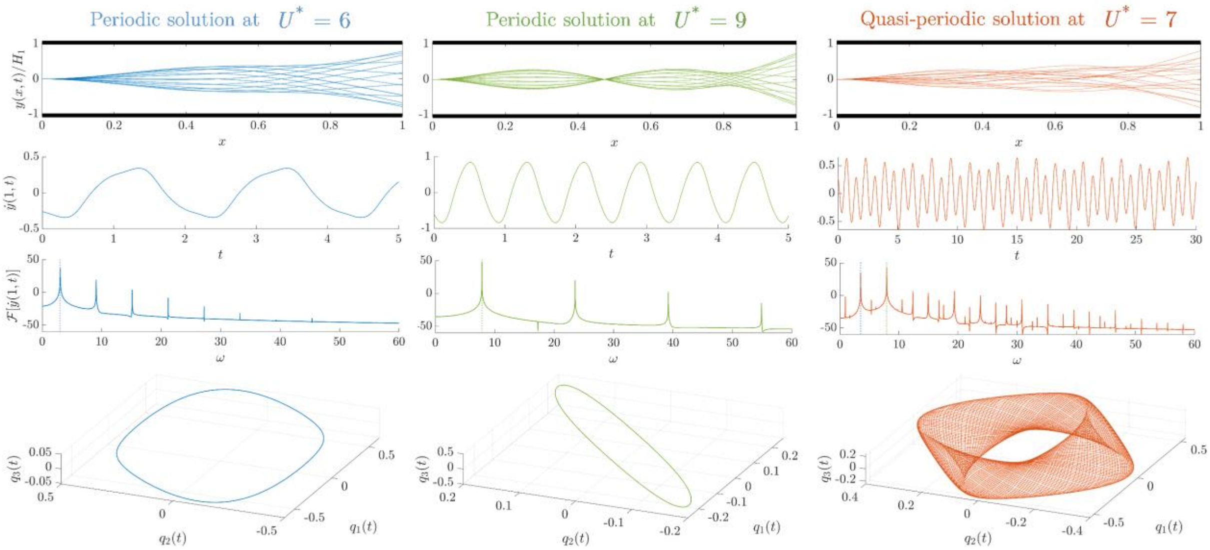

Figure 5.15 – Resulting nonlinear motions for a system with $M^* = 0.5$ and three different velocities $U^* = [6,\ 9,\ 7]$. From top to bottom: snapshots of the beam motion; temporal evolution of the beam-tip velocity $\dot{y}(1,t)$; spectra of the beam-tip velocity; 3-D phase-portrait in the modal displacement space $[q_1(t),\ q_2(t),\ q_3(t)]$.

At $U^* = 6$, since the only stable solution is periodic, the temporal simulation naturally converged to a limit cycle oscillation associated with the single-neck beam motion (blue branch in Figure 5.14). As predicted by the continuation results, its frequency of oscillation was at $\Omega_0 = 3.03$. At $U^* = 9$, the system is in a multi-stable region and the chosen initial conditions led the motion towards the stable periodic solution of the double-neck type (green branch in Figure 5.14), with a base frequency of $\Omega_0 = 7.84$. However, we constate that the dynamics are rather sensitive to initial conditions, and for example, simulations with larger amplitude perturbations also led to quasi-periodic regimes. Due to the symmetry of the system, the frequency content of both these periodic solutions contains only odd harmonics of their respective frequencies, i.e. $(2n-1)\Omega_0$. Finally, at $U^* = 7$, the system has no stable periodic solutions and temporal simulation eventually converged to a stable quasi-periodic motion. As usual, the (3D) orbit of the quasi-periodic solution does not remain in a line, as in the periodic cases, but rather in a torus (closed invariant surface). The spatial distribution of the beam motion in the quasi-periodic regime is less regular but can be roughly regarded as a combination of the single- and double-neck periodic solutions. In fact, its frequency content contains a linear combination of two base frequencies, $\Omega_1 = 3.51$ and $\Omega_1 = 7.92$, which are close to those found for the associated periodic regimes. For the quasi-periodic solutions, the spectrum of the beam-tip velocity shows peaks at

$$\omega_{n,m} = \left| \pm n\,\Omega_1 \pm m\,\Omega_2 \right| \qquad \text{for} \quad n,m = 1,2,3... \tag{5.16}$$

However, additionally, the harmonics $\omega_{n,m}$ where $(-1)^n = (-1)^m$ are null. In analogy to the lack of even harmonics in periodic solutions of symmetric systems, this condition is also a property of quasi-periodic oscillations in symmetric systems.

It is also worthwhile discussing the origin of the torus bifurcations. From Figure 5.12 it becomes evident that these stem from a double-Hopf bifurcation, i.e. the crossing point on the Hopf branch, where the critical equilibrium has two pairs of purely imaginary eigenvalues (black star in Figure 5.12). Double-Hopf (or Hopf-Hopf) bifurcations are co-dimension 2 bifurcation from which, generally, two torus branches emanate (Kuznetsov, 2004). This is illustrated clearly in Figure 5.12, where two branches evidently travel in each surface of solutions (both blue and green). Each torus bifurcation in the solution branch will generate an invariant torus on which quasi-periodic orbits will develop. This analysis brings a new perspective on the nonlinear dynamics of flexible beams in axial flow, both in confined and open flow configurations. Effectively, the discontinuities in the common cascading linear-stability boundaries represent double-Hopf bifurcations and hence, it is expected that quasi-periodic oscillations will occur near these regions of the parameter space. Note that this is the case in both confined and unconfined configurations. For example, the experimental results from Eloy et al. (2012), where the dynamics of a plate in unconfined axial flow are studied, show very similar behaviour. Figure 5.16 shows their measured critical velocities for the threshold of periodic oscillations (triangles) as well as the velocities where the fluttering motion loses periodicity (circles). Notably, the trend of the measured critical velocities for loss of periodicity compares remarkably well with the torus bifurcations shown in our numerical results (Figure 5.12).

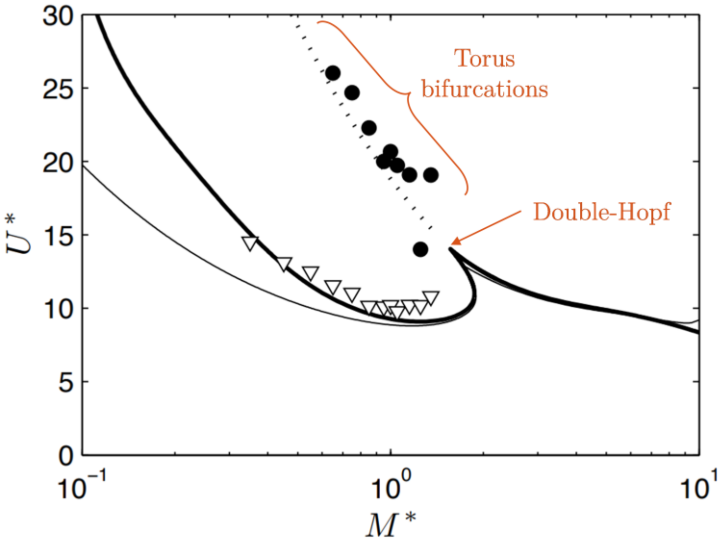

Figure 5.16 – Experimental results from Eloy et al. (2012) for a plate in unconfined axial flow. The measured critical velocities for the start of oscillations are shown by the triangles while the circles mark the loss of periodicity. The solid lines represent the Hopf bifurcations using a conservative (thin) and dissipative model (thick). The annotations in orange were appended by the present authors to the original figure in (Eloy et al., 2012).

5.4 Summary

→ The nonlinear dynamics of a flexible beam in axial flow were studied numerically using tools for the continuation of periodic solutions and bifurcation analysis. A one-dimensional model was considered, where a modal beam is surrounded by confined flow on both sides. The flow was modelled using bulk-flow equations including both localised and distributed head-losses. The system is discretized in space via Galerkin procedures and in time using the Harmonic balance method. Numerical continuation with respect to one (or multiple) system parameters is achieved using the asymptotic numerical method.

→ The question of hysteresis and sub-critical bifurcations was discussed extensively. Results suggest that flutter instabilities in such systems can be a product of both sub- and super-critical Hopf bifurcations, depending on the specific parametric configurations. Our numerical results indicate that structural damping not only stabilises the system (leading to larger critical velocities), but also tends to supress sub-critical behaviour. Even though sub-critical behaviour was found for inviscid flow, the inclusion of nonlinear flow dissipation (distributed frictional term) will promote the occurrence of sub-critical behaviour. In contrast with previous hypothesis, which attempted to explain the phenomena through structural nonlinearities, flow or structural three-dimensional effects, undesired planeity defects, etc., our results suggest that sub-criticality and hysteresis are essentially a product of flow nonlinearities.

→ A method for an "augmented" linear stability analysis was proposed, where not only Hopf bifurcation branches can be calculated with respect to two system parameters, their super-/sub-critical nature can also be easily distinguished. Essentially, the method consists in adding a constraint equation that fixes the amplitude of limit cycle oscillations to a arbitrarily small value ε . Continuation of the *near*-Hopf branch then allows the distinction between sub- and super-critical behaviour by examining the stability of the periodic solutions.

→ Grazing boundaries were also calculated, allowing the separation of parameter-regions where limit-cycle oscillations with and without impacts will occur. Our results indicate that heavier beams with tend to have narrow regions with contactless LCOs, i.e. limit-cycles with intermittent impacts between the beam and the channels walls will arise promptly after the equilibrium becomes unstable.

→ A detailed mapping of the system dynamics in the $M^* - U^*$ plane revealed a number of complex nonlinear phenomena like internal resonances, multi-stable configurations and quasi-periodic dynamics. Notably, a feature common to both open- and channel-flow configurations, is the occurrence of double-Hopf bifurcations. These represent the "modal-transitions" commonly mentioned in previous studies, where the primary unstable fluttering mode changes shape. Our results suggest that such bifurcation points also give birth to torus branches, which lead to a loss of stability of the periodic solutions and generate quasi-periodic (and potentially chaotic) dynamics.

Chapter 6

Experimental studies

The experimental part of this thesis was motivated by two distinct aspects. On one hand, we wanted to validate the simplified theoretical model and assess to what extend it is able to describe the dynamics of a real system. On the other hand, we aimed at documenting a detailed characterisation of the nonlinear behaviour of fluttering beams in confined flow, including intermittent impacts, which is not readily available in the literature. In this chapter we provide a detailed account of the design considerations and construction of the experimental apparatus along with discussions on delicate aspects of the experimental procedure that are often neglected. Stability maps, including the occurrence of hysteresis, are drawn and compared to modelling predictions. Measured results are discussed in detail through bifurcations diagrams illustrating the evolution of the measured limit-cycle oscillations (in terms of amplitude, base frequency, spectral content, etc.) as a function of the inlet flow velocity. Results are compared to the bifurcation diagrams stemming from the model using the methods detailed in the previous chapter.

6.1 Scope, aims and design considerations

The primary objective of these experimental studies is to assess to what extend the numerical results presented in previous chapters are representative of the dynamics of a real system. Contrary to many previous studies, which focused on measuring the conditions for critical (linear) stability, here we give considerable attention to the characterization of the (post-stable) nonlinear dynamics. The overall design of the experiment was aimed at recreating, to the best of our efforts, the assumptions made in the model, notably the relatively narrow confinements assumed by the bulk-flow modelling approach and the bi-dimensionality of the system (infinite spanwise dimension), which ignores torsional motions of the plate and 3-D flow effects.

A large number of experimental studies on the dynamics of cantilever beams/plates in open-flow, neglecting confinement effects, can be found in literature (Eloy et al., 2008) (Taneda, 1968) (Yu et al., 2019). A recent review by M. Païdoussis (2004), gives a detailed account of the work done in the last decades. Even though most studies focus on the conditions for critical stability, typically to validate models using linearized equations of motion, a few works have explored some aspects of the post-stable nonlinear behavior in unconfined configurations (Yu et al., 2019) (Eloy et al., 2012) (Taneda, 1968). Namely, the characterization of limit-cycle oscillations, the evaluation of hysteresis, sub-critical bifurcations, quasi-periodic and chaotic motions have all been reported to different degrees. However, it is worth noting that studies dealing with open-flow greatly outnumber their counterparts, in confined scenarios. Only a handful of published studies is available (Jankee & Ganapathisubramani, 2022) (Gallegos & Sharmaa, 2019), and once again, they are mostly focused on measuring critical velocities, and how they vary as a function of different system parameters. Perhaps one of the most challenging aspects, particular to fluttering beams in confined flows, is the common occurrence of impacts between the beam and the side-walls. In cases of narrow confinement, experiments often report periodic oscillations with intermittent impacts right after the equilibrium loses stability. Previous studies are limited to generic qualitative statements and a systematic and detailed characterization of the post-stable nonlinear regimes of fluttering beams in confined flows is, to the author's best knowledge, not readily available. Hence, another important goal of the present study, is to document and provide some detailed experimental data for the characterization of the nonlinear dynamics of beams in confined flow.

In our simplified 1-D model we consider an infinite span system. This means torsional motions of the plate are neglected as well as three-dimensional flow effects. In the experiments however, the choice of the plate's width (and it's aspect ratio) is posed. Two key features were considered: the size of the clearance gap and the influence of torsional modes. The clearance gap c is the distance, in the spanwise direction, between the plate edges and the side walls, as illustrated in Figure 6.1.

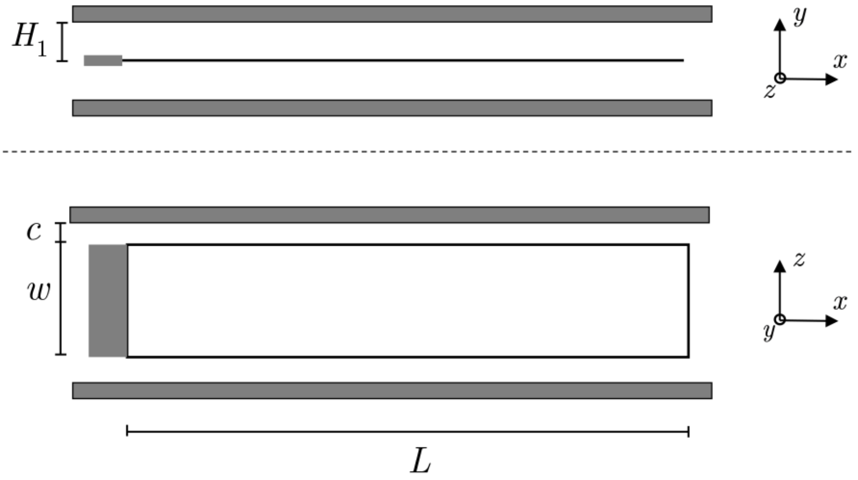

Figure 6.1 – Illustration of the clearance gap: top and side views of the plate confined in the vertical and spanwise directions.

The effect of this clearance, in dimensionless form $c^* = c / w$, was studied theoretically and experimentally in the two studies by Doaré et al. (2011a, 2011b), where the authors demonstrate that larger clearances will stabilize the system (larger critical velocities) due to an attenuation of the pressure jump across the plate. Moreover, authors state that convergence to the 2-D case, i.e. $c \to 0$, is so slow that it is virtually impossible to emulate 2-D conditions experimentally. Considering this, it is expected *apriori* that modelling predictions will tend to underestimate critical velocities. Nevertheless, we aimed to reduce this clearance effect to a practically feasible minimum. A value of 1.5mm seemed like a reasonable practical choice. Then, the reduction of the dimensionless clearance was achieved by larger plate width w. On the other hand, the effect of torsional modes is decreased for plates with narrower widths. This can be illustrated by noting the frequencies of torsional modes in relation to those of bending modes, as shown in Figure 6.2 for varying aspect ratios (calculations were made using a 2-D finite-element model). Ideally, an extremely narrow plate (very small w) would place the frequencies of the first few torsional modes well above those of the bending modes. However, this would greatly increase the dimensionless clearance c^*. Hence, a compromise must be made. Additionally, we aimed to avoid aspect ratios that would have torsional resonance frequencies close to that of the first few bending modes, to prevent eventual coupling effects. A reasonable compromise was taken at $w^* = w / L = 0.2$.

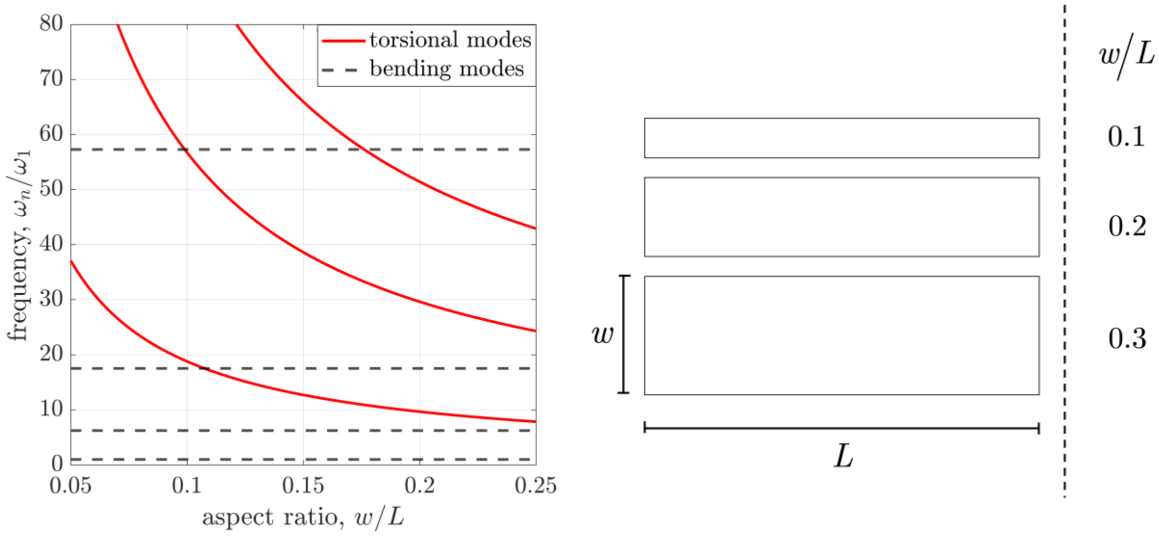

Figure 6.2 – Left: frequencies of plate modes (computed via finite element method) as a function of the aspect ratio, normalised by the frequency of the first bending mode; Right: illustration of various plates with different aspect ratios.

As is usual, experiments were performed in a small-scale open-circuit wind tunnel. Similar experiments in the past have used set-ups inducing flow in blowing or suction configurations. In our case, some preliminary tests were made in a blow-down configuration, using a compressed-air supply. However, this led to extremely unsteady flows inside the test section, despite our best efforts of flow conditioning. Ultimately, it was decided to proceed with the experiments in suction, which provided steadier flow conditions. An axial fan with a variable speed EC-motor was used (AC Infinity Cloudline S10). Including typical circuit resistance, this unit was capable of delivering flow rates up to approximately 1500 litres/minute (0.025 m^3/s). This maximum allowable flow rate was one of the considerations for the overall size of the test section. Naturally, a small test section (small beams and narrow channels) would allow us to reach larger velocities. However, this would also imply more delicate construction.

Finally, considerations regarding the confinement ratio H^* were also addressed. Due to time limitations, we have decided to perform experiments using a constant confinement ratio, as varying this parameter, alongside with variations in the mass-ratio M^*, would entail a more delicate and time-consuming construction process (note that both H^* and M^* depend on the system's length L). As demonstrated in Section 3.3.3, the bulk-flow model used here does not converge to open-flow scenarios when $H^* \to \infty$. Comparison of linear stability curves between our simplified model and a more complete 2-D viscous model suggested a range of validity of $H^* < 1/5$. Hence, we have chosen to build the experimental channel at a constant $H^* = 1/8$, as smaller sizes would entail very minute dimensions and additional difficulties in construction.

Since both the confinement H^* and mass ratios M^* depend on the beam length L, variations of the mass-ratio were more practically achieved by testing multiples beams of different thickness e. A total of 25 beams were available with thickness ranging from $0.01\,\text{mm} < e < 1\,\text{mm}$, leading to $0.04 < M^* < 4$. The beams were made of hardened carbon spring steel (type 1.1274) and had base dimensions (excluding clamped boundary) of $300\,\mathrm{mm} \times 50\,\mathrm{mm}$.

The final set-up consisted of clamped beams of length $L =$ 250mm and the following fixed dimensionless parameters: $w^* = 0.2$, $c^* = 0.03$ and $H^* = 1/8$. The dimensions of the confinement channel were of $53\,\mathrm{mm} \times 31\,\mathrm{mm}$, in the spanwise and transverse directions, respectively.

During the experiments, only variations in the dimensionless velocity U^* and mass-ratio M^* were explored. Note that two dimensionless parameters are not maintained constant: the Reynolds number and the structural damping. While Reynolds numbers inside the test channel can be estimated, they will vary with the velocity. It will be seen later that the modal damping ratios of the beams, although showing some variability between different modes and beams, remain approximately within the same order of magnitude.

6.2 An overview of the experimental set-up

The experimental apparatus consisted in a small-scale open-circuit wind tunnel working in suction, as illustrated in Figure 6.3. The test section channel was made of transparent acrylic panels to allow for easy visualization and, to bypass the effects of gravity, it was placed vertically, with the free-end of the beam pointing downwards. The motion of the beam was captured by both a laser displacement sensor and a high-speed camera. The displacement sensor (Keyence LK-G152) measured the motion of the beam-tip ($x \approx 1$), centralized in the spanwise direction. The high-speed camera had a resolution of 1280 by 720 pixels and captured the transverse motion of the beam at 240 frames per second. Additionally, two LED panels were used to provide proper lighting of the test section and ensure good quality images.

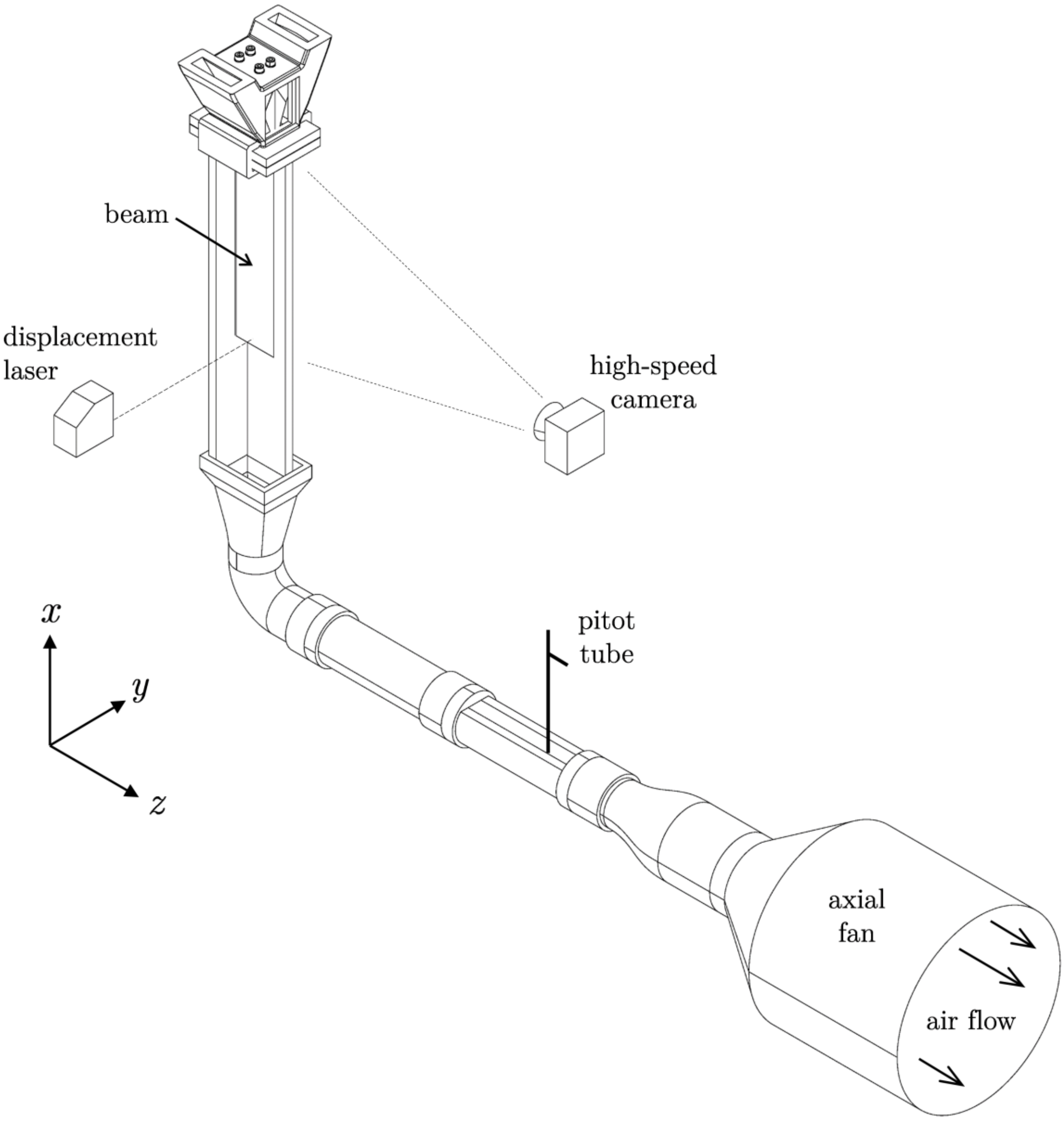

Figure 6.3 – Overview of the experimental set-up.

A detailed view of the flow entry point and the mechanism used for the beam clamping is shown in Figure 6.4. The flow enters independently in each channel and “flow straighteners” made of plastic straws were used to minimize off-axis velocity components. Additionally, the interior surfaces of the 3-D printed piece that connects the two channels were carefully smoothened - using fine sand paper and varnish finish - to minimize boundary layer effects. Since many beams where tested, there was a need to build a clamping mechanism that was relatively easy to mount and dismount. A second important criterion was that the clamps should provide minimal disturbance of the flow. The pair of angled clamps illustrated in Figure 6.4 was the opted solution. The clockwise rotation of the screws connected to the clamps moves them upwards. Moreover, because of the angled junction, this upward motion also applies a lateral force that is sufficiently large to ensure a proper clamped boundary condition.

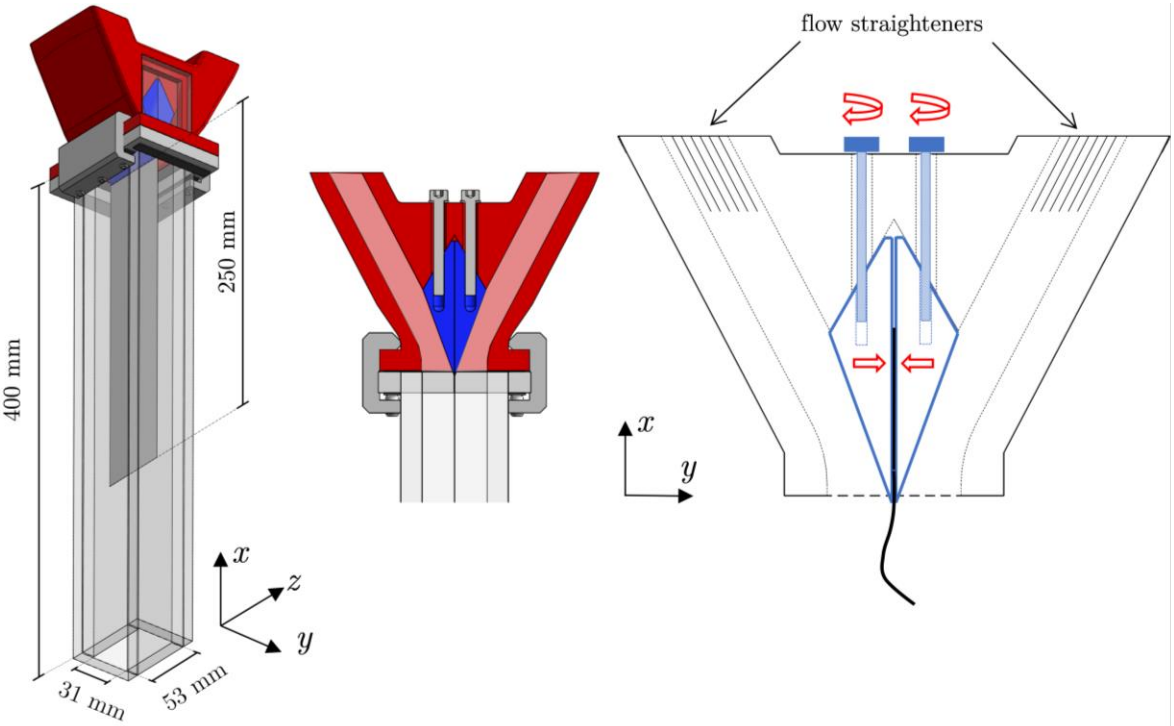

Figure 6.4 - Isometric and cross-sectional views of the test section and detail of the clamping mechanism.

The tubing downstream of the test section consisted of several sections of 3-D printed cylindrical pipes, as illustrated in Figure 6.5. The L-shaped section was followed by a flow conditioning part with honeycomb screens to aid flow stabilization and minimize off-axis velocity components. Subsequently, a cylindrical section with a 2cm radius was used to place a pitot-tube. A small strip of transparent acrylic with a small hole was placed side-ways to allow the visualization and proper alignment of the pitot tube along the central axis of the pipe. The static and total pressure outputs from the pitot tube were connected to a digital manometer (Furness Controls – FC016), from which dynamic signals of the differential pressure were recorded. Finally, a smooth expansion connects the circuit to an axial-fan with a variable speed EC motor (AC Infinity Cloudline S10). Accounting for the circuit resistance, the power of the axial fan motor allowed for average flow velocities in the test section up to 15 m/s (Reynolds numbers up to approximately 40,000). The flow velocity was measured at the central axis of the cylindrical pipe to estimate a mass-flow rate. Based on the cross-sectional areas of the measurement and test sections, the flow rate was then used to estimate an average velocity at the test section upstream. Considerations of the flow profile inside the measurement section and the need of a correction factor for the measured flow velocity are presented in a subsequent section.

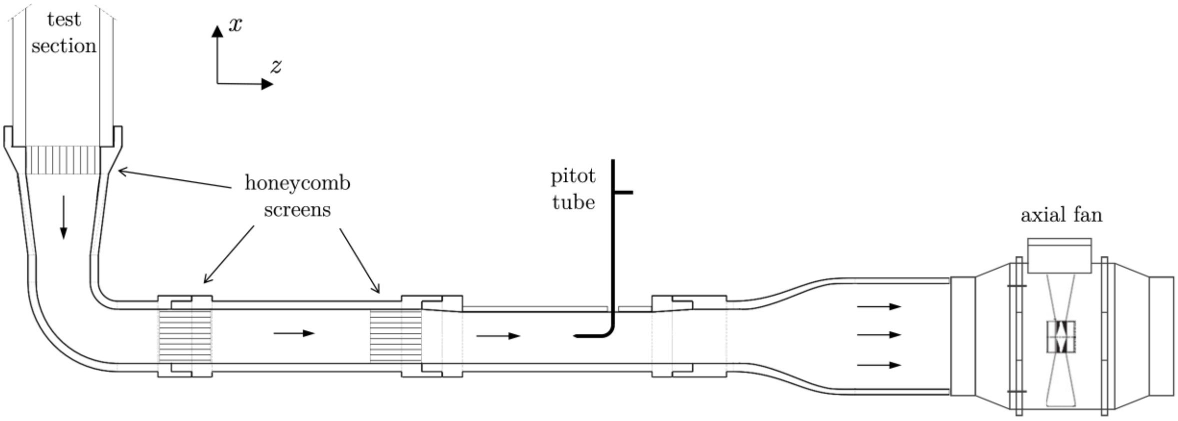

Figure 6.5 – Diagram of the horizontal flow circuit downstream of the test section.

The main aims of these experiments concern the nonlinear behavior of the coupled system. However, it would also be of interest to characterize the properties of the coupled system when its equilibrium is in a stable state. An experimental study of this type was performed by Aurégan & Depollier (1995), where a similar apparatus was connected to a vibration exciter. The forced excitation of the (linearly stable) system allowed the authors to measure the frequencies and damping of the beam modes with and without flow. Even though here we have not foreseen this type of measurements, interesting observations during preliminary tests indicated that this type of analysis could be possible, even without forcing from a vibration exciter. Essentially, small amplitude fluctuations of the beam (typically in the order of 0.1 to 0.5 mm) were observed, presumably caused by what is often called *turbulent boundary layer excitation* (Rosa & Franco, 2008). Due to the broadband nature of the flow turbulence, the response of the beam-tip showed, in most cases, very clear peaks in the frequency domain, from which we were able to retrieve the frequencies of the coupled modes of the linearly stable system. To illustrate, Figure 6.6 shows the responses of the beam-tip displacement and flow velocity in the time and frequency domains, for a beam with thickness $e = 0.15\,\mathrm{mm}$, in a stable equilibrium scenario. This allowed us to track the evolution of the frequencies of the coupled-modes as a function of flow velocity and compare results to the linear stability analysis of our model.

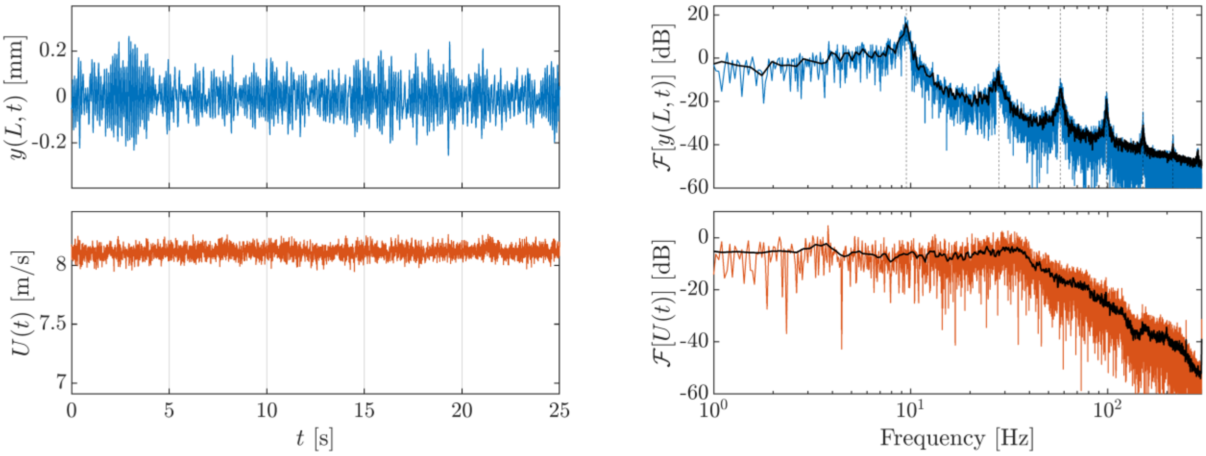

Figure 6.6 – Temporal and spectral responses of the beam-tip displacement (top) and velocity measurements (bottom) in a linearly stable configuration with $M^* = 0.26$ and $U^* = 10$, with an associated Reynolds number $\mathrm{Re} \approx 20,000$. Note: the measured axial velocity $U(t)$ is as defined in section 6.3.2.

The experimental procedure consisted in two phases of increasing and decreasing flow velocity. The flow velocity was changed in an incremental manner, and smaller steps were taken in the vicinity of critical points. At each flow velocity level, a 30 seconds acquisition of the signals from the laser displacement and the digital manometer were recorded at a sampling frequency of 12,800 Hz (minimum sampling frequency of the used acquisition system – NetdB DAQ12). Additionally, for each measurement, a short video of about 5 seconds was captured using the high-speed camera.

To conclude, the aims of the experimental procedure can be summarised as follows:

1. Measure the evolution of the coupled-mode frequencies as a function of the flow velocity in linearly stable configurations;
2. Measure the critical velocities at which an initially static beam starts oscillating (Hopf bifurcations) – in increasing flow velocities;
3. Evaluate hysteretic phenomena: measure the critical velocities at which an oscillating beam will go back to a static state (Fold bifurcation associated with a subcritical Hopf) – in decreasing flow velocities;
4. General characterisation of the beam post-stability behaviour for different flow velocities: evolution of beam motion, base frequency, spectral density, the role of impacts, amongst others,

An overview and some details of the experimental set-up are shown by several pictures in Figure 6.7.

Figure 6.7 – Several views of the experimental set-up.

6.3 Preparation of the experimental apparatus

6.3.1 Characterization of the experimental beams

The importance of characterizing the experimental beams is two-fold. On one hand, knowledge of the beams dynamical response will permit us to feed the model with accurate parameters in the attempt to recreate measurement conditions precisely. On the other hand, material properties like the density ρ_s or bending stiffness EI will serve as normalization factors affecting the estimation of dimensionless parameters (reduced velocity U^*, mass ratio M^*, dimensionless frequency Ω^*, etc.). This seemingly simple problem has in fact some nuances when one considers particular experimental difficulties. In this section we present results of the experimental modal analysis of the beams and discuss some of these somewhat delicate issues.

The used experimental beams were precision metal foils made of hardened carbon spring steel (type 1.1274). These metal sheets are relatively robust even at very thin thicknesses and are commonly used to calibrate precise dimensional measurement equipment. A total of 25 different beams were available, having constant length L = 300mm and width w = 50mm, and thickness ranging from 0.01mm up to 1mm. However, due to limitations in the power of the used axial fan, flow velocities were not sufficiently large to destabilise the heavier beams. Hence, only the 16 thinner beams were tested in flow conditions, i.e. those ranging from 0.01mm to 0.3mm, leading to $0.12 < M^* < 4$.

The density of the beams was estimated in a straightforward manner by weighting the beams in a scale with a 0.001g precision. Division of the measured weight by the volume of each beam lead to the estimated density values, illustrated in Figure 6.8. Larger variability is seen in the thinner beams but thicker beams showed rather stable values around the average $7760 \text{ kg}\cdot\text{m}^{-3}$.

Notice nevertheless that variability was relatively small, with maxima at ±2%. Hence, the averaged value was used as the reference to calculate the dimensionless mass-ratios and reduced velocities.

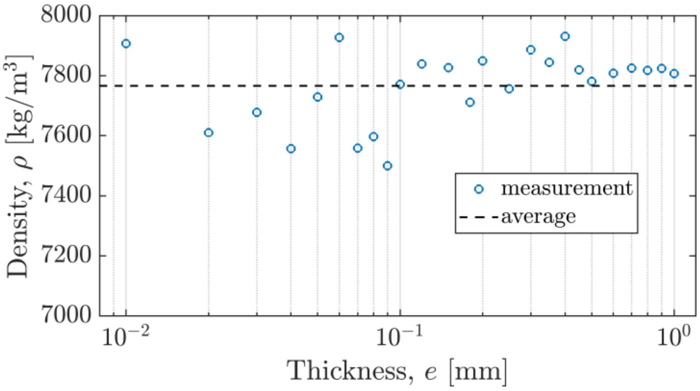

Figure 6.8 – Estimated density of the 25 carbon spring steel beams.

Estimation of the Young modulus E, or the bending stiffness EI, is a considerably more difficult task. This parameter can have significant effect on measured results as it serves as a time normalizing factor to calculate the dimensionless quantities. In most experimental studies, measurements are not shown, indicating that authors most likely assumed tabled values (Jankee

& Ganapathisubramani, 2022) (Nagakura & Kaneko, 1993). In other cases, E or EI values were estimated through static tests, (e.g. measuring plate deflections under the action of gravity (Eloy et al., 2008)) or through the measurement of the frequency of the first mode (Doaré et al., 2011). However, it is well-known that the clamped boundary conditions of beams and plates are notoriously hard to recreate experimentally, and measured results often drift from modelling predictions. Moreover, deviations from theory are typically more pronounced in lower order modes, particularly in the first mode (the most prominent in static tests). Lack of this type of considerations can potentially lead to misleading results. Since the coupled problem is ultimately dynamic, here we propose the estimation of the Young modulus based on a more generic *dynamic* (modal) response of the beam.

An experimental modal analysis was conducted for all beams, using base excitation with a shaker (B&K Type 4809), as illustrated in Figure 6.9. This set-up allowed the estimation of the transfer function between the base excitation, measured with an accelerometer, and the beam-tip response, captured with a laser vibrometer (Polytech PDV-100). The modal parameters extracted from these transfer functions are equivalent to those of a free cantilever beam with a fixed base. The transfer functions were measured using the exponential sweep method. Long sweeps (300 seconds) were performed to: (1) improve the signal to noise ratio and (2) because some beams had relatively low fundamental frequencies (near 1 Hz) hence, a finer frequency resolution was required. It is worth mentioning that, because some beams were extremely thin (as low as 0.01mm), base excitation was set to low amplitudes to avoid any nonlinear geometric effects. Moreover, in these extreme cases, simply breathing near the test foils could affect results and hence, tests were performed in an empty room.

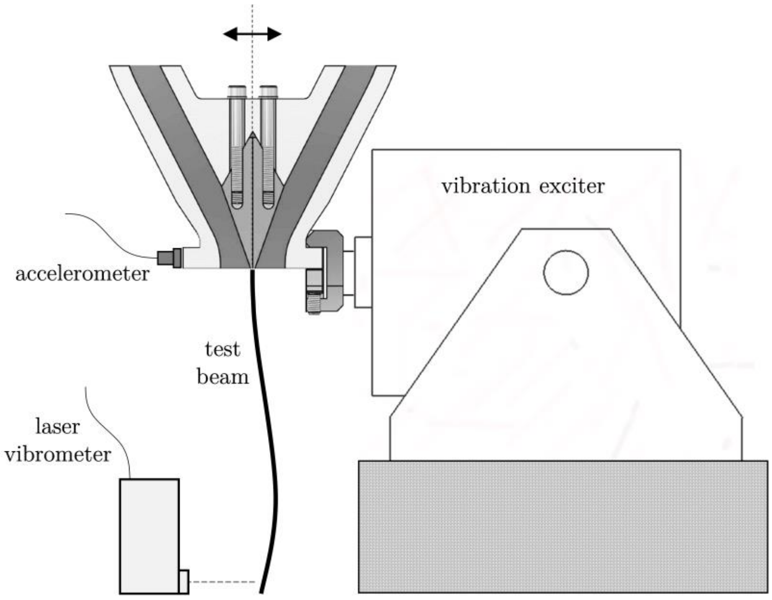

Figure 6.9 – Diagram of the set-up used for the experimental modal analysis of the test beams.

Although not illustrated in Figure 6.9, two laser sensors were used in the experiment. While the main laser sensor measured the motion of the beam-tip at the central axis, a secondary laser captured the motion at the corner of the beam-tip. This was aimed at aiding the identification/distinction between bending and torsional modes, since the centralised laser is located at a nodal line of the torsional modes.

The measured transfer functions were then used to perform the modal analysis using an eigensystem realization algorithm (ERA). Because many beams needed to be tested and measurements were delicate and time consuming, we were not able to measure transfer functions at several points along the beam's length. Aside from modal frequencies and damping ratios, these additional measuring points would have provided an estimation of the beam mode shapes and associated modal masses. However, these parameters are not expected to vary significantly compared to theoretical values. Hence, for the recreation of experimental conditions in the model, theorical values for the mode shapes and modal masses were used.

The identified modal frequencies for the first 8 bending modes are shown in Figure 6.10. The left plot (a) shows the non-normalized frequencies, in Hertz. The right plot (b) shows the frequencies using the typical normalization factor ω_0, assuming a constant value for the Young's modulus $E = 190\,\text{GPa}$ (tabled value for this type of carbon steel).

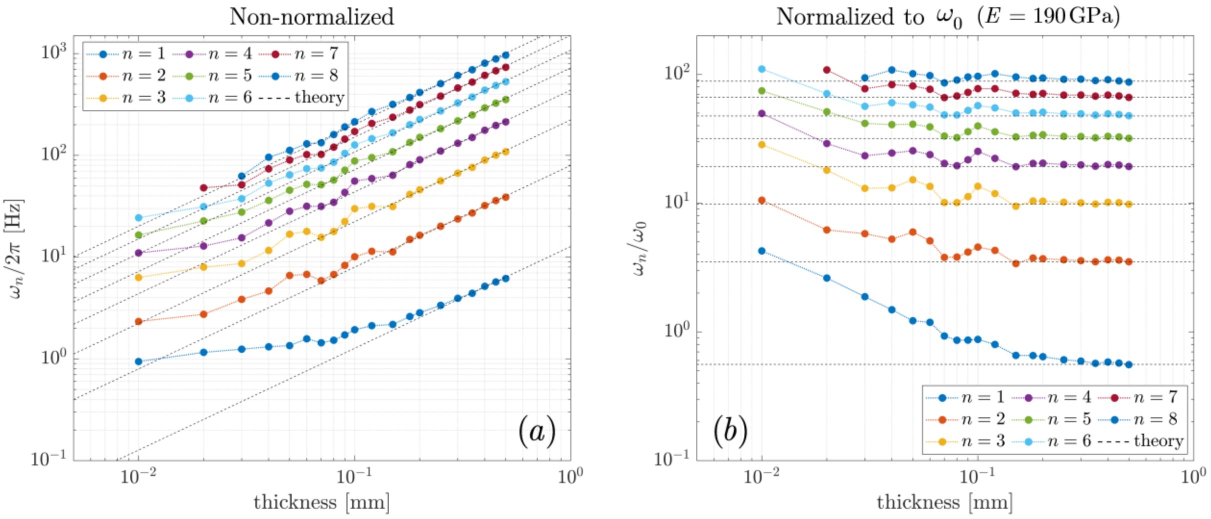

Figure 6.10 – Identified modal frequencies in (a) non-normalized form, in hertz; and (b) normalized by the characteristic frequency ω_0. The black dotted lines indicate the theoretical values considering a uniform Euler-Bernoulli beam, assuming $E = 190\,\text{GPa}$.

While thicker beams fit well with theoretical values, it becomes clear that, as the beam thickness is reduced, the measured frequencies are larger than those predicted by theory. This deviation is particularly significant for the lower order modes and more pronounced in the thinner beams. For example, in the thinnest beam (0.01mm), the frequencies of the first two modes are 7 and 3 times larger than theoretical ones. It is well-known (Maia & Silva, 2003) that imperfections in experimental clamped boundary conditions usually affect the lower order modes to a larger degree. However, deviations from imperfect clamped boundaries typically lead to lower natural frequencies and usually affect heavier beams, where the clamped-end requires stronger forces. This is the opposite in our case, where frequencies are larger than expected and affect mostly the lighter beams. In our case, these unexpected deviations can be explained by gravity effects, which are neglected in the model. In a study by Virgin et al. (2007), the axial load due to the self-weight of a downwards facing cantilever (free-end pointing down), is shown to have a stiffening effect. A simple model for the vibrations of a downwards pointing cantilever beam is given by

$$EI\frac{\partial^4 y}{\partial x^4}+\rho_s S\frac{\partial^2 y}{\partial t^2}-\rho_s Sg\frac{\partial}{\partial x}\left[(L-x)\frac{\partial y}{\partial x}\right]=0 \tag{5.1}$$

where g is the gravitational acceleration. Using the *in-vacuo* beam modes as before (Chapter 2), the continuous problem can be discretized as

$$m_m\ddot{q}_m(t)+m_m\omega_m^2 q_m(t)=\sum_{n=1}^{N}G_{mn}q_n(t) \quad , \quad \text{for } m=1,2...M \tag{5.2}$$

where

$$G_{mn}=\rho_s Sg\int_0^L\left[(L-x)\frac{\partial^2\varphi_m(x)}{\partial\delta x^2}\varphi_n(x)-\frac{\partial\varphi_m(x)}{\partial x}\varphi_n(x)\right]dx \tag{5.3}$$

The frequencies of the vertical cantilever under self-weight $\hat{\omega}_n$ can then be calculated by solving the eigenvalue problem

$$\left[\mathbf{M}\lambda^2+(\mathbf{K}-G_{mn})\right]\Phi=0 \quad , \quad \text{where } \hat{\omega}_n=\mathrm{Im}(\lambda) \tag{5.4}$$

where $\mathbf{M}$ and $\mathbf{K}$ are the diagonal mass and stiffness modal matrices of the *in-vacuo* beam. In (Virgin et al., 2007), the authors underline the role of a non-dimensional parameter that controls the stiffening effect $\rho_s SgL^3 / EI$, which relates gravity-induced axial tension to the bending stiffness of the beam. One can easily note that the gravity induced stiffness changes as $\rho_s SgL^3 \propto e$, while the bending stiffness $EI \propto e^3$. That is, a reduction in beam thickness e will enhance the role of gravity compared to the bending stiffness. To illustrate the effect of this improved model, the experimentally identified frequencies are compared to the gravity-based model in Figure 6.11(a). The interested reader can find a more detailed analysis of the effects of gravity on vertically mounted beams in Appendix C.

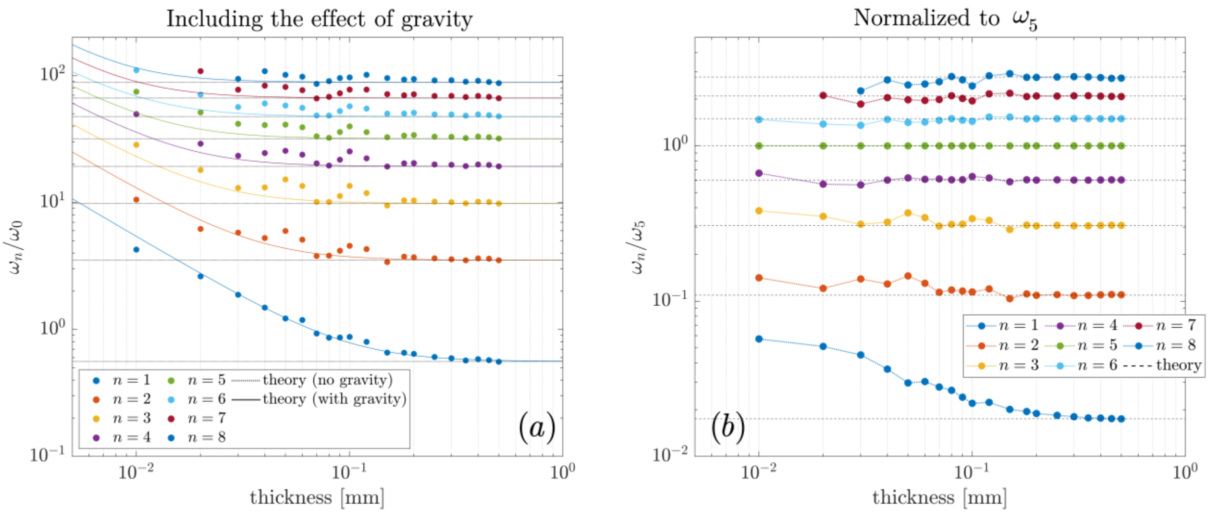

Figure 6.11 – (a) Identified modal frequencies (normalized by ω_0) compared to the theoretical values including (solid coloured lines) and excluding (black dotted lines) the axial tension induced by gravity; (b) identified modal frequencies normalized by the measured frequency of the fifth mode, ω_5.

It becomes clear from Figure 6.11(a) that the deviations seen in the thinner beams are caused by the self-weight induced stiffness. It is worth pointing out that the effect of gravity does not affect all modes uniformly and the frequencies ratios between several modes (i.e. ω_n / ω_1) will change when gravity is accounted for. Namely, lower order modes will be more strongly modified/stiffened by the gravity induced tension. Effectively then, the gravity effect cannot be precisely compensated by simply considering a beam with larger bending stiffness EI. Unfortunately, these conclusions were reached at a late stage in the writing of this thesis and there was not enough time to include the gravity in our model, which implied the definition of an additional dimensionless parameter, and re-writing code for the continuation of periodic solutions, stability boundaries, etc. Due to these time constraints, we have chosen to take a more pragmatic approach based on the definition of an "equivalent" bending stiffness $E_f I$, aimed at approximating the effects of gravity while using the classical beam model (neglecting the self-weight).

Because higher order modes are less affected by the self-weight effects, normalizing the identified frequencies to the measured frequency of a higher-order mode is a more reliable approach. Using the frequency of the fifth-order mode as a reference, the deviations from theory are reduced and significant errors are concentrated on the fundamental mode, as shown in Figure 6.11(b).

The "equivalent" Young modulus E_f was then estimated considering Euler-Bernoulli beam theory which approximates the frequencies of a cantilever beam by

$$\omega_n = \beta_n^2 \left(\frac{1}{L^2} \sqrt{\frac{E_f I}{\rho_s S}} \right) \tag{5.5}$$

where β_n are the solutions of the characteristic equation $1+\cos(\beta)\cosh(\beta)=0$, given approximately by $\beta_n = [1.875,\ 4.694,\ 7.855,\ 10.996,\ 14.137,\ \ldots]$. Therefore, an estimation of the "effective" Young modulus, using the fifth-order mode as a reference, is given by

$$E_f = \frac{\rho_s S}{I}\left(\frac{\omega_5^{\text{meas}}}{\beta_5^2} L^2\right)^2 \tag{5.6}$$

where ω_5^{meas} is the measured frequency of the fifth bending mode, and $\beta_5 \approx 14.137$. To clarify, Figure 6.12 shows the estimated values for the "equivalent" Young modulus for each experimental beam. Finally, the reference frequency used for the (time) normalization of the experimental results (dimensionless reduced velocity U^*, dimensionless frequencies Ω^*, etc.) of each beam was calculated from

$$\omega_0 = \frac{1}{L^2}\sqrt{\frac{E_f I}{\rho_s S}} \tag{5.7}$$

It is worth pointing out that for the two thinnest beams $(e = 0.01 - 0.02\,\text{mm})$, the "equivalent" Young modulus is significantly larger than 190GPa and hence experimental results for these beams, presented in the following section, have to be taken carefully.

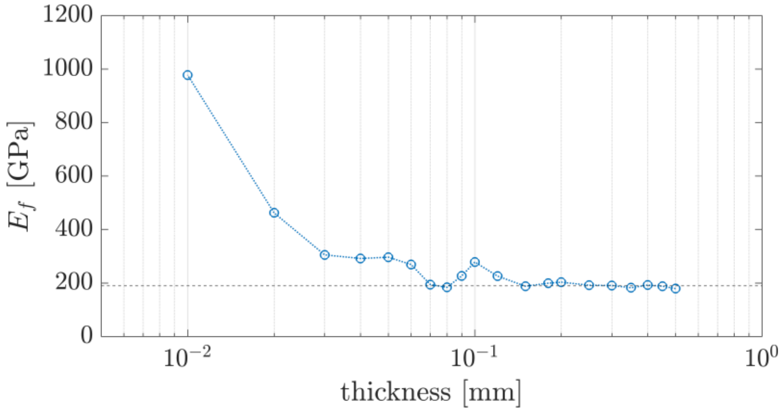

Figure 6.12 – Results for the estimated "equivalent" Young modulus E_f of the experimental beams. The dotted line shows the tabled value $E = 190\,\text{GPa}$.

The identified modal damping ratios of the first 8 bending modes are shown in Figure 6.13. The values for the lowest three bending modes are highlighted to emphasize that these modes generally have larger values than higher-order ones. The overall average (over 8 bending modes of all beams) was of $\bar{\zeta} = 0.42\%$, while the average for the first three bending modes across all beams was of $\bar{\zeta} = 0.69\%$. In model simulations at constant M^*, the actual measured values were used. But for the "global" model calculations (in the $M^* - U^*$ plane), the later value was used as the lowest beam modes are generally the most important in the fluttering dynamics (at least in the tested parametric ranges). As a note, all the numerical values for the identified modal frequencies and damping ratios associated with the first 8 bending and 6 torsional modes of tested beams are shown in Appendix B.

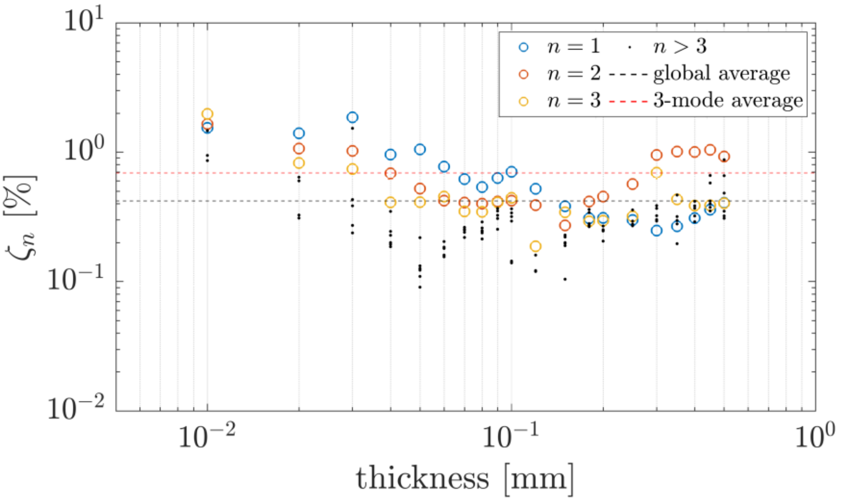

Figure 6.13 – Identified modal damping ratios ζ_n for the first 8 bending modes of all beams.

6.3.2 Characterization of flow profile and flow rate estimation

The flow velocity was measured with a pitot-tube placed in the central axis of a circular section of the circuit, downstream of the test section. The pitot-tube is a pressure probe that measures both total pressure P_T and static pressure P_S. It works on the Bernoulli principle, from which the flow velocity U can be estimated using the two measured pressures (P_T and P_S), that is

$$P_T = P_S + \frac{\rho}{2}U^2 \quad \Rightarrow \quad U = \sqrt{\frac{2(P_T - P_S)}{\rho}} \tag{5.8}$$

Because the relation between the flow velocity and the pressure difference $\Delta P = P_T - P_S$ is quadratic $\Delta P \sim U^2$, pitot-tubes are less accurate at lower flow velocities. This was one of the arguments for the flow velocity measurement to be performed in a part of the circuit with a narrower cross-section (larger velocities and more turbulent flows). To estimate the average velocity passing in the test section, a flow rate Q must be estimated from the velocity U measured in the central axis of the circular section downstream. However, due to viscous effects, the flow profile through a circular pipe is not uniform. To estimate an average velocity U_{avg} (and hence the flow rate) in the flow-measurement section, a correction based on the flow profiles must be made to adjust the measured on-axis values (point of maximum flow velocity).

In fully developed laminar flows through circular pipes with smooth surfaces, the velocity profile $u(r)$ is parabolic and given by

$$u(r) = U_{\max}\left(1 - \frac{r^2}{R^2}\right) \tag{5.9}$$

where r is the distance from the central axis, R is the radius of the circular pipe and $U_{\max}$ is the on-axis velocity. For turbulent flows, many models have been proposed to approximate the (time averaged) velocity profiles from measured data. A commonly used model is the so-called 1/7th power-law (Cengel & Cimbala, 2010). However, a more recent study (Salama, 2021) provided a more generic model for turbulent flow profiles that not only ensures continuity of derivatives but also converges to laminar profiles at low Reynolds numbers. It is given by

$$u(r) = U_{\max}\left[1-\left(\frac{r}{R}\right)^{m}\right]^{1/n} \tag{5.10}$$

Extensive numerical tests and comparisons with experimental data (Salama, 2021) lead the authors to suggest a constant value $m = 2$, and a variable value for n, dependent on the Reynolds number, typically in the range $2 \leq n \leq 7$ for turbulent flows. For laminar flows, $n = 1$ leads to the parabolic profile expression (5.9).

Despite the available models, we have measured the flow profile in our particular set-up at 9 different flow rates, representative of the flow rates used in the experiments, with Reynolds numbers in the measurement section ranging between 5,000-40,000. The measurement set-up is illustrated in Figure 6.14.

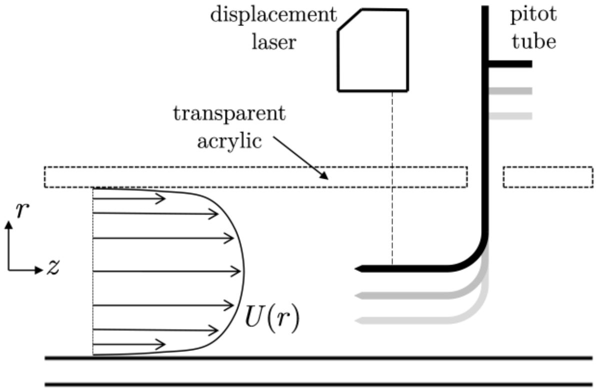

Figure 6.14 – Diagram of the set-up to measure the flow profile.

The pitot-tube was moved vertically in a step-wise manner while its position was tracked precisely with a laser displacement sensor. The time-averaged flow velocities were measured at 14 positions along the cross-section of radius $R = 20\,\text{mm}$. Readings near the walls of the pipe were deemed inadequate, due to artificial effects caused by the proximity of the sensor to the walls. The measured velocity profiles are shown in Figure 6.15: (a) in non-normalized form, in meters/second; (b) normalized to the on-axis velocity $U_{\max}$; and (c) compared to the theoretical predictions using the model presented above.

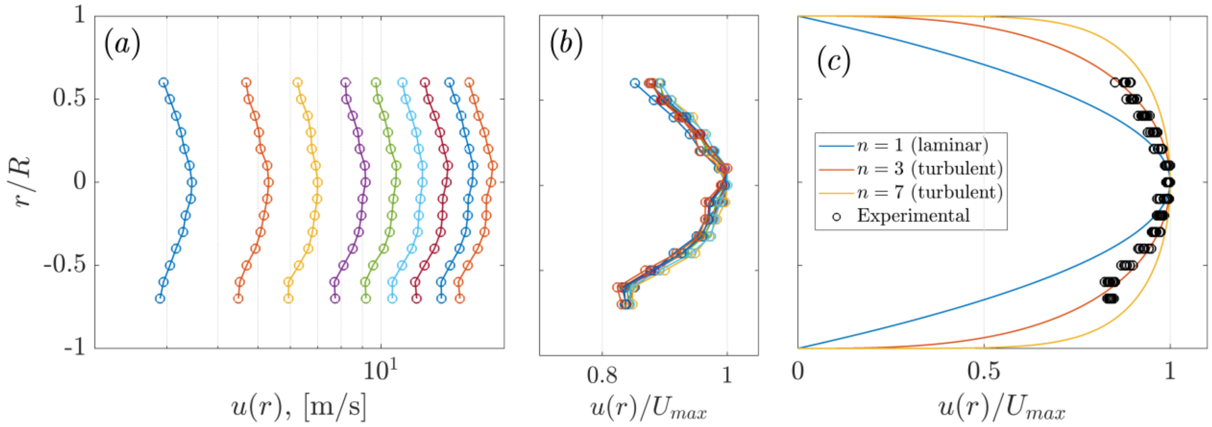

Figure 6.15 – Measured flow profiles at various flow-rates, representative of the flow-rates used in the experiment. (a) Raw velocity readings in m/s; (b) normalized velocity profiles; (c) experimentally measured profiles compared to modelling results with $n = 1$, $n = 3$ and $n = 7$.

The measured velocity profiles, despite covering a wide range of (turbulent) Reynolds numbers (5,000-40,000), did not show significant variations in their (normalized) shapes. Comparisons with the model results suggest a value of $n \approx 3$ gives an appropriate approximation. The average flow velocity can be estimated from the measured on-axis velocities by

$$U_{\text{avg}} = \left[2\beta\left(\frac{2}{m}, \frac{n+1}{n}\right) \Big/ m \right] U_{\max} \tag{5.11}$$

where β is the beta function. Assuming the experimental flow profiles approximate the model results when $n = 3$, regardless of the Reynolds number in the measuring range, the correction factor is given explicitly by

$$U_{\text{avg}} = 0.75 \times U_{\max} \tag{5.12}$$

Multiplying by the cross-sectional area of the measurement section (πR^2), gives us a flow rate Q, which can then be used to estimate the average flow velocity in the test-section upstream.

6.3.3 Video capture and processing

The video capture in the experiments was aimed at a qualitative assessment of the beam motion during limit cycle oscillations. The detection of frequencies or precise beam displacements was not pursued. The high-speed camera was place 500mm away from the test section, centralized along the beam's length. A short 5 second video was captured for each value for the flow velocity.

To highlight the beam motion, an initial step is to perform a background subtraction. This was done using Dynamic Mode Decomposition (DMD). The DMD method (Kutz et al., 2016) was initially developed for the analysis of experimental and numerical flow data, and relies on a computationally efficient low-rank dynamic discretization based on Singular Value Decomposition (SVD). In the context of video processing, DMD treats each pixel as a degree of freedom in a large and complex/nonlinear dynamical system. Performing a SVD enables the extraction of key low-rank spatio-temporal features in the system. Our context relies on a stationary video recording of periodic motion. In this case, the DMD will extract a background mode with zero-frequency, product of high pixel correction regions in between frames. Additionally, the DMD will also identify several “foreground” modes, associated with different frequency components in the motion. Because our motion is periodic, the algorithm identifies the spatial patterns (eigenmodes) associated with each harmonic component. To illustrate, Figure 6.16-(a) shows the original frames from a video capture while Figure 6.16-(b) shows the background (0 Hz) and foreground modes identified by the DMD algorithm. Additionally, Figure 6.16-(c) shows the frames after background subtraction.

The background mode detection is quite robust, since it is essentially an average over the entire recording. Even though we have not used foreground modes for the analysis, it is interesting to note they show an accurate description of the beam motion envelope as well as a smeared illustration of the beam motion. Moreover, the frequency of oscillation and its harmonics are accurately extracted from the DMD. After background subtraction, the treated frames can then be overlapped to provide an illustration of the beam motion in a single image.

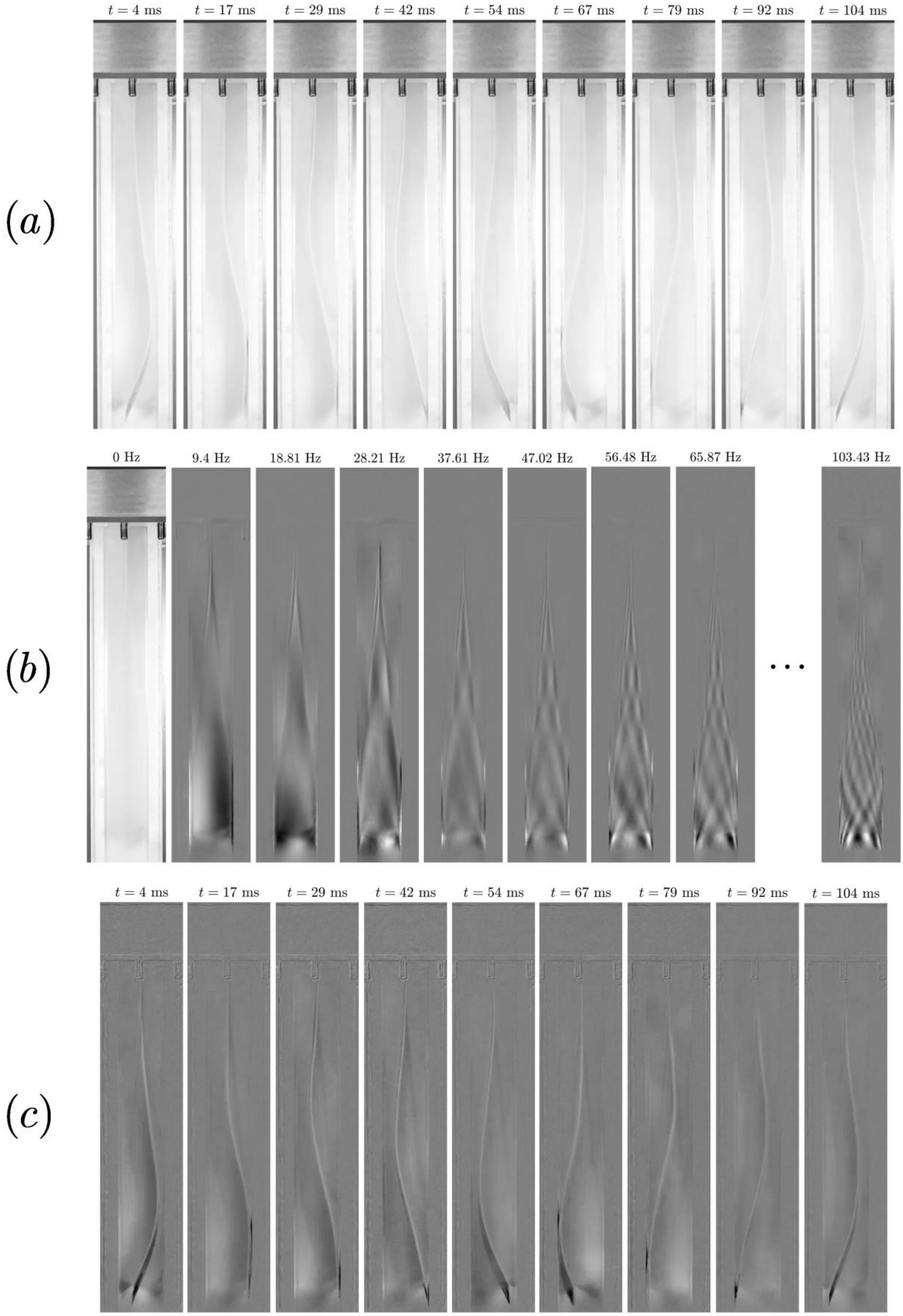

Figure 6.16 - Example of the DMD decomposition and background subtraction on a limit-cycle oscillation with impacts: (a) original video frames; (b) background and foreground DMD modes; (c) video frames after background subtraction.

6.4 Results & discussion

6.4.1 Overview I: Linear stability boundaries

A good starting point is to show an overview of the experimental results in terms of the measured critical velocities in the (M^*, U^*) plane. Once again, it is worth underlining that critical velocities were measured in both ascending and descending flow velocities. The former case will be typically associated with Hopf bifurcations, while the later can indicate both Hopf or Fold bifurcations (depending on the existence of hysteresis).

The analogous modelling results were calculated with the following fixed parameters $H^* = 1/8$, $K_0 = 0$, $K_L = 1$. Additionally, the beam was considered uniform with modal damping $\zeta_n = 0.7\%$ (average of measured values). The sole dimensionless parameter with some associated uncertainty is the friction factor f. This is because our model assumes a constant value for this parameter, even though in reality, it depends on the Reynolds number. Because tested beams were of different thicknesses, the *physical* critical flow velocities varied significantly and hence also their associated Reynolds number. That is, thin beams destabilized at much lower (dimensional) velocities than thicker ones. Based on the measured critical flow velocities (ranging between 1 to 14m/s, depending on the beam), the Reynolds number at the critical boundary was estimated between 1,500-30,000. Relying on the typical Moody diagrams, the associated values for the friction coefficient should lie between 0.01-0.05. For illustrative purposes, experimental results are compared to two different stability boundaries from the model, using $f = 0.01$ and $f = 0.05$.

The measured and modelled critical points in the ascending flow velocity case are presented in Figure 6.17 in the (M^*, U^*) plane, as well as the corresponding instability frequencies in the (M^*, Ω^*) plane. Note that, because hysteresis was found for most measured beams, the instability frequencies were taken as the most prominent frequency in the stable case just prior to instability.

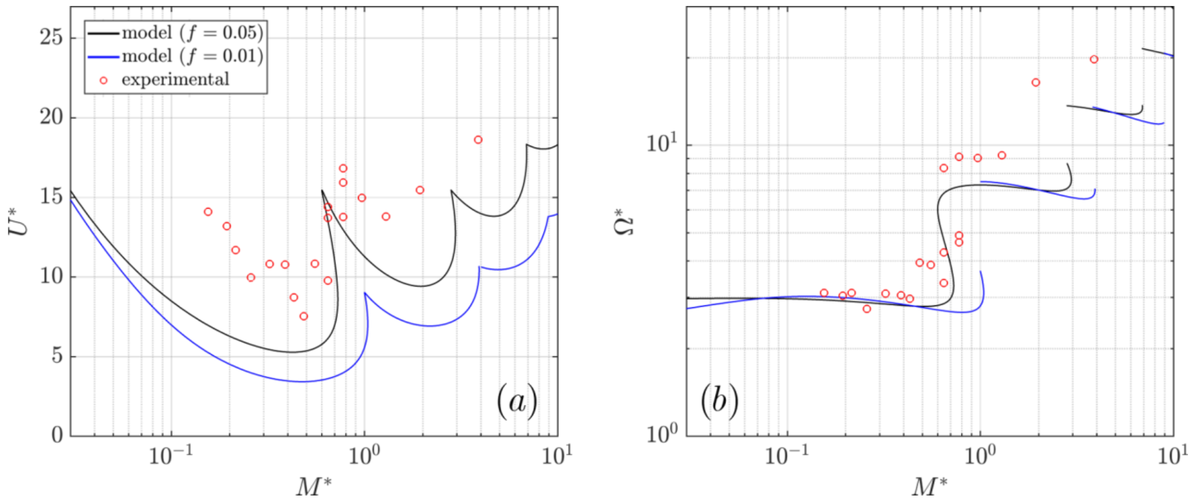

Figure 6.17 – (a) Measured and predicted critical velocities in the ascending case, in the (M^*, U^*) plane with (b) its associated instability frequencies. Note the that sub/super critical nature of the Hopf bifurcations is not shown here.

In relation to Figure 6.17(a), we note firstly the somewhat scattered natured of the measured critical velocities. This is perhaps an indication that experimental conditions were not particularly uniform in-between beams of different thicknesses. This is undoubtably a difficult task, as various aspects of the mounting conditions can be very delicate: clamping of the beam, ensuring alignment and verticality, variations of the clearance gap (1.5mm in each side), alignment of pitot tube, flow conditioning, etc. Unfortunately, time constraints have prevented us from repeating all experiments after remounting to verify the repeatability of mounting conditions. Despite this, it is clear that the model underestimates the measured critical velocities, notably at lower mass-ratios, where values differ by a factor of 1.5-2.5. However, this is not unexpected. As discussed before, this disparity is commonly observed and is a widely discussed question in the field. In fact, the measured critical velocities fall within the same range of other studies. A clear definite explanation to this disparity has not yet been uncovered, however, the studies by Doaré et al. (2011a, 2011b) on the stabilizing effects of the clearance gap provide perhaps the most convincing argument.

On the other hand, the measured instability frequencies are coherent with model results, giving some confidence that a meaningful comparison can be made, at least qualitatively. We also note that the model results with larger friction coefficient provide a better approximation. As will be seen later, this is the case quantitatively, but also qualitatively. Henceforth, for illustrative purposes, we use this model $(f = 0.05)$ as a reference for comparison.

6.4.2 Overview II: Sub-criticality and hysteresis

Aside from the critical velocities in the ascending case (Figure 6.17), presumably associated with Hopf bifurcations, the critical velocities in the descending case were also measured. With a few exceptions, hysteresis was found for almost all tested beams. Moreover, the width of the hysteresis loops was in the same order of magnitude reported by similar experiments, i.e. typically in the range of $\eta = 10\text{-}60\%$. Figure 6.18 illustrates both sets of measured critical velocities as well as the modelling results using the “augmented” linear stability analysis method, described in Section 5.2.2.

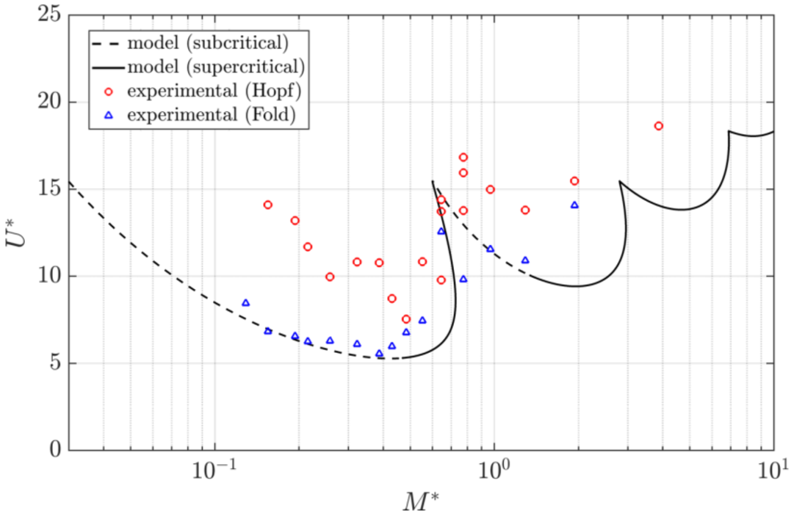

Figure 6.18 – Illustration of measured critical velocities in ascending (red circles) and descending (blue triangles) flow velocity. The dashed and solid lines denote the nature of the Hopf bifurcation predicted by the model $(f = 0.05)$, either sub- or super-critical, respectively.

We note that hysteresis is observed for almost mass-ratios, except the thinnest beam $(M^* = 3.9)$ as well as in an interesting case in the “mode-transition” region $(M^* = 0.66)$. Note that in two cases near the mode-transition $(0.6 < M^* < 0.8)$, there are several critical points – this will be discussed in more detail in the following sections. Another distinctive aspect of the measured critical velocities in the descending case is that, contrary to the ascending case, they seem much more uniform (smooth changes in-between beams), particularly at low-mass ratios. It is difficult to say why this is the case, but one might conjecture that the critical points in the descending case (when the beam is initially fluttering), are more “robust” to mounting conditions compared to the ascending case (when the beam is initially static).

Seemingly coherent with the measured results, the model also predicts large regions with sub-critical bifurcations (and hence hysteresis) at low and moderate mass-ratios. Aside from the low-mass-ratio regions that were also studied in the previous Chapter (Section 5.2), the model predicts an additional sub-critical region after the first mode-transition $(0.5 < M^* < 1.2)$. Note that this is consistent with the analytical results presented previously (Figure 3.5).

It will be seen in the following sections that, despite the model predicting large regions of sub-critical bifurcations, the width of the hysteresis loops η are generally underestimated: the model predicting values ranging up to $\eta < 10\%$ while measured results show $10\% < \eta < 60\%$. This disparity has also been a widely discussed topic in recent years (Eloy et al, 2012) (Tang & Païdoussis, 2007). It is difficult to provide definite answers to this disparity but our model results (Section 5.2) have suggested that sub-critical bifurcations and the width of the hysteresis loops could be encouraged by the effects of flow dissipation. It is possible that a more precise account of flow dissipation could provide results that better approximate experimental observations. It is worth underlining that our model assumes constant values for both the distributed and the localised head-losses (coefficients f and K_L). Perhaps more refined models concerning these (relatively simplified) terms could improve model realism. Moreover, the effects of the clearance gap, neglected in the model, could also be a factor that induces further dissipation and could potentially promote the occurrence and size of the hysteresis loops. Another potential factor that might influence the width of measured hysteresis loops is the concept of *delayed* Hopf bifurcations, whereby the presence of noise (in our case flow turbulence) might induce delays in the arrival of unstable dynamics. The interested reader can find more details, for example, in (Bergeot & Vergez, 2022).

In the following we will examine in more detail the behaviour of the system in linearly unstable scenarios. Experimental bifurcation diagrams will be presented for several beams (constant M^*) as a function of the reduced velocity U^*. At this point it is worth underlining that in many cases the oscillating beams made contact with the side walls, leading to LCOs with intermittent impacts. In similar studies, particularly in unbounded flow configurations, an indicator of the amplitude of oscillation is given by the maximum beam-tip displacement. Naturally, when impacts occur, an indicator of this type is less adequate as it does not distinguish different types of LCO amplitudes with impacts. Here we present results in terms of a more generic amplitude indicator given by

$$A^* = \frac{1}{T}\int_0^T \left|\frac{y(L,t)}{H_1}\right| dt \tag{5.13}$$

where H_1 is the height of the channel and T is a sufficiently long measurement time, including multiple cycles of oscillation, allowing for a robust average value. For the modelling results, simply replacing T by the period of the solution T_0 suffices.

6.4.3 Behavior at low mass ratios: single-neck solutions

We start by examining the behavior of the system at relatively low mass ratios. At these regions, the flutter instability of the (relatively) heavy beams lead to single-neck solutions, as predicted by the model. It is also in these regions $(0.1 < M^* < 0.5)$ where the width of the hysteresis loops η was largest - generally between 30-60%. To illustrate, Figure 6.19 shows the evolution of the amplitude A^* as a function of the reduced velocity U^* for the configuration at $M^* = 0.25$, in both the measurements and the model predictions.

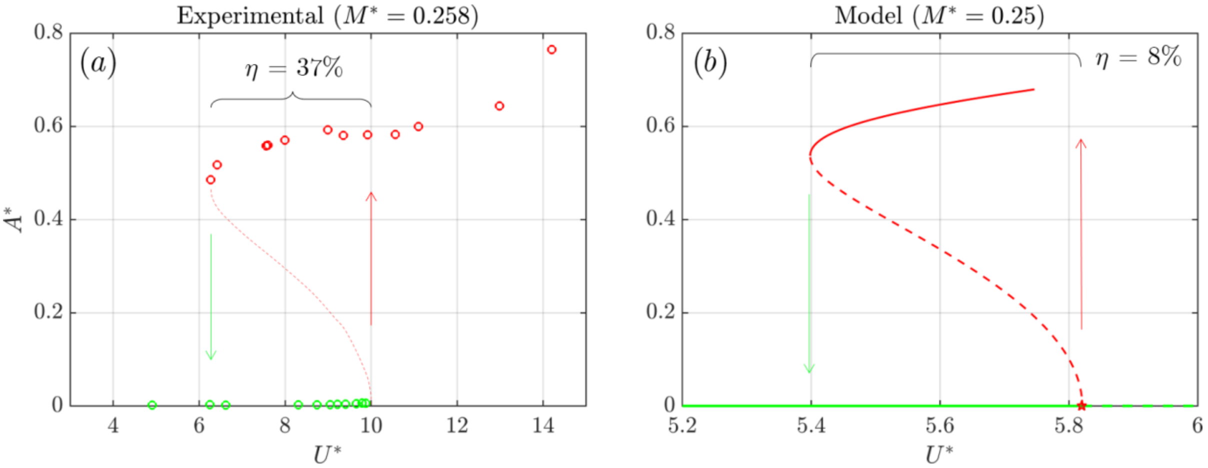

Figure 6.19 – Measured (a) and modelled (b) bifurcation diagrams as a function of the reduced velocity U^* for a system with $M^* = 0.25$. The thin dotted line in (a) was drawn arbitrarily to illustrate the implicit unstable branch. In (b) solid and dotted lines represent stable and unstable period solutions, respectively.

The same type of sub-critical behavior is observed in both the modelled and measured results. However, we underline that the width of the hysteresis loop is significantly underestimated by the model, by a factor of about 4. The amplitudes A^* of the oscillations also seem coherent. The captured beam motions associated with some illustrative points in Figure 6.19(a) are shown in Figure 6.20.

The plots shown in Figure 6.20 confirm that, at these mass ratios, the instability leads to beam motions of the single-neck type, where the contribution of the second beam mode dominates. For larger velocities, we note that impacts start occurring, firstly at the tip of the beam. From this point onwards, increasing flow velocity leads to stronger impacts with an increasingly large contact area. In the last shown case ($U^* = 14$) the beam motion is severely different from the single-neck solution, and we notice a prominence of the third beam mode.

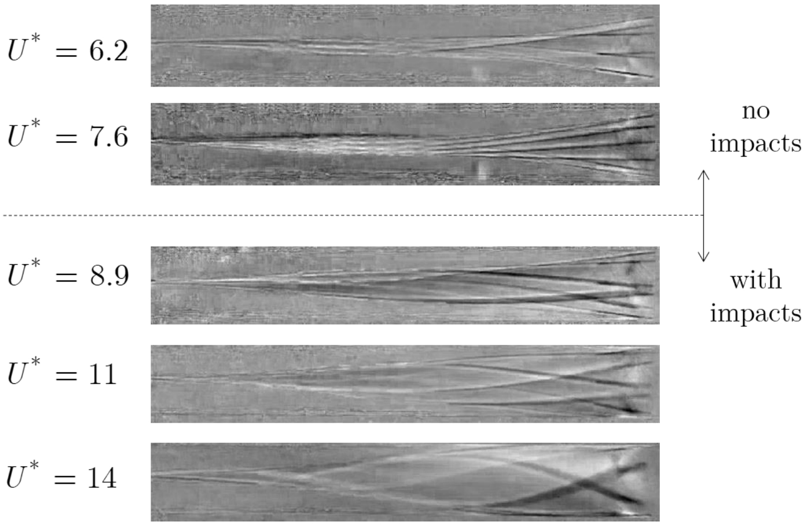

Figure 6.20 – Overlapped frames of the beam motion captured at different velocities U^* for the system with $M^* = 0.258$. The videos associated with these figures are provided under the label "video_M0.258.mp4".

Another perspective of the measured LCOs is illustrated in Figure 6.21, showing the measured beam-tip displacement and corresponding spectra as well as a phase diagram of the beam-tip motion. In Figure 6.21(a) we see how the waveform of the tip motion evolves as the velocity is increased. Starting from a near-sinusoidal motion at $U^* = 6.2$, the spectral content is gradually enriched with increasing flow velocity. Eventually, intermittent impacts start occurring near $U^* = 11$. As mentioned before, at larger velocities ($U^* = 14$), the contact area between the beam and the side walls during impacts increases and in fact, contact starts initially along the beam, preceding the contact between the beam-tip and the side wall (see provided video labelled "video_M0.258"). This effect is shown in the phase diagram (blue curve) where sharp decelerations of the beam tip are seen before it actually makes contact with the side walls. It is worth noting that this behaviour differs from what was simulated by the model (see for example Figure 3.13), where larger velocities lead to stronger impacts, but always concentrated at the beam-tip (at least for symmetric configurations). These differences are probably attributed to the simplified nature of the flow model. Particularly at such intricate moments where the beam is near or in actual contact with the wall, several simplifications in the model might be abusive: the dynamical aspects of the exit head-loss term (which the model takes from a constant coefficient K_L), the effects of the clearance gap, which might become prominent in such narrow-flow scenarios, etc.

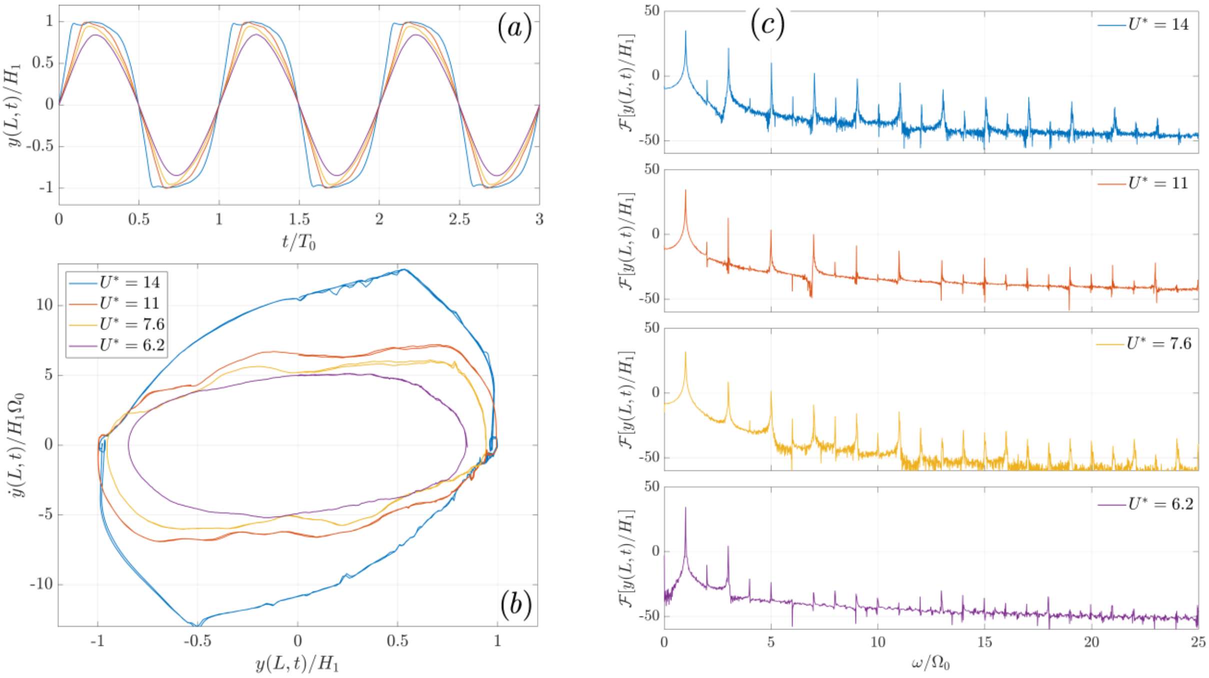

Figure 6.21 – Measured (a) beam-tip displacement, (b) phase diagrams and (c) spectra of the beam-tip displacement for various reduced velocities $U^* = [6.2,\ 7.6,\ 11,\ 14]$ in the system with $M^* = 0.258$. Note that time and frequency scales are normalized by the base frequency/period of the LCO, $\Omega_0 = 1/T_0$.

Finally, we now examine the evolution of the frequency of the oscillations as a function of the reduced velocity. Moreover, to contextualize the frequencies of the measured limit cycles, we show as well the frequencies of the (fluid-beam) coupled modes in linearly stable conditions. Figure 6.22 shows the measured results as well as the analogous results from the linearized model.

Note however that, when unstable solutions are concerned, the results from the linearized model give only an indicative comparison, as nonlinear effects (e.g. hysteresis) are not taken into account.

From Figure 6.22, it becomes clear that the instability is the result of an interaction between the first and second beam modes. Before the instability, increasing flow velocity leads to a clear stiffening effect on the first mode and a slight (but noticeable) softening effect on the second mode. All higher order modes remain approximately at the same frequency. Aside from the clear effect of hysteresis, the results in Figure 6.22(b) illustrate how the model is able to predict, at least qualitatively, the behaviour preceding to the flutter instability.

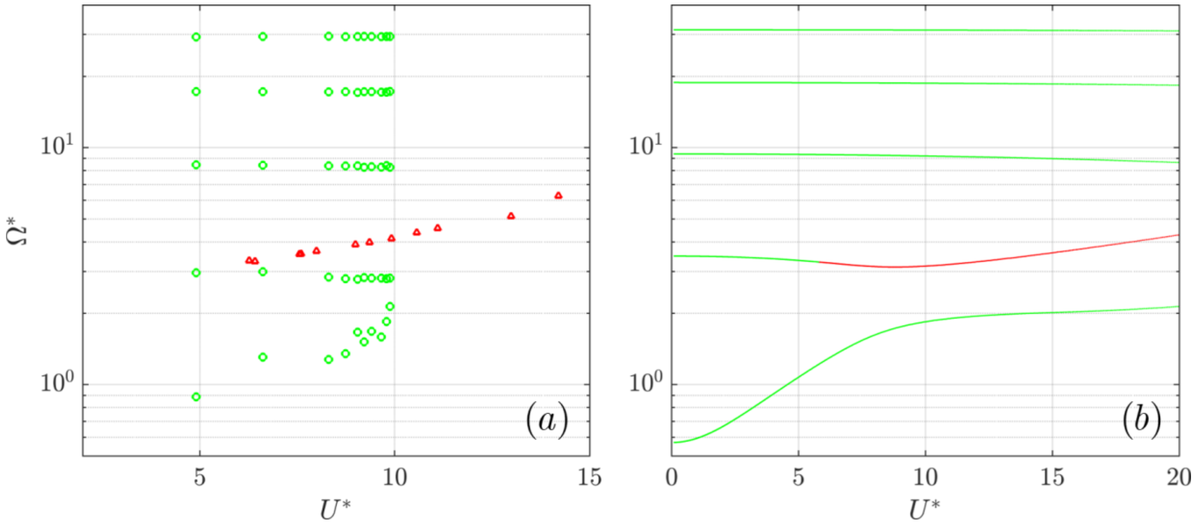

Figure 6.22 – (a) Measured frequencies of the coupled modes in linearly stable scenarios (green circles) and the base frequency of the limit cycle oscillations (red triangles) as a function of flow velocity, for a system with $M^* \approx 0.258$. (b) Evolution of the coupled modes frequency in the linearized model (green and red lines denote stable and unstable equilibria, respectively).

6.4.4 Behavior at mode-transition region

At slightly larger mass-ratios ($M^* = 0.5$) there is a qualitative change in the bifurcation diagrams. To illustrate, Figure 6.23 shows the bifurcation diagrams resulting from both the experiments and the model. Firstly, it is worth pointing out that while some hysteresis, albeit weaker (9%), was seen in the measurement, the model predicts a super-critical Hopf bifurcation. In both the experimental and modelling results, we see a clear transition in the amplitude of the LCOs. In fact, this transition is marked by a change in the nature of the beam motion, evolving from single-neck to double-neck type. In these cases, we notice a *continuous* transition between the two types of solutions, where the influence of the third beam mode is gradually increased, as shown clearly in Figure 6.24. Overall, despite some clear quantitative differences, the model is able to recreate important features of the measured behavior.

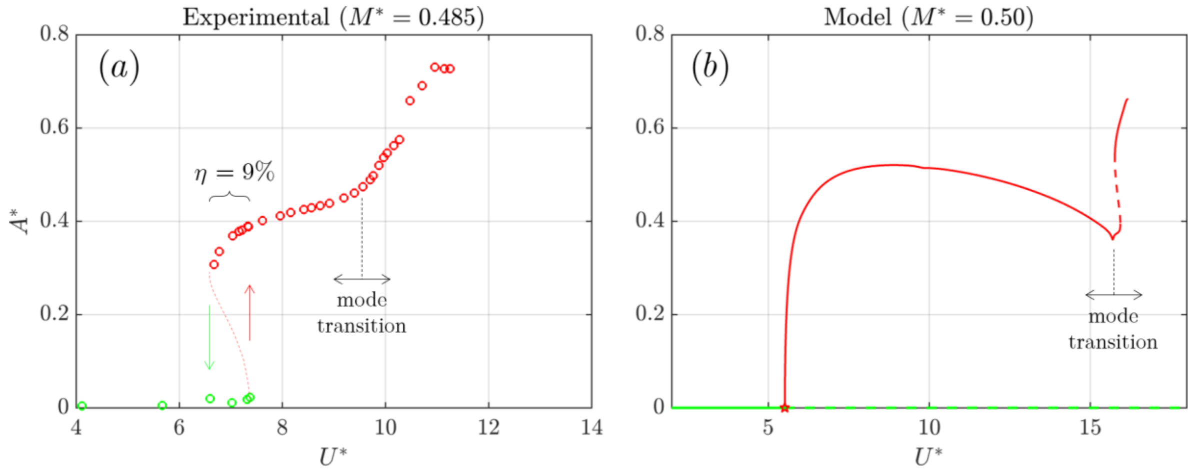

Figure 6.23 - Measured (a) and modelled (b) bifurcation diagrams as a function of the reduced velocity U^* for a system with $M^* \approx 0.5$. The thin dotted line in (a) was drawn arbitrarily to illustrate the implicit unstable branch. In (b) solid and dotted lines represent stable and unstable period solutions.

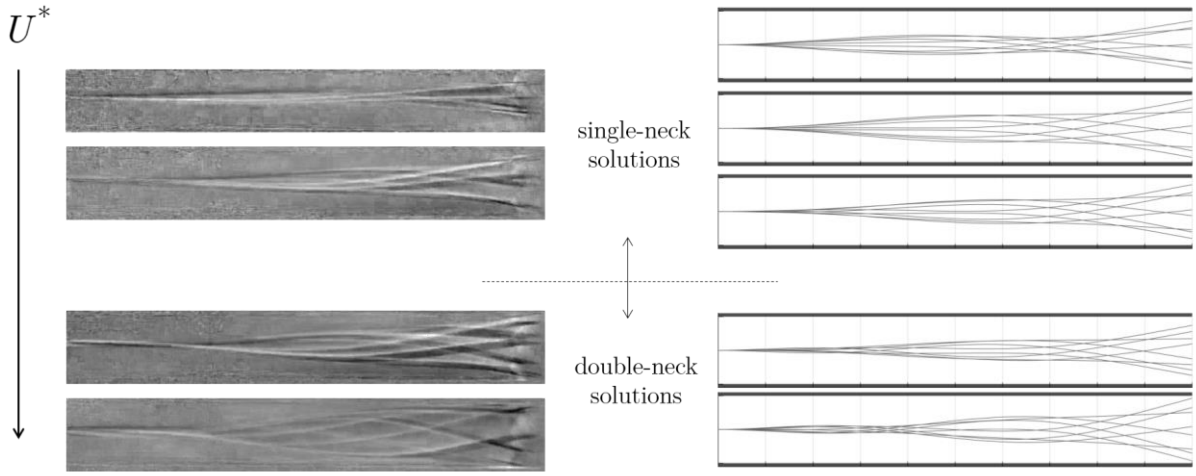

Figure 6.24 – Captured beam motion at increasing flow velocities, illustrating the transition between single- and double-neck solutions (left plots) for a system with $M^* = 0.485$. The plots on the right illustrate the analogous modelling predictions at $M^* = 0.5$. The videos associated with these figures are provided - labelled “video_M0.485.mp4”.

Another view of this transition is shown by the evolution of the frequencies of both the linearly stable and unstable cases, as shown in Figure 6.25. Contrary to the previously shown case, here the flow does not seem to have a softening effect on the second mode. While the initial instability is clearly dominated by the second mode, we notice that an increasing frequency of the unstable solution together with a “softening” effect on the third mode, eventually leads to a crossing, resulting in a prominence of the third mode and the arrival of double-neck solutions. Here it is remarkable how the linearized model, despite ignoring nonlinear effects, is able to correctly approximate the measured behavior.

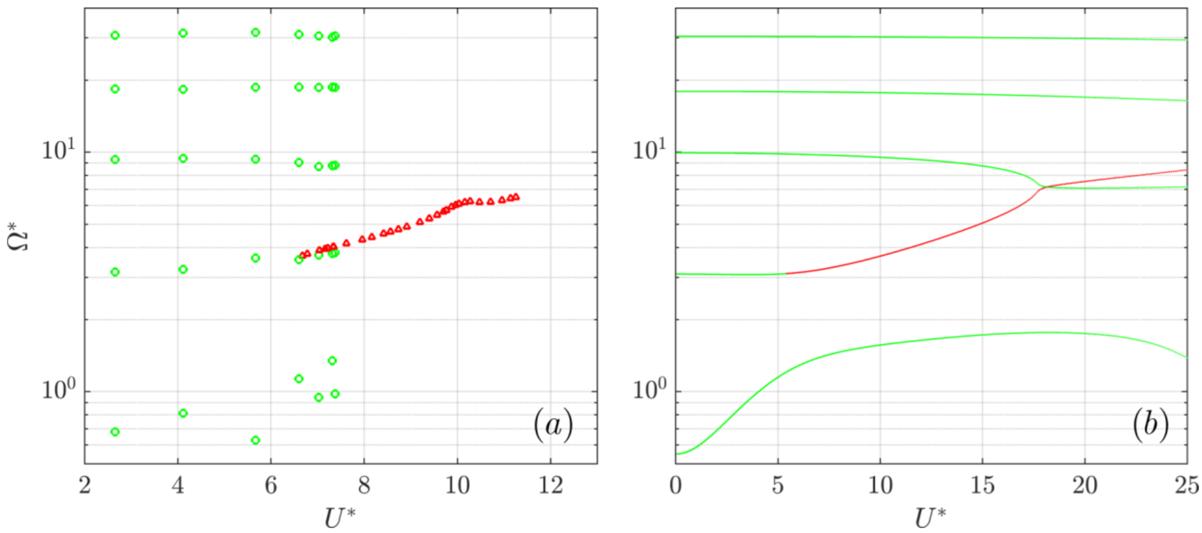

Figure 6.25 - (a) Measured frequencies of the coupled modes in linearly stable scenarios (green circles) and the base frequency of the limit cycle oscillations (red triangles) as a function of flow velocity, for a system with $M^* \approx 0.485$. (b) Evolution of the coupled modes frequency in the linearized model (green and red lines denote stable and unstable equilibria, respectively).

For reference, we show in Figure 6.26 the measured beam-tip motion along with its corresponding spectra and phase diagrams.

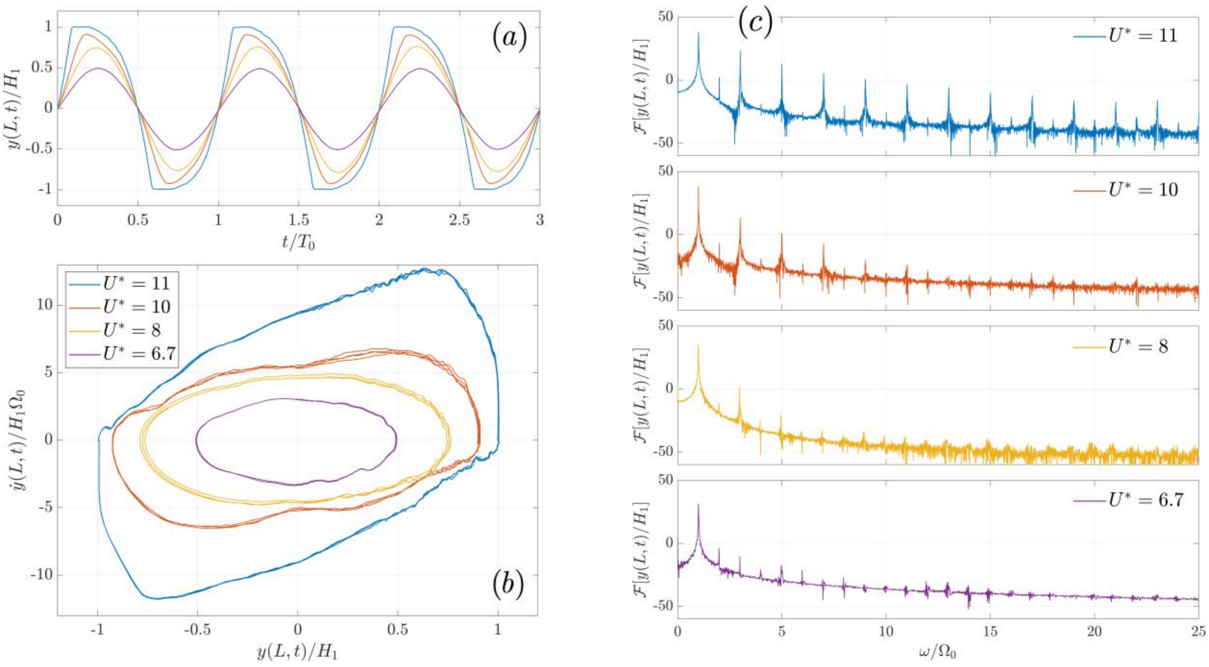

Figure 6.26 - Measured (a) beam-tip displacement, (b) phase diagrams and (c) spectra of the beam-tip displacement for various reduced velocities $U^* = [6.7,\ 8,\ 10,\ 11]$ in the system with $M^* \approx 0.5$. Note that time and frequency scales are normalized by the base frequency/period of the LCO, $\Omega_0 = 1/T_0$.

We continue our analysis for increasing mass-ratios. We now look at a particularly interesting behavior where the transition from single-neck to double-neck solutions occurs in a discontinuous manner. Namely, we examine the mass-ratio configurations that showed multiple critical velocities in Figure 6.18. The bifurcation diagrams for two mass-ratios near the mode-transition region $(0.6 < M^* < 0.8)$ are shown in Figure 6.27 and Figure 6.28.

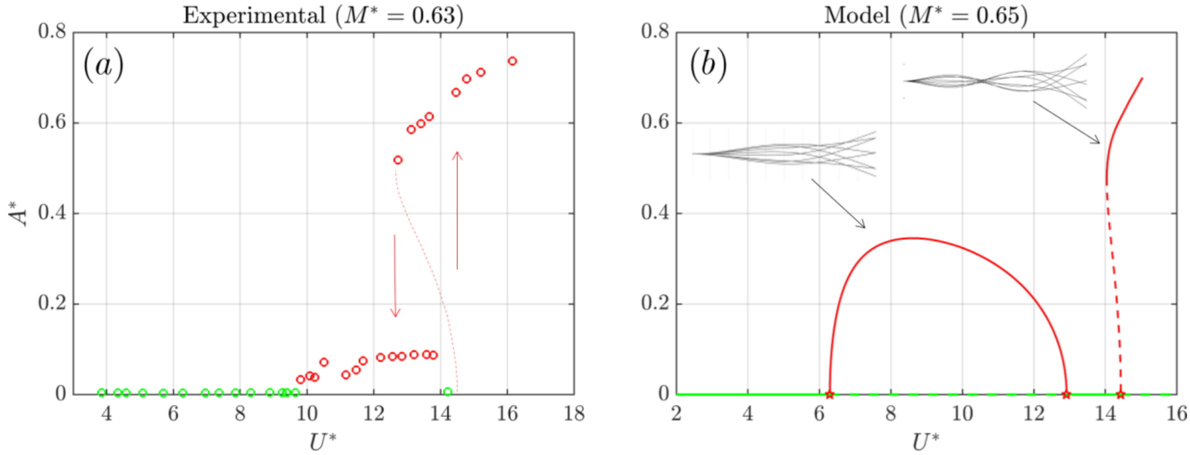

Figure 6.27 - Measured (a) and modelled (b) bifurcation diagrams as a function of the reduced velocity U^* for a system with $M^* \approx 0.65$. The thin dotted line in (a) was drawn arbitrarily to illustrate the implicit unstable branch. In (b) solid and dotted lines represent stable and unstable period solutions.

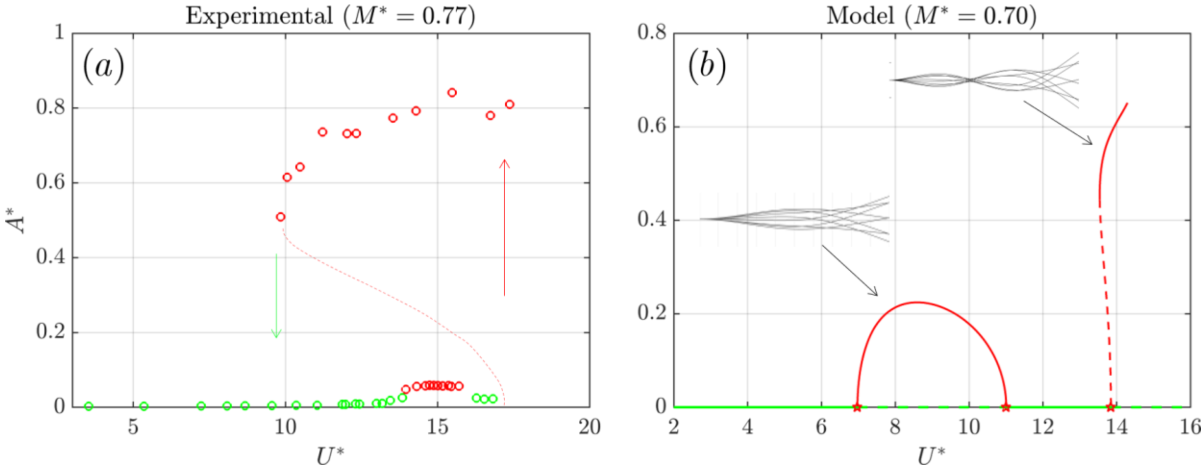

Figure 6.28 - Measured (a) and modelled (b) bifurcation diagrams as a function of the reduced velocity U^* for a system with $M^* \approx 0.75$. The thin dotted line in (a) was drawn arbitrarily to illustrate the implicit unstable branch. In (b) solid and dotted lines represent stable and unstable period solutions.

Here, both measured and experimental results show the existence of three Hopf bifurcations. In both cases, the first solution branch is of small amplitude and associated with the single-neck solutions. Increasing the flow velocity after this initial instability eventually leads to a re-stabilisation of the equilibrium. There is a small window at relatively large velocities where the beam is stable. Subsequently, the equilibrium loses stability once again leading to solutions of the double-neck type. There are significant quantitative differences between measured and modelled results – disparity in the values of critical velocities, amplitudes of the oscillation and the width of the hysteresis loops. Nevertheless, qualitatively, the model is able to recreate the measured behaviour.

To clarify the nature of these two solution branches, Figure 6.29 shows the captured beam motion at various velocities in the two solution branches. The amplitude of the first solution branch (single-neck) is very small, hence it is difficult to illustrate clearly using overlapped frames. However, visualization of the motion picture confirms this is a single-neck solutions (see supplementary material: “video_M0.63.mp4”).

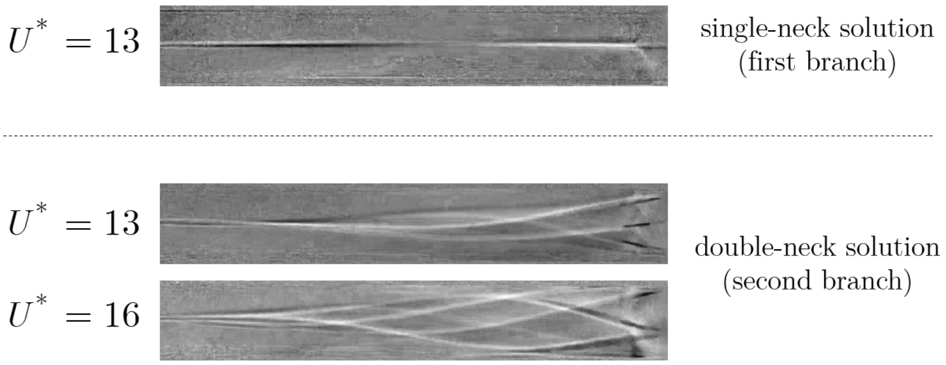

Figure 6.29 - Captured beam motion at different flow velocities for the system with $M^* = 0.63$, illustrating the different beam motions associated with each solution branch shown in Figure 6.27. The videos associated with these figures are provided - labelled “video_M0.63.mp4”.

Another perspective on the character of these two solution branches is given by the frequency plots shown in Figure 6.30. The measured results illustrate clearly that the first (small amplitude) branch stems from a flutter instability of the second mode. Moreover, because amplitudes of oscillations are small, the nonlinear effects are less significant and we notice how the frequency of the LCOs forms a “bridge” between the frequencies of the linearly stable case. This behaviour is also well captured by the linearized model. On the other hand, the second branch presents a large hysteresis loop, whose width ($\eta = 41\%$) is much large than model expectations ($\eta \approx 1\%$). By default, the frequencies predicted by the linearized model do not take this into account.

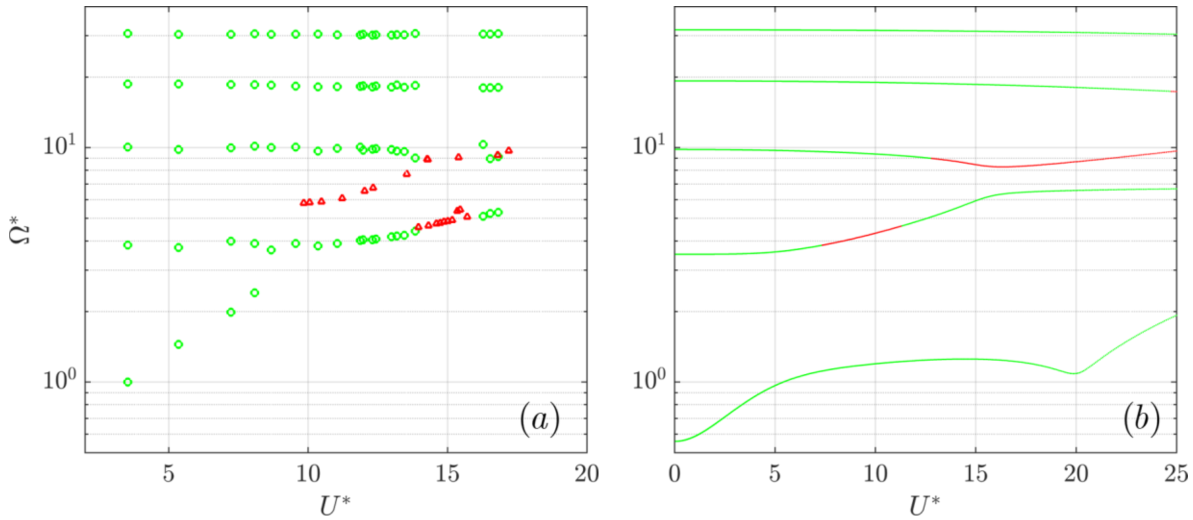

Figure 6.30 - (a) Measured frequencies of the coupled modes in linearly stable scenarios (green circles) and the base frequency of the limit cycle oscillations (red triangles) as a function of flow velocity, for a system with $M^* \approx 0.77$. (b) Evolution of the coupled modes frequency in the linearized model (green and red lines denote stable and unstable equilibria, respectively).

6.4.5 Behavior at moderate mass ratios: double-neck solutions

After the mode-transition region $(M^* > 0.8)$, where we saw configurations with multiple stable oscillatory states, the response of the system simplifies once again, where now the double-neck solutions dominate. Figure 6.31 shows the bifurcations diagrams for solutions in the second "step" of the cascade near $M^* = 1$. Once again, we notice the typical sub-critical behavior with an associated hysteresis loop width of $\eta \approx 21\%$. Although the model results also predict a sub-critical Hopf bifurcation, the hysteresis loop width is severely underestimated $\eta \approx 1\%$.

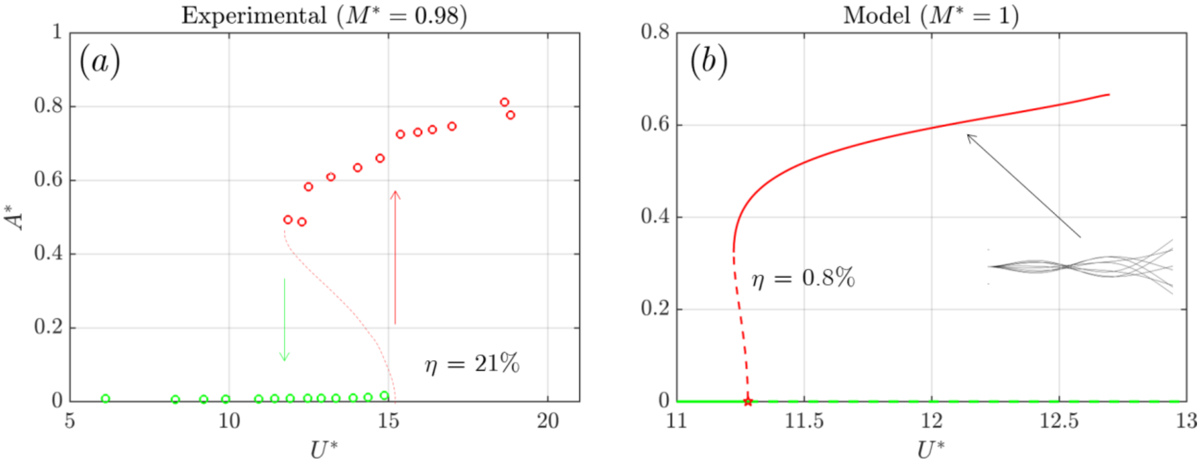

Figure 6.31 - Measured (a) and modelled (b) bifurcation diagrams as a function of the reduced velocity U^* for a system with $M^* \approx 1$. The thin dotted line in (a) was drawn arbitrarily to illustrate the implicit unstable branch. In (b) solid and dotted lines represent stable and unstable period solutions.

Figure 6.32 shows the captured beam motion at different flow velocities, illustrating the expected double-neck solutions and how they evolve in the presence of increasingly stronger impacts. The evolution of the LCO and coupled-mode frequencies as a function of the flow velocity is shown in Figure 6.33. It is worth pointing out that the frequency of the first mode in these cases (thin beams - here 0.04mm) was very low, in the order of 1-2Hz. Therefore, it was often difficult to identify the low frequency coupled modes (in linearly stable scenarios) due to masking by low frequency noise (excitation from turbulent boundary layer). Nevertheless, the role of the first mode is no longer significant at these relatively large mass-ratios.

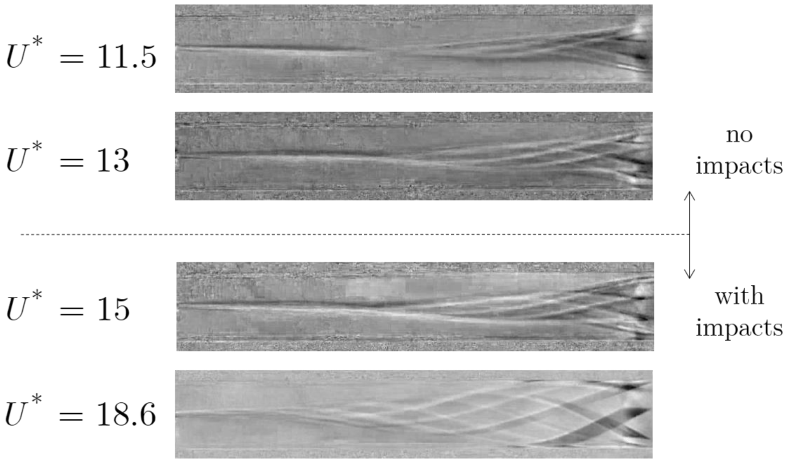

Figure 6.32 - Captured beam motion at different flow velocities for the system with $M^* = 0.98$. The videos associated with these figures are provided - labelled “video_M0.98.mp4”.

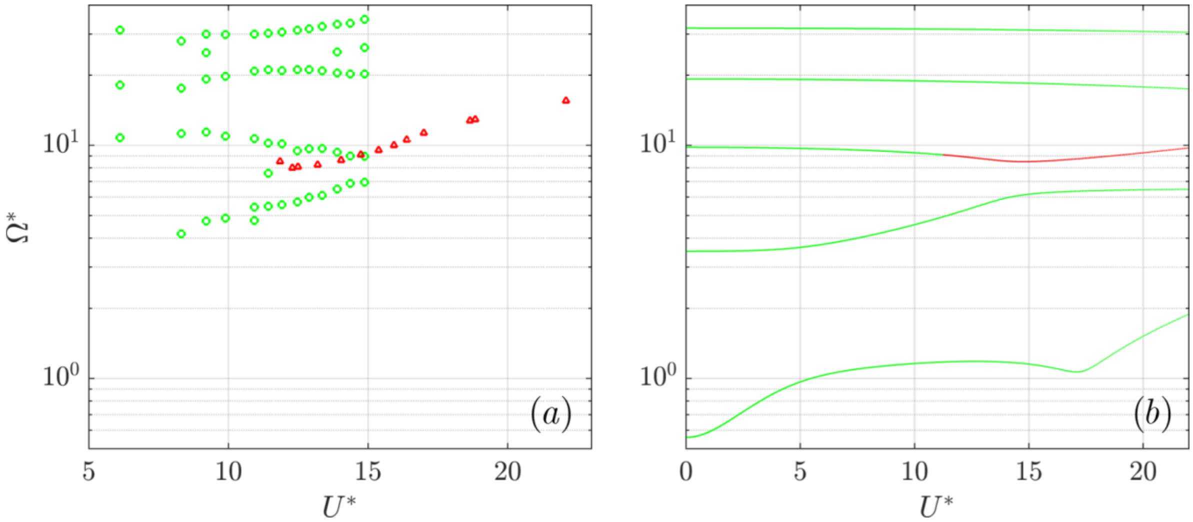

Figure 6.33 - (a) Measured frequencies of the coupled modes in linearly stable scenarios (green circles) and the base frequency of the limit cycle oscillations (red triangles) as a function of flow velocity, for a system with $M^* = 0.98$. (b) Evolution of the coupled modes frequency in the linearized model (green and red lines denote stable and unstable equilibria, respectively).

Once again, the measured signals describing the beam-tip motion are shown in Figure 6.34. A notable feature in these measurements is shown by the results from $U^* = 18.6$. In this regime, composed of very strong impact dynamics (see video labelled “video_M0.98.mp4”) we notice indications that the periodicity is not strict. For example, in the phase diagram we see that the beam-tip motion does not repeat itself exactly. This is also evident in the spectra, where a broadband noise-like content appears, evading the sharp peaks observed in preceding solutions.

This behaviour was also observed in the modelling results shown in Figure 3.13, whereby the unsynchronised motion of the intermittently excited higher-order beam modes led to what we have tentatively named *perturbed* periodic motion since, despite noise-like spectral behaviour typically associated with aperiodic dynamics, the low frequency components are still dominant and largely unaffected. This is perhaps an indication that chaotic motions might arrive, among other paths, from a gradual growth of this modal asynchronicity.

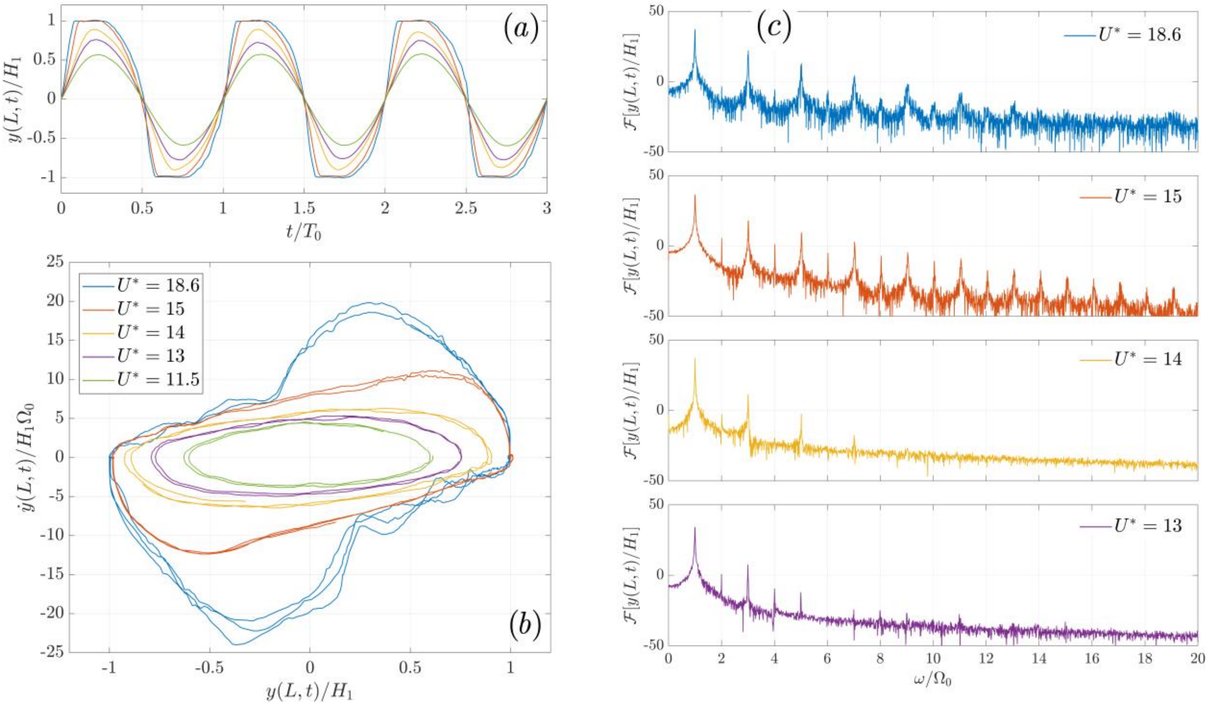

Figure 6.34 - Measured (a) beam-tip displacement, (b) phase diagrams and (c) spectra of the beam-tip displacement for various reduced velocities $U^* = [11.5,\ 13,\ 14,\ 15,\ 18.6]$ in the system with $M^* = 0.98$. Note that time and frequency scales are normalized by the base frequency/period of the LCO, $\Omega_0 = 1 / T_0$.

6.4.6 Behavior at high mass ratios: higher order modes

To conclude, we illustrate the bifurcation diagrams (Figure 6.35) and beams motions (Figure 6.36) associated with configurations at large mass-ratios $(M^* \approx 4)$. Contrary to all previously shown configurations, here we see a clearly super-critical bifurcation, which is also predicted by the model. From Figure 6.36 it is clear that the nature of the solution has several “necks”. The model predicts a triple-neck solution but the beam motion recorded experimentally is slightly harder to qualify – especially since the transverse displacement of the beam near the clamped end is of very small amplitude – but suggest the presence of either three or four “necks”. On this point is it worth noting that the motions predicted by the model suggest larger displacements near the clamped-end, while the recorded motion shows oscillating patterns with motion mostly concentrated near the beam-tip. One potential explanation for these differences is that, at these extremely fine beam thicknesses (0.01mm here), nonlinear structural effects are likely to become important. However, we are convinced that, on this point, the effects of gravity are the most likely explanation. As mentioned before, for very slender beams, the gravity-induced axial tension becomes important. Moreover, because the distribution of the axial tension is not uniform along the beam (the clamped end will “feel” the full weight of the beam while the free-end will be unaffected), the resulting beam mode shapes will also show larger motions near the free-end. A more detailed analysis of the effects of gravity on the mode shapes is presented in Appendix C.

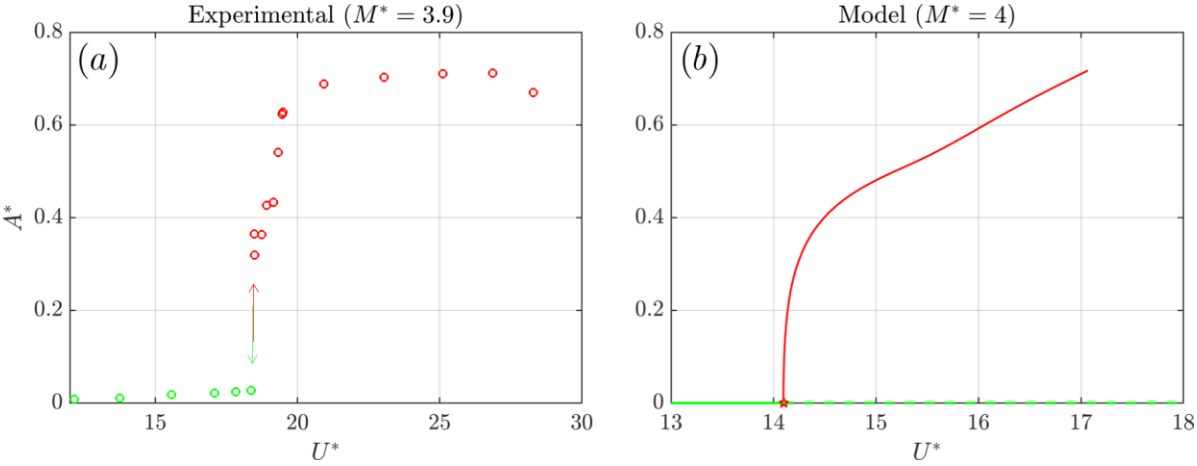

Figure 6.35 - Measured (a) and modelled (b) bifurcation diagrams as a function of the reduced velocity U^* for a system with $M^* \approx 4$. In (b) solid and dotted lines represent stable and unstable period solutions.

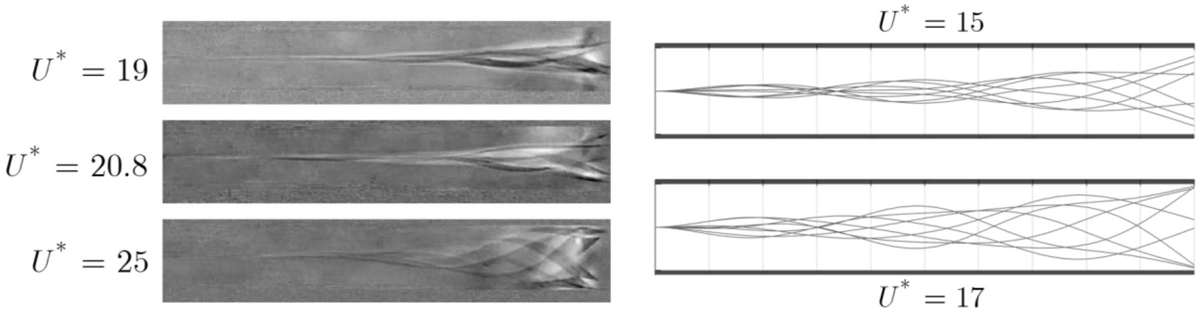

Figure 6.36 - Captured beam motion at different flow velocities for the system with $M^* = 4$, as well as the analogous results from the model. The videos associated with these figures are provided - labelled “video_M4.mp4”.

6.5 Summary

The contents presented in this chapter are summarized in the following points:

- → The design considerations and main objectives of the experiments are presented together with a detailed description of the experimental set-up and its preparation. These included: the choice of dimensions for the apparatus, the parametric ranges to be studied, measurements of the beam's dynamical characteristics, characterization of the flow profiles and estimation of the flow rates, video capture and image processing, amongst others.
- → A wide variety of experimental results are presented including linear stability boundaries, quantification and characterization of hysteresis as well as experimental bifurcation diagrams for the characterization of the nonlinear regimes stemming from a linearly unstable equilibrium. All results are presented in parallel with modelling predictions.
- → In terms of the critical stability boundaries, the model is seen to consistently underestimate measured values. However, this is not unexpected and most studies on the subject confront the same disparity. This is a widely discussed question and several arguments have been proposed to explain these differences. The most convincing being that the influence of the clearance gap will have an important stabilizing effect, possibly by lowering the mean dynamical pressures and increasing the system damping.
- → Hysteresis phenomena was found for most of the beams studied and the width of the hysteresis loop was usually in the range of 10-60%. This is consistent with experiments performed in the past. The *existence* of hysteresis (sub-critical bifurcations) in the studied parametric regions is well captured by the model. However, the width of the hysteresis loops is generally underestimated, typically falling between 1-10%. The role of flow dissipation as well as the unaccounted effects of the clearance gap (which likely induce additional dissipation) have been pointed as possible causes for this discrepancy.
- → In particular configurations, experimental results have shown the existence of two stable oscillatory states for the same flow velocity. This interesting behavior has been reported in past experiments, but only descriptive accounts were given. Here, we document it for the first time in a systematic manner and analyze it with respect to modelling predictions, that correctly emulate this behavior.
- → The effects of impacts between the beam and the side-walls seem to be well captured by the model at relatively low velocities, where contact occurs solely at the beam-tip. However, for larger flow velocities and stronger impacts, measured beam motions showed an enlarging contact area with impacts starting along the length of the beam, further away from its tip. This deviates from modelling predictions, in which stronger impacts generally remain concentrated at the tip.
- → Despite significant quantitative differences, the simplified model is able to capture important features of the observed dynamical behavior, including the character of the instability with regards to the involved beam modes, the existence of configurations with multiple stable oscillatory states and the evolution of the frequencies of oscillations.

As a final note, is it worth mentioning that, aside from the symmetric configurations studied in this chapter, experiments were also conducted in asymmetric configurations, where one of the channels was partially closed, inducing an asymmetry in terms of flow resistance between channels. This set-up resulted in very interesting dynamical behavior which, to the authors knowledge, as not yet been reported. These include: LCOs branches with periods converging to infinity, intermittent regimes and period doubling phenomena. Unfortunately, time constraints prevented us from conducting a thorough comparison with modelling predictions. Nevertheless, the encountered dynamical behavior was documented in detail and results are presented in Appendix D.

Summary, conclusions and future work

The work in this thesis has analyzed the nonlinear dynamic behavior of a benchmark example of flow-induced vibrations: a flexible cantilevered beam subject to axial flow in a confined passage. Novel methodological approaches have been proposed mainly focusing on the nonlinear dynamical aspects of the flow-structure coupled system. The results presented give a new perspective on the rich dynamics of these systems and provide novel insights into the fundamental physics of the problem. Moreover, most of the methods proposed are generic in character and can certainly be used to analyze similar problems dealing with slender structures in axial flow.

The developed analytical formulation has the advantage of providing exact expressions for the flow variables, where no error-inducing spatial discretization procedures are involved while, at the same time, reducing the continuous problem to a very compact system of differential equations that can be solved numerically at very low computational cost. Using this approach, the nonlinear oscillations of the coupled problem were then calculated via temporal integration, illustrating the nature of limit cycle oscillations in a variety of scenarios. Additionally, the inclusion of an elastic impact model allowed, for the first time, the computation of limit cycles with intermittent contact between the plate and the confinement walls. Aside from various types of limit cycle oscillations, results illustrated the existence chaotic motions at sufficiently large velocities, and indicated the possibility of period doubling bifurcations. The linearized version of this formulation also led to a compact system that can be used to calculate stability boundaries quickly, allowing for broad parametric studies. The sole disadvantage of this approach is that it did not prove adequate for the use of continuation algorithms and bifurcation analysis.

Subsequently, a Tau-Galerkin discretization procedure was proposed that was suitable for bifurcation studies. In this method, the system of PDEs is converted into a set of time-dependent nonlinear equations (ODEs and algebraic) by developing all variables in terms of series of efficient space-dependent orthogonal functions. A Tau-variant enabled the enforcement of the nonlinear time-dependent boundary conditions in a well-posed manner. Ultimately, the system is reduced into a set of nonlinear DAEs that can be truncated at any suitable numbers of terms, leading to exploitable reduced formulations. An attractive aspect of this method is its generic character. In principle, it can be applied to a wide variety of continuous fluid-structure interaction problems leading to compact time-dependent formulations for nonlinear analysis.

Based on the developed Galerkin formulation, we provided an initial impulse for a comprehensive nonlinear dynamic analysis of these systems using, for the first time, methods for the continuation of periodic solutions and bifurcation analysis. A combination of the harmonic balance method with the asymptotic numerical method allowed for the continuation of periodic solutions in terms of one, or multiple, system parameters. This provided a broad overview of the possible dynamics and brought a new perspective on some ill-explained phenomena commonly observed in experiments. The question of hysteresis and sub-critical bifurcations was discussed in detail and, additionally, a numerical method for an “augmented” linear stability analysis was proposed, allowing the continuation of Hopf bifurcation branches, including their sub- or super-critical nature. The same method, based on constrained continuation, also allows for the prediction of grazing boundaries, i.e. frontier separating limit cycle regions with and without intermittent impacts. The nonlinear dynamics were explored with respect to various dimensionless parameters and results illustrate a large variety of dynamical behavior including: internal resonances, regions with multiple oscillatory solutions, torus bifurcations and associated quasi-periodic motions, amongst others.

Finally, experiments were performed on a small-scale wind tunnel to validate various aspects of the model results. Additionally, the collected data provided a detailed documentation of nonlinear dynamics of beams in channel flow including limit-cycles with intermittent impacts, which is relatively rare in literature. On a qualitative level, experimental results compare well with modelling predictions. However, the simplicity of the proposed model prevents a more refined quantitative comparison.

In the following, some suggestions for new avenues of research are presented, that could improve on the modelling and analysis efforts presented here. In terms of the refinement of the physical model:

→ *Nonlinear structural effects* – Throughout this manuscript, the geometric and inertial nonlinear effects associated with the structural motion were ignored for simplicity. Inclusions of these effects, using for example the formulation presented in Chapter 2, could bring an additional realism to the modelling of the structure.

→ *Refinement of impact model* – The impact model used here was essentially pragmatic, and there is certainly room for improvement. A more detailed model, with parameters tuned to the specific geometries of the contacting bodies or the inclusion of dissipation are a good starting point. More importantly however is the treatment of the flow conditions when the two elements are in contact and the channel is effectively closed. This is surely a delicate matter, but its effects on the overall dynamics are likely important.

→ *Refined modelling of the localized head-loss coefficients* – Here we have assumed a constant value for the head-loss coefficient K_L at the trailing edge (quasi-steady assumption). This is perhaps reasonable in a linearized scenario. However, it is likely that letting this value change, in a quasi-steady or unsteady manner, in accordance to some geometric properties like the beam-tip velocity or the displacement gradient at the trailing edge, could bring some realism to the results at larger amplitude motions. Here, the problem lays in the lack of experimental data to feed such a model.

→ *Expansion of the friction coefficient* – Similarly, we have assumed a constant value for the friction coefficient describing the distributed head-losses. At the cost of increasing model complexity, one could eventually expand this term as a function of the Reynolds number (dependent on flow velocity and beam motion), perhaps leading to a more precise description of the real flow dissipation at large amplitude beam motions.

→ *Including the effects of spanwise confinement* – As mentioned before, past studies have pointed out to the fact that the underestimation of critical velocities by 2-D models is likely rooted in the effects of the spanwise confinement and the “clearance gap”. The inclusion of a physically based adjustment of the pressure jump due to the clearance gap will likely lead to results that are quantitively closer to measured critical values. Another possibility might be to consider a beam with some artificial porosity, for example.

Moreover, the methods and analysis presented in this thesis are mostly illustrative and can surely be developed further, to name a few examples:

→ *Effects of channel profile variations* – The physical model and resolution methods presented here allow the possibility of asymmetric channels as well as channel with a smooth varying section along the domain. The lack of time has prevented us from engaging in the analysis of these configurations, although they would certainly be of interest for a number of practical applications like the design of energy harvesting devices or in the modelling of human snoring.

→ *Closing one channel* – Similarly, one could also explore scenarios where one of the channels is closed. The present model allows for these types of variations, while still accounting for the presence of a static fluid in the closed side.

→ *Continuation of fold bifurcation branches and the study of hysteresis* – The results presented in Chapter 5 illustrate how the detection of Bautin bifurcations and the continuation of the fold branches stemming from them can bring a more comprehensive view of the hysteresis phenomena. The continuation of these fold bifurcation branches, and how they change with respect to different system parameters can eventually bring new insights to this still poorly understood phenomenon.

→ *Continuation of torus bifurcations and the loss of periodicity* – Similarly to the points made above, the detection of double-Hopf bifurcations and the continuation of the ensuing torus branches could eventually lead to the definition of boundaries separating periodic from quasi-periodic motion. Moreover, it is not unlikely that these torus bifurcations could be one of the root causes for the chaotic behavior observed experimentally. This is still an open question but a more detailed analysis of these bifurcations could potentially bring some clarifications.

References

Abderrahmane, H., & Païdoussis, M. (2011). Flapping dynamics of a flexible filament. *Physical Review E, 84*(066604).

Aittokallio, T., Virkki, A., & Polo, O. (2009). Understanding sleep-disordered breathing through mathematical modelling. *Sleep Medical Reviview, 13*(5), 333-343.

Alben, S. (2015). Flag flutter in inviscid channel flow. *Physics of Fluids, 27*(033603).

Alben, S., & Shelley, M. (2008). Flapping States of a flag in a inviscid fluid: bistability and the transition to chaos. *Physical Review Letters, 100.*

Antunes, J., & Piteau, P. (2010). A nonlinear analytical model for the squeeze-film dynamics of parallel plates subject to axial flow. *Journal of Fluids and Structures, 52*, 1491-1504.

Aurégan, Y., & Depollier, C. (1995). Snoring: Linear Stability Analysis and In-Vitro Experiments. *Journal of Sound and Vibration, 188*(1), 39-54.

Avanzini, F., & Walstijn, M. (2004). Modelling the mechanical response of the reed-mouthpiece-lip system of a clarinet. Part 1: a one-dimensional distributed model. *Acta Acustica United with Acustica, 90*, 537-547.

Axisa, F., & Antunes, J. (2007). *Modelling of Mechanical Systems: Fluid-Structure Interaction.* Elsevier Ltd. .

Balde, B., & Étienne, J. (2011). The flapping of a flag. Numerical investigation of a Kelvin-Helmholtz type instability. *Physics.*

Balint, T., & Lucey, A. (2005). Instability of a cantilevered flexible plate in viscous channel flow. *Journal of Fluids and Structures, 20*, 893-912.

Bergeot, B., & Vergez, C. (2022). Analytical prediction of delayed Hopf bifurcations in a simplified stochastic model of reed musical instruments. *Nonlinear Dynamics.*

Blevins, R. (1984). *Fluid Dynamics.* New York, USA: Van Nostrand Reinhold Company.

Boyd, J. P. (2000). The tau-method. In *Chebyshev and Fourier Spectral Methods* (pp. 473-479). New York, USA: Dover Publications.

Cengel, Y., & Cimbala, J. (2010). *Fluids Mechanics: Fundamentals and Applications.* McGraw-Hill.

Chai, Y., Gao, W., Ankay, B., Li, F., & Zhang, C. (2021). Aeroelastic analysis and flutter control of wings and panels: A review. *International Journal of Mechanical System Dynamics, 1*, 5-34.

Chen, M., Jia, L.-B., Wu, Y.-F., Yin, X.-Z., & Ma, Y.-B. (2014). Bifurcation an chaos of a flag in an insviscid flow. *Journal of Fluids and Structures, 45*, 124-137.

Cisonni, J., Lucey, A., Elliot, N., & Heil, M. (2017). The stability of a flexible cantilever in viscous channel flow. *Journal of Sound and Vibration.*

Cochelin, B. (1994). A path-following technique via an asymptotic numerical method. *Computers & Structures, 53*(5), 1181-1192.

Cochelin, B., & Medale, M. (2013). Power series analysis as a major breakthrough to improve the efficiency of asymptotic numerical method in the vicinity of bifurcations. *Journal of Computational Physics, 3*(2), 281-297.

Colinot, T. (2020). *Numerical simulation of woodwind dynamics : investigating nonlinear sound production behavior in saxophone-like instruments.* (PhD Thesis) Aix-Marseille Université.

Colinot, T., Vergez, C., Guillemain, P., & Doc, J.-B. (2021). Multistability of saxophone oscillation regimes and its influence on sound production. *Acta Acustica, 5*(33).

Debeurre, M., Grolet, A., & Thomas, O. (2023). Extreme nonlinear dynamics of cantilever beams: effect of gravity and slenderness on the nonlinear modes. *Nonlinear Dynamics*, 1-29.

Dike, M. V. (1982). *An Album of Fluid Motion.* Stanford: The Parabolic Press.

Doaré, O., Mano, D., & Ludena, J. C. (2011). Effect of spanwise confinement on flag flutter: Experimental measurements. *Physics of Fluids, 23*(111704).

Doaré, O., Sauzade, M., & Eloy, C. (2011). Flutter of an elastic plate in channel flow: Confinement and finite-size effects. *Journal of Fluids and Structures, 27*, 76-88.

Dowell, E. (1975). *Aeroelasticity of plates and shells.* Leyden: Noordhoff International Publishing.

Eloy, C., Kofman, N., & Schouveiler, L. (2012). The origin of hysteresis in the flag instability. *Journal of Fluid Mechanics, 691*, 583-593.

Eloy, C., Lagrange, R., Souilliez, C., & Schouveiler, L. (2008). Aeroelastic instability of cantilevered flexible plates in uniform flow. *Journal of Fluid Mechanics, 611*, 97-106.

Eloy, C., Souilliez, C., & Schouveiler, L. (2007). Flutter of a rectangular plate. *Journal of Fluids and Structures*, 904-919.

Fujita, K., Morikazu, H., & Shintani, A. (2007). A consideration on pre- and post-instability of an axisymmetric elastic beam subject to axial leakage flow. *Journal of Fluids and Structures, 23*, 463-478.

Gallegos, R., & Sharmaa, R. (2019). Small flags in rectangular channels: Dynamics and mean wake characteristics. *International Journal of Mechanical Sciences, 155*, 518-535.

Gibbs, S., Fichera, S., Zanotti, A., Ricci, S., & Dowell, E. (2014). Flow field around the flapping flag. *Journal of Fluids and Structures.*

Guillot, L. (2020). *(PhD Thesis) On a quadratic formalism for the continuation of the solutions of dynamical systems and their bifurcations - Application to reed instruments.* Marseille: Aix-Marseille Université.

Guillot, L., Cochelin, B., & Vergez, C. (2019). A generic and efficient Taylor series-based continuation method using a quadratic recast of smooth nonlinear systems. *International Journal for Numerical Methods in Engineering, 119*(5).

Guillot, L., Cochelin, B., & Vergez, C. (2019). A Taylor series-based continuation method for solutions of dynamical systems. *Nonlinear Dynamics, 98*(11).

Guillot, L., Lazarus, A., Thomas, O., Vergez, C., & Cochelin, B. (2020). A purely frequency based Floquet-Hill formulation for the efficient stability computation of periodic solutions of ordinary differential equations. *Journal of Computational Physics, 416*(109477).

Guo, C., & Païdoussis, M. (2000). Stability of rectangular plates with free-edges in two-dimensional inviscid channel flow. *Journal of Applied Mechanics, 67*, 171-176.

Hairer, E., & Wanner, G. (1996). *Solving Ordinary Differential Equations II: Stiff and Differential-Algebraic Problems.* New York: Springer-Verlag.

Hartlen, R., & Currie, I. (1970). Lift-Oscillator Model of Vortex-Induced Vibration. *Journal of the Engineering Mechanics Division.*

Hidalgo, P., Jha, S., & Glezer, A. (2015). Enhanced heat transfer in air cooled heat sinks using aeroelastically fluttering reeds. *Thermal Investigations of ICs and Systems (THERMINIC)*, 1-6.

Hirs, G. (1973). A bulk-flow theory for turbulence in lubricant films. *ASME Journal of Lubrication Technology, 95*, 137-146.

Howell, R., Lucey, A., Carpenter, P., & Pitman, M. (2009). Interaction between a cantilevered-free flexible plate and ideal flow. *Journal of Fluids and Structures*, 544-566.

Huang, L. (1995). Flutter of cantilevered plates in axial flow. *Journal of Fluids and Structures, 9*, 127-147.

Huang, L. (1995). Mechanical Modeling of Palatal Snoring. *Journal of the Acoustical Society of America, 97*, 3642-3648.

Huang, L., & Zhang, C. (2013). Modal analysis of a cantilever plate flutter. *Journal fo Fluids and Structures*, 273-289.

Huang, W.-X., & Sung, H. J. (2010). Three-dimensional simulation of a flapping flag in uniform flow. *Journal of Fluid Mechanics, 653*, 301-336.

Idel'Cik, I. (1994). *Handbook of Hydraulic Resistance* . Boca Raton, USA: CRC Press.

Inada, F., & Hayama, S. (1990). A Study on the Leakage-Flow-Induced Vibrations. Part 1: Fluid Dynamic Forces and Moments Acting on the Walls of a Narrow Tapered Passage. *Journal of Fluids and Structures, 4*, 395-412.

Inada, F., & Hayama, S. (1990). A Study on the Leakage-Flow-Induced Vibrations. Part 2: Stability Analysis and Experiments for Two-Degree-of-Freedom Systems Combining Translational and Rotational Motions. *Journal of Fluids and Structures, 4*, 413-428.

Jankee, G., & Ganapathisubramani, B. (2022). Influence of geometrical parameters on the hyteresis of flutter onset in confined configurations. *Experiments in Fluids, 63*.

Juang, J., & Pappa, R. (1985). An eigensystem realization algorithm for modal parameter identification and model reduction. *Journal of Guidance Control and Dynamics, 8*(5), 620-627.

Kaneko, S., Nakamura, T., Inada, F., Kato, M., Ishihara, K., Nishihara, T., . . . Langthjem, M. (2008). *Flow-Induced Vibrations: Classifications and Lessons from Practical Experiences.* Amsterdam, Netherlands: Elsevier.

Karkar, S., Cochelin, B., & Vergez, C. (2013). A high-order, purely frequency based harmonic balance formulation for continuation of periodic solutions: The case of non-polynomial nonlinearities. *Journal of Sound and Vibration, 332*(4).

Kornecki, A., Dowell, E., & O'Brien, J. (1976). On the aeroelastic instability of two-dimensional panels in uniform imcompressible flow. *Journal of Sound and Vibration, 47*(2), 163-178.

Krack, M., & Gross, J. (2019). *Harmonic balance for nonlinear vibration problems.* Springer.

Kutz, J., Brunton, S., Brunton, B., & Proctor, J. (2016). *Dynamics Mode Decomposition: data-driven modeling of complex systems.* Philadelphia: Society for Industrial and Applied Mathematics.

Kuznetsov, Y. (2004). *Elements of Applied Bifurcation Theory.* Springer.

Lanczos, C. (1956). The tau-method. In *Applied Analysis* (pp. 465-469). Englewood Cliffs, USA: Prentice Hall.

Lee, H. J., Sherrit, S., Tosi, L. P., Walkemeyer, P., & Colonious, T. (2015). Piezoelectric Energy Harvesting in Internal Fluid Flow. *Sensors, 15*, 26039-26062.

Lee, J., Kim, D., & Kim, H.-Y. (2021). Contact behavior of a fluttering flag with an adjacent plate. *Physics of Fluids, 33*.

Li, Z., Zhou, S., & Yang, Z. (2022). Recent progress on flutter-based wind energy harvesting. *International Journal of mechanical system dynamics, 2*, 82-98.

Mahooti, M. (2022, August). *Radau IIA.* (MATLAB Central File Exchange) Retrieved from https://www.mathworks.com/matlabcentral/fileexchange/56162-radau-iia

Maia, N., & Silva, J. (2003). *Theoretical and Experimental Modal Analysis.* Research Studies Press.

Manlab: An interactive path-following and bifurcation analysis software. (n.d.). Retrieved November 23, 2022, from http://manlab.lma.cnrs-mrs.fr/

Michelin, S., Smith, S., & Glover, B. (2008). Vortex shedding model of a flapping flag. *Journal of Fluid Mechanics, 617*, 1-10.

Modarres-Sadeghi, Y. (2022). *Introduction to Fluid-Structure Interactions.* Springer.

Morris-Thomas, M., & Steen, S. (2009). Experiments on the stability and drag of a flexible sheet under in-plane tension in uniform flow. *Journal of Fluids and Structures*, 815-830.

Mulcahy, T. M. (1988). One-dimensional Leakage-flow vibration instabilities. *Journal of Fluids and Structures, 2*, 383-403.

Nagakura, H., & Kaneko, S. (1993). Stability of a cantiliver beam subject to one-dimensional leakage flow. *Proceedings Asia-Pacific Conference '93, Kitakyushiu, Japan, 1*, 352-359.

Nagakura, T., Kaneko, S., Inada, F., Kato, M., Ishihara, K., Nishihara, T., & Mureithi, N. (2014). *Flow-Induced Vibrations: Classifications and Lessons from Practical Experiences.* San Diego, California: Academic Press.

Nayfeh, A., & Pai, F. (2004). *Linear and Nonlinear Structural Mechanics.* Wiley-VCH.

Païdoussis, M. P. (2004). *Fluid-Structure Interactions: Slender Structures and Axial Flow.* San Diego, California: Academic Press.

Païdoussis, M., & Issid, N. (1974). Dynamic stability of pipes conveying fluid. *Journal of Sound and Vibration*, 267-294.

Païdoussis, M., Li, G., & Moon, F. (1989). Chaotic oscillations of the autonumous system of a constrained pipe conveying fluid. *Journal of Sound and vibration, 135*(1), 1-19.

Païdoussis, M., Li, G., & Rand, R. (1991). Chaotic motions of a constrained pipe conveying fluid: comparison between simulation, analysis, and experiment. *Journal of Applied Mechanics, 58*, 559-565.

Païdoussis, M., Price, S., & Langre, E. (2011). *Fluid-Structure Interactions: Cross-flow-induced instabilities.* New York: Cambridge University Press.

Pappa, R., & Elliot, K. (1993). Consistent mode indicator for the eigensystem realization algorithm. *Journal of Guidance Control and Dynamics, 16*(5), 852-858.

Perotin, L. (1994). Fluid-structure coupling between a vibrating cylinder and a narrow annular flow. *Nuclear Engineering and Design*, 279-289.

Pintelon, R., Guillaume, P., Belder, K., & Rolain, Y. (2003). Measurement of young's modulus via modal analysis experiments: a system identification approach. *IFAC System Identification*, (pp. 375-380). Rotterdam .

Piteau, P., & Antunes, J. (2012). A theoretical model and experiments on the nonlinear dynamics of parallel plates subject to laminar/turbulent squeeze-film forces. *Journal of Fluids and Structures, 33*, 1-18.

Prasanth, T., Premchandran, V., & Mittal, S. (2011). Hysteresis in vortex-induced vibrations: critical blockage and effect of m*. *Journal of Fluid Mechanics, 671*, 207-225.

Rayleigh, L. (1879). On the Instability of Jets. *Proceedings of the London Mathematical Society, 10*, 4-13.

Rosa, S. D., & Franco, F. (2008). Exact and numerical responses of a plate under a turbulent boundary layer excitation. *Journal of Fluids and Structures*, 212-230.

Salama, A. (2021). Velocity profile representation for fully developed turbulent flow in pipes: a modified power law. *Fluids*.

Seydel, R. (1994). *Practical Bifurcation and Stability Analysis: from Equilibrium to Chaos.* New York: Springer.

Shamloo, H., Norooz, R., & Mousavifard, M. (2015). A review of one-dimensional unsteady friction models for transient pipe flow. *Cumhuriyet University Faculty of Science Journal (CSJ)*, 2278-2288.

Shelley, M., & Zhang, J. (2011). Flapping and bending bodies interacting with fluid flows. *Annual Review of Fluid Mechanics, 43*, 449-465.

Sherrit, S., Lee, H., Walkemeyer, P., Winn, T., Tosi, L., & Colonius, T. (2015). Fluid flow nozzle energy harvesters. *Sensors and Smart Structures Technologies for Civil, Mechanical, and Aerospace Systems, 9435.*

Shoele, K., & Mittal, R. (2016). Flutter instability of a thin flexible plate in a channel . *Journal of Fluid Mechanics, 786*, 29-46.

Slaughter, W. S. (2001). *The Linearized Theory of Elasticity.* New York: Springer Science + Business Media, LLC.

Soares, F., Antunes, J., Debut, V., Vergez, C., Cochelin, B., & Silva, F. (2022). A nonlinear analytical formulation for the 1D modelling of a flexible beam in channel flow. *Journal of Fluids and Structures, 113.*

Soares, F., Antunes, J., Debut, V., Vergez, C., Cochelin, B., & Silva, F. (2023). A Galerkin formulation for the nonlinear analysis of a flexible beam in channel flow. *Journal of Fluids and Structures*, vol. 118.

Soares, F., Vergez, C., Antunes, J., Debut, V., Cochelin, B., & Silva, F. (2023). Bifurcation analysis of cantilever beams in channel flow. *Journal of Sound and Vibration, vol. 567.*

Strogatz, S. H. (1994). *Nonlinear Dynamics and Chaos: with applications to physics, biology, chemistry and engineering.* New York: Perseus Books.

Taneda, S. (1968). Waving Motions of Flags. *Journal of the Physical Society of Japan, 24*(2), 392-401.

Tang, D., Yamamoto, H., & Dowell, E. (2003). Flutter and limit cycle oscillations of two-dimensional panels in three-dimensional axial flow. *Journal of Fluids and Structures, 17*, 225-242.

Tang, L., & Païdoussis, M. (2007). On the instability and post-critical behaviour of two-dimensional cantilevered flexible plates in axial flow. *Journal of Sound and Vibration, 305*, 97-115.

Tang, L., Païdoussis, M., & Jiang, J. (2009). The dynamics of variants of two-dimensional cantilevered flexible plates in axial flow. *Journal of Sound and Vibration*, 214-231.

Tanida, Y. (2001). Stability of a soft plate in channel flow (aerodynamic aspects of palatal flutter). *JSME International Journal, 44*, 8-13.

Tavallaeinejad, M., Salinas, M. F., Païdoussis, M. P., Legrand, M., Kheiri, M., & Botez, R. M. (2021). Dynamics of inverted flags: Experiments and comparison with theory. *Journal of Fluids and Structures, 101*(103199).

Tetlow, G., & Lucey, A. (2009). Motions of a cantilevered flexible plate in viscous channel flow driven by a constant pressure drop. *Communications in Numerical Methods in Engineering, 25*(5), 463-482.

Tosi, L. (2018). *Fluid-Structure Instability in an Internal Flow Energy Harvester (Ph.D. Thesis).* California Institute of Technology.

Tosi, L. P., & Colonious, T. (2019). Modelling and simulation of a fluttering cantilever in channel flow. *Journal of Fluids and Structures, 89*, 174-190.

Tosi, L. P., Dorschner, B., & Colonious, T. (2021). Flutter instability in an internal flow energy harvester. *Journal of Fluid Mechanics, 915.*

Touzé, C., & Thomas, O. (2004). Reduced-order modelling for a cantilever beam subjected to harmonic forcing. *EUROMECH 457.* Fréjus, France.

Virgin, L., Santillan, S., & Holland, D. (2007). Effect of gravity on the vibration of vertical cantilevers. *Mechanics Research Communications*, 312-317.

Virot, E., Amandolese, X., & Hémon, P. (2013). Fluttering flags: an experimental study of fluid forces. *Journal of Fluids and Structures, 43*, 385-401.

Walstijn, M., & Avanzini, F. (2007). Modelling the Mechanical Response of the Reed-mouthpiece-lip System of a Clarinet. Part II: A Lumped Model Approximation. *Acta Acustica united with Acustica, 93*, 435-446.

Wang, J., Geng, L., Ding, L., Zhu, H., & Yurchenko, D. (2020). The state-of-the-art review on energy harvesting from flow-induced vibrations. *Applied Energy*, 114902.

Watanabe, Y., Suzuki, S., Sugihara, M., & Sueoka, Y. (2002). An experimental study of paper flutter. *Journal of Fluids and Structures, 16*(4), 529-542.

Woiwode, L., Balaji, N., Kappauf, J., Tubita, F., Guillot, L., Vergez, C., . . . Krack, M. (2020). Comparison of two algorithms for harmonic balance and path continuation. *Mechanical Systems and Signal Processing.*

Wu, X., & Kaneko, S. (2005). Linear and Nonlinear analyses of sheet flutter induced by leakage flow. *Journal of Fluids and Structures, 20*, 927-948.

Wu, Y., Cheng, Z., McConkey, R., Lien, F., & Yee, E. (2022). Modelling of flow-induced vibration of bluff bodies: a comprehensive survey and future prospects. *Energies.*

Yadykin, Y., Tenetov, V., & Levin, D. (2001). The flow induced vibration of a flexible strip hanging vertically in parallel flow. Part 1: temporal aeroelastic instability. *Journal of Fluids and Structures, 15*, 1167-1185.

Yamaguchi, N., Yokota, K., & Tsujimoto, Y. (2000). Flutter limits and behaviors of a flexible thin sheet in high-speed flow - I: analytical method for prediction of the sheet behavior. *Journal of Fluids Engineering*, 65-73.

Yamahuchi, N., Sekiguchi, T., Yokota, K., & Tsujimoto, Y. (2000). Flutter limits and behavior of a flexible thin sheet in high-speed flow - II: experimental results and predicted behaviors for low mass ratios. *Journal of Fluids Engineering*, 74-83.

Yu, Y., Liu, Y., & Amandolese, X. (2019). A Review on Fluid-Induced Flag Vibrations. *Applied Mechanics Reviews, 71*(010801).

Zhang, J., Childress, S., Libchaber, A., & Shelley, M. (2000). Flexible filaments in a flowing soap film as a model for one-dimensional flags in a two-dimensional wind. *Nature, 408*, 835-839.

Zhao, W., Païdoussis, M., Tang, L., Liu, M., & Jiang, J. (2012). Theoretical and experimental investigations of the dynamics of cantilevered flexible plates subject to axial flow. *Journal of Sound and Vibration*, 575-587.

Appendix A

A. Exploiting the orthogonality of Chebyshev polynomials

Here we illustrate the structure of the matrices (4.1.4) resulting from the orthogonal projection of the momentum equations. The matrix associated with the time-derivative of the velocity field is given by

$$E_{nr} = \int_0^1 \bar{T}_n(x)\bar{T}_r(x)\bar{w}(x)dx = \frac{1}{2}\int_{-1}^{1} \frac{T_n(x)T_r(x)}{\sqrt{1-x^2}}dx \quad , \quad \begin{cases} n = 0,1,\cdots,N \\ r = 0,1,\cdots,R-1 \end{cases} \tag{A.1}$$

Notice the relation between the shifted $\bar{T}_n(x)$ and unshifted basis $T_n(x)$. This matrix is diagonal and has the following structure

$$E_{nr} = \frac{\pi}{4}\begin{bmatrix} 2 & 0 & \cdots & 0 \\ 0 & 1 & 0 & \\ \vdots & 0 & 1 & \\ 0 & & & \ddots \end{bmatrix} \tag{A.2}$$

The matrix associated with the pressure term is

$$H_{tr} = \int_0^1 \bar{T}_t'(x)\bar{T}_r(x)\bar{w}(x)dx = \int_{-1}^{1} \frac{T_t'(x)T_r(x)}{\sqrt{1-x^2}}dx \quad , \quad \begin{cases} t = 0,1,\cdots,R \\ r = 0,1,\cdots,R-1 \end{cases} \tag{A.3}$$

and has the following upper-triangular structure

$$H_{tr} = \pi\begin{bmatrix} 0 & 1 & 0 & 3 & 0 & 5 & 0 & \\ & 0 & 2 & 0 & 4 & \ddots & 6 & \\ & & 0 & 3 & \ddots & 5 & 0 & \ddots \\ \vdots & & & \ddots & 4 & 0 & 6 & \\ & & & & 0 & 5 & 0 & \ddots \\ & & & & & 0 & 6 & \\ 0 & & & & & & & \ddots \end{bmatrix} \tag{A.4}$$

The tri-dimensional matrix associated with the nonlinear convection term is given by

$$F_{nsr} = \int_0^L \bar{T}_n'(x)\bar{T}_s(x)\bar{T}_r(x)w(x)dx = \int_{-1}^{1} \frac{T_n'(x)T_s(x)T_r(x)}{\sqrt{1-x^2}}dx \quad , \quad \begin{cases} n = 0,1,\cdots,N \\ s = 0,1,\cdots,N \\ r = 0,1,\cdots,R-1 \end{cases} \tag{A.5}$$

and its structure can be illustrated by the following

$$F_{0sr} = 0 \quad ; \quad F_{1sr} = \frac{\pi}{2}\begin{bmatrix} 2 & 0 & 0 & \cdots & 0 \\ 0 & 1 & 0 & & \\ 0 & 0 & 1 & & \\ \vdots & & & \ddots & \\ 0 & & & & \end{bmatrix} \; ; \; F_{2sr} = \pi\begin{bmatrix} 0 & 2 & 0 & \cdots & 0 \\ 2 & 0 & 1 & \ddots & \\ 0 & 1 & 0 & 1 & 0 \\ \vdots & \ddots & 1 & & \ddots \\ 0 & & 0 & \ddots & \end{bmatrix}$$

$$F_{3sr} = \frac{3\pi}{2}\begin{bmatrix} 2 & 0 & 2 & 0 & \cdots & 0 \\ 0 & 2 & 0 & 1 & 0 & \\ 2 & 0 & 1 & 0 & 1 & \\ 0 & 1 & 0 & 1 & \ddots & \ddots \\ \vdots & 0 & 1 & \ddots & \ddots & \\ 0 & & & \ddots & & \end{bmatrix} \; ; \; F_{4sr} = 2\pi\begin{bmatrix} 0 & 2 & 0 & 2 & 0 & 0 & \cdots & 0 \\ 2 & 0 & 2 & 0 & 1 & 0 & & \\ 0 & 2 & 0 & 1 & 0 & 1 & \ddots & \\ 2 & 0 & 1 & \ddots & 1 & \ddots & \ddots & \\ 0 & 1 & 0 & 1 & & \ddots & & \\ 0 & 0 & 1 & \ddots & \ddots & & & \\ \vdots & & \ddots & \ddots & & & & \\ 0 & & & & & & & \end{bmatrix} \; ; \; \text{etc.} \tag{A.6}$$

Appendix B

B. Experimentally identified modal parameters

Table B.1 - Identified modal frequencies for the bending modes of all tested beams.

	Bending mode frequency (Hz)							
	1	2	3	4	5	6	7	8
0.3	3.937	23.71	66.75	131.5	218.5	327.9	458.9	609.6
0.25	3.358	20.1	56.18	110.3	182.6	273.2	381.8	506.5
0.2	2.84	16.38	45.87	90.42	150.3	225.2	314.8	415
0.18	2.608	14.92	41.4	81.03	134	199.9	278.4	370.2
0.15	2.179	11.25	31.38	63.68	108.5	166.4	236.8	316.8
0.12	2.12	11.40	31.5	59.1	95.1	145.8	205.7	268.9
0.1	1.933	10.08	29.9	55.85	87.96	126.6	171.4	213.7
0.09	1.719	8.301	22.37	43.25	71.44	104.5	144.3	190.2
0.08	1.524	6.747	17.85	34.57	57.19	85.6	120.3	159.9
0.07	1.439	5.868	15.65	31.5	51.43	75.04	102.2	133.1
0.06	1.575	6.764	17.91	31.61	51.91	73.91	101.8	129.9
0.05	1.35	6.60	16.8	28.23	45.4	64.2	89.9	112.0
0.04	1.315	4.646	11.63	21.69	36.03	53.32	73.64	95.76
0.03	1.245	3.843	8.642	15.49	27.64	37.49	51.34	62.46
0.02	1.159	2.74	7.972	12.85	22.68	31.35	47.92	-
0.01	0.942	2.331	6.30	11.00	16.49	24.35	-	-

Table B.2 - Identified modal damping ratios for the bending modes of all tested beams.

	Bending mode damping ratio (%)							
	1	2	3	4	5	6	7	8
0.3	0.25	0.95	0.69	0.29	0.30	0.32	0.39	0.37
0.25	0.30	0.57	0.32	0.27	0.27	0.28	0.29	0.36
0.2	0.31	0.45	0.30	0.25	0.21	0.25	0.25	0.27
0.18	0.31	0.42	0.29	0.27	0.28	0.27	0.34	0.36
0.15	0.38	0.27	0.34	0.22	0.20	0.19	0.20	0.23
0.12	0.52	0.39	0.19	0.16	0.12	0.12	0.19	0.22
0.1	0.71	0.42	0.44	0.36	0.34	0.32	0.29	0.14
0.09	0.63	0.42	0.41	0.37	0.25	0.35	0.33	0.31
0.08	0.54	0.40	0.35	0.29	0.24	0.25	0.21	0.25
0.07	0.62	0.41	0.35	0.24	0.22	0.26	0.25	0.25
0.06	0.77	0.42	0.45	0.20	0.18	0.18	0.16	0.16
0.05	1.05	0.52	0.41	0.22	0.13	0.12	0.13	0.11
0.04	0.96	0.69	0.41	0.35	0.24	0.20	0.19	0.19
0.03	1.86	1.02	0.74	0.43	1.53	0.24	0.38	0.27
0.02	1.40	1.07	0.82	0.64	0.60	0.33	0.31	-
0.01	1.54	1.65	1.97	1.47	0.86	0.95	-	-

Appendix C

C. Effect of gravity on the vibrations of a vertical cantilever beam

The content in this appendix is based on the model presented in Virgin et al. (2007), where the vibrations of a vertically mounted cantilever beam are studied. A simple model for the small vibrations of a downwards pointing conservative cantilever beam is given by

$$EI\frac{\partial^4 y}{\partial x^4} + \rho_s S\frac{\partial^2 y}{\partial t^2} \pm \rho_s Sg\frac{\partial}{\partial x}\left[(L-x)\frac{\partial y}{\partial x}\right] = 0 \tag{C.1}$$

where g is the gravitational acceleration. The ± sign refers to the orientation of the beam, i.e. the plus sign is used for a upright beam (free-tip pointing up) while the minus sign is used for a downward facing beam (free tip pointing down). Note that the gravitational term corresponds to a gravity-induced axial tension. Furthermore, the distribution of this tension is not uniform, as defined by the term $(L-x)$. For example, in a downwards facing beam, the clamped end will feel the tension induced by the full weight of the beam, while the free-tip will not be affected.

In dimensionless form, using L and ω_0 (defined in Eq.(2.29)) as the characteristic length and time scales, Eq.(C.1) can be written as

$$\frac{\partial^4 y}{\partial x^4} + \frac{\partial^2 y}{\partial t^2} - \alpha\frac{\partial}{\partial x}\left[(1-x)\frac{\partial y}{\partial x}\right] = 0 \tag{C.2}$$

where all variables are now dimensionless (as opposed to their physical counterpart as in (C.1)); and α is a dimensionless parameter governing the gravity-induced tension

$$\alpha = \frac{\rho_s SgL^3}{EI} \tag{C.3}$$

Note that here we will assume a positive α only (free tip pointing downwards). There are different ways to solve this equation. Consistent with the framework used in this thesis, we discretize the problem in terms of M *in-vacuo* beam modes, in absence of gravity, leading to

$$\ddot{q}_m(t) + \omega_m^2 q_m(t) = \alpha\sum_{n=1}^{N} G_{mn}q_n(t) \quad , \quad \text{for } m = 1,2...M \tag{C.4}$$

where

$$G_{mn} = \int_0^1 \left[(1-x)\frac{\partial^2\phi_m}{\partial x^2}\phi_n - \frac{\partial\phi_m}{\partial x}\phi_n\right]\partial x \tag{C.5}$$

The frequencies $\hat{\omega}_n$ and mode shapes $\hat{\phi}_n(x)$ of the vertical cantilever under self-weight can then be calculated by solving the eigenvalue problem

$$\left[\mathbf{M}\lambda^2 + (\mathbf{K} - \alpha G_{mn})\right]\Phi = 0 \quad , \quad \text{where } \hat{\omega}_n = \mathrm{Im}(\lambda) \tag{C.6}$$

where $\mathbf{M}$ and $\mathbf{K}$ are the diagonal mass and stiffness modal matrices of the *in-vacuo* beam.

The natural frequencies of the cantilever beam under self-weight are shown in Figure C.1 with respect to α, normalized to either (a) the characteristic frequency ω_0 or (b) the fundamental frequency of the cantilever $\hat{\omega}_1$. One can see that when $\alpha \to 0$, the frequencies converge that of a classical cantilever beam (ignoring gravity). On the other hand, increasing α leads to a stiffening effect that increases all natural frequencies. Notably, in Figure C.1(a) we see that lower order modes are more strongly affected (i.e. their frequencies begin to shift at lower values of α). When $\alpha \to \infty$, results converge to the classical "hanging chain" solution (as if the bending stiffness term in Eq.(C.1) was ignored). As a note, the values of α for the experimental beams used in this thesis ranged from $0.75 < \alpha < 750$.

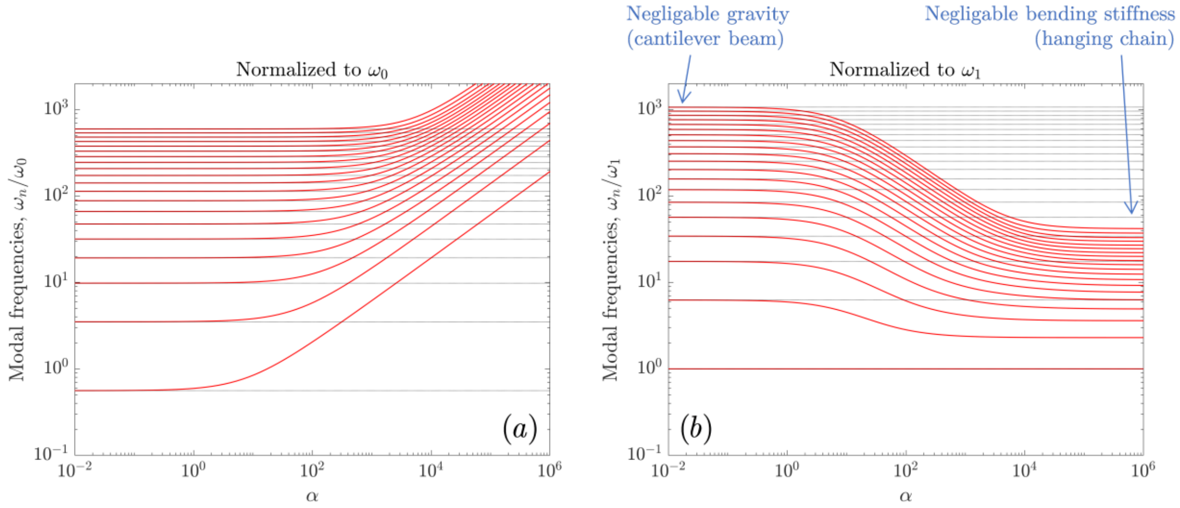

Figure C.1 – Evolution of the first 20 natural frequencies of a vertically mounted (downwards facing) cantilever beam under the effect of gravity, as a function of the dimensionless parameter α. The same results are shown normalized to (a) the characteristic frequency ω_0 and (b) the fundamental frequency of the beam ω_1. Black dotted lines correspond to the frequencies of the beam when ignoring gravitational effects.

Due to the uneven distribution of axial tension along the beam, the mode shapes will also be affected by gravity. To illustrate, Figure C.2 shows the shapes of the first four beam modes for various values of α. Notably, because the axial tension is larger near the clamped end, larger values of α will lead to mode shapes where the motion is more concentrated at the free-tip.

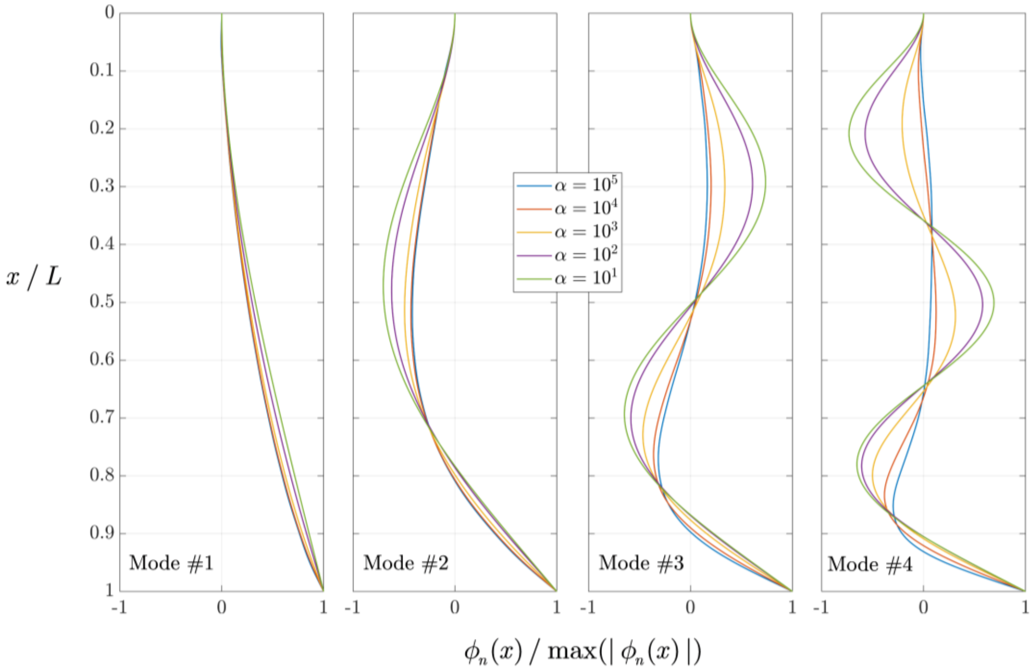

Figure C.2 – First four mode shapes of a downwards facing cantilever beam for various values of α .

As a final note to the interested reader, it is worth underlining that the developments presented here are referring to the effect of gravity on the *small* amplitude vibrations of slender beams. As we have seen, gravity will have a stiffening or softening effect depending on the orientation of the beam (downwards or upright). A very recent publication (Debeurre et al., 2023) has dealt with the effects of gravity in nonlinear contexts, with large amplitudes of vibrations. They have found, among other things, that gravity will have a linear stiffening effect but a softening nonlinear effect in downwards (hanging) configurations. The situation is reversed for upright (standing) configurations. This shows that, particularly when dealing with extremely slender/ long beams, dynamics will be significantly perturbed by gravity, in complex manners, and the classical beam models will often become ineffectual.

Appendix D

D. Nonlinear dynamics in systems with asymmetric flow

In this section we report on some interesting dynamical behavior observed during the experiments. Contrary to previously presented results, based on symmetric configurations, here asymmetry is induced in the system by limiting the flow rate entering one of the channels. This was achieved by adding an obstruction to the entry of the one channel, while the other is left unobstructed. A piece of blutack (Bostik) was placed at the entry of the left-hand channel which allowed for the complete closure (no flow), but also to different levels of partial obstruction, as illustrated in Figure D.1. Therefore, we were able to explore the system behavior in the whole range between a fully open (symmetric system, as before), partially obstructed and fully closed left-hand channel. The reduction of the area at the entrance of the channel increases flow resistance and hence leads to asymmetric flow velocities in the two channels (lower in the partially obstructed channel).

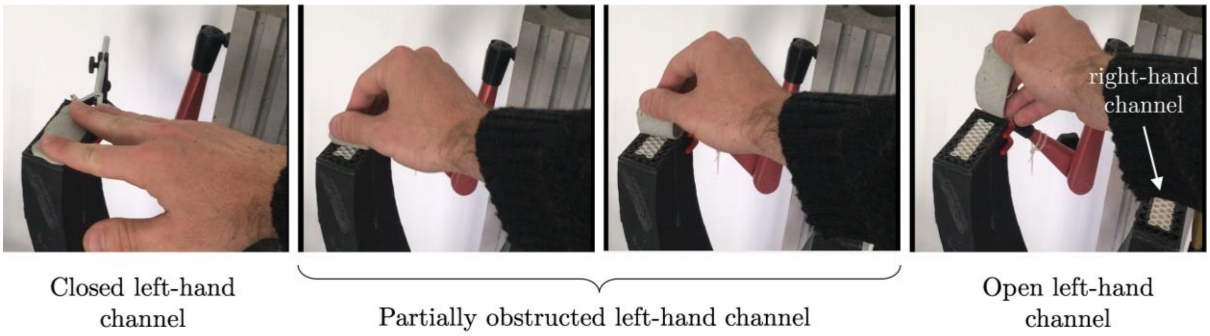

Figure D.1 – Illustration of the mechanism used to gradually increase flow resistance in the left-hand channel. The piece of blutack served to reduce the entry area in one of the channels, hence increasing flow resistance.

In these tests, the fan-speed of the aspiration unit remained constant, while the flow resistance was increased gradually (entry area reduced). It is worth noting that, unfortunately, we were not able to measure the flow velocity at each channel independently, which would have provided important quantitative information. However, the aim of this sub-section is mostly to showcase, qualitatively, the encountered behavior. Certainly, a dedicated experimental set-up would have to be built for a more precise quantitative assessment. As mentioned before, the limited power of the axial fan motor was unable to maintain a constant flow rate when the flow-circuit resistance was increased upstream. Hence, in these experiments, the global flow rate decreases slightly (10-20%) as the entry area in the left-hand channel is reduced. As consequence, the global flow rate (here expressed by U^*, defined as earlier) was used as a control parameter in the experimental results that follow. Note that, effectively, increasing the flow resistance in the left channel does not reduce its velocity while maintaining a constant velocity in the open channel. Rather, this resistance introduces an asymmetry in the velocities in the two channels. In fact, flow velocities in the open channel will actually increase when the entry area of the left channel is reduced.

Finally, we note that, due to time constraints, we were not able to presents modelling results that attempt to recreate these experimental configurations. However, we believe that such configurations could eventually be explored by the presented model by gradually increasing the value of the entry head-loss coefficient K_0 in one of the channels.

D.1 Closed-open configuration and the modified static equilibrium

Perhaps the first aspect to discuss is that, when one of the channels was fully closed, we have observed no dynamic instabilities. Independent of the velocity of the flow (passing through the right-hand channel only), the sole solution observed was a static equilibrium where the beam is moved towards the side of the closed channel, as illustrated in Figure D.2(a). As flow velocities increase, the beam is further pushed against the wall of the closed channel. It is not entirely intuitive why the beam would be pushed towards the closed-channel side. It is worthwhile considering that, due to the clearance gap (beam-wall distance in the spanwise direction), the two channels are not truly separated, even when the beam is touching the left wall.

In an attempt at explaining this behavior, some static pressure measurements were performed on the side wall, along the beam length, as illustrated in Figure D.2(b). Here, a series of small side-holes were drilled in the channel walls (perpendicular to the flow direction). Then, placing pressure sensors (tubes) were then used to measure the *static* pressure along the beam's length, for each channel. The aim was to get an idea of the pressure fields involved in this equilibrium solutions. A qualitative illustration of the results obtained are shown in Figure D.2(b). Note however, that these pertain to static pressure only. That is, the variations of dynamic pressure due to the passing flow in the open channel are not accounted for. Results indicate that, even when the beam is touching the side wall, the pressure at the closed channel side correspond to the driving pressure P_L.

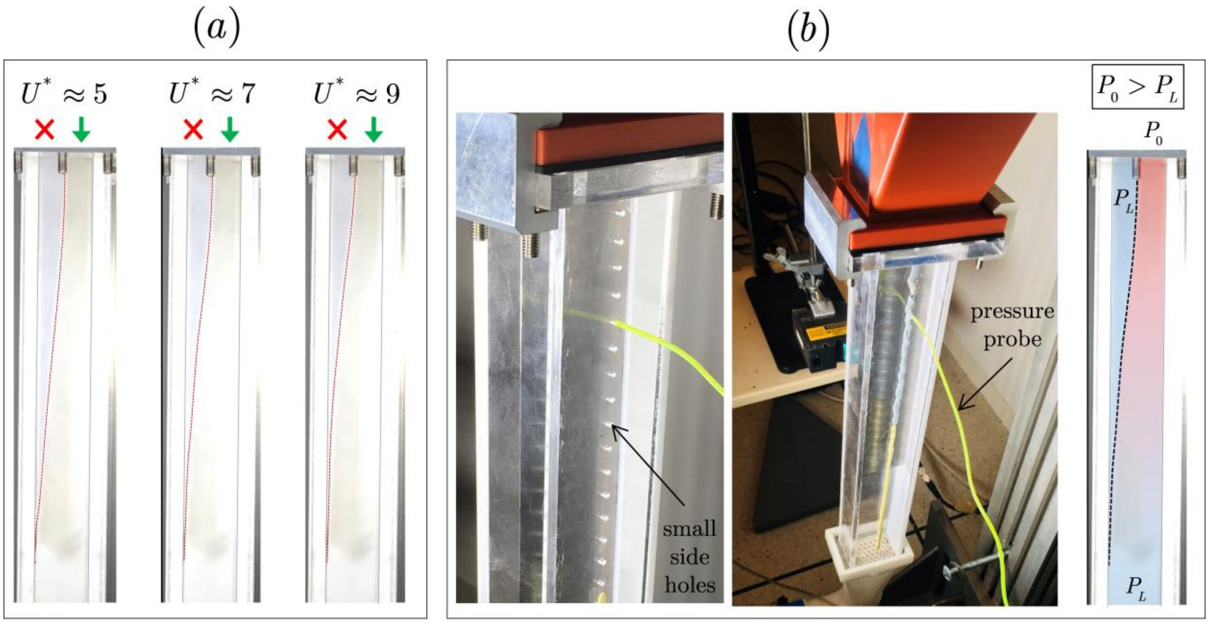

Figure D.2 – (a) Static equilibrium position at different flow velocities when the left-hand channel is completely closed, in a system with $M^* = 0.54$. Note: lines were drawn over the images to aid visibility. (b) Static pressure measurements along the channels: measurement set-up and qualitative illustration of results (blue and red areas refer to the downstream and atmospheric pressures, P_L and P_0, respectively).

D.2 Dynamics in a system with partially obstructed channel

When the obstructed channel is not fully closed but only partially obstructed, the equilibrium loses its stability a sufficiently large velocities leading to limit cycle oscillations. In the results that follow, the axial fan was set to a relatively large velocity with the two channels fully open (symmetric). Then, the resistance upstream was increased step-by-step until the left-hand channel was fully closed. These tests were performed for a set of different beams with different thicknesses, with associated mass ratios ranging from $0.2 < M^* < 2$. Figure D.3 shows the evolution of the amplitude A^* and base frequency Ω^* of the LCOs as a function of the flow resistance, here portraited by the reduction in the (global) flow velocity U^*. Additionally, the spectra of the normalized beam-tip displacement $y(L,t)\,/\,H_1$ is shown. It will become evident further on that, due to the nature of the new equilibrium (where $\overline{y}(L) = 1$), the amplitude of the LCOs here are more appropriately defined by

$$A^* = \frac{1}{T}\int_0^T \left| \frac{y(L,t)}{H_1} - 1 \right| dt \tag{D.1}$$

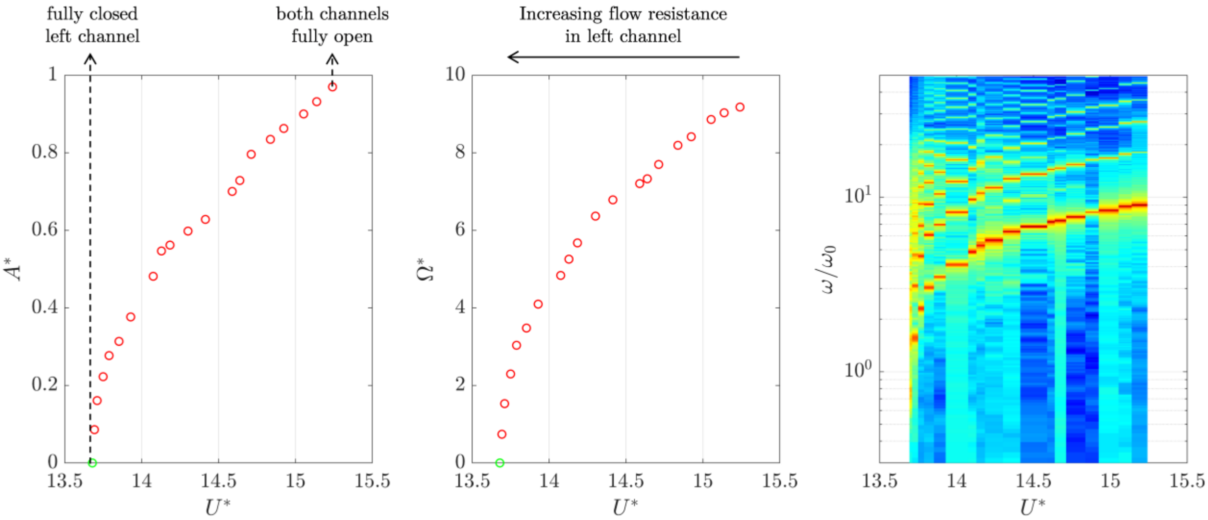

Figure D.3 - Evolution of the amplitude A^* (left), base frequency Ω^* (center) of the LCOs as a function of the (global) flow velocity U^*, in a system with $M^* = 1.25$. The right plot illustrates the spectra of the beam-tip displacement $y(L,t) / H_1$.

As the resistance in the left-hand channel is increased, the amplitude of oscillation decreases but, more notably, the frequency of the LCO also decreases steadily, approaching zero $\Omega^* \to 0$ (infinite period) as the channel approaches full closure, where the oscillations finally stop and the system remains in a static equilibrium as discussed above.

To better illustrate the nature of the dynamics encountered, Figure D.4 shows the beam-tip displacement in the time domain as well as the corresponding spectra for different flow velocities. The top plots in Figure D.4 refer to the symmetric case (left channel fully open). As expected, this leads to a symmetric oscillation of the beam tip, confirmed by the low amplitude of the even harmonics. Note that intermittent impacts occur against the side walls. As the resistance in the left channel increases, the frequency of the oscillation decreases and the asymmetry leads to oscillations where the beam-tip impacts the left wall $(y(L,t) / H_1 = 1)$ more prominently. At the bottom case, where the channel is nearly closed, the beam-tip stays attached to the side wall for most of the limit-cycle, detaching in an abrupt manner (in a “whip”-like motion) once every second (approximately $\Omega \approx 1\,\text{Hz}$). To clarify this behavior, Figure D.5 shows a set of overlapped frames illustrating the change in beam motion as the resistance in the left channel is increased. Furthermore, a sequence of frames is shown in Figure D.6, to better illustrate the motion of the beam during these low-frequency regimes. It becomes clear that as the flow rate in one of the channels is decreased, the beam motion tends to be pushed towards the side with less flow. In the low frequency regimes where the channel is nearly closed, while the beam-tip is attached to the side wall for a large part of the limit cycle (Figure D.6), the rest of the beam is slowly and gradually pushed towards the side with more flow, until a critical point is reached where the beam tip detaches the side wall and, in an abrupt manner, the whole beam is pushed towards the right side, before again returning its initial position (close to the equilibrium discussed above). Videos of these LCOs are provided along with the thesis.

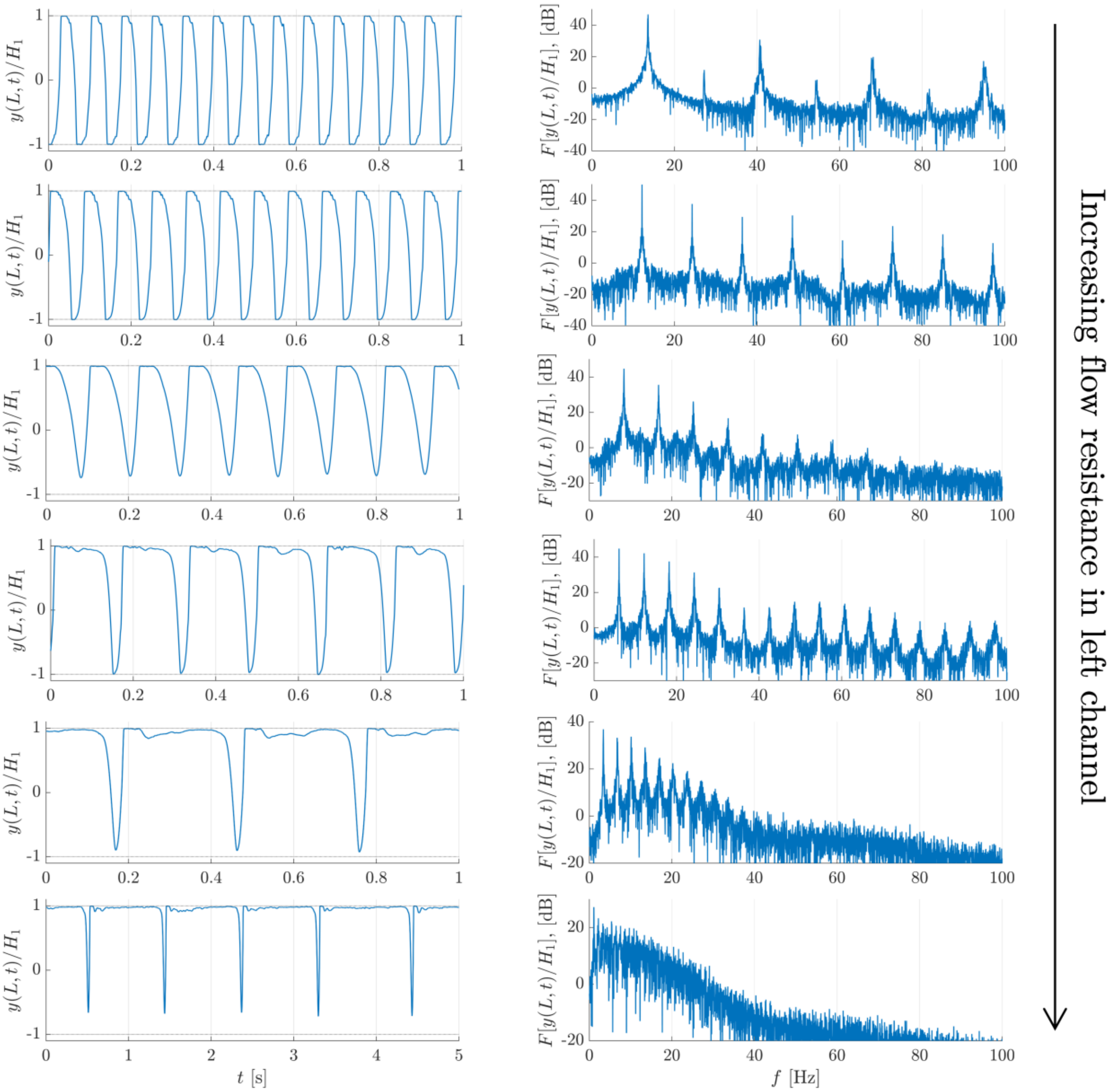

Figure D.4 – Evolution of the beam-tip displacement $y(L,t)\,/\,H_1$ during various LCOs (left) along with its spectra for a system with $M^* = 1.25$. The top plot shows the case where both channels are fully open (symmetric system), while the following results pertain to gradual increases in the flow resistance. The bottom plot shows the case where the left channel is almost fully closed. Note that time and frequency scales are shown in physical units.

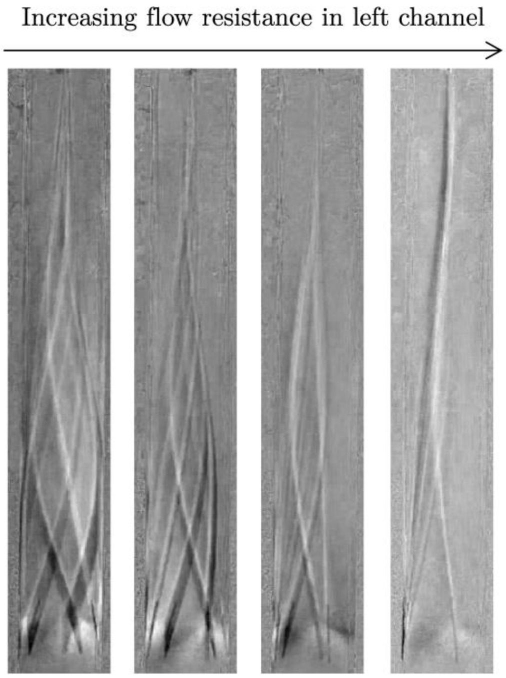

Figure D.5 – Overlapped frames from the video capture illustrating the changes in beam motion as the resistance in the left channel is increased.

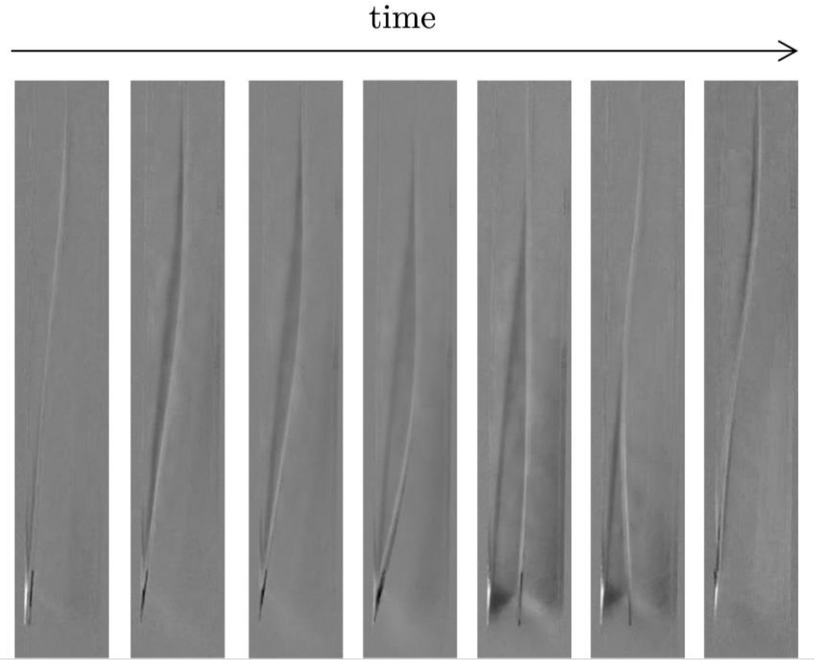

Figure D.6 – Video frames illustrating the beam motion during a low-frequency regime.

D.3 Period doubling and intermittent regimes

Several beams were tested in the previously presented configurations. Overall, their behavior was similar to what was described in the above, demonstrating that this is not spurious behavior encountered for a particular set of parameters, but rather a relatively generic behavioral tendency. We refrain from showing the results of all tested beams for compactness. However, in some cases we have also found other dynamic behavior worth reporting. To illustrate, Figure D.7 shows the evolution of the amplitude A^* and base frequency Ω^* of the LCOs as a function of the flow resistance, for a system with $M = 0.54$. Contrary to the previously shown case, here we note what seems to be some sort of period doubling phenomena. This is noticeable clearly from the spectral evolution at around $U^* = 9.3$. In these cases, we note a break from the general tendency, whereby the fundamental frequency of the LCO appears to be halved, even though in these cases, the second harmonic tends to be the most prominent spectral component. To better illustrate the nature of these regimes, the temporal evolution of the beam-tip and its spectra is shown in Figure D.8 for several illustrative cases at different resistances. Here, the period doubled cases are highlighted with a red background.

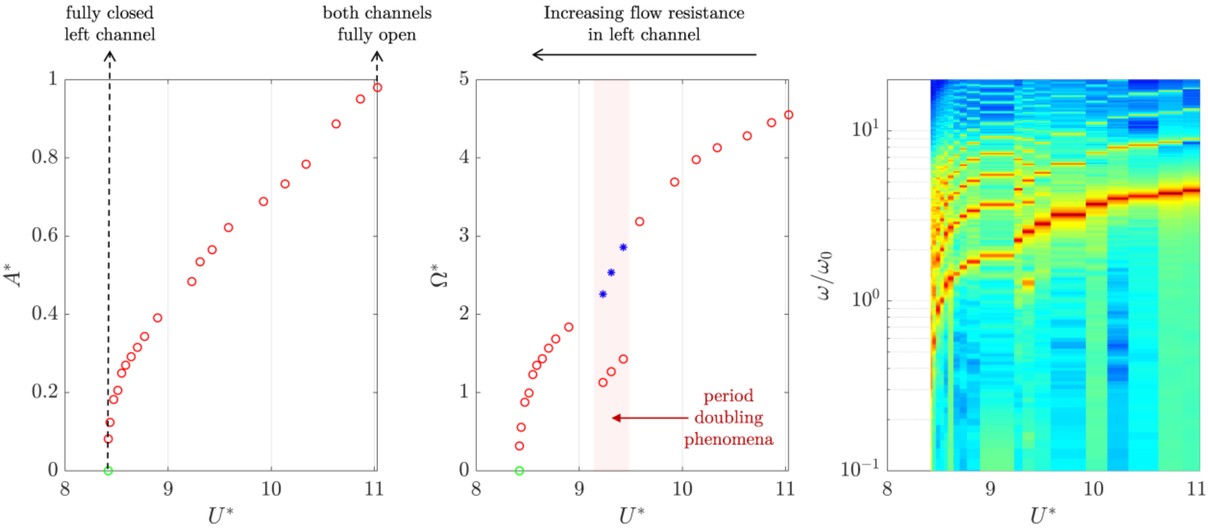

Figure D.7 - Evolution of the amplitude A^* (left), base frequency Ω^* (center) of the LCOs as a function of the (global) flow velocity U^*, in a system with $M^* = 0.54$. The right plot illustrates the spectra of the beam-tip displacement $y(L,t) / H_1$. The red area in the central plot indicates the LCOs where a period doubling phenomena occurs. The blue starts in these cases denote the frequency of the most prominent harmonic component.

In Figure D.8, we notice two LCOs where the period doubling occurs. In the first LCO (second from the top), this period doubling effect is barely noticeable. The solution is almost identical to its neighboring solution (top plot). Its spectra also show odd harmonics with very low amplitude. In the central plot however, we notice a clear distinction between the two beam-tip “detachments”. The period is halved and now the beam-tip impacts the wall twice in each cycle. It is worth pointing out the remarking resemblance of the LCO patterns shown here to the modelling results presented in Figure 3.18. There we also deal with an asymmetric system (channels of different height), and a very similar period doubling phenomena occurs. The video capture associated with this LCO will be provided, for clarity. It is worth noting that such behavior was also found for other beams, again suggesting that this phenomenon is probably not a product of a very specific parametric configuration. Another interesting aspect is related to the regimes where the channel is almost fully closed, as seen in the bottom plots of Figure D.8. As the resistance is increased the frequency of the LCOs can go down to about 1Hz. However, increasing the resistance from there will generally break the periodicity and lead to the intermittent regimes as that shown at the bottom of Figure D.8. The nature of the waveform is close to its neighboring results (which are periodic), but the time interval in between “bursts” becomes irregular, ranging between 1-2 seconds.

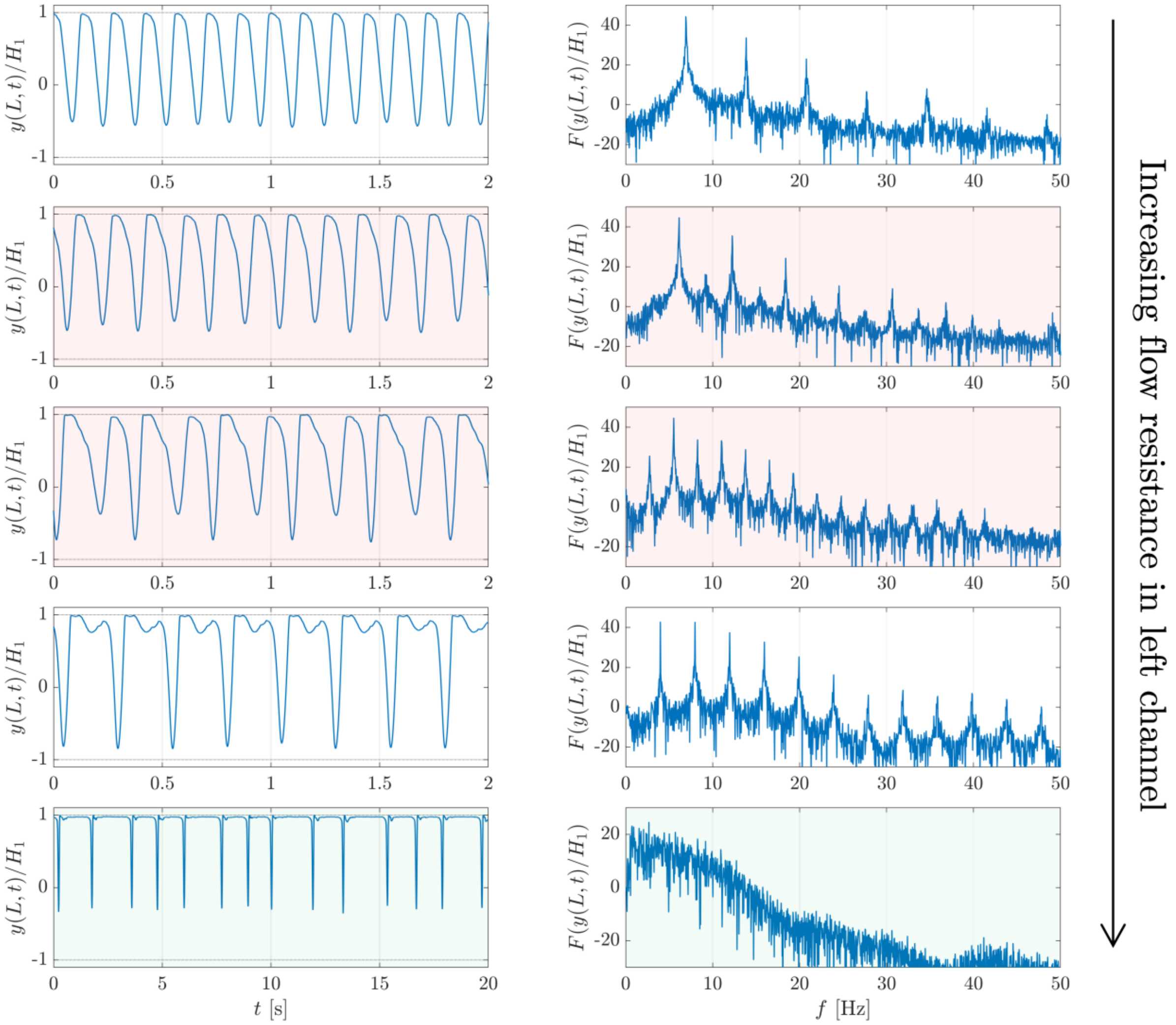

Figure D.8 – Evolution of the beam-tip displacement $y(L,t)\,/\,H_1$ during various LCOs (left) along with its spectra for a system with $M^* = 0.54$. The bottom plot shows the case where the left channel is almost fully closed and the dynamics are not periodic, but rather composed of intermittent bursts, separated by intervals of 1-2 seconds. The red background highlights the LCOs where a period doubling phenomena occurs. Note that time and frequency scales are shown in physical units.

As a final note, the measured behavior in this set-up strongly suggests the existence of a *homoclinic* bifurcation, a type of infinite-period bifurcations. These are relatively rare and commonly observed in conservative systems (often in idealized models). This type of bifurcations is a part of what is often branded *global bifurcations* which represent, like the more common (local) Hopf bifurcation, the emergence or disappearance of periodic orbits (limit-cycle oscillations). However, in these cases, the dynamical behavior at the vicinity of the bifurcation presents different properties compared to the Hopf bifurcation. Notably, the period of oscillation tends to infinity as one approaches the critical point. In homoclinic bifurcations in particular, the stable periodic orbit collapses against a saddle point and the limit cycle effectively disappears at the bifurcation point. These properties are discussed in more detail in (Strogatz, 1994) using simple examples. It is also worth point out that, as underlined in (Strogatz, 1994), in systems with a larger number of degrees-of-freedom (as is our case), many additional bifurcations are possible in the vicinity of a homoclinic bifurcation, often resulting in complex, potentially chaotic, dynamics. Indications of such behavior were also observed in our experiments where intermittent regimes as well as period doubling phenomena were recorded. Without a theoretical model, it becomes difficult to classify precisely this type of bifurcation and its inherent properties and dynamical behavior. However, our experimental results strongly suggest a homoclinic bifurcation, a rare sight in the context of experimental nonlinear dynamics.